SAPIENZA
UNIVERSITÀ DI ROMA

Faculty of civil and industrial engineering
Department of Chemical Engineering Materials Environment
Ph.D. degree in electrical, materials and nanotechnology engineering
XXXIV cycle (2018 -2021)

Ph.D. Thesis

Kinetics and thermodynamic study of the indium electrowinning process using different metal cathodic supports: operative conditions optimization and deposit characterization

Ph.D. candidate
Erwin Ciro Zuleta

Supervisor
Prof. Carla Lupi

Co-tutor
Prof. Alessandro Dell'Era

2018-2021

A thesis submitted in fulfillment of the requirements for the degree of Ph.D. in Electrical, Materials and Nanotechnology Engineering

This thesis was evaluated by the two following external referees:

Prof. Joanna Wojewoda, Polish Academy of Sciences

Prof. Luis Cisternas Arapio, University of Antofagasta

This thesis was also evaluated by the following internal committee:

Prof. Fabio Crescimbini, University of Rome “tre”

Prof.sa Rossana Bellopede, University of Turin

Prof.sa Francesca Nanni, University of Rome “Tor Vergata”

Prof. Giovanni Spinelli, Giustino fortunato University

The time and effort of the external referees in evaluating this thesis, as well as their valuable and constructive suggestions, are appreciated and greatly acknowledged.

To Lindsey and my close relatives

Acknowledgments

I would like to warmly thank the University of Rome Sapienza and Professor Carla Lupi for trusting me and allowing me to grow academically and personally. Her exemplary conduct, patience, dedication, guidance, and respectful judgement is the best training I could have received. In the same way, I wish I would like to thank Professor Dell'Era because of his helpful and kind guidance.

Furthermore, I would like to thank Lindsey Quintero. for her permanent support and accompaniment in every decision. Her presence is invaluable. Likewise, I wish I thank my parents, siblings and close friends who have always enthusiastically encouraged this adventure from the beginning. To all of them, my deep respect and gratitude.

Last but not least, I would like to thank all Sapienza staff (professors and technicians) who charismatically allowed me to make part of its everyday routine.

Table of contents

List of figures

List of tables

List of symbols and acronyms

List of symbols

i_c	Capacitive current
R_{ct}	Charge-transfer stage resistance
C_o^*	Concentration of bulk solution
D_o	Diffusion coefficient
i_0	Exchange current density
C_g	Geometrical capacity
$E_{1/2}$	Half-wave potential
C_i	Internal capacity
C_t	Total capacity
J_p	The current density peak

List of Greek letters

η_c	Cathodic overpotential
α	Dimensionless charge transfer coefficient
δ	Helmholtz plane
k_0	Heterogeneous charge transfer rate constant
μ	Morphology factor
φ	Roughness factor
ν	Scan rate

List of acronyms

AAS	Atomic absorption spectrometry
CA	Chronoamperometry
CD	Current density
CCFL	Cathode fluorescent lamps
CE	Current efficiency
CF	Color filters
CIGS	Copper indium gallium diselenide
CTA	Cellulose triacetate
CV	Cyclic voltammetry
DES	Deep-eutectic solvents
DMSO	Dimethylsulfoxide
EDDS	Ethylenediaminedisuccinate
EDS	Energy Dispersive Spectroscopy
EDTA	Ethylenediamine tetraacetic acid
FWHM	Full Width at Half Maximum
HDD	Hard disk drive
HER	Hydrogen Evolution Reaction

ICP-AES	Inductively coupled plasma atomic emission spectroscopy
ICP-MS	inductively coupled plasma-mass-spectrometry
ICP-OES	Inductively coupled plasma optical emission spectrometry
IGZO	Indium gallium zinc oxide
IL	Ionic liquids
IR/UV	Infrared/ultraviolet
ITO	Indium tin oxide
LC	Liquid crystal
LCD	Liquid crystal display
LDS	Lead smelting dust
LED	Light-emitting diode
LSV	Linear sweep voltammetry
PCB	Printed circuit board
PET	Polyethylene terephthalate
PMMA	Polymethyl methacrylate
PVC	Polyvinyl alcohol
SCE	Saturated kcl Calomel Electrode
SEC	Specific energy consumption
SHE	Standard hydrogen electrode
TFT	Film transistor system
TPP	Triphenyl phosphate
WEEE	Waste of electrical and electronic equipment
XRD	X-ray diffraction
XRF	X-ray Fluorescence
I_{pa}	Anodic current peak
I_{pc}	Cathodic current peak
E_{pc}	Cathodic potential peak
E_{pa}	Anodic potential peak
E^o	Formal potential
E_p	Peak potential
OCV	Open circuit voltage

Abstract

The excessive indium demand in the existing markets for the manufacture of indium-based high-tech devices (solar panels, optoelectronic systems and liquid-crystal display (LCD) units) has promoted a shortage scenario of indium from primary supply routes. With emerging indium supply restrictions, the spotlight is on determining painful secondary sources and their respective efficient and eco-friendly treatments. Wet electrometallurgy, combined with separation/leaching /enrichment stages, has been highlighted as one of the most useful methodologies to recover indium from electronic waste (obsolete LCD screens) due to the operative parameter adaptation and high occupational and environmental safety. To date, chloride electrolytes have been widely used for indium electrowinning without considering critical challenges. In contrast, sulfate electrolyte shows lower environmental impact and higher efficiencies than conventional acidic solutions. This solution has been disregarded to carry out the indium electrowinning. In this doctoral investigation, the indium electrowinning process is studied from sulfate solutions considering the kinetic features of the indium reduction reaction near the cathodic surface. Also, the influence of operative parameters on productivity and energy consumption has been analyzed. Initially, a critical outlook of the indium processing was performed considering different sources, electrolytes and methodologies to determine the main strengths, drawbacks, and targeting concerns that should be studied. Apart from this, the kinetic study of the indium reduction reaction near the cathodic surface was carried out using copper, titanium, aluminum, nickel and stainless-steel cathodes (Cu, Ti, Al, Ni and AISI 316L) as cathodic supports. These metal cathodes were assessed by cyclic voltammetry (CV) and chronoamperometry (CA) techniques. CVs described features of the indium cathodic curve and the hydrogen evolution reaction (HER) influence. Since HER is a parasitic reaction, kinetic parameters, such as heterogeneous charge transfer rate constant (k_0), charge transfer coefficient values (α), diffusion coefficient (D_0), roughness factor (φ) and the exchange current density (i_0), were calculated without HER interference. In the case of the i_0, the values were equal to 1.20 mA/cm^2, 0.30 mA/cm^2 and 0.075 mA/cm^2 for Cu cathode Ti and Al cathodes, respectively. Further correlations for previous parameters were held using both CV and CA. In fact, the k_0 values for Cu, Ti and Al cathodes were $7.1 \cdot 10^{-5}$ cm/s, $6.2 \cdot 10^{-5}$ cm/s and $5.4 \cdot 10^{-5}$ cm/s. Once indium reaction reduction kinetics near the cathodic support were analyzed, the indium electrowinning process was performed in long-lasting tests to achieve high and low energy consumption. In addition, operative conditions were optimized using five different metal supports. Therefore, the indium electrowinning was evaluated by varying operative conditions (current density, electrolyte composition, pH and temperature) using different metal supports (AISI 316L, Ni, Cu, Ti and Al). The optimization of the indium electrowinning process was focused on achieving high current Efficiency (CE) and low specific energy consumption (SEC). The performance of AISI 316L, Ni and Cu supports were significantly influenced by the electrolyte composition, while Al and Ti showed better results using merely the indium

sulfate solution. Comparing AISI 316L, Ni and Cu support, nickel showed a significant increase in productivity (around 83% and 2.4 kWh/kg) working at 100 A/m^2 with respect to AISI 316L and Cu supports, that can efficiently operate at 25 and 50 A/m^2, respectively. Otherwise, Ti and Al depicted high CEs above 80% and reasonable SEC values using an etched cathode to improve the adhesion conditions between cathode and deposit. These electrowinning outputs for both cathodes demonstrated that the surface pretreatment improved the productivity in terms of high CE and low SEC for the indium recovery. The deposit showed very-well defined polygonal grains covered by a lamellar morphology. While in most cases, temperature increases negatively affect the crystallographic features of indium deposits.

Introduction

The increasing demand for indium as indium-tin-oxide (ITO) has led this metal to become a strategic material for the international technology markets. Most of these devices are represented by flat displays, televisions and cellphone screens, optical sensors, optoelectronic systems and solar panels [1]. Recently, indium has been declared by the European Commission and the United States Department of the Interior as a critical material for technological development due to its relationship with industry and its application in modern renewable energy technologies [2–4]. The denomination of indium as 'critical material' has also been based on the excessive requirement and supply risk from conventional primary sources [2]. To permit worldwide indium supply, industrial extraction has widely been carried out from traces or by-products in sulfide ores of zinc, copper, tin and lead [5]. Although it is well known that indium concentration in the earth's crust reaches low values close to that of silver (~ 0.1 ppm) [6], its production has increased about 81% in the last three decades to support the ITO consumption [7]. Belgium, France, Canada, South Korea and China constitute the most relevant countries responsible for the global supply [8], controlling almost third-quarters of the total manufacture of indium (545.000 t/year) [9,10]. The imbalance ratio between availability and indium demand exhibits an evident shortage scenario [8,9].

Recently, indium was also found in the waste of electrical and electronic equipment (WEEE), with contents between 100 and 400 ppm [5], meaning a significant potentiality to recover these strategic metals through efficient and affordable recovery methodologies. In this regard, hydrometallurgical processes have often focused on ITO to obtain indium in the metallic state. By using electrowinning, it is possible to achieve low energy consumption and high recovery efficiencies. These desirable outcomes can be reached by controlling operative parameters (temperature, pH, current density and electrolyte composition). Attempts for indium recovery via electrowinning have been the subject of several studies using chlorine and nitric solutions [11,12], while sulfate solutions were hardly employed. Chloride solutions have offered current efficiency (CE) values above 85% in a broad range of current densities. However, the fact that chlorine evolution occurs during electrowinning, which is a toxic gas responsible for poisonings and chemical corrosion of facilities [13], the performance is altered by environmental and safety concerns. Therefore, significant investments in sealed cells and collection/abatement of chlorine gas at the anodic compartment are required.

On the other hand, other sulfate solutions could contribute to indium recovery via electrowinning, presenting safer, more affordable, and eco-friendly conditions. In fact, by working with sulfate solutions, the anodic reaction is related to water oxidation, where diatomic oxygen gas is produced. In that context, sulfate solutions are a promising alternative to recovering indium by electrowinning since they are less

susceptible to endangering the environment than chloride ones. Nonetheless, the indium electrowinning from sulfate solutions has not been considered. The first, reliable works indicated that sulfate baths for indium electrowinning barely could reach 80% CE, and energy consumption analysis was practically omitted despite being a remarkable parameter foreseeing the energetic viability of the process at pilot or industrial scales [14,15]. Thus, the main reasons to undertake this doctoral investigation are the lack of enough related literature to understand the indium reduction reaction near the cathodic surface and the influence of the operative conditions on the electrowinning outputs. In that perspective, this doctoral research has demonstrated that indium production via electrowinning could be carried out by more eco-friendly, economic and versatile means from sulfate solutions to achieve high productivity and low energy consumption. Thus, the doctoral research hypothesis is stated following:

Indium production via electrowinning from sulfate solution is a versatile, economical and eco-friendly way to achieve high productivity and low energy consumption.

Due to limited literature about indium recovery from sulfate solutions, it is essential to consider initially the indium/metal support interactions before performing electrowinning. Thereby, an electrochemical study of the indium electrodeposition is proposed to determine phenomena near cathodic support and the viability of the indium reduction process from sulfate solutions. Furthermore, such viability is also focused on the gas evolution at the anodic side, given that the conventional indium electrowinning utilizes chloride-based solutions, causing a problematic chlorine evolution at the anodic compartment for health workers and facilities. Analogously, it is necessary to evaluate the indium electrowinning process to determine if this metal could be galvanostatically electrowon by using different metal supports and sulfate solution as an electrolyte. Once indium electrowinning is feasible, it is required to optimize the electrowinning outputs by studying the influence of both cathodic and operative conditions (current density, temperature, pH, electrolyte composition). Two research questions were outlined, seeking to strengthen the doctoral research hypothesis.

- *Does indium reduction reaction near cathodic support using different metal supports and sulfate solutions as electrolytes occur?*
- *Does indium reduction occur on the metal supports without the presence of hazardous gas evolution?*
- *Is it possible the optimization of the galvanostatic indium electrowinning outputs by analyzing cathodic support metal supports and operative conditions?*

Therefore, this doctoral research initially focused on the kinetic study near the cathodic surface and other electrochemical features to understand the indium reduction reaction in sulfate aqueous solution. Based on these statements, this doctoral research evaluates the sulfate solution effectiveness for the indium recovery by electrowinning. Typical metals were selected as cathodic supports: stainless steel, nickel, copper, titanium and aluminum (AISI 316L, Ni, Cu, Ti and Al). These metal cathodic supports were evaluated to optimize the electrowinning outputs (CE and SEC) and analyze the deposit quality in terms of the morphology and crystallographic features of the deposit. Also, the indium electrowinning process in sulfate solutions was optimized with operating condition variations (pH, temperature, electrolyte composition and current density) in each metal support. Prior to starting with electrowinning tests, the metal supports were analyzed by cyclic voltammetry (CV), chronoamperometry (CA), linear sweep voltammetry (LSV) and potentiostatic tests to determine electrochemical features, such as reduction-oxidation process, the overlapping process between hydrogen evolution and indium reduction, stripping reaction, nucleation potential, etc. Furthermore, this electrochemical evaluation permitted individuating the interactions between metal cathode surface and sulfate solution (bulk) and the influence of the parasitic hydrogen evolution reaction (HER). This doctoral thesis introduces a brief outlook of indium as raw material from mineral and secondary sources, followed by the most representative recovery methodologies (Chapter 1). Chapter 2 discusses electrowinning principles and the most representative findings using aqueous and non-aqueous electrolytes. Chapter 3 is associated with experimental methods used. Also, a kinetic study about the indium reduction reaction was performed using Cu, Al, Ti, Ni and AISI 316L cathodes. The previous findings were presented in Chapter 4, including nucleation and determining electrochemical features from the indium electrodeposition reaction. Moreover, the optimization of the indium electrowinning process using different metal supports and operative conditions (temperature, pH, chemical composition of electrolyte, and current density) arises in Chapters 5-9. At the end, synergic comparisons among metal supports were performed to establish the proper metal cathodic support and its respective operative conditions, in which indium electrowinning can be efficiently and affordably carried out (Chapter 10).

Chapter 1:
Indium recovery from primary and secondary sources: critical outlook

1.1. Indium as a technological material

The great interest in indium has been justified by its countless applications, mainly summarized in solders, flat panel displays, solar cells, thermal interface materials, surface heaters, batteries, camera lenses, mirrors, smart windows, etc. [16]. Indium versatility is due to many properties such as high ductility, malleability and low melting temperature (156.6 °C) [6]. The United States government and European Commission led indium to be designed as a critical and strategic metal due to its shortage risk from primary sources [7,17]. The current high-tech market and emerging renewable energy technologies promote a critical scenario characterized by the misbalance between the availability of mineral quota and its excessive demands. The increasing manufacture of indium-based applications started with a fleeting apparition as a pure metal in protective coatings on aircraft engines [18]. Although a good performance was hardly observed due to low mechanical properties, the best performance has been observed in alloys and complex compounds. A vast range of indium alloys has been manufactured and studied according to their properties. Some of them comprise indium-bearing welds (In-Pb and In-Ag) and light-emitting diode (LED) [19]. Nonetheless, a considerable number of studies has been driven to explore intensely high optoelectronic properties.

The maximum semiconductive performance has been reflexed on ITO, generally composed of 90% In_2O_3-10% SnO_2. The use of ITO has exponentially grown in the last decades due to suitable optoelectronic performance that can be applied as coatings for flat screen displays, smart windows, polymer-based electronics, photovoltaic cells and IR/UV polarization glass etc. [16]. Among those applications, liquid crystal display (LCD) uses indium as transparent conductive thin films in more than 50% of the indium market. These films reach anti-reflective, high transparency and electroluminescence performance on screens [20]. Moreover, the versatility of indium in the sensoring field and green energy production have demonstrated a potential route. For instance, as applications also can be seen: light-emitting diodes (LED) [21], transistors and laser diodes [22]; as well as the manufacture of photovoltaic cells using quaternary compound (Ga, Se, Cu) to form the second generation thin-film CIGS solar cells [23]. Therefore, the elastic properties make indium highlight in different technological fields, promoting a progressive rise of the global indium-quota threaten the development of ITO-bearing devices with an eventual shortage scenario of primary sources.

Primary extraction has represented the only manner to supply metals for a long time, including indium. In fact, indium has been commonly extracted from aggregates or by-products in sulfide ores of zinc, copper, tin and lead [5,24]. The worldwide output of indium primary mining from 2010 to 2019 can be seen in Figure 1. One of the most significant suppliers corresponds to China, which reached around 55% of the total primary indium production in 2010 (340 t/y), followed by other countries such as the Republic of Korea, Belgium, Canada, Japan and Peru [25,26]. In the following years, China continuously increased the growth till reaching 535 t/y in 2019 [27], whereas the

Republic of Korea has followed a similar tendency with growth greater than 31%. Otherwise, Japan and Canada virtually remained unchanged during this interval; nonetheless, the Japanese country has been highlighted by consuming around 60% of the total indium (primary and secondary) declared in 2011 [21]. Both experts and trends agreed that movement occurred likely due to widespread leadership of the Japanese high-tech manufacture. Furthermore, it is well-known that indium concentration in the earth's crust reaches low values close to that of silver (~ 0.1 ppm) [6], but its production has suffered a notable increase in the last years [7], as can be seen on red-dotted line in Figure 1 passing from 609 t in 2010 to 960 t nine years later. Thereby, the current indium supply exhibits critical concerns from different perspectives, involving replacement strategies, novel sources of raw material, as well as affordable and lower-impact environmental extraction methodologies.

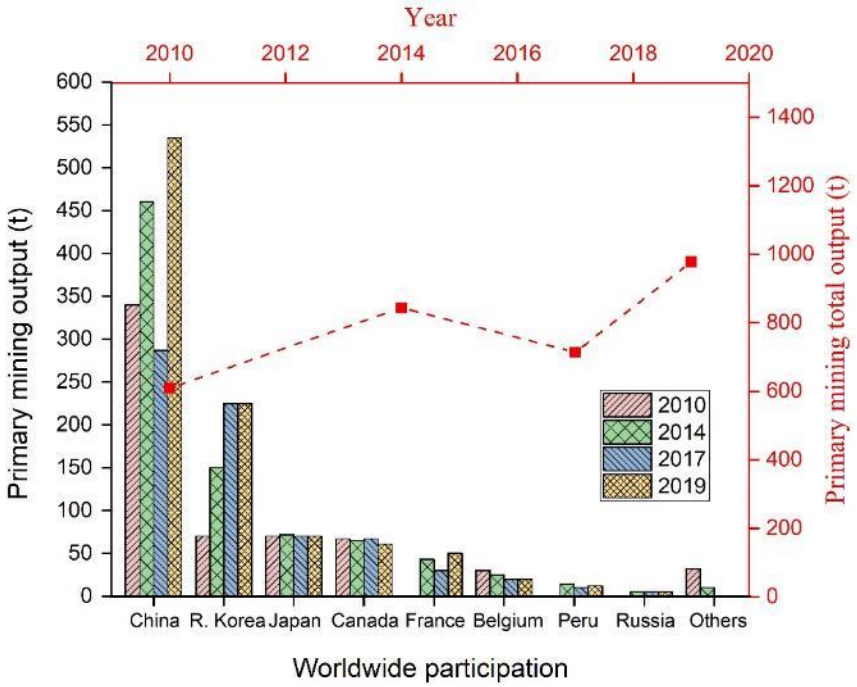

Figure 1. Worldwide output of primary indium mining contained in refinery production and reserves. The red-dotted line indicates the primary mining total output in the last decade. This figure was performed based on the data published by U.S. Geological Survey [21,27–29].

1.2. Indium recovery from primary and secondary sources

The ongoing shortage scenario for indium supply has led to considering primary sources and alternative ones, latter known as secondary sources. Since indium from minerals corresponds to a natural formation denominated aggregates or by-products from zinc, copper, tin and lead ore, actual amounts of indium are limited, varying in a concentration range from 50 to 200 ppm [6]. In numbers, global reserves that contain indium are estimated to be around 16-19 kt representing one-sixth of the available gold ore [30]. The indium extraction from primary sources is currently carried out because of the zinc, copper, lead production [31,32], but indium mining is virtually disdained due to environmental and energy consumption concerns. Investigations have addressed their scopes toward indium recovery from mineral tailings or slags, attempting to reach a maximum benefit from remaining minerals [33–36]. Cost-benefit, unstable availability and varying indium concentration could suppress effectiveness and positive features from extractive methodologies, causing those tailings to be underestimated.

On the other hand, indium recovery from WEEE is considered a novel and environmentally friendly way to supply indium. In most cases, WEEE is defined as a secondary source or even the base of the so-called urban mining. Therefore, a considerable extension of works explains the indium recovery mainly from LCD panels, ITO targets, and ITO glass. Although this overview considered minerals as part of samples used for the indium recovery, most of the present work will take into account the spent LCD panels and other electronic waste as secondary sources to carry out the indium recovery.

WEEE is considered an evident raw material that has several advantages rather than primary ores, such as lowering sources consumption (electricity, reagents and water), the benefit of high concentration of metals in WEEE, and occupational health improvements because of hazardous minerals and metals absence (asbestos, radioisotopes). Nonetheless, different concerns regarding high productivity and efficient energy consumption are the main outputs affected and required to be investigated. Those concerns are presented in different categories: (i) sample complexity and (ii) suitable extractive processes. Regarding the sample complexity, serious questioning on the internal disposition of metals within end-of-life devices encourage novel extractive treatments as the subject of study. Metals often arise in WEEE as bulk pieces (Nd-Fe-B magnets), wires, thin films (ITO, In_2O_3-SnO_2) or coating in high purity rates (Au, Ag, Cu). Those metals play a crucial role in devices by which they are firmly integrated or embedded in matrixes made of steel sheets, polymers and glasses. Therefore, suitable methods to treat complex samples represent the main shortcoming that should be defeated to reach an efficient, continuous and affordable metal recovery.

In this context, although inert fractions are recoverable and have an economic value in the market, the target extraction is focused on metals where their physical, optoelectrical and chemical properties are superlative. Then the electronic waste

requires attention on both metal concentration and its arrangement inside the end-of-life equipment. By illustrating this statement, magnetic alloys (Nd-Fe-B magnets) from discarded hard disk drives (HDD) are a clear example that bulk pieces can be feasibly recovered, even via manual dismantling [37–39]. In the case of samples in which valuable metals are present in coatings of few-micron layers, such as printed circuit board (PCB) and liquid-crystal display (LCD), real challenges can occur. Firstly, PCBs are targeted as a suitable gold secondary source allowing its recovery through conventional leaching processes [40]. Secondly, LCD is a complex, multilayer structure conformed by compact sandwich-type planes at which two glass plates (substrates) are filled by a liquid crystal (LC) layer in the middle. Without further dismantling processes, such complexity in arrangement prevents the indium recovery. Hence, this is a critical step for indium recovery from LCD, but remarkable indium concentrations in that residue (100 – 700 In mg/kg glass ITO) still make their recovery attractive [41,42]. In Figure 2a-b it is observed the exploded view and the cross-section of the LCD panel, respectively. The layer arrangement indicates that two substrates have a polarizing film that filters the input and output light signal. These polarizing films are commonly conformed by polyethylene terephthalate (PET), cellulose triacetate (CTA), polyvinyl alcohol (PVC) and triphenyl phosphate (TPP) [43].

Furthermore, both the thin-film transistor system (TFT) and the color filters (CF) are embedded in glass substrates from the bottom and top sides of the LC layer, respectively. The former refines the polarized light, while the latter can distinguish red, green and blue patterns (RGB filter), giving a coloring display. Those substrates are generally characterized by simple glasses (low alkalinity and thermal expansion coefficient) [44]. Likewise, ITO, containing 90 wt.% In_2O_3 and 10 wt.% SnO_2 (doping material) is immediately found on both the top and bottom sides of LC, working as pixel and a common electrode for TFT and CF sections due to its remarkable properties such as high conduction and transparency (Figure 2b).

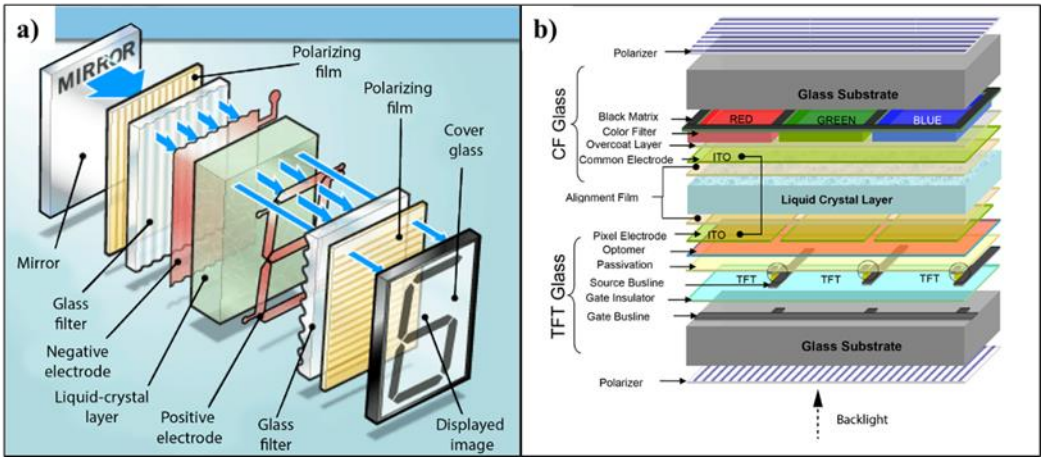

Figure 2. Graphical representation of the LCD panel: a) exploded view and b) cross-section [44,45].

Beyond the place that indium takes up in LCDs, another relevant aspect to be considered is indium availability. The indium metal in end-of-life devices is presented in discarded liquid crystal displays (LCD) of several flat screens (laptops, televisions, touchscreens, cellphones, photovoltaic cells, etc.). This heterogeneity proposes pretreatments of collecting and classification to homogenize LCD glasses samples for indium extraction [46]. In that context, given that indium is deposited in thin films on the glass screens, different sizes suggest a variation in indium concentration. Souada et al., in 2018 have estimated the indium concentration in LCD waste based on the thickness of ITO layers [47]. Considering ITO contains about 74 wt.% and 8 wt.% Sn, around 2 g and 3 g could be recovered from an LCD monitor with 85 inches in diagonal (4 m^2) if it presents ITO layers close to 100 and 150 nm [47]. However, there is a limited number of reports considering the indium concentration from ITO layers. This fact causes difficulties for comparison since most of them have employed a more functional relationship between indium weight and ITO glass weight (mg In/kg ITO glass).

Four typical values of thicknesses for ITO glass of 0.4, 0.55, 0.7 and 1.1 mm have been considered, where the latter is the cheapest and consequently the most common thickness. Thus, larger sizes should imply higher indium amounts to be recovered, meaning that the target LCD glass is placed on monitors (from 10 to 30 in) and TV screens (from 19 to 105 inches). Since different dimensions of panels can take place, attempts to estimate the indium content, in some way, could be confused or misunderstood. Hence considering the surface of both layers (TFT and CF), standard ITO density, the indium concentration and supposing 0.11 cm ITO glass thickness, it is possible to suggest a relative value of indium content in grams [47]. For instance, Li et al. used 14 inch LCD screen panels, with a 1210 cm^2 surface and 244 mg In/kg ITO, estimated around 81 mg In [48]. Similarly, by following this analysis on different works considering screen types and their indium concentrations, it has been obtained that 19 and 40 inch LCD screens have a potential indium weight to be recovered (around 0.5 and 1 g, respectively) [44,49].

The indium content in obsolete LCD, minerals and other secondary sources, along with the respective characterization technique used, can be seen in Table 1. This examination allows identifying in the published literature that the indium content varies broadly between 120 and 636 mg/kg in LCD waste, while ITO targets show relevant indium concentrations and high purity. This lack of uniformity is also observed in how authors nominate LCD samples, referring LCD screen or ITO glass to the indium in LCD panels or just the glass released from polarizing films. Based on the previous, there is no precise terminology to properly define the obtained pieces throughout the available literature on indium recovery since each author defines its terms. Thus, henceforth, the LCD panel, unit, screen, or electronic waste will refer to the dispositive without modification. In the case of glass pieces that still contains polymeric fraction including polarizing films, CF, TFT or LC layer, this outlook will be uniquely defined as LCD glass, ITO panel or ITO LCD. Whereas if only the glass is free of polymeric coatings and contains ITO will be named ITO glass. Overall, based on the above mentioned, LCD

waste is undoubtedly a suitable secondary source of indium where the indium concentration is presented in high contents compared to primary resources [50]. Furthermore, although subsequent extractive processes are required to obtain pure indium metal from LCD waste, environmental and technical advantages from secondary sources markedly highlight rather than conventional mining. Therefore, it is necessary to promote the design and development of methodologies to obtain strategic metals from waste.

Table 1. Several indium-bearing sources (LCD screen, ITO glass and targets, and mineral tailings). n. a.: not available

Starting sample	Characterization Method	Indium content (mg/kg)	Reference
ITO glass	XRF	120	[51]
ITO glass	EDS	n. a.	[52]
ITO glass	AAS	~34 g/L	[53]
LCD screen	ICP-AES	108	[54]
LCD screen	ICP-AES	315	[55]
LCD screen	ICP-AES	n. a.	[49]
LCD screen	ICP-AES/XRF	494	[56]
LCD screen	ICP-MS	530	[57]
LCD screen	ICP-MS	~125	[58]
LCD screen	ICP-MS	356	[59]
LCD screen	ICP-OES	393	[60]
LCD screen	ICP-OES/XRF	258	[61]
LCD screen	ICP-OES	244	[48]
LCD screen	ICP-OES	n. a.	[62]
LCD screen	ICP-OES	200 ± 50	[46]
LCD screen	XRF	636	[50]
LCD screen	XRF	164	[63]
LCD screen	XRF/ ICP-AES	480 ± 25	[64]
LCD screen	ICP-MS	272 ± 31	[65]
LCD unit	AAS	~288	[66]
LCD unit	ICP-EOS/XRF	276	[67]
ITO target	ICP-OES	22.2 g/kg	[68]
ITO target	Volumetric analysis, Polarography and ICP-AES	712 g/kg	[69]
Zinc residue	Titration	942	[31]
Zinc residue	ICP-MS	86	[70]
Indium-bearing Zinc ferrite	ICP-MS	510	[33]
Zinc Slag	ICP-OES	3.5 g/kg	[36]

1.3.Secondary material dressing for the indium recovery

The significant amount of indium in electronic waste (LCD panels, ITO targets) makes them as a secondary source, the need for adequate methodologies capable of reaching proper waste management that involves terms like the green economy or circular economy, where there is a fair combination of both high indium recovery rates and environmentally friendly treatments (Figure 3). Firstly, due to the zinc, lead or copper extraction process in primary extraction, the indium appears as by-products to be alternatively treated. Once those primary ores undergo comminution, concentration and extraction treatments, by-products are then concentrated, refined and melted to obtain indium metal (ingots). Primary extraction is necessary processing since indium only arises after an enormous volume of minerals are removed, causing critical drawbacks such as high water and energy consumption, as well as fine powders, overburden and pollutant emission (liquid and solid tailing discharges, piles, and wastewater, etc.) [63]. Even though industrial-scale mining tackles complex environmental challenges, strict governmental regulations have been already imposed, more intense in developed countries than developing ones, to carry out this economic activity with the lower negative effect on fauna, flora and human health. When indium is produced from mining, it follows the productive chain where many kinds of devices, gadgets and products are manufactured (TVs, LCD flat screens, LCD glass, sputtering targets, welding, etc.). However, the rapid obsolesce has led these products to have intentionally short life spans, faster replacement and overproduction. Since metals used in those devices come from primary sources and are present in a limited concentration in nature, it is evident that metal such as indium faces an eventual shortage.

Secondly, when devices are thrown out and considered WEEE, they must be collected. This first step must be utilized to classify and stock up several waste types. Hence, similar to minerals, WEEE has to be undergone a dressing process. These early stages are required to accomplish a significant role in homogenizing WEEE, including LCD waste. The classification also will be reflexed on the effectiveness and efficiency of the recycling process. Reuse and repairing seem to be the most economical treatments for re-utilization, yet this option is only possible if original models work and exactly match starting ones. Some proposals for traceability of LCD waste, for example, have also been suggested to reduce uncontrolled residue streams in storage and return reusing pieces to manufacturers [71]. However, this conception remains worldwide in developing stages. The fact that most LCD panels have been treated, where the output quality can be roughly maintained, make unlikely the reuse. Therefore, the successful re-utilization is depicted in follow-up methodologies that separate and extract the most valuable fractions. These steps will be explained below in detail.

Currently, indium recycling is considered a profitable business involving huge economic possibilities and technical challenges. The chance of an affordable indium recovery has been suggested to maintain at least a concentration in electrolyte between

2 and 3 g/kg (lowest economic grade reported in hydrometallurgical indium refiners) [63]. This recovery could be achieved if different indium sources (LCD waste, spent ITO targets and mining tailings) are integrated into the recovery process. Since LCD waste could represent the leading source for indium recovery, the eventual commercial indium recycling bottlenecks falls on cost-efficiency aspects [72]. To date, all published investigations have been developed at a laboratory scale, designing processing layouts for dismantling, grinding, acid leaching, and diverse methodologies for extraction and purification. However, the recovery from waste still referred to indium refining from metallurgical plants for zinc and lead ores. Suggestions for this situation is associated with the available indium tailings and extraction facilities. Although sufficient investigations for indium extraction from end-of-life LCD, it seems that it is not enough to articulate businesses at larger scales for lucrative scopes. Based on the literature, ITO-based waste recycling could be economically affected on transportation and storage. Nonetheless, favorable policies start to be promoted (depending upon each country) to well-disposed dangerous, volumetric and difficult-treating electronic waste. In short, it is clear that large scale businesses for indium recycling require much more investments than those mentioned above. However, the present conditions lead to indium recycling being considered a potential supply source.

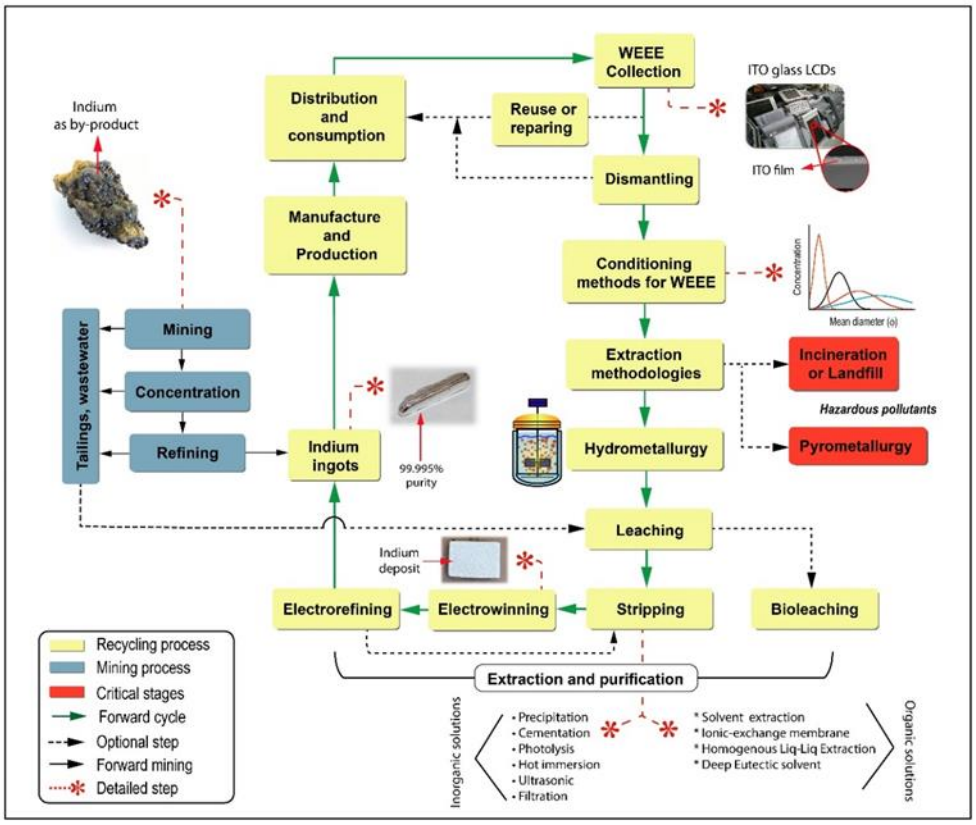

Figure 3. Closed-loop flowsheet of the indium recovery from secondary sources, revealing both indium supply can be reached from ITO waste (mainly ITO LCD) and primary mining residues. Some images were taken and adapted from [73–75].

1.3.1. Dismantling and mercury separation from LCD waste

The main ITO source is attributed to LCD waste more than others. Nevertheless, this waste comprises issues related to complex ITO access. Thereby dismantling is a mandatory stage in which LCD panels must be undergone to homogenize and concentrate indium, influencing the recovery process downstream [76]. The dismantling consists of separating, classifying and homogenizing metals, polymers and glass inside LCD waste from useless fractions. Given that indium is the desired metal, recycling is driven to its separation from obsolete LCD panels. Several LCD processing flowsheets have individualized a logical guideline to treat LCD glass to obtain ITO glass in powders using different LCD types. Regardless of the treated residue, these processes then agree that the dismantling, collection, polarizing film removal and comminution are required steps to obtain ITO glass from protected or attached polymeric phases (polarizing films, LC layer, etc.) [48,53,54,57,77].

Recently, a detailed dismantling process has been developed by Ferella et al. [67]. This work focuses on the complete description of the LCD panel components in order to valorize relevant fractions from obsolete LCD panels, including indium [67]. Figure 4 shows the schematic flowsheet for the manual dismantling of LCD screens that allows reaching adequate conditions for physic mechanical treatments where LCD panels are subsequently ground. Manual operations should roughly separate high amounts of metals, polymers and glass fractions through standard workshop tools in short periods [78]. The subsequent classification then gives rise to the main component classification for screens: the back/top cover (representing 30% wt.) can be removed to obtain PCBs and cables (those pieces correspond to 11% wt.). Zinc-coated steels in sheets and crews (around 33% wt.), and mounting frames polymeric seals and similar parts (polycarbonate, Teflon, PET, PMMA and silicone) are related to about 6% wt. Whereas the LCD panel corresponds to around 11% wt. and the lighting system comprised close to 9% wt. [67].

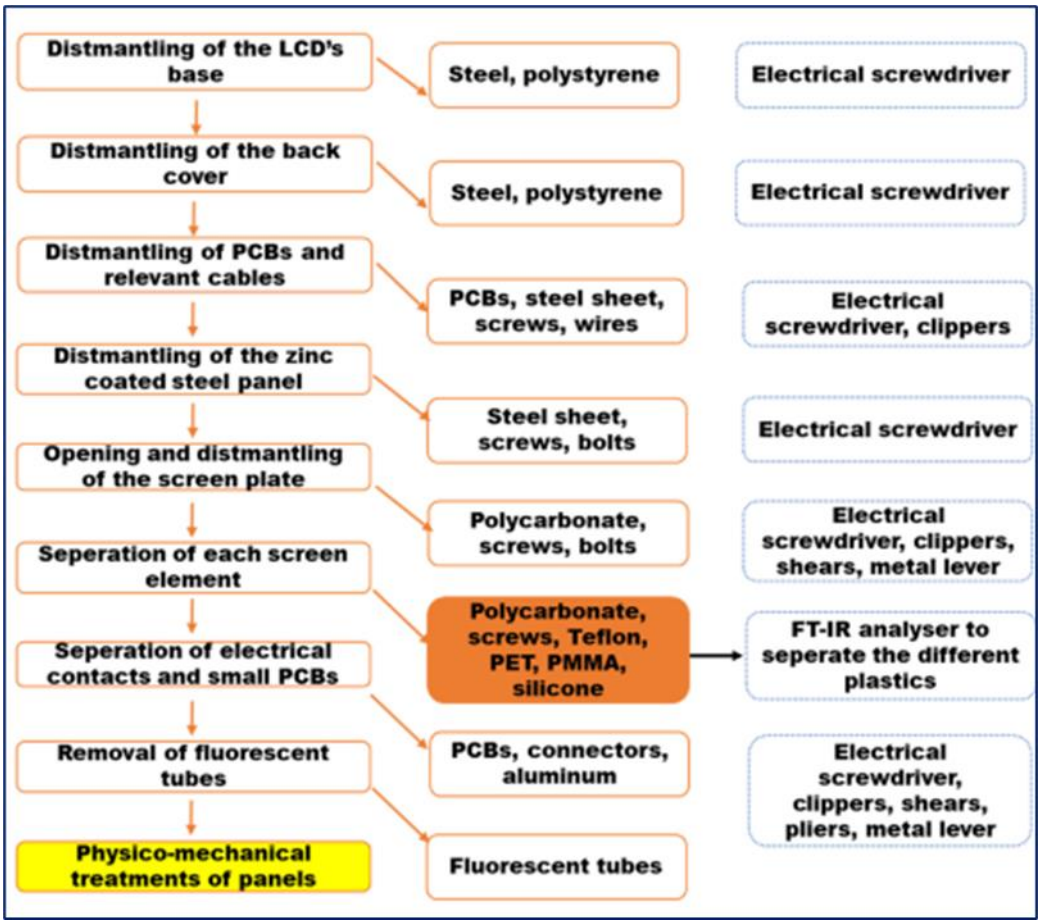

Figure 4. Flowchart of the manual dismantling process from LCD monitor entails the separation of metal, polymeric and glass fractions till reaching the physic-mechanical treatments [67].

Prior to going through the comminution processes, screen waste must be inspected to identify whether LCD units are equipped with cold cathode fluorescent lamps (CCFL), whose chemical composition might reflect the mercury presence. Thus, the mercury isolation from backlighting units is a mandatory step to avoid a potential mercury spread and preserve both the environment and the worker's occupational safety during the recycling process. Thereby backlight and lightbox units should be isolated from the indium recycling process. Although mercury is a minority in those units (1% of the overall LCD, [78]), its intrinsic physical properties make mercury inadmissible and challenging. Further, sealing conditions and even non-anthropic operations are recommended to preserve the environment and worker safety during the dismantling process. For instance, 80 million LCDs were worldwide distributed in 2010, estimating significant Hg amounts to be recovered (between 290 and 490 kg) [78]. Therefore, at an industrial scaling-up forecast for indium recovery, the presence of mercury in the backlight containing CCFL comprises one of the most severe challenges to achieve proper disposal and elude its release outdoors and contaminate waste free of mercury.

1.3.2. Physic-mechanical treatments for release ITO glass from LCD waste

From physic mechanical treatments, indium concentration and quantification are favored by detaching the polarizing film from different ITO-bearing samples (ITO glass, LCD screens) [50,77]. Cutting, crushing, grinding, shredding, milling, sever milling and other procedures have been recommended in most published investigations to reduce the particle size. Table 2 summarizes the main pre-treatments used to ground, separate and concentrate indium from LCD waste from the open literature. Although the particle size reduction is undeniably required for the indium recovery from ITO glass, spotlighted drawbacks are high energy consumption and environmental problem due to fine powders (lower 100 μm) overproduction. Although faster kinetics could be reached in the leaching and recovery process, ecological and technical concerns are involved due to dusty pile abatement (effectively handling powders) [64]. Therefore several investigations have focused on optimizing the mechanical treatments by comparing different equipment regarding particle size and energy consumption [50,59,63,77]. However, a systematic analysis in terms of the lower energy consumption and implementation of alternative non-crushing methodologies should often be carried out in order to valorize not only metal but also glass. To date, few studies have taken into account the glass recovery after the ITO stripping, giving an added value for ceramic and cement fields [79,80]. Additionally, Notable profits regarding lower energy consumption and lower chemical reagents have been achieved compared to those obtained with conventional crushing treatments [51,62].

The indium, plastic and glass recycling from ITO panels at an industrial scale have been rarely undertaken. In some cases, that residues are landfill and incinerated. However, those methodologies are useless to valorize them or even recovery metals. Thus, novel extractive methodologies are required to recover indium through an industrial valorization route. Therefore, by considering the valorization of alternative material streams, treating hazardous waste in proper dismantling facilities and critical optimizing steps like comminution, indium recycling could achieve an industrial valorization.

Table 2. Main physic mechanical treatments employed to prepare indium-bearing samples for the subsequent recovery process.

Sample	pre-treatment	Particle size (μm)	Scope	Ref.
LCD screen	Shredding	n. a.	Shredding process without polarizing film removal. Inhomogeneity in metal concentration (Al, Cu, Zn and Fe) included indium was attributed to shredding effectiveness to separate ITO glass from polymeric parts in LCD. Improvements in mechanical treatments were suggested.	[46]
LCD screen	Dismantling, thermal shock and ultrasound	0.5	Thermal shocks held between 230 and 240 °C detaching PVA from LCD glass. Lower temperatures than 230 °C only softened polymers, but higher temperatures than 240 °C cannot melt polymeric fraction, but it did carbonize, emitting hazardous smells.	[48]
LCD screen	Manual dismantling	< 137	Both CF and TFT glass were manually removed and ground.	[49]
LCD screen	Selective Attrition scrubbers	< 600	Abrasion was considered an indium concentration route from ITO glass without polarizing films. The particle size reduction should be carried out till 177 μm followed up screening. Although long residence times of grinding favored the indium enrichment (grade, mg/kg), finer fractions alter the recovery. This paper explained the surface size of LCD screen glass affects indium recovery since lower costs and higher control of indium concentration by using attrition scrubbing could be achieved.	[63]
LCD screen	Manual dismantling, polarizing removal and milling	i. a. 150	Manual dismantling of cellphones was divided into three stages: i) removal of polymeric fraction, ii) polarizing film stripping by solvent, iii) comminution ((knife mill, hammer mill, and ball mill). The best result was ball mill at 60 rpm for 2 h.	[50]
LCD screen	Manual dismantling, alcohol and acetone washes, and cutting	14 cm^2	Ultrasonic influence avoided crushing treatments at 300 W for 60 min by reaching clean, unground glass fractions. Alcohol made adhesives less sticking, while the pure liquid crystal can be recovered after acetone washes for 4 h and distillation.	[51]

ITO glass	Manual dismantling, polarizing removal and milling	< 150	Polymeric fraction removal and milling for 4 h at 160 rpm were performed.	[53]
LCD screen	Manual dismantling and shredding	< 4000	Polymeric fraction removal and ITO layer, glass, and polarizing film were shredded.	[54]
LCD screen	Milling and pyrolysis	1.28 - 221	LCD screens were crushed without a previous dismantling. Pyrolysis was assisted at 500 °C, 20 Pa, 15 min and fine milling at 300 rpm for 20 min reached a narrow size distribution.	[56]
LCD screen	Collecting, manual dismantling, polarizing removal and milling	~ 1 cm^2	ITO glass was isolated after stripping two polarizing sheets by thermal shocks at 200 °C for 7 min without gas emission.	[57]
LCD screen	Shredding/milling	< 1 cm	A large particle size distribution processed 1 cm particles favoring energy save and adapting results at the industrial level.	[58]
LCD screen	Mechanical abrasion and heat, laser, and plasma treatments	n. a.	This work explains how the relevance of pretreatments on the hydrometallurgical process. Abrasion processes removed the ITO layer from LCD glass, but impurities increased. According to the purity and recovery rate, heat and plasma treatment slightly affected the following brushing. Laser treatment evaporated the ITO layer without extra recovery steps. The cost-benefit analysis indicated that the mechanical treatment followed by the plasma treatment offer good economic profits.	[59]
LCD screen	Cutting	1 cm^2	n. i.	[60]
LCD screen	Roll milling, incineration and electrical disintegration	n. a.	The dismantling process was performed comparing milling and incineration with the electrical disintegration. Electrical disintegration allowed to separate two polarizing films with lower energy consumption, lower dissolution reagents and lower environmental impact.	[62]
LCD screen	Collecting, manual dismantling, polarizing removal and milling	75 - 35	Rapid PHEBM was carried out for 30 min to obtain a fine powder particle size lower than 75 μm. Finer fractions showed agglomerations and produced hetero coagulation in the subsequent leaching step.	[64]

LCD unit	Polarizing removal (thermal, chemical and ultrasound)	25 cm^2	Thermal and chemical tests were used to individualize the best conditions to remove polarizing films. Thermal tests consisted of cooling down at cryogenic temperatures, removing the film at -196 °C after 20 min. Chemical tests followed soaking LCD glass in acetone, ethyl acetate and limonene at an L/S ratio of 3 mL/g assisted by ultrasound at 35 kHz for a long time (> 2 h).	[66]
LCD unit	Manual dismantling and comparative analysis for ground treatments	< 212	Dismantling influenced the following steps until achieving leaching and recovery. A combined wet and dry process for separation obtained 85% wt. In/glass mixture.	[67]
ITO target	Hand hammer and milling	≤ 75	ITO targets were grounded by a two-step process passing from hand hammer around 5 mm to milling process near 105 μm.	[69]
LCD screen	Manual dismantling, polarizing removal and milling	< 10	Manual separation eliminated negligible fractions; thermal shocks stripped polarizing films, while ultrasonic separated LC layers. ITO glass was downsized by milling at 1100 rpm.	[77]

n. a.: not available

1.4. Extractive methodologies for indium recovery: pyrometallurgy

Pyrometallurgy and hydrometallurgy are the most representative branches of extractive metallurgy. These methodologies have shown likely results in mineral processing, extraction and metal refining. Although several pro-and-con aspects from these methods are regularly confronted with the maximum throughput for recovery, it is often accepted that their versatility and adaptability allow them to deal with the intrinsic environmental and occupational safety drawbacks. In the last decades, many pyrometallurgical attempts have been developed based on pyrolysis [30,43,81–86] and vaporization [87,88], as can be seen in Figure 5a-b, respectively. On the one hand, pyrolysis is defined as a thermal decomposition method to remove the organic fraction (PCB, tire and plastic scraps), stripping LC, polarizing films, filters and other organic parts from the LCD panel waste, and consequently releasing the LCD glass. The main output of these processes is characterized by generating oils and gases [82,83]. Lu et al. in 2012 removed around 88% of the organic phase in LCD waste via pyrolysis at 1123 °C after dismantling and crushing pretreatments. Near 67 wt.% of these outputs corresponded to oils containing acetic acid/ triphenyl phosphate, while the remaining fractions were 21 and 12 wt.% related to gases and residues. The first fraction of oils can

be stored after distillation, while the remaining can be used as fuel and raw material for indium recovery [82]. With integrated wet stripping processes, inert atmosphere or vacuum pyrolysis has also been developed to avoid spontaneous combustion and hydrolysis reactions, a lower melting point of by-products, and organic resins production without undesirable pollutants [30,43,81,84–86].

On the other hand, vaporization principles have been described by Itoh et al. in a two-step process that reduces ITO scraps in In-Sn alloy at 730 °C by the carbon monoxide assistance. At the second stage, by taking advantage of the fact that indium and tin have quite different vaporization temperatures, indium can be vaporized at 1100 °C and recovered as a metal after cooling down (Figure 5b) [87]. Similar work had been previously carried out by Takahashi et al., which added a chlorination bath before vaporization. ITO-bearing scrap was washed in that bath to chloride compounds ($InCl_3$, $SnCl_4$), then metallic tin and subsequently indium recovery were achieved. This modification decreased the vaporization temperature (T_{Sn}: 300 °C and T_{In}: 200 °C) [88].

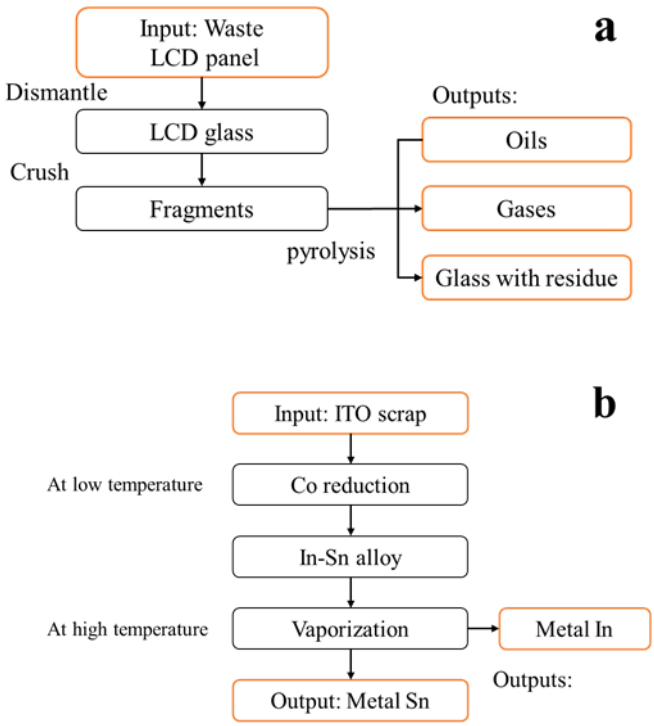

Figure 5. Flowsheet for indium recovery via pyrometallurgy by using a) pyrolysis and b) vaporization process proposed by Lu et al. in 2012 [82] and Itoh et al. in 2011 [87].

Concerning thermal treatments, promising findings indicate that pyrometallurgy still has many targets that should be undertaken, from both metal recovery and environmental issues. Some of the most critical bottlenecks in pyrometallurgical indium recovery involve:

i) Expensive facilities and equipment are needed.
ii) High investment of energy in fossil fuels.
iii) Highly concentrated process streams are required.
iv) Production of hazardous, complex compounds (gases and oils) must be appropriately managed to inhibit environmental and economic concerns.
v) Large scale operation could represent an advantage, but it could also enlarge the previous drawbacks.

Thereby, although notable improvements have been reached, alternative proposals based on a less carbon dependence have attempted to achieve the indium recovery avoiding the disadvantages described above.

1.5. Extractive methodologies for indium recovery: hydrometallurgy

Another methodology widely used to recover indium from WEEE is hydrometallurgy. This method offers remarkable advantages that could achieve successful extraction rates, maintaining the energy and financial requirements from the so-called circular economy [7,17,72]. Although hydrometallurgy also presents drawbacks that should be considered, such as large volume of electrolyte, enrichment of solution and long-lasting processes, the most significant advantages involve a fast adaptation of different types of samples (origin and size) and rapid processing tuning up. Also, low-temperature requirements, lack of hazard pollutants production and low investments in maintenance are involved. Moreover, cost-efficient treatments, environmental impact of reagents, detailed physical and chemical control of electrolyte are other technical profits that hydrometallurgy can be developed at a small and medium scale or even industrial scale. Unless ores and primary resources accomplish specific features, hydrometallurgy could be similar to pyrometallurgical extraction.

1.5.1. Leaching: indium dissolution

Hydrometallurgy processes have been divided into three steps: metal leaching, metal concentration, and pure metal recovery. Firstly, leaching comprises metal dissolution performed using pure and mixed acids, alkaline attack, and organic acid etching. At the same time, the extraction step has been highlighted by crystallization, solvent extraction,

coagulation, ionic exchange, membrane separation etc., where the main scope is to concentrate metal targets and eliminate the insignificant and not desired ones. If extractive techniques obtain metals with high purity, no further procedures are followed. Yet it is widely known that cementation, selective precipitation, electrowinning and electrorefining allow achieving the recovery of targeted metals. Without a doubt, hydrometallurgical recovery has permitted valorizing metals from WEEE through precious metals recovery from obsolete PCB [40,89–92], Nickel and cobalt from lithium batteries [93], and rare-earth metals extraction from end-of-life HDD [37–39,94,95]. Likewise, indium from LCD screens, indium-mineral tailings, wastewater, ITO/IGZO targets, indium liquors, etching waste, and others have been recovered via hydrometallurgy. Most of the authors in the literature have developed the indium extraction by using HNO_3, Aqua Regia, HCl, mixtures and H_2SO_4 electrolytes [54]. In contrast, alkali solutions (NaOH, NH_4OH, KOH, etc.) favor indium precipitation as hydroxides rather than the leaching electrolyte [96,97].

Furthermore, considering leaching as a fundamental method in hydrometallurgy, indium liberation from LCD screens is a bottleneck that must be overcome. As above mentioned, non-mechanical and mechanical treatments perform the indium liberation from waste. In this regard, some authors have used sonication assistance to eliminate grinding, accelerate leaching times and enhance leaching rates [48,49,55]. An acid leaching process assisted by hydrochloric solution and sonication dissolved around 97% at room temperature for one hour [51]. The experimental conditions set up by Zhang et al. at 300 W (ultrasonic activation) led to accelerating kinetic oxidation reactions, avoiding crushing and heating steps during the leaching process [51]. Other interesting approaches have dealt with stripping polarizing film from LCD waste without physic mechanical treatments. Upon sub-critical conditions of harmless water, an exfoliation process of multilayer LCD was followed, releasing undissolved ITO films from ITO glass [44]. Regardless of how ITO films are obtained, further dissolution and extraction stages should be carried out to reach pure indium metal. Under these conditions, Yoshida et al. also carried out a pilot-scale process (4 t/day) proposing a potential industrial pilot batch application to obtain undissolved ITO films via continuous sub-critical water. From this approach, the ITO stripping from ITO glass arises promising features based on using no chemical reagents, simple facilities, without previous mechanical treatments and lower energy consumption; however, technical and cost-benefit analysis, control of temperature and residence time, pumping systems and internal corrosive wear of metallic reactor demand further investigations. Similarly, flotation can be considered an alternative approach to collecting ITO films from ITO glass. The samples reached a size fraction of 320 μm after grinding, and around 93% of ITO films were obtained with an indium enrichment ratio of 18.4 [98].

On the other hand, conventional leaching processes have also been developed using grinding to cut down ITO glass in small size fractions that significantly enhance the indium extraction rate. Moutiy et al. proposed the indium leaching from several kinds

of indium content within LCD screens (50 – 400 mg/kg) using 0.2 M H_2SO_4, 70 °C for 30 min [54]. A comparative study from indium-and iron-bearing sphalerite was also performed into a reactor containing sulfuric acid and ferric sulfate solution. This investigation summarizes an improved indium leaching from mineral sources, enhancing the temperature and concentration of sulfuric and ferric ions. A similar result on leaching was obtained when particle size was lowered, while the kinetic analysis showed a two-stage mixed-control mechanism. The first stage for indium dissolution was controlled by the chemical reaction process on sphalerite particle surfaces, whereas the mass transfer process through the sulfur layer was the second stage [32]. In general, it has observed an inverse relationship, increasing the leaching rate when particle size decreases. Nonetheless, as time grinding rises, both kinetic reactions and energy consumption increase. For that reason, many reports in charge of indium recovery, no matter the electrolyte (HCl, HNO_3 and H_2SO_4), have tried to optimize their operative conditions to reach the complete leaching with higher particle size distribution and lower leaching time [50,54,99].

Otherwise, the low indium concentration after the dissolution process is another problem at the end of the leaching process. This problem was evidenced by Ferella et al., proposing two successful experimental oxidative combinations: i) 1 M H_2SO_4, 10% wt./vol S/L ratio for 3 h and ii) 0.75 M H_2SO_4, 10% wt./vol S/L ratio, 10% vol H_2O_2 for 3 h, even though pregnant solutions were poor in indium content [67]. However, despite those optimized conditions, it was mentioned that other concentration processes are required to favor the electrolyte enrichment and make profitable the indium recycling from LCD waste. Recently, serious concerns about the cost-effectiveness and viability at real processing scales have arisen due to the low indium concentration at the end of the leaching. A single leaching step is not recommended to maximize both leaching efficiency and economic viability. The isolation of the other metal species in the solution promotes innovative pathways to enhance the indium concentration and purity during the recovery process. Based on those considerations, cross-current multistage configurations has been developed [58,100]. Rocchetti et al. investigated the indium recovery by fixing the best leaching conditions at 2 M H_2SO_4, 0.2 kg/L pulp density at 80 °C and 10 min. Since LCD waste involves a complex configuration, complete metal dissolution is the most convenient process. Thus if leaching lasts a long time, both indium dissolution and co-mobilization of other metals (Fe, Ca, Mg, and Al) in the leach liquor will be unavoidable [58]. The oxidative species into electrolyte eventually can run out means that the efficiency will decrease after each operative step demanding a regular integration of fresh liquor. Rocchetti et al. enhanced the indium concentration from around 35 to 105 mg/L after six leaching steps via cross-current multistage configuration [58].

The dissolution capacity of electrolytes is mainly caused by the chemical affinity between solution and metals. Hence indium, being a trivalent element, is easily dissolved by proton donator agents such as pure or mixture acidic solutions. The most

common acidic solutions are HNO_3, HCl and H_2SO_4, which are considered affordable and adaptable to carry out recovery methodologies [58,66,69,101,102]. Furthermore, aqua regia, nitric acid and strong acid mixtures (HCl-HNO_3-H_2SO_4) have also been used to rapidly leach metal samples, showing that dissolution should be even assisted in most cases with external stimulus [49,52]. However, environmental adversities and employee safety combined with high corrosive power are the top causes to claim that those strong acidic solutions are inconvenient at an industrial scale. The problems mentioned above are the most critical drawbacks that those acids must face, being a weak strategic direction for faster leaching processes. In this regard, conventional and advanced methodologies used to favor the kinetic reactions are summarized in several works [44,51,103]. By way of illustration, Deng et al. evaluated different oxidative systems (atmospheric leaching with and without $KMnO_4$, roasting-atmospheric leaching, and oxygen pressure leaching). The most efficient indium extraction was achieved from zinc slags in an oxidative pressure system at 0.4 MPa and 100 °C by using 3.1 M H_2SO_4, 10 mL/g Liquid/Solid (L/S) ratio and 600 rpm. After 5 h, process leaching dissolved 94.1% indium, leaving residues containing indium, copper and lead [36]. To our knowledge, autoclave leaching, similar to that used in PCB and some mineral tailings [36,40,104,105], have not been widely developed for indium recovery from electronic waste to date. Hence, after a polarizing film stripping, autoclave oxidation–leaching could represent a plausible method to fast oxidation of indium from LCD waste within the framework of sustainability and scaling-up.

Other oxidants such as alkaline solutions and oxidative salts have also been used for indium recovery [96,97,106]. Alkaline dissolution, less considered though, shows some approaches for indium recovery from ITO targets by hydrothermal leaching [96] and the initial cleaning for etching waste treatment [97]. Whereas, concerning oxidative salts, sodium tripolyphosphate ($Na_5P_3O_{10}$) arises like an alternative medium with effective recovery rates that could be eventually explored [106], as well as it is the case of thiosulfate group that has been used for metal recovery from WEEE [37,40,107].

For the indium concentration from indium-bearing electrolytes, this review was herein able to screen from literature a single work led to concentrate ITO films from milled ITO glass. Flotation and cementation have been adapted from traditional hydrometallurgical processes. But the latter has a better reception to perform the indium recovery with high selectivity and purity levels. The obtained results from the conventional copper-zinc alloy production suggest that this method could be reproduced for indium concentration from ITO-bearing electrolytes at operative scales larger than laboratory facilities. However, either coprecipitation by alternating galvanic reactions or reduction agent excesses (Zn) promotes recent investigations to deplete undesirable secondary reactions [100,108].

Jiang and others developed an efficient cementation process with more than 97% indium recovery and high purity at pH 3, 25 °C and 1.8 Zn/In ratio after a long process of 7 h [106]. Likewise, another longer cementation process lasted 40 h, reaching almost a

complete recovery (99.9%) from the total leaching of ITO targets powders using 1 M H_2SO_4 at 90 °C after 2 h using a liquid/solid ratio of 10. This work also explained the tin separation from residues, containing around 4% wt In. Both metals were independently obtained in different process steps, while indium recovery only consumed H_2SO_4, Na_2CO_3 and zinc [69]. Conversely, Rocchetti cemented indium from an indium-bearing solution varying Zn concentration, pH and time cementation. The most remarkable results indicated that it is possible to reach 99.8% indium recovery at pH 2, 100 g/L Zn concentration, 55 - 60 °C and 10 min from the start of the cementation process. Around 62% wt indium in the solid product was effectively obtained, while the remaining percentage corresponded to co-extracted metals (Ca, Fe, and mainly Al). As part of their conclusions, it was mentioned that further purification stages should be performed despite the high indium recovery, suggesting solvent extraction to reach a purity higher than 95% [108]. In turn, Lahtela et al. studied different pretreatments employed to release ITO from LCD screens to concentrate indium through cementation. Those authors separated the CF films array (mass black in LCD panels), which was undergone a hydrometallurgical process. The treatment consisted of soaking it in 1.5 M H_2SO_4 at 50 °C for 24 h, reaching 100% leaching with 96% of purity (lower metals concentration in solution). In agreement with cementation results performed by Rocchetti et al., before starting with indium cementation via zinc powders additions, a pH adjustment led to hydroxides precipitation of all metals, including indium (22.4 - 62%). Although indium cementation was not occurred, other reactions with higher reduction standard potential (E°) were preferred ($E°_{Fe^{3+}/Fe^{2+}} > E°_{Sn^{2+}/Sn^0} > E°_{Fe^{2+}/Fe^0} > E°_{In^{3+}/In^0} > E°_{Zn^{2+}/Zn^0} > E°_{Al^{3+}/Al^0}$) [59]. Therefore, the cementation mechanism draws a faster reduction reaction for Fe^{3+} species than Fe^0 and In^0 time precipitation. The indium cementation was completed after 6 h at room temperature. Based on these works, there is no doubt that cementation is an efficient method to recover indium with lower energy consumption. However, most authors concluded that further purification stages are required to eliminate the remaining trace of contaminants and enhance the purity rate (solvent extraction, liquid-liquid extraction and electrowinning) [59].

1.5.2. Bioleaching process: alternative indium dissolution

The necessity of developing eco-friendly and efficient processes has led to bioleaching for wastewater treatment and metals recovery, which are conventionally dominated by chemical reagent assistance. Bioleaching is a biotic process where acidophilic microorganisms in acidic conditions can dissolve metals and sulfide-based minerals as a consequence of metabolic processes. As part of the bio-hydrometallurgy field, bioleaching supports the dissolution processes of metals, acidic drainage and bioremediation treatments that have been denominated as environmental-friendly and low-cost procedures. Contrary to other methods, bioleaching demands low costs due to low energy supply, gaseous pollutant production, or even the absence of hazardous

effluents as might be formed in steelmakers or acidic plants [109]. Bioleaching, initially, was considered an intricate method; however, this methodology has remained in continuous evolution, highlighting a straightforward elucidation of dissolution mechanisms and some evidence of economically viable metal extraction from minerals. As bioleaching is widely recognized by following similar recovery rates reached by those conventional hydrometallurgical methods, this technique is also evoked to be a comparative alternative to deal with secondary sources such as WEEE [110–114].

From sulfide-bearing minerals, A*cidithiobacillus thiooxidans, Acidithiobacillus ferrooxidans and Leptospirillum ferrooxidans* are the most popular acidophilic microorganisms that researchers have employed to undertake their dissolution process. Different microorganism types are being used to recover metals from secondary sources: chemolithotrophs (*Acidithiobacillus thiooxidans* and *A. ferrooxidans*), cyanogens (*Chromobacterium violaceum*, *Pseudomonas sp.*, and *Bacillus megaterium*), and fungi (*Aspergillus niger* and *Penicillium simplicissimum*) [115]. Bioleaching extraction from minerals like indium-containing tailings and Pb/Zn smelting slag has been recently conducted by Martin et al. and Wang et al., respectively [109,116]. Martin et al. performed bioleaching of sulfur-based tailings (PbS, ZnS, FeS) that could not be recovered by the flotation process (fine powders are inefficiently recovered [117]). Further, the dissolution of sphalerite-bearing tailings containing around 400 mg/kg indium was carried out in a shake flask and column reactor. Acidophilic sulfur-oxidizing and iron-oxidizing bacteria reached a yield of about 80% leaching of indium [109]. In comparison, Wang et al. used a similar strain media in autotrophic bioleaching. The obtained indium yield was around 71% [116].

Otherwise, Jowkar et al. developed an optimized process using adapted *A. thiooxidants* from LCDs at pH 2.6, 1.6% (w/v) pulp density, and 8.6 g/L as the initial sulfur concentration [118]. Based on these conditions, the complete indium fraction was recovered (100%), while Sr scarcely reached 10%. An analogous methodology was also followed by Pourhossein et al., considering spent touch screens as indium and strontium sources, whereas adapted *A. ferrooxidans* was the culture medium [114]. From this research, it was also indicated 100% indium and 5% strontium recovery. This work notably concluded that there was no ferrous sulfate and sulfur passivation. However, the culture medium was considered inappropriate for that recovery due to the strontium insolubility [114]. In another investigation, LCD panels have been treated with *A. niger* fermentation to perform an optimized indium recovery. Once the bioleaching conditions were optimized at pH 4.0, 125 rpm shaking speed, and 50 g/L sucrose addition. The yield of indium extraction reached 100% [110].

The leaching results are satisfactory, showing complete dissolution. Thus, some researchers have recovered indium using bio-absorbents capable of microbially uptake metallic species from the solution. For instance, Ogi et al. proposed a novel environmentally friendly microbial method to extract soluble indium from aqueous solutions. More in detail, the indium collection was achieved using *Shewanella algae* at a

pH range between 2.4 and 3.9, room temperature after a short length of 10 min. After the extractive process, a precipitated mass was calcinated to obtain highly concentrated indium [113].

The advantageous characteristics of bioleaching made this method a novel, eco-friendlier and economically manner to dissolve minerals and WEEE. Nevertheless, concerns about cost-benefit, complex adaptation at industrial scales, and strict biotic system care (pH, temperature, concentration) are some challenges that bioleaching has overcome to achieve robust processing compared to conventional chemical methodologies [115]. Likewise, the integration of intrigues biotechnologies to bioleaching (biosorbents, biomineralization, bioelectrochemical) means novel alternatives to reach indium recovery, but these proposals still demand industrial viability verifications. Therefore, considering that these biological methods require further attention, the available techniques (cementation or electrowinning) to extract and purify indium from any solution (no matter source) could be currently used to obtain indium metal.

1.5.3. Selective extraction of indium from different sources: precipitation and solvent extraction processes

Methodologies such as precipitation and solvent extraction have been extensively used as a selective pathway to obtain indium from pregnant solutions in hydrometallurgy. On the one hand, precipitation has been conducted in acid electrolytes and adjustments of temperature and pH. In most of the study cases, they use alkaline solutions to precipitate indium, forming insoluble indium hydroxides. Although precipitation is categorically displayed as a selective method, further post-treatments are required to obtain the metallic state of indium, such as calcination, cementation, electrowinning, etc. By adding NH_4OH till pH 7.4 and stirring for 24 h from an acidic solution of 1 M H_2SO_4, Silveira et al. evaluated indium precipitation till obtaining 99.8% indium present in the solution. Acceptable results were even observed at pH 6.3 and 9.2 around 97.9% in both cases; however, the best experimental condition was set up at pH 7.4 [50].

In the same way, Lee et al. focused on Sn recovery with a pH value at 2, reaching precipitation of 99.69% to leave only indium into solution. Precipitation in this work showed a strong dependence on temperature and solution content, provoking coprecipitation of 10.3% indium, indicating further steps for indium separation [119]. This influence of temperature and concentration on the indium recovery, using ammonium bisulfate as an oxidative agent, was also studied by Fan et al. [120]. ITO target powders were leached (125°C, pH 2.2, 4 M NH_4HSO_4 and 600 rpm), lasting around 105 min reaction time due to the autoclave assistance. The following precipitation occurred at 2.2 pH value after adding ammonia solution and temperature at 60 °C for 2

h. These parameters achieved total tin precipitation at 2.2 pH, while almost all indium was retained in the supernatant. At pH 7.5, indium hydroxide was formed, obtaining around 99.82% recovery, while subsequent calcination steps produced indium oxide. The ammonium sulfate electrolyte could develop a sustainable process with negligible further emissions. Hence ammonia vapor can be collected, and the exhausted electrolyte can be thermally treated to decompose ammonium sulfate at 275 °C and obtain ammonium bisulfate. This transformation then allowed refeeding the initial oxidative electrolyte [120].

Other authors have used precipitation to purify electrolytes from undesirable metals (i. e., Sn, Al, Cu). Song et al. investigate the behavior of indium and tin oxides from ITO targets. A complete dissolution for indium (In^{3+}) was achieved by fixing 1 M H_2SO_4 at 70 °C, 320 rpm and two hours as processing time, while SnO_2 remained undissolved. This investigation demonstrated a spontaneous dissolution and precipitation as a consequence of Sn^{4+} species hydrolyzation that tended to form $SnO_2{\cdot}xH_2O$ at H_2SO_4 concentration higher than 1 M. This study has also shown interesting findings to separate indium from the tin without additional chemicals to adjust the pH solution being an attractive and convenient method for the purification. The intrinsic chemical properties of tin oxide prevent its leaching favoring a selective indium dissolution with lower sulfuric acid concentration [56]. Otherwise, the novel chemical composition of electrolyte and indium sources were considered in other works. Jiang et al. proposed a pressure oxidative leaching using $Na_5P_3O_{10}$ as an oxidative agent. The optimized operative conditions were defined at low temperature (25-65 °C), 2.6 pH value, 0.91 molar ratio of $Na_5P_3O_{10}$/In and 1.5 h. At the end of the process, $NaIn_3(P_3O_{10})_2{\cdot}12H_2O$ precipitates were generated. Thus, the precipitation process allowed to recover near 95% indium, but solvent extraction and Zn cementation were used to concentrate and obtain metallic indium, respectively. Under these conditions, metallic indium was recovered with 97% purity [106].

Similar ITO targets, lead-smelting dust (LDS) and zinc ferrite tailings, can be considered other indium sources due to high indium contents. Initially, the copresence of lead, zinc and indium is one of the main disadvantages for indium recovery from LDS. Chelate washing, acid leaching, and alkaline precipitation were established as part of the operative pathway. The alkaline precipitation was reached at pH 7, L/S ratio of 100 L/g and 25 °C for 5 h after chelating solvents extracted lead by using ethylenediaminedisuccinate (EDDS). The chemical similarity between zinc and indium complicated the process selectivity leaving the effectiveness precipitation of indium hydroxide around 88%, while most zinc remained within supernatant. Although other chelates (Ethylenediaminetetraacetic acid and hydroxyiminodisucinic acid) extracted feasibly lead, EDDS highlighted by its eco-friendly features. The leaching was effectively reached around 94% after 24h, and 88% of indium hydroxide was recovered [102].

On the other hand, extensive literature was herein reviewed about solvent extraction. Many extractants have been employed to selectively recover indium from different

sources (LCD waste, lead dust, zinc by-products, oxide mixture, spent sputtering targets). These extractants have lately emerged with a broad range of physic-chemical properties. In the last years, indium has been recovered using liquid/liquid reactions where solvating, cation exchange, anion exchange and chelating extractants are the most representative reactions. Cation extractant used for indium extraction is the di(2-ethylhexyl) phosphoric acid (D2EHPA), which is derived from phosphoric acid with easy ionizing alkyl groups diluted in both toluene or kerosene [5,46,53,66,68,100,101,121–130]. Similarly CYANEX group (272 and 923) [5,46,125,131,132], PC88A [68,97], IONQUEST 801 [5], Cyphos IL104 (tetradecyl-(trihexyl) phosphonium bis-(2,4,4-trimetylpentyl) phosphinate) diluted in toluene [133], Versatic 10 acid [134] and Tributyl phosphate (TBP) [135]. Furthermore, chelating extractants Zonyl FSA ($CF_3(CF_2)_nCH_2CH_2SCH_2CH_2COOH$, n = 6–8, Du Pont Co.) [61], nitrilotriacetic acid (NTA), disodium dihydrogen ethylenediamine tetraacetate dihydrate (EDTA) [60] and LIX 63 [134], and anion exchange extractants: N,N-di(1-methylheptyl) acetamide (N503), [125], tertiary amine A327 [136], trialkyl amine (N235) [125], and mixtures of sec-octylphenoxyacetic acid (CA12, H_2A_2) and the primary amine N1923 [137] have been used to recover indium. In Table 3, it is shown an overview of the latest works on indium recovery by using solvent extractants. Comparing these works suggests that D2EHPA in kerosene is the most used extractant for indium extraction from aqueous solutions. This solvent is normally referred to as a better extractant for indium separation from acidic solutions than other organophosphorus solvents. Simple synthesis from phosphoric acid, high affinity and loading capacity with indium and other metals indicates that D2EHPA can obtain indium in good environmental standards, avoiding intermediate precipitation and re-leaching steps [46,53,100,101,121–124,126,127,138,139]. Different indium sources have been considered such as spent targets [122], WEEE [46,53,123,139] and zinc plant wastewater [70,138]. No matter the indium origin, the solvent extraction process consisted of indium loading within the organic phase created by D2EHPA followed by a stripping step to recover indium selectively. Koleini et al. separated indium from a real zinc plant effluent, where iron contents were also present. The followed conditions for extracting indium were 30% D2EHPA in kerosene, 0.2 M H_2SO_4, A:O (Aqueous:Organic) phase ratio of 3:1 and 10 min contact time [138]. At the same time, indium stripping was carried out at 3 M H_2SO_4, A:O phase ratio of 1:4 at room temperature for 5 min. Chen et al. employed spent targets to obtain indium, gallium and zinc separately. Both extraction and stripping reached 99.9% and each metal was recovered as oxide after alkaline precipitation and calcination [122]. Yang et al. proposed improvements on the typical solvent extraction process using lower acid sulfuric concentration and 0.1 M D2EHPA in kerosene, suggesting even better results than that obtained in chloride solutions for leaching. They found undesirable the iron presence since there was a similar concentration to that of indium. This iron caused co-existence in the organic phase, and therefore, further optimization processes for the following works were suggested [46].

In that same way, De-la-Cruz-Moreno et al. recovered indium from residues of zinc refinery by using a combined process of leaching, solvent extraction, exchange membrane and precipitation. After a long leaching process (100 h) assisted by 6.8 M HCl electrolyte, around 97% was dissolved, while solvent extraction and polymeric membranes recovered 100% indium, increasing the concentration electrolyte in 97.1 mg/L and 110 mg/L (C_0: 16 mg/L) at the end of the process. This methodology could be considered another route to perform the indium extraction from mineral wastes targeting alternative sources of strategic elements. However, this methodology should deal with relevant improvements as long times of processing, complex electrolyte formation post-treatment, and further energy investments for hydroxide transformation (roasting) [70].

Furthermore, the solvent extraction by D2EHPA followed up stripping stages showed advances in terms of the indium extraction concentration reaching more than 97% and the increases of indium concentration after stripping. Pereira et al. used an indium-bearing solution from mobile phones, which were treated using a chloride solution composed of 30% D2EHPA in kerosene as a diluent, A:O phase ratio 40:1 and 20 min contact time. After the stripping process at 10 min contact time, A:O phase ratio of 1:10 and 4 M HCl, the indium extraction effectiveness was 61.1%, while the indium concentration enhanced 236 times from the initial diluted solution. Contrastingly, Lahti et al. used nanofiltration to separate the leachate from the organic contaminants (polarizing films, polymers and glues) produced by a previous crushing process of LCD waste. The step also increased the indium concentration passing from 126 mg/L to 677 mg/L. With the results of this work, it was also possible to skip one of the most critical problems for LCD recycling consisting of manual dismantling. Although diverse in how they were conceived, those works proposed by Pereira et al. and Lahti et al. demonstrated the indium concentration increase by solvent extraction [53,123].

Moreover, the indium isolation via solvent extraction has been widely carried out by D2EHPA diluted in kerosene, showing a particular interest among researchers because of the advantages mentioned above. Most of the works have attempted indium recovery using sulfuric solutions as the acidic aqueous phase. However, other authors have recently focused on chemical interaction between different acidic media and extractants. For instance, Lupi and Pilone demonstrated the influence of the acidic aqueous electrolyte on the metal-extractant interaction [5]. Extractants such as D2EHPA, IONQUEST 801, LIX 984 and Cyanex 272 in kerosene were evaluated into H_2SO_4, HCl and HNO_3, revealing that IONQUEST 801 and D2EHPA are the most effective extractants using sulfuric and nitric acid in concentrations lower than 2 M. Under those conditions, LIX 984 carried out the worst performance for indium extraction because of the tendency of chelates to form specific, stable complexes from metal ions in the solution. However, the pH increase could imply enhancing the indium extraction using LIX 984, which also concorded with that found by [134] using LIX 63 and Versatic 10 acid diluted in ShellSol D70 at pH higher than 3. By comparing the performance of those

alkyl phosphorus extractants, those obtained by IONQUEST 801 highlighted using all types of acidic solutions, followed by D2EHPA with lower affinity into chloride ones. Both pH and acid concentration indicated relevant participation on indium extraction when Cyanex 272 and D2EHPA were used. The former was affected by varying alkyl chains at low pH values, while the latter was altered in high HCl concentration (> 1 M), also promoting the solvation mechanism [5,53]. To sum up, D2EHPA and IONQUEST 801 were considered efficient extractants using nitric and sulfuric acid and much less in chloride medium. Based on this research, the results conclude that indium extraction by organic extractants is a highly effective technique if strict control of the interaction between metal ions and the extractant is guaranteed.

The indium extraction by solvent concentration and stripping has gained attention due to reasonable extractive rates, broad access to many extractants and versatile performance under different operative conditions. However, one critical issue encloses the low metal concentration when the indium-enriched electrolyte is stripped. Thus, stripping has been undertaken through countercurrent stages to overcome low metal concentration in the electrolyte. Typically, indium stripping is related to indium enrichment of the organic phase followed by direct metal desorption changing pH with acidic solutions (commonly HCl). If this process is continuously repeated, the obvious result will be enhanced both indium concentration and the final recovery rate. The previous hypothesis was adopted by Virolainen et al. They developed a two-countercurrent process where initial concentration increased around 16.5 times (C0: 735 mg/L). This process was assisted by sulfuric media and a solution of 0.2 M D2EHPA and 0.8M TBP in kerosene. Hence purification was satisfactorily performed with a low trace of Sn (~0.02 g/L) [101]. Likewise, Dhiman and Gupta similarly carried out the solvent extraction of indium by a two-countercurrent process with Cyphos IL104 diluted in toluene extractant. They although reached a lower final concentration of indium (9.79 g/L) than that obtained by Virolainen et al., it is fair to mention that this work used a more realistic solution, giving; as a result, actual outputs with metals interference such as Sn, Fe, Zn, Ca, Al, Sr, Mn [133]. Analogously X. Li et al. and X. Li et al. proposed countercurrent processes established in three or more stages, reaching remarkable increases of indium concentration around 32 (C0: 131 mg/L) and 15 (C0: 735 mg/L) times the initial indium concentration, respectively [100,121]. In Table 3, it is observed the conditions in which countercurrent processes were performed.

Recently, the absence of recognized industrial recovery processes of indium has promoted realistic proposals at the industrial pilot scale [68,97,140,141]. Mainly, Swain et al. developed a pilot-scale liquid-liquid extraction process integrating solvent extraction and electrorefining whose scope was to treat ITO etching industry wastewater. This 300 L batch pilot process also was simulated in similar conditions to validate the effectiveness recovery. The indium was obtained via a scrubbing-solvent extraction-stripping-cementation route. After the complete cementation process, more than 99% indium was recovered. In addition, the starting solution, composed of other

metals such as Sn, Mo, Al, Cu, was scrubbed using Cyanex 272 to separate Sn and Mo, while DP-8R in kerosene extracted Cu and Al out the solution after three extraction stages. Finally, ascorbic acid addition was considered to remove Cu from Al selectively [140,141]. Otherwise, Kang et al. implemented an indirect indium recovery following the leaching of spent ITO sputtering targets. This work targeted tin removal by cementation-solvent extraction pilot-scale continuous treatment assuming around 500 L bath for a 2000 L daily operative process [68,97]. Immediately thereafter, indium was extracted by PC88A in kerosene followed by stripping with HCl. The obtained indium was then cast to form an anode and purified (99.997%) by electrorefining at 200 A/cm2 at room temperature for 24 h [68,97].

Table 3. Comparison of solvent extraction investigations for indium recovery. All information and indexes are presented based on indium recovery.

Organic phase	Aqueous phase (M)	Extraction conditions	Other elements	E (%)‡	Stripping conditions	S (%)†	L. C. (g/L)	C_{In}*	Ref.
15% D2EHPA in kerosene	HNO_3 or H_2SO_4 (pH > 1.5)	1:1 A/O, 1.0 pH, r.t.	Cu, Zn, and Fe	100	6 M HCl, 15 min	80	-	-	[5]
0.1 M DEHPA in in kerosene	0.1 H_2SO_4	1:1 A/O, r.t.	Al, Cu, Fe, Sn, Zn	96	1 M HCl, 1:1 A/O	90.5	-	-	[46]
30% D2EHPA in kerosene	4 HCl	40:1 A/O, 0.5 pH, r.t., 20 min	-	99.3	4 M HCl, 1:10 A/O, 10 min	61.1	7.7	32.7	[53]
20% D2EHPA in kerosene	2 H_2SO_4	6:1 A/O, 0.5 pH, 2 min, three c.c.s.	Zn and Fe	96.1	4 M HCl, 6:1 A/O, three c.c.s.	99%	0.85	6.5	[100]
0.2 M D2EHPA in kerosene	1 H_2SO_4	1:8 A/O, 0.5 pH, r.t., 20 min, two c.c.s.	Sn	100	20% D2EHPA > 1.5 M HCl, 2:1 A/O, two c.c.s.	94	12.2	16.5	[101]
15% D2EHPA in kerosene	2 H_2SO_4	6:1 A/O, 0.5 pH, 2 min, three c.c.s.	Zn and Fe	96.1	4 M HCl, 6:1 A/O, four c.c.s.	96	11	86	[121]
0.02 M D2EHPA in kerosene	3 HNO_3	2:1 A/O, 1.0 pH, r.t., 5 min	Ga and Zn	99.9	1 M HCl, 5 min	99.9	-	-	[122]

0.25M D2EHPA in kerosene	1 H_2SO_4	1:1 A/O, 34 s, r.t.	Al, Cu, Fe, Zn	97	1.5 HCl, 1:1 A/O, 3 h	87	0.5	3.8	[123]
20% D2EHPA in kerosene	0.5 H_2SO_4	1:10 A/O, 3 min, r.t.	-	100	4 M HCl, 10:1 A/O, 10 min	97.3	-	-	[124]
50 mM DEHAA in toluene	1 NH_4NO_3	2.5 pH, 10 min	Ga, Cu, Zn, Co, Ni, Cd	95	1 M HNO_3	95.6	-	-	[126]
50 mM DEAPP in toluene	1 NH_4NO_3	0 pH, 60 min	Ga and Zn	100	5 M HNO_3	80.3	-	-	[127]
30% D2EHPA in kerosene	0.2 H_2SO_4	3:1 A/O, 3.0 pH 5-10 min, r.t.	Fe	93	3 M H_2SO_4, r.t 1:4 A/O	74.5	-	-	[138]
25% D2EHPA in kerosene	0.3 H_2SO_4	2:1 A/O, 0.25 s	Fe	99	3 M HCl	99	-	-	[139]
CA100 and N235 in n-heptane	0.3 HCl	1:1 A/O, 3.0 pH 1 min, r.t.	Ga	-	-	-	-	-	[125]
0.05 M (CA12 + N1923) in n-heptane	20% HCl	1:1 A/O, 3.0 pH, 2 min, three c.c.s	Ga and Zn	-	-	-	-	-	[137]
1M PC88A in kerosene	0.3 H^+	1:3 A/O, 5 min, r.t.	Sn, Fe, Mo	97	2 M H^+, 1:1 A/O, 1-2 h, 2 to 4 stages	99.9	0.2	1.5	[97]
15% Ionquest 801 in kerosene	HNO_3, HCl H_2SO_4 (pH > 1.5)	1:1 A/O, 1.8 pH, r.t.	Cu, Zn and Fe	100	6 M HCl, 15 min	83	-		[5]
25% PEG 12% NH_4SO_4 1,10 phen.	6 HCl	~ 5.5 pH, r.t.	Sn, Al, Cr	> 90	-	80	0.1	1.3	[66]
0.5 M DP-8R in kerosene	HCl pH 0.03	1/8.5 A/O, r.t. three stages	Cu, Al	~99	4 M HCl 1:10 A/O,	99	51	28.3	[140]
1 M TBP in $[N_{1116}][TFSA]$	0.01 M HNO_3	1:1 A/O, 1.5-4 pH 5 min, r.t.	Zn, Ni	100	-	-	-	-	[135]
0.25 M Cyanex 923 in kerosene	0.85 HCl	1:1 A/O, 5 min, r.t.	Al, Cu, Fe, In, Y and Zn	91	1 M HNO_3 1:1 A/O, two stages	> 90	0.085	4.3	[132]

0.056 M LIX 63 and 0.12 M Versatic 10 acid in ShellSol D70	0.05 H_2SO_4	6:1 A/O, 3.0 pH, 40 °C four stages	Ga	86	0.05 M H_2SO_4 1:16 A/O, 40 °C two stages	100	8	10.4	[134]
1.25% $A327H^+Cl^-$ in Solvesso 100	7 HCl	1:1 A/O, pH 10 min, r.t.	-	-	5% $A327H^+Cl^-$, 2:1 A/O, 0.1 M HCl, 5 min	99	-	-	[136]
0.1 M Cyphos IL 104 in toluene	3 HCl	1:4 A/O, 1.0 pH, r.t., 5 min, two stages	Sn, Fe, Zn, Ca, Al, Sr, Mn	100	4 M HNO_3, 4:1 A/O, two c.c.s.	98	0.3	3	[133]

‡ *Indium extraction yield from the solvent phase.*

† *Indium recovery yield from stripping.*

* *Increase ratio of the indium concentration after stripping ($[In]_f/[In]_0$)*

L.C.: Loading capacity

r.t.: Room temperature.

c.c.s.: Counter-counter stages

In contrast, alternative chelating and anion exchange extractants for indium purification from indium pregnant electrolytes have been seldom considered. By comparing these works with those addressed at organophosphorus solvents, it turns out evident that they have been rarely investigated. Fontana et al. developed an indium recovery process divided into leaching and solvent extraction. Once the polarizing film was eliminated from LCD waste, 90% indium was leached in 6 M HCl at 25 °C and 3 mL/g as an L/S ratio, without further energy consumption in grinding. The indium recovery was carried out by using a polyethylene glycol-$(NH_4)_2SO_4$-H_2O system, where the most relevant result in this research is that extraction rate of indium (80-95%) together with the enhancement of the final indium concentration (30%) in the organic phase [66]. Moreover, Kato et al. completely leached metals from mobile phone waste into 2.40 M HCl [61]. Indium was then targeted for recovery using homogeneous liquid-liquid extraction with Zonyl FSA. Thus the indium into the sedimented liquid phase after the chelating extraction (indium-1,10-phenanthroline formation) represented 96.7% [61].

Aminopolycarboxylate chelating agents also drew outstanding results. By undergoing LCD waste under pressure and high-temperature environments, Hasegawa et al. used both EDTA and NTA combined with microwave irradiation to remove more than 80% indium from the electrolyte. The optimal conditions were fixed at pH 5, more than one hour as the processing time, around 50 bar and ≥ 120 °C. Although indium was successfully separated, tin remained in the supernatant and required further detailed purification processes. From this investigation, reasonable points have shown outstanding profits of the use of chelates extractants in indium extraction: i) recovery

aided by extractants that can be reused, ii) no crushing stage, and iii) cost-saving reflexed on the minimization of processing time and chelate utilization [60].

Otherwise, other studies conducted into synthetic solutions were presented to recover metals, including indium. Mixtures of CA100 with N235, N503, TBP and C923 were compared to demonstrate that CA100 with C923 can separate gallium (III) and indium (III) selectively in a hydrochloric acidic solution [125]. Those metals, including zinc, also were part of the research proposed by Ma et al. utilizing a synergistic extraction system containing both CA12 and N1923 [137]. By considering hydrochloric media, an inverse behavior was observed for metal recovery as CA12 concentration increased. The synergistic effect was maximized by adjusting an N1923 molar concentration ratio of 0.6 in the CA12 and N1923 system and recovering indium selectively [137].

In contrast, Alguacil used $A327H^{+}Cl^{-}$ as a product of the tertiary amine synthesis, A327 and 7 M HCl. The proper performance of loaded liquid membrane allowed stripping indium from the $A327H^{+}InCl_4^{-}$ species formed by using a low acidic solution [136]. Similarly, Nusen et al. developed a stripping process of indium from simulated zinc refinery solutions containing Ga, Cd, Ge, Co, Ni, Fe, Al, Mn and Mg. These authors carried out the experiments using a mixture of 0.056 M LIX 63 and 0.12 M Versatic 10 acid at an A/O ratio of 1:1 and 40 °C. Once the other metals were removed to avoid the typical co-extraction, indium and gallium were successfully stripped. Finally, indium was selectively isolated by pH adjustments and Cyanex addition increasing 266-fold indium concentration [134]. Based on these alternative extractants' results, it is worth mentioning that there is a promising prospect for both indium recovery and industrial implementation. However, some features require more consideration, such as the formation of complex solutions, flammability, vapor pressure, viscous liquids and further subsequent purification steps. Regardless of such observations, it remains unknown why the scientific community has not developed a more exhaust appropriation of indium recovery through chelating extractants.

1.5.4. Wet electrometallurgy: indium metal extraction

Electrometallurgy is mainly based on electrowinning and electrorefining methods. These methodologies extract metals from solutions no matter the origin: primary and secondary sources. In electrowinning, several works have been proposed from different acid solutions (HNO_3, HCl and H_2SO_4). Chou and Huang used wastewater solutions acidized with HNO_3 to recover indium. The current density (CD) at 64 A/m^2 showed CE and SEC around 90% and 0.5 kWh/kg, respectively. The use of hydrochloric solutions was performed by Lee and Oh [142]. The indium recovery process had a CE of around 90% CE on stainless steel cathode using 100 mA/cm^2 and $InCl_3$–HCl–NaOH–H_2O as CD and electrolyte, respectively [142]. Rehim et al. also studied the indium electrowinning on stainless steel as cathodic support varying operative parameters ($InCl_3$ content, temperature and current density). The CEs arrived at 80% using their experimental

conditions [143]. Otherwise, Lee et al. studied indium electrodeposition on copper cathodes. Although their research was not focused on the CE and SEC determination, the deposit purity was 99.99 % within different hydrochloric solutions [12]. Currently, secondary sources have been considered as raw materials. Gustafsson et al. and Choi et al. have taken advantage of electrowinning to recover indium from spent devices. Similarly, Gustafsson et al. extracted 98% of indium and suggested the chloride gas collection to refeed the electrolyte [144]. On the other hand, Choi et al. recovered ITO from obsoleted LCD anodizing the ITO surface with 0.2 A/cm^2. At the end of the process, both ITO and glass were recovered [145].

However, environmental concerns about nitric and chloride solutions have taken place. Nitric-based electrolytes are highly corrosive, while the chloride ones can evolve chlorine at the anodic compartment. Although chloride solutions are frequently used, chlorine must be collected to avoid risks. Thus, the indium and all metals electrowinning should be carried out using safer and affordable solutions.

Furthermore, sulfate solutions have been used in the first place by Walsh et al. [14,146–148]. Their findings revealed more inconsistent results than those obtained in chloride solutions. Although a deep investigation was not developed, the sulfate solutions were slightly considered for the following years. Recently, few studies have been undertaken using sulfate baths to recover indium. Environmental, occupational and economic advantages are some of the most relevant reasons for sulfates solutions utilization [58,59,65]. Ciro, Dell'Era and Lupi recovered indium from sulfate electrolytes varying operative parameters. Comparing the metals supports in a similar electrolyte, they released that stainless steel and Ni have the highest CEs at 25 A/m^2 [149,150].

Otherwise, by performing two potentiostatic tests, Song et al. extracted copper and indium selectively, reaching around 96%. However, the hydrogen evolution (HER) occurred on the cathodic surface, affecting the indium electrodeposition [56]. Otherwise, Xu et al. performed electrorefining to purify the indium ingots containing impurities. This work achieved electro refined indium (4 N-indium) [151]. Similarly, an electrorefining methodology was followed by Burkitbayeva et al. to obtain indium metal 90 times more pure than the rough one [152]. The necessity of developing electrodeposition procedures at temperatures higher than aqueous solution boiling point has led some investigations to use ionic liquids (IL) and deep-eutectic solvents (DES) [153–155]. Since HER is promoted in aqueous electrolytes at low enough potentials, the use of these solvents also hinders this parasitic reaction.

From IL, the most representative exponents have been 1-butyl-1-methylpyrrolidinium dicyanamide ($[BMP]^+[DCA]^-$) and 1-ethyl-3-methylimidazolium chloride/tetrafluoroborate, whereas quaternary ammonium salts with an amide, carboxylic acid or alcohol are ionic systems widely known as Deep Eutectic Solvents (DES). The IL systems have raised some critics about the electrode/IL interface reactions causing adverse effects on the cathodic surface performance [154]. Indium recovery from DES has shown relevant results for the indium thin layer production. Although HER

absence is evident in this electrolyte, other defects must be handled, such as high viscosities, lower mass transfer (diffusion conditions), lower CEs and irregular morphologies. Different electrolytes with higher potentialities to be used at an industrial scale are the molten salts [155]. Higher temperatures and lack of hydrogen issues on the cathodic surface make these salts a novel field for investigation. However, more studies on this matter are necessary due to the scarcity of available reports. Therefore, based on the actual scenario of electrolyte for indium electrowinning, some obstacles should be overcome in terms of high viscosities, weak diffusion conditions, irregular morphologies of deposits and energy consumption.

1.6. Summary and final remarks

- Recent indium demands for high-tech devices have developed novel indium recovery processes considering different supply sources. Although primary sources have initially supplied indium, the involved extraction process usually is carried out from Zn, Pb and Cu ores, where this metal is a by-product present in tailings. Thus, as the indium quota increases, a shortage scenario combined with environmental problems will be unavoidably increased. Therefore, significant advantages found in alternative sources have gained attention, such as the absence of hazardous mineral and radioactive metals, more indium concentration, easy-adaptation of extractive technology and end-of-life materials valorization (recycling). Nonetheless, the developed extractive technology remains at a lab scale, few works have started to be considered pilot-scale processes, and almost no recovery plants of indium are rarely identified.

    - The indium recovery from primary sources involves a critical environmental state due to the increasing indium demand for high-tech manufacture. Therefore, the secondary sources (mainly ITO LCD) have been adequately considered to recover indium. However, some drawbacks have been presented in the early stages of dismantling. Dismantling then becomes a fundamental stage to release indium-containing parts from other negligible fractions (polymers, glass and other metals), but those insignificant fractions also can be valorized in aid of reaching a circular recycling process. Once LCD waste is concentrated, removing the polarizing film raises the first obstacle to be overcome.

    - The removal of polarizing film for the hydrometallurgical route is often suggested. No matter the removal method is used, it is clear that the intrinsic design of the LCD panel represents a hindrance that the pyrometallurgical route does not present. Pyrometallurgy has been undertaken via pyrolysis, separately

obtaining oils, gases, and metals. Even though this route could be seemed the most convenient methodology to recover indium, several disadvantages, already mentioned, discourage an industrial implementation. On the other hand, hydrometallurgy is widely performed, despite its drawbacks, because of lower working temperature, lower energy consumption, lower investments in facilities and environmentally safe procedures. Although novel sources of indium can be easily adapted, conventional mineral sources also can be appropriately treated. Although some pyrometallurgy proposals have been carried out, diffuse industrial processes for indium recovery from secondary sources via hydrometallurgy have been not observed yet.

- Based on the hydrometallurgical procedures, leaching has been carried out in several ways indicating acidic dissolution is the most suitable method according to the chemical properties of metals within ITO glass. The most relevant results propose sulfuric acid at low concentrations (0.1 M) as an effective electrolyte to dissolve indium more than nitric and chloride acid. A considerable number of approaches on the indium leaching from ITO waste more than those from minerals suggesting that leaching is a versatile procedure with enough available knowledge, but many unresolved doubts remain regarding the effect of type of waste, increasing volume bath, adopting new oxidative both reagents and systems etc. In fact, from the open literature reviewed in this brief overview, oxysalts and oxidative pressure systems have been slightly studied.

- Furthermore, solvent extraction has been utilized to increase the indium concentration and favor the subsequent recovery stage once indium is dissolved. Several discussions have been held on the organic phase utilization, arguing complex phase formation and generations of problematic pollutants. Analogously cementation and precipitation have also indicated the viability to recover indium from leach liquor. Cementation seems to be a promising technique to extract indium at an industrial scale, but selectivity is somewhat a weakness. Finally, bioleaching could be recognized as an alternative that has been detailly developed in minerals much more than WEEE. Sulfide samples (pyrite, galena and sphalerite) and LCD have undergone bioleaching conditions. Although this affordable technique can recover indium, similar obstacles presented in minerals (sensitive systems and long-lasting process further purification stages) remain for secondary sources that should be overcome before looking to industrial-scale proposals.

- Electrowinning is displayed as a versatile methodology that extracts indium as a metal. Its versatility is summed up using indium-containing solutions regardless of its origin (mineral or waste leaching) and easy adaptation of different

conditions: pressure, temperature, current density, viscosity, concentration, pH, flow rate, metal support cathodes, etc. Since primary mineral extraction is considered less and less, most investigations have currently pointed out indium recovery from secondary sources like WEEE. By putting this latter matter aside, indium electrowinning has been developed in most cases at laboratory scales. This conception should be improved, taking the next pilot/industrial scale step. Although chloride solutions have been broadly used for the indium electrowinning/electrodeposition for many years, it is not clear why sulfate solutions performance was underestimated to date. However, the corrosive and environmental concerns demand a change to recover indium at higher scales subsequently. Hence, this scenario proposes novel ways to understand the effect of operative parameters on indium electro-recovery and the kinetics between the electrolyte and reactions near the cathodic surface. Therefore, based on all the findings from this overview, the indium electrowinning from sulfates solutions needs to be investigated from a productive and kinetic point of view to analyze the operative parameters influence on CE, SEC and deposit quality, along estimating reactions near cathodic surface including relevant electrochemical parameters (diffusion coefficient, redox potentials, heterogeneous charge transfer rate constant, etc.)

Chapter 2:
Indium recovery via electrowinning from primary and secondary sources

2.1.Fundaments of the electrowinning

Electrometallurgy, applied to aqueous solutions containing metals, is one of the most representative fields to produce and purify metals. This methodology is based on electrowinning and electrorefining methods. Those methodologies use the pregnant indium solutions (regardless of the origin: primary and secondary sources) to obtain alloys or pure metals on the cathodic surface. Electrolytic systems are characterized by producing or requiring electricity. However, the context of this investigation involves electrolytic systems (electrowinning and electrorefining), where an external potential allows a relative current to flow throughout from cathodic to anodic support within the conductive electrolyte [156,157]. In electrowinning, two half-reactions occur at cathodic and anodic support. The reduction reaction commonly takes place when targeted metals are deposited at the cathodic surface from pregnant solutions.

In contrast, the oxidation reaction occurs at the unreactive anode, where a gas evolves (usually oxygen). Otherwise, electrorefining deals with the metal purification by the metal electrodeposition on the cathodic surface. Meanwhile, the impure anode is contemporaneously consumed at the other side reaction. Exhaustive literature about electrowinning agrees that operative parameters (electrolyte composition, material cathode, temperature, pH, current density, etc.) dramatically affect the reduction reaction mechanism, altering how charge carriers are transferred within the solution to the cathodic metal surface. Thereby, to carry out an efficient performance in electrowinning, the electrolyte, at least, should satisfy high ionic conductivity, high chemical stability, and high solubility of the reactant ionic species [156,157].

Furthermore, both electrodes significantly contribute to the polarization effect. The electrode polarization is a phenomenon that can determine the course of the metal electrodeposition on the cathode and the proper working of the electrolytic cell. Once the equilibrium state is broken, the electrode itself suffers an internal migration of electrons. This non-equilibrium state causes a potential difference between surface and bulk (the double layer), meaning that the electrode potential turns to more negative with respect to that of the solution and its potential at equilibrium conditions. If the electrode-solution system is not stimulated, an increase of the electric field is registered in an attempt to reach the equilibrium state. But if so, a cathodic current flow is established, and an equilibrium state is not achieved. Then, the thermodynamic irreversibility state is created, and the polarization of the electrode is formed. From this phenomenon, the overpotential (η) appears as the difference between the reversible electrode potential (E_r) and new polarized condition (E_p) (Eq. 1).

$$\eta = E_p - E_r \qquad (1)$$

Since both electrodes participate in the electrolytic process, the polarization occurs both cathode and anode, following Eq. 2 and Eq. 3, respectively. Thereby, in an

electrolytic system, when an electrode behaves like a cathode, E_p is lower than E_r; consequently, the overpotential will be negative. While the anode will polarize with a positive value, assuming that the polarized condition will be higher than E_r.

$$\eta_c = E_{p,c} - E_r \quad (2)$$

$$\eta_a = E_{p,a} - E_r \quad (3)$$

Based on those statements, three types of polarization (η) can be distinguished: activation polarization (η^A), concentration polarization (η^C) and resistance polarization (η^R) [157]. Initially, to achieve a reaction between the metal surface and the same metallic species in the electrolyte, a specific overpotential should be applied to suppress the free energy at the initial equilibrium state. This defines the activation overpotential, where the deposition or dissolution reaction requires the same activation free energy, though, in a thermodynamically reversible process, they have opposite directions. Since the reaction pathway involves many activation energy steps, the reaction rate will be defined by the step with the highest activation energy and the slowest reaction speed. The most common example is usually represented by HER [158], which shows one or several steps before the hydrogen discharge (adsorption or migration) according to the metal surface. Thus, activation overpotential can be expressed by the generalization of the Tafel equation (Eq. 4).

$$\eta^A = a + b \cdot \log i \quad (4)$$

Where a and b are temperature-dependent parameters, and i is the current density. From this equation, it can be seen that η^A linearly depends on log i. However, it has been seen that for overpotentials lower than 0.052 V, the linear dependence is hardly fitted. In that case, there is a linear relationship between the overpotential and directly i. On the other hand, irreversible conditions are the most frequent working systems. Once reduction reaction occurs at the cathodic surface, ions may diffuse hardly from the bulk of the electrolyte through the double layer. A not fast enough replacement of discharged ions can create a concentration gradient in the double layer, and accordingly, a limiting reaction rate. Taking into account that a limiting CD and Nernst Equation, a concentration overpotential expression at a cathode (η_c^c) can be obtained (Eq. 5). A reasonable interpretation could suggest that increasing CD near the limiting value could increase the deposition rate due to a very high overpotential. These high overpotential conditions involve a possible HER, at least within aqueous solutions. And at really extreme overpotential conditions (exceeding the limiting current density), new limiting CD values can be reestablished.

$$\eta_c^c = 2.3\frac{R.T}{n.F} \cdot \log(1 - \frac{i}{i_L}) \quad (5)$$

Another remarkable polarization that electrolytic systems can suffer is the resistance polarization (η^R). The electrical resistance between the electrode surface and the electrolyte can be increased by oxide layer, patina or adsorbed gas films. Hence, an extra potential must be applied to force a current flow to pass through those isolating layers, and the latter explains the resistance overpotential. It is clear that any change within the electrolytic cell increases the resistance polarization making difficult its absolute determination. Nonetheless, a relationship has been proposed in Eq. 6, where *I* corresponds to the extra current and R required for each resistive behavior.

$$\eta^R = I \cdot R \tag{6}$$

Overall, the total overpotential (η) on an electrode is given by the sum of the three types of overpotential above described (Eq. 7). Since the electrolytic system comprises cathodic and anodic metal supports, there should be a total anodic and cathodic overpotential [157].

$$\eta = \eta^A + \eta^C + \eta^R \tag{7}$$

Alike electrolytes, material cathode also plays a relevant role in electrometallurgy. If the efficiency is based on minimizing power requirements, electrical and physical properties of material electrodes should be fulfilled. The former properties involve suitable conductive metals and low overpotentials (ohmic, concentration and activation). At the same time, the latter includes no passivation or solution interaction with cathodes during cell operation, easy manufacture, good dimensional stability and affordable metals [156]. Without underestimating the relevance of physical features, activation and concentration overpotentials are usually limiting conditions that alter the discharge reaction at the electrode interface. Firstly, the difference in concentration of the reacting ionic species between bulk and the metal surface of the cathode causes the activation overpotential increase [156]. Secondly, activation overpotential corresponds to the energy necessary to activate the reactants on the electrode, which involves the transfer reactions needed to go through Helmholtz's double-layer [156]. A low value for concentration and activation overpotentials are expected, allowing feasible conditions for the reduction reaction. These parameters are established to achieve high effectiveness, maintaining a close relationship between the deposit obtained and the charge flowing through the cell. In other words, high CE. However, this output is not the only one that should be considered. The SEC value relates to the power requirement during the reaction reduction. Therefore, the electrowinning cell design and processing optimization of operative parameters are a matter of study. In Eq. 8 and Eq.9, it can be seen the mathematical representation of both CE and SEC, respectively, where m_e and m_t correspond to the experimental and theoretical weight. The *I* is the current expressed

in A, t is time in hours, n_{eq} is the electrochemical equivalent for indium and E_{cell} is the cell voltage in V.

$$CE = \frac{m_e}{m_t} = \frac{m_e}{I * t * n_{eq}} * 100\% \quad (8)$$

$$SEC = \frac{E_{cell}}{m_e} = \frac{E_{cell}}{n_{eq} * CE} \quad (9)$$

2.2.Aqueous and non-aqueous electrolytes for indium electrowinning

The most common aqueous solutions used to perform indium electrowinning are the acidic solution, particularly HNO_3, HCl and H_2SO_4. Initially, nitric and hydrochloric acid attempts have been carried out [11,12,142,143,145,152,159]. Wastewater baths as an electrolyte, acidized with HNO_3, pH lower than 6.1 and 25 °C temperature, were studied by Chou and Huang to obtain the electrowon indium using 64 A/m^2 CD. CE and SEC showed to reach around 90% and 0.5 kWh/kg, respectively. In that work, although NaCl used as a supporting agent increased the solution's conductivity, temperature and indium concentration strongly impacted both CE and SEC [11]. Another significant contribution has been proposed by Choi et al. to recover ITO from LCD panels. Once the polarizing film was removed from the LCD screen, ITO glass was undergone an electrolysis process at 0.2 A/cm^2 as an anodic condition in 15 wt.% NaNO3 solutions recovering 75% ITO. The anodic reaction, being the oxygen evolution, only induces cracks with consequent lift-off of ITO layer parts. Oxygen evolution reached the interface ITO layer and glass place, removing ITO without dissolution. After filtration and CF and TFT removal treatments, the ITO layer and clean glass were obtained at the end of the process [145]. Hydrochloric solutions, assisted by NaCl and other salts, have also recovered indium. Lee and Oh obtained around 90% CE on stainless steel cathode using 100 mA/cm^2 and $InCl_3$–HCl–NaOH–H_2O as CD and electrolyte, respectively [142]. The experimentations were carried out at room temperature, NaCl additions and indium concentration higher than 50 g/L. This work showed the effect of NaCl addition on the overpotential cell: as NaCl concentration in electrolyte increases, the overpotential cell decreases. Further assessments were performed at different pH values. Although it was expected that low pH deteriorates the CE as a result of the excessive presence of hydrogen ions on the cathodic surface, pH showed no significant changes on CE.

Rehim et al. also studied the indium electrowinning on stainless steel as cathodic support varying $InCl_3$ content, temperature and CD. Also, the aspect and microhardness of deposits were analyzed. From their findings, increasing both temperature and $InCl_3$ gave an overpotential decrease. Further, current efficiencies reached 80% from 12 to 3 A/m^2 at 35 °C and 5 g/L $InCl_3$. Although the temperature was increased for those

conditions, it was only observed an increase of CEs at higher current densities [143]. Furthermore, a copper plate cathode within different hydrochloric solutions composed of $InCl_3$, LiCl and NaCl was used by Lee et al. to carry out the indium electrowinning. Supporting agents demonstrated a positive effect on the indium discharge because of the enhanced conductivity and discharge overpotential lowering. At the end of these processes, indium was electrodeposited with a purity of 99.99 % [12].

Moreover, other investigations have been performed to consider dynamic conditions in an electrochemical flow reactor. Wu et al. developed an indium removal process from wastewater after modelling different flow conditions. From modelling, two relevant outcomes indicated that the mass transport performance showed a linear dependence of flow and bath system type. Likewise, the indium concentration indicated an extended diffusion layer followed by a progressive indium concentration decrease. Those modelling and experimental results of the indium electrolysis fitted. The balance between SEC and cost-benefit led those authors to recommend two flow cells in series at 3810 mL/min as the most favorable scenario [160]. The novelty of the operative conditions was also exhibited by changing conventional plate electrodes that reduce the resistance characteristics at the electrode surface and maximize metal deposition even at low concentrations. Grimes et al. recovered indium from dilute leach solutions using a cylindrical mesh electrode configuration. Although the electrolyte was a mixture of nitric, perchloric and acetic acid leach solutions and a cyanate complexing agent, the indium recovery was successfully recovered (98%) after an extensive three-stage process strip tin and lead [159].

Furthermore, the CD has been defined as an essential parameter for electrowinning. It could be suggested that higher CDs gives higher rates of metal deposition. However, this assumption is not entirely true since high values of CD exacerbate the cell overpotential affecting the goodness of the process. One of these issues is the metal depletion near the cathodic surface, increasing activation cathodic overpotential that contributes to the resistive phenomenon known as concentration polarization. Such resistive process affects metal electrodeposition rate, CE and SEC. The cell overpotential rise favors parasitic reactions like HER, which negatively affects the power efficiency and even the deposit quality. Some voltammetric approaches have proposed metal separation via adjusting a constant pulse of cathodic potential. Gustafsson et al. separated copper and indium from the semiconductor material CIGS using an ammonium chloride solution. The indium separation was completed around 98%, while the copper indicated values close to 76.7% [144]. Nonetheless, the same authors suggested that optimization studies should be performed to obtain the optimum CD where smooth and dense deposits and increased CEs can be obtained. Additionally, they propose to collect the chloride gas from the anodic compartment to reuse it in the same process instead of new ammonium chloride [144].

Regarding the nitric and chloride solutions, the environmental, technical and economic concerns are the most critical issues that those solutions must tackle. Mainly,

electrowinning with chloride solutions involves the evolution of poisoning-chlorine at the anodic compartment. Chlorine is also a green vapor with extreme corrosive characteristics that demands significant investments in facilities maintenance, sealed reactors, abatement gas systems and special attention to occupational safety. Therefore, more environmentally friendly electrolytes without by-products and hazardous emissions that endanger the environment and human beings are required to perform more affordable and safer indium electrowinning processes.

On the other hand, sulfates solutions are widely recognized due to the lowest prices in markets and lower environmental impact, entailing the absence of hazardous emissions at the anodic compartment or endangering pollutants production [58,59,65]. Initially, sulfate solutions were used in pioneer works by Walsh et al. [14,146–148]. The most relevant findings indicated that these solutions could generate irregular morphologies with lower CE than those obtained with chloride solutions. However, no further investigations were performed to determine novel behaviors on CE, SEC and aspect quality of deposits. Recently, some preliminary studies have been undertaken by using sulfate baths to resolve some of these interrogations on indium recovery [149]. That investigation is focused on the indium metal recovery from sulfate electrolyte by using different metal supports (stainless steel, Ni, Cu, Ti and Al). This work evaluated the effectiveness of the indium electrowinning under the same operative conditions (25 A/m^2, 2.3 pH and 40 °C). The obtained results from those specific experimental conditions individuated different behaviors on each cathode for indium electrowinning from the sulfate solution. High CE and low SEC on AISI 316L and Ni were achieved, while that obtained on Ti cathode indicated acceptable values. In the case of Al and Cu supports, their performance reached poor results at those conditions [149]. Based on that preliminary work, it was evident that the influence of metal cathode is relevant and requires to be independently studied to achieve high productivity and low energy consumption. Therefore, five different metal supports are evaluated in this doctoral investigation, focusing on the electrochemical phenomena close to the indium reduction reaction. Also, the electrowinning process was studied in terms of the operating conditions (current density, pH, electrolyte composition and temperature) to optimize CE, SEC and the final deposit quality on each of those metals.

Other approaches have recently used sulfate solutions assisted by NaCl as the supporting additive. Song et al. leached LCD waste focused on indium extraction. A successful separation allowed to achieve an indium-rich electrolyte with an undesirable metals such as copper and aluminum [56]. By performing two potentiostatic tests, copper was selectively extracted out of the solution at 0.125 V, reaching around 96%, followed by a similar rate of indium recovery at -0.65 V after 4 h. However, both copper and indium electrodeposition on titanium (working cathode) presented CE values of 70.55% and 65.20%, respectively. Those values were evidently affected by the parasitic hydrogen evolution reaction (HER), which is increasingly dominant on the cathode surface during electrodeposition. Although high recovery rates were fulfilled with this

methodology, indium deposits presented impurities in copper and aluminum [56]. The impurity presence is avoidable in realistic electrowinning conditions; therefore, electrorefining is the subsequent treatment to purify indium deposits containing metal traces. Xu et al. developed the indium purification via electrorefining following similar conditions (60 A/m^2, pH 2-2.3 and 40 °C) studied in other works [149,150]. With impure indium place as the anode, CE around 97% and 0.06 kWh/kg SEC were achieved. Highly pure indium was then obtained from the indium sulfate solution assisted by Na_2SO_4 [151]. Although the process was driven to eliminate metal traces, cadmium was co-deposited along with indium on the cathode surface. Similar work obtained good results on CE and SEC using a chloride solution containing 0.5 M $InCl_3$ and 2.0 M NaCl at pH = 1.5. This electrolytic refining process incorporated bismuth in the anode material, producing indium ingots with 99.9989% purity. Such bismuth addition decreased the anodic overpotential during the indium dissolution at the anodic reaction. Thus, the electrorefining process achieved 90 times more pure metal [152].

Furthermore, the influence of operative conditions in the electrowinning process is highlighted at the laboratory scale, but they are much more influential at the industrial scale. For instance, in the case of the electrowinning plants of copper, temperature varies in the range between 35 and 50 °C, where higher temperature values make the operation improper. Due to diverse conditions in plants, the suitable temperature should be determined under realistic working conditions to evaluate the effect on the cathodic overpotential, microstructure and crystallography of deposits [161]. However, temperature is not the only parameter that plays an important role in electrowinning. The CD usually operates a high range in operating plants, for example, from 200 to 450 A/m^2 or from 500 to 1500 A/m^2 for copper and Zn electrowinning, respectively [161,162]. Beyond the limiting CD, deposits usually acquire a powdery aspect and the intense HER can negatively affect the electrowinning outputs. Although high CE values are expected close to the limiting CD, the realistic conditions entail using less than 50% of the limiting CD [163]. Thus, the CD is a determining parameter must consider in this kind of process.

On the other hand, additives are another relevant part of the electrowinning process. Small additions then modify the deposit aspect or the current-potential relationship within the electrolytic bath. These compounds mainly can be classified as brightening, smoothing, refining grain or depolarizing additives. Brighteners modify the orienting grain structure through a change of the nucleation process. Furthermore, grain refiners mainly control new nucleation seeds. The morphology of the deposit surface can be changed by levelers or smoothing additives, which homogenize the growth rates of the deposit. In addition, depolarizing additives hinder the dendrites formations [163]. Based on these parameters, the indium electrowinning system in an aqueous solution involves different working temperatures, electrolyte contents, CD ranges according to the cathodic metal support. Interactions among those operative parameters allow optimizing process productivity. Then the best process performance is this one of the most relevant scopes in several investigations.

Recently, researchers have sought non-conventional electrolytes to perform the indium electrodeposition at higher temperatures (> 100 °C) and free of the HER to avoid undesirable consequences such as enhanced overpotentials, low CE and high SEC etc. Several organic solvents, ionic liquids (IL), deep-eutectic solvents (DES) and molten salts have been considered more promising electrolytes, which can maintain high electrochemical and thermal stabilities and proper working conditions in a wide temperature range [153–155,164–168]. In previous studies, indium methanesulfonic and dimethylsulfoxide (DMSO) from organic solvents were used to study the indium electrodeposition from non-aqueous solutions. The most remarkable results were related to kinetic investigations, where the proposed mechanism for indium reduction reaction initially indicated the reduction pathway: In(III)/In(I) following In(I)/In(0) and In(0)/In(III). The diffusion constants for In(III) and In(I) were 2.2 and $3.3 \cdot 10^{-10}$ m^2/s at 26 °C, respectively. The temperature variation gave a morphological change for indium deposits, as shown in Figure 6a-b. At room temperature, the deposit appeared thin, smooth layer, but increasing this parameter until 160 °C; the morphology was similar to spheric droplets [153].

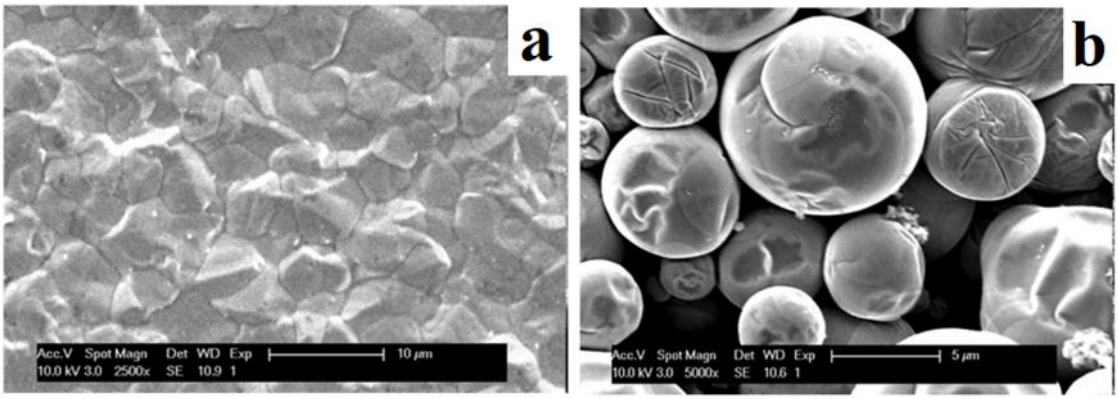

Figure 6. Effect of the temperature on the deposit morphology using DMSO at (a) 26 °C and (b) 160 °C [153].

ILs present similar organic solvent characteristics, like melting points lower than 100 °C because of the asymmetric forces of cations and anions. Other properties have been highlighted as high conductivity, thermal stability (no volatilization or inflammability) and a wide potential window before starting HER [164]. However, the main drawbacks are associated with the interaction electrode/IL interface at an applied potential. Lui et al. investigated the indium electrodeposition by using 1-butyl-1- methylpyrrolidinium dicyanamide ($[BMP]^+[DCA]^-$) as an IL electrolyte [164]. In this work, it was evaluated an anomalous behavior on a glassy carbon/IL interface. The problematic behavior was weakened by changing the IL composition and enhancing temperature [164].

In comparison, Yang et al. proposed a study on glassy carbon, tungsten and nickel electrodes in a basic 1-ethyl-3-methylimidazolium chloride/tetrafluoroborate IL. The electrokinetic results indicated the possibility of complexing indium chloride as $[InCl_5]^{2-}$ and reducing it as indium metal. However, the problematic electrode/IL interface demands enough availability of chloride ions on the surface. The nucleation analysis for glassy carbon and tungsten electrodes indicated a 3D instantaneous nucleation growth, while the nickel electrode arose a 3D progressive nucleation growth [154]. Another ionic system is often used based on quaternary ammonium salts with an amide, carboxylic acid or alcohol moiety. These ionic fluids are nominated Deep Eutectic Solvent (DES), whose main features involve harmlessness, biodegradable, easy manipulation, low cost and zero water interaction.

Recently, Barrado et al. and Rahman et al. studied the indium electrodeposition in DES using different indium precursors [165,166]. Firstly, Barrado et al. determined the reduction reaction and nucleation mechanism using glassy carbon, tungsten and copper as cathodic electrodes, while 1:2 M ratio of choline chloride-ethylene glycol (Ch-EG) system together with anhydrous InCl and $InCl_3$ worked as an electrolyte. The chloride species were reduced in one step after lnCl was disproportionally dissolved, while the nucleation and crystal growth on tungsten a 3D instantaneous nucleation growth favored by the diffusion-controlled mechanism. As a remarkable result of that work, it was possible to perform In-Cu alloys through the indium electrodeposition working with a metal copper electrode and DES [165]. Secondly, Rahman et al. proposed the indium production from DES using choline chloride and Urea systems and indium sulfate. As was previously evidenced by Barrado et al., metal support influences the indium electrodeposition mechanism. This influence means that during the indium discharge on the molybdenum electrode, nucleation was like that obtained previously on tungsten (instantaneous nucleation with diffusion-controlled growth). However, changing the metal support, in this case, by gold, the reduction reaction proceeded through a progressive nucleation process with diffusion-controlled growth [166]. From these works, operative parameters played an essential role in the indium reduction reaction: the metal support modified the nucleation process, and the CD variation changed the aspect of the indium deposit. The DES electrolyte has been studied varying electrolyte compositions to obtain In-As and In-Cu alloys [167,168]. To obtain indium alloys, these investigations could contemporaneously electrodeposit different metals, including indium. For In-As alloys, the deposition was performed via potentiostatic electrolysis, the As content within alloys increased applying more negative potentials. This electrodeposition also must be assisted by high-As content solutions [167]. In contrast, In-Cu alloys were obtained with a mass ratio different from thermodynamic diagrams due to metastable phases. Nonetheless, metastable phases were studied to produce Cu-In intermetallic alloys by varying potential and electrolyte composition [168].

Even though some works have carried out indium electrodeposition by both ILs and DES to avoid the HER formation and negative consequences, molten salts have been implemented for the same necessary. A molybdenum electrode within a eutectic LiCl-KCl arrangement at 450 °C was used in this electrolytic system. Unlike voltammetry tests from DES, molten salts indicated a two-step reduction reaction process defined by a quasi-reversible diffusion-controlled mechanism where In(III)/In(I) and In(I)/In occurred at -0.4 and -0.8 V vs Ag/AgCl, respectively. The respective coefficient diffusions for In(III) and In(I) were estimated in 1.8×10^{-5} cm^2/s and 1.4×10^{-4} cm^2/s [155]. The attractive conditions that those non-aqueous electrolytes offer for the indium electrodeposition have led many technological fields (photovoltaic, electronic applications) to produce thin films composed of indium alloys. Nevertheless, this electrodeposition view is away from an industrial consideration for indium recovery. Although the absence of water allows avoiding parasite reactions and adverse effects on the deposit quality, it is evident that molten salts required extensively thermal energy inputs rending the large-scale implementation scarcely affordable. Therefore, some of the most frequent problems for several organic electrolytes (IL and DES), such as high viscosities, lower mass transfer (diffusion conditions), lower CEs and irregular morphology of deposits because of ineffective current densities on the cathodic surface, should be improved before achieving the indium alloy production.

Based on the findings of indium electrowinning available in the literature, electrowinning is a versatile methodology capable of obtaining indium metal from any indium-bearing electrolyte, no matter the origin. Another evidence of its versatile features involves the implementation of both aqueous and non-aqueous baths. Although the latter solutions could overcome drawbacks in parasitic reactions and improve diffusive conditions, the lack of widespread literature still promotes intriguing questions that should be solved. On the other hand, electrowinning from an aqueous electrolyte currently exhibits a higher possibility to recover indium at both laboratory and industrial scales. Nevertheless, environmental, effectiveness and safety concerns are the most highlighted concerns that researchers should deal with.

Therefore, this doctoral investigation aims to evaluate the sulfate solution effectiveness for the indium electrowinning using different metal supports, avoiding toxic gas production at the anodic compartment and minor occupational risks. To render electrowinning a feasible and practical process, common metals (AISI 316L, Cu, Ni, Ti and Al) were selected as metal supports, and they were undergone all the proposed experimental arrays. Since metal materials influence the effectiveness process, an electrochemical approach of the interaction between indium and metal surface was undertaken by cyclic voltammetry, linear sweep voltammetry, polarization and chronoamperometry tests. Also, HER made part of the analysis during the indium electrodeposition reaction. Moreover, the influence of operative conditions (pH, current density, electrolyte content and temperature) was evaluated on indium electrowinning, attempting to achieve the operative condition optimization to obtain the highest CE and

lowest SEC. The deposit quality was analyzed due to the operative parameters in the electrowinning process. This deposit quality was studied according to morphology and crystallography.

Experimentation: kinetics of the indium reduction reaction and the influence of the operative parameters on the indium electrowinning process from sulfate solutions using different cathodic supports

To carry out the experimentation of this doctoral investigation, five different metal cathodic supports and sulfate electrolytes were used. This investigation is focused on evaluating two different aspects: the kinetic study near the cathodic surface to individuate the main electrochemical features of the indium reduction reaction. While the performance of the indium electrowinning process is investigated to achieve the highest effectiveness in productivity and energy consumption from sulfate solutions. The metal cathodic supports are stainless steel, nickel, copper, titanium and aluminum (AISI 316L, Ni, Cu, Ti and Al). Firstly, cyclic voltammetry (CV), chronoamperometry (CA), linear sweep voltammetry (LSV) and potentiostatic tests allow determining electrochemical features of the indium reduction reaction such as reduction-oxidation potentials, overlapping phenomena between hydrogen evolution and indium reduction peak or stripping reactions, nucleation potential, etc. The electrochemical evaluation focuses on analyzing the interaction between the metal cathode surface and sulfate solution (bulk), and the limiting process effect of the indium reduction reaction. Secondly, the indium electrowinning is carried out to analyze CE, SEC and deposit quality. The latter study consists of an optimization assessment of CE and SEC varying operating conditions (pH, temperature, electrolyte composition and current density).

Chapter 3: **Materials and methods**

Electrolytes for tests were prepared with high purity reagents (99.9% Carlo Erba Reagents) into distilled water. Each reagent was added at a time until the complete dissolution. Once the solution acquired a transparent aspect, the pH was adjusted according to each study. The pH adjustment was completed by either caustic soda or sulfuric acid. The metal supports were selected by considering the available literature for indium electrodeposition; metals such as stainless steel, copper, nickel (AISI 316L, Ni, Cu) have been widely used in the indium electrowinning using other electrolyte systems [143,154,165], while there are few works using titanium and aluminum (Ti and Al) cathodes. In addition, another reason to use those metal supports was the fact that the indium electrowinning from sulfate solutions has been slightly studied in the past. In that way, AISI 316L, Ni, Cu, Ti and Al as metal supports were selected since they are widely utilized in the electrodeposition field, allow practical and rapid comparison with other already studied systems, and supply a broad and novel knowledge about the indium electrowinning from sulfate solutions.

Metal samples (AISI 316L, Ni, Cu, Ti and Al) were cut considering a surface of around 4 cm^2. These metal pieces were used as cathodes and were independently embedded into polymethyl-methacrylate (Perspex) to evaluate the cathodic phenomena only on the face in contact with the electrolyte. After each test, the metal supports were polished with the same number of sandpaper to obtain similar starting conditions and eliminate remaining deposits that could affect the following tests. The schematic representation of experimental assessments for indium reduction reaction close to the cathodic support and electrowinning process is shown in Figure 7.

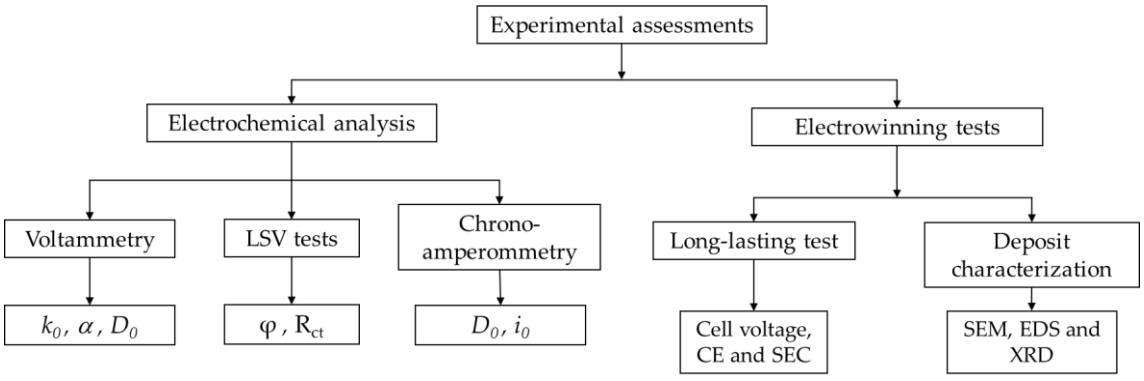

Figure 7. Scheme of experimental assessments for indium electrochemical and electrowinning process.

The indium reduction reaction close to the cathodic support was studied by performing electrochemical analysis using different techniques such as cyclic voltammetry (CV), chronoamperometry (CA), polarization tests. These methodologies allowed to determine kinetic features and nucleation of the reduction reaction, as well

as the cathodic surface relationship during the indium discharge. Indeed, kinetic parameters such as indium diffusion coefficient (D_0), roughness factor (φ), charge-transfer stage resistance (R_{ct}), heterogeneous charge transfer rate constant (k_0) and the charge transfer coefficient (α) were calculated. CV tests were performed at room temperature within a potential window between -1.8 and 1.0 V vs SCE. A solution containing indium sulfate anhydrous reaching 70 g/L In^{3+} (Sigma Aldrich, ≥ 99.9%wt.), 5 g/L boric acid (Carlo Erba, ≥ 99.5%wt.), 30 g/L sodium sulfate (Carlo Erba, ≥ 99%wt.) and 20 g/L aluminum sulfate (Carlo Erba, ≥ 99%wt.) was prepared as the testing electrolyte. These tests were initially carried out to evaluate the electrochemical phenomena on the metal supports, such as the indium deposition and hydrogen discharge overpotential, the reduction and oxidation processes of In^{3+} species, followed by determining limiting currents, discharge and onset potentials, etc. Furthermore, by varying the scan rate from 5 to 20 mV/s, the reduction reaction speed was progressively changed, allowing to perform a kinetic assessment through the calculation of the heterogeneous charge transfer rate constant and the charge transfer coefficient (k_0 and α, respectively). To carry out the CV tests, a three-electrode cell was used. A 99.99% platinum sheet worked as the counter electrode, while a saturated KCl Calomel Electrode (SCE, E_{SHE} = + 241 mV) was used as the reference electrode. The working electrodes (AISI 316L, Ni, Cu, Ti and Al) were used. In each measurement, the cathodes were cleaned by a previous cleaning process by sandpaper polishing, while the platinum electrode was etched using nitric acid and then washed by distilled water.

Furthermore, potentiostatic tests allowed to examine the nucleation process. These tests were carried out in short periods maintaining unchanged the potential value. Cu, Ti and Al supports were selected to evaluate the effect of the metal support and the electrodeposition overpotential. Since there was no HER in a wide cathodic potential range, adverse effects of this parasitic reaction were not observed during testing. After CVs, potentiostatic tests were selected close to the nucleation potential to analyze the nucleation process. Moreover, CA tests were carried out to calculate the D_0 for In^{3+} species into the sulfate solution, while k_0 was also calculated in order to compare these results with those obtained, in this investigation, by using other methodologies. The LSV technique evaluated the capacitive contribution of the double layer. The analysis consisted of the scan rate variation at the non-faradic region of each voltammogram to calculate the roughness factor of the cathode. Considering that roughness factor, Tafel's equation was plotted through cathodic polarization curves. The ohmic drop compensation was considered for all these assessments to obtain representative results. Thus, the obtained findings contributed to understanding the substrate effectiveness on the indium reduction reaction and determining the i_0 value. In addition, these results were correlated to the previous α values obtained by CV tests. Each electrochemical test was performed at least three times to validate the reliability and reproducibility of the results.

On the other hand, the indium electrowinning was carried out through galvanostatic tests to optimize the operative conditions and achieve a proper relationship between high CE and low SEC. Electrowinning tests lasted 22 h using the metal supports as cathodic support, while the anodic electrode was a lead alloy electrode (Pb-0.7Ag) with a higher surface (5.7 cm^2) than that selected for cathodes to avoid the formation of undesirable dendritic structures at the cathodic surface edges due to the edge effect. The selected electrode pair, 30 mm apart as is usually employed in electrowinning tests, was placed into a polypropylene electrowinning cell assisted by a thermostatic bath. Before each test, both cathode and anode were polished by silicon carbide sandpaper to eliminate the remaining attached deposit, as well as the oxide-lead layer that can cause anodic overpotential increases. The operative parameters were CD, pH, temperature and electrolyte composition. The starting operative parameters were selected in preliminary tests to understand its effect on CE, SEC and deposit quality. These experimental conditions were eventually changed to optimize CE and SEC, while the deposit quality of each indium electrowinning process was also evaluated regarding the aspect, morphology and crystallographic features. The summary of the operative conditions using five different metal support from are gathered in Table 4.

Table 4. Operative conditions for the electrowinning tests using different metal cathode supports from sulfate solutions

Operative conditions \ Metals supports		AISI 316L	Ni	Cu	Ti	Al
CD (A/m^2)		25-300	25-200	25-200	25-200	50-200
Temperature (°C)		15-40	25-40	25-60	25-60	25-40
pH		1.0-2.7	1.5-2.7	1.5-2.7	1.5-2.7	1.5-2.7
Electrolyte composition (g/L)	In^{3+}	30-60	50-70	70	70	70
	H_3BO_3	0-20	0-40	0-40	0-40	0-40
	Na_2SO_4	10-40	0-30	0-30	0-30	0-30
	$Al_2(SO_4)_3$	0-30	0-40	0-30	0-30	0-30

It is worthwhile to mention that both electrochemical and electrowinning tests maintain clear differences, and a direct correlation could be inaccurate sometimes. The former focuses on the kinetic phenomena near the metal support, whereas the latter is driven to the productivity in long-lasting tests, according to high CE and low energy consumption. However, the understanding of phenomena near metal support allows one to individualize the most typical features (hydrogen discharge potential, limiting currents, diffusion coefficient, exchange current density, heterogeneous charge transfer rate constant, etc.) that can infer with the indium reduction reaction during the electrowinning process. Therefore, the kinetic study is considered a relevant part of this investigation to understand the phenomena close to the metal support. Those findings

also contribute to integrating the following optimization assessments of the operative conditions in terms of the CE and SEC.

A galvanostat instrument was an Amel Instruments 2053 operated as Potentiostat/Galvanostat mode for CV, CA, polarization and galvanostatic assessments. The samples from electrochemical analysis and indium deposits obtained from electrowinning tests were washed and dried with distilled water and acetone, respectively. During electrochemical analysis, the scanning electron microscope equipped with an energy dispersive X-ray analyzer (Hitachi S-2500, SEM/EDS) was used to evaluate the nucleation process and corroborate the roughness of the metal supports. Furthermore, indium deposits from electrowinning tests were detached and cleaned to analyze the aspect and purity of deposits. The detached deposits were weighted to calculate CE. The SEC was obtained, relating the cell voltage to the electrochemical equivalent and CE (Eq. 8 and Eq. 9), as reported in the literature [169,170].

Moreover, SEM/EDS was employed to evaluate the morphology and composition of indium deposits. The structural analysis was carried out by using a PHILIPS PW 1830 diffractometer (XRD) with a Cu Kα source: λ= 1.5418 Å in a 2θ-slow-scanning angle between 30° and 80°. The XRD analysis was conducted by identifying crystallographic patterns using the crystallography open database (C.O.D).

Chapter 4:
Study kinetic of the indium electrodeposition reaction on different metals supports from sulfate solutions

4.1.Theoretical approach of indium electrolysis

A suitable approach to understanding the limiting processes near the cathodic surface surroundings can be achieved by the CV technique. The CV allows to depict several processes (reduction-oxidation reactions, electron-transfer and coupled chemical or adsorption reactions on the electrode surface, etc.) because of the relationship of CD and sweep potential in the voltammogram. In the most typical case, the peak formation preserves an intrinsic correlation with a species concentration gradient between bulk and cathodic-metal surface, allowing to calculate the limiting stage of reactions. Furthermore, other relevant information can be obtained from the voltammogram. When peaks form, peak shapes indicate the type of reversibility (reversible, pseudo reversible and irreversible) of electrode reactions [171,172]. It is worth emphasizing that the electrochemical reversibility describes the symmetry of the activation energy barrier for the redox reactions. The asymmetry condition for the activation energy barrier could represent irreversible features [173]. Hence, the standard electron-transfer (k_0) rate constant has been introduced to qualitatively evaluate the reversible and irreversible features of electrochemical reactions. However, some qualitative characteristics have been firstly identified from voltammograms, such as:

i) The separation between each corresponding cathodic and anodic peak (ΔE_p) concerns a representative value lower than 59/n mV (n: electron exchanged).

ii) The anodic and cathodic ratio of current peak (I_{pa}/I_{pc}) should be close to 1.

iii) No variation of cathodic potential peak (E_{pc}) should not be observed as increasingly scan rates.

iv) Lineal correlation between CD and the square root of scan rate (described by Randles–Ševćik expression).

Voltammograms can also supply relevant information on the nucleation process, which is attributed to a limiting step purely governed by diffusion conditions (mass-transport process) [174,175]. Once reduction reactions at cathode present quasi-reversible and even irreversible features, the above-mentioned considerations are barely accomplished. Instead, such reactions are usually ruled by charge-controlled processes (electron-transfer process) that alter curve stretching in the voltammogram. The curve change can be represented by the distancing of cathodic and anodic peaks.

Furthermore, although electrode reactions can be controlled by one or more surface electrode mechanisms, the slowest process defines the rate of limiting reactions. Therefore, fast electron-transfer processes between electroactive species and the electrode are likely related to reversible systems described by Nernstian principles. On the contrary, irreversible-prone processes suitably fit the kinetic model represented by a mix of electron transfer and mass transport processes. The irreversible electrode

reactions require other concerns rather than the typical Nernst equation used in reversible systems. As above-mentioned, k_0 permits the analysis of the irreversibility conditions. When systems near the cathodic surface are entirely irreversible, they can be expressed by Klingler and Kochi model at ΔE_P (peak to peak separation voltage) higher than 220 mV [176–179]. In Eq. 10 and 11, it is possible to observe the mathematical correlation used to determine k_0 and α values.

$$k_0 = 2.18\left(\frac{D\alpha nFv}{RT}\right)^{1/2} exp\left[\frac{-\alpha^2 nF}{RT}\left(E_p^a - E_p^c\right)\right] \quad (10)$$

$$|E_p - E_{p/2}| = \frac{1.857\,RT}{\alpha nF} \quad (11)$$

Where E_p, R and F are the peak potential (V), ideal gas (J/mol K) and Faraday's constant (C/mol), respectively; T is the temperature in K; n corresponds to electron exchanged in the limiting step reduction reaction; k_0 is heterogeneous electron transfer rate constant (cm/s), while α is the dimensionless charge transfer coefficient. C_o^* is the bulk concentration (mol/cm^3), v is the scan rate (V/s) and D_o represents the diffusion coefficient (cm^2/s).

4.2.Kinetic analysis for indium electrodeposition reaction on different metal supports

Figure 8 shows the representation of the indium electrodeposition mechanism highlighting the indium species motion from bulk to the indium metal discharge on the cathodic support. Indium (In^{3+}) species shift from the bulk to the metal surface due to the diffusion process. Once indium species go through the Helmholtz plane ($0 < x < \delta$) and are enough close to the metal support, they are deposited as indium metal ($In^0_{(s)}$). To carry out the indium reduction reaction, the indium species follows a stepwise reduction process from $In^{3+}/In^0_{(s)}$. The related literature is still unclear about the number of determining steps for indium reduction indicating only one step, more than one step [180] or even the absence of some reduced species [153] because of the operative conditions [14,181]. Some works show that indium reduction in sulfate solution can take place varying CD in two manners. At high current densities (more than 85 A/m^2) the limiting step is referred In^{3+}/In^+ reaction with 2 moles of electron exchange ($In^{3+}\rightarrow In^+\rightarrow In^0_{(s)}$) [182]. However, if current densities are lower than 25 A/m^2, a different mechanism is observed, where the limiting step with the slowest reaction takes place at In^{3+}/In^{2+} couple reaction with 1 mole of electron exchange [15,182]. Considering the used current densities in this investigation, the latter suggestion concords with that pathway for the indium reduction reaction from aqueous sulfate solutions indicating a reduction

reaction stepwise ($In^{3+} \rightarrow In^{2+} \rightarrow In^{+} \rightarrow In^{0}_{(s)}$) with 1 mole of electron exchange as will be below demonstrated.

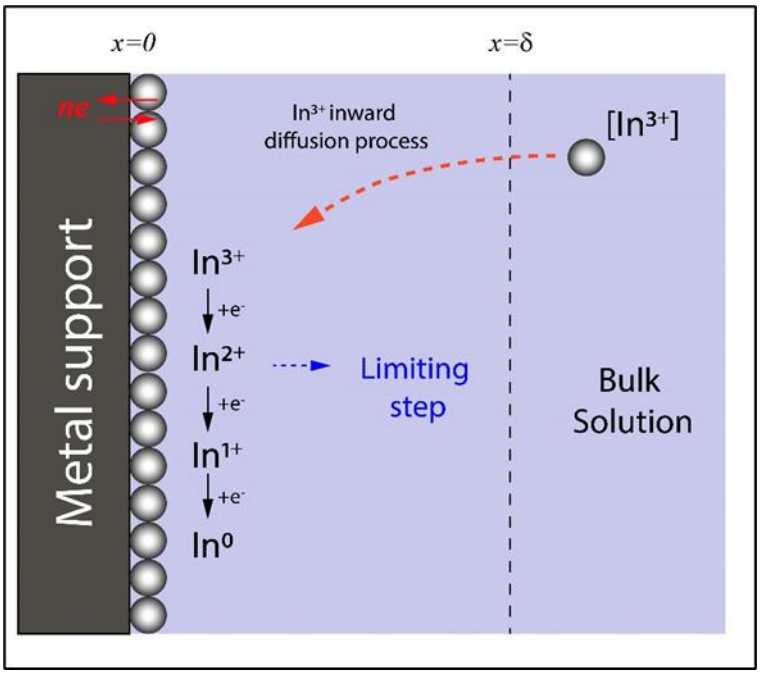

Figure 8. Representation of the indium electrodeposition process indicating the reduction reaction stepwise from In^{3+} species in the bulk and the diffusion step towards the In^{0} discharge.

In literature, the half cathodic reaction for the indium reduction can be expressed in a sequential pathway and the respective equilibrium potential (vs SHE) [181], such as the following equations (12-14):

$$In^{+} + e^{-} \rightarrow In^{0} \qquad E°= -0.14\ V \qquad (12)$$

$$In^{2+} + e^{-} \rightarrow In^{+} \qquad E°= -0.40\ V \qquad (13)$$

$$In^{3+} + e^{-} \rightarrow In^{2+} \qquad E°= -0.49\ V \qquad (14)$$

A general approach for the hydrogen discharge potential on each metal cathode was carried out using the CV technique. The solution used was private of the indium sulfate favoring the discharge of the parasitic HER reaction. Figure 9 shows voltammograms at 20 mV/s for Al, Ti, Cu, Ni and AISI 316L cathode from a sulfate solution without indium. Hydrogen discharge on Al cathode begins at a lower potential than -1.75 V followed by Ti and Cu cathode at -1.35 V and -0.85 V vs SCE, respectively. While AISI 316L and Ni cathode present, at more positive potentials, the hydrogen evolution around -0.75 and -0.65, respectively. Although AISI 316L and Ni cathode show a lower potential for

hydrogen discharge, it is possible to indicate that Cu, Ni and AISI 316L cathode experiment HER intensely at higher potentials.

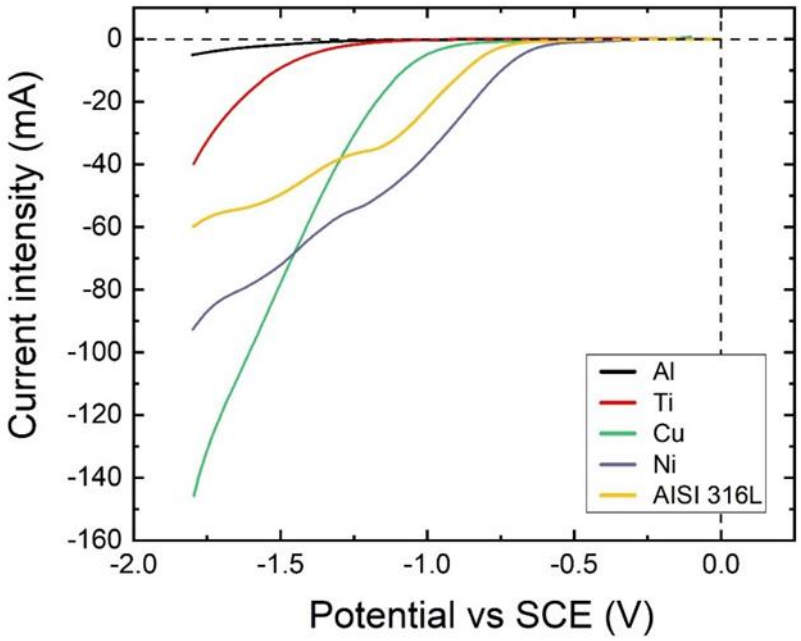

Figure 9. Cyclic voltammograms at 20 mV/s on Al, Ti, Cu, Ni and AISI 316L cathode using a sulfate solution without indium (5 g/L H_3BO3, 20 g/L $Al_2(SO_4)_3$ and 30 g/L Na_2SO_4) at pH 2.3 and 25 °C.

Figure 10 shows the cyclic voltammograms on a) Cu, b) Al, c) Ti, d) Ni and e) AISI 316L vs SCE varying the scan rate between 5 and 20 mV/s at pH 2.3 and 25 °C. This figure also presents a respective inset to observe the behavior of indium reduction peak in higher magnification. The CV test starts setting up a sweep voltage that goes forward from OCV (forward sweep) until the switching potential (-1.8 V vs SCE), where sweep potential returns to the origin (reverse sweep) defined at 1.0 V vs SCE and the cycle closes. From voltammogram, three typical reactions can be observed on each cathode:

i) Indium reduction ($In^{3+}/In^{0}_{(s)}$) [180,181].
ii) Indium stripping ($In^{0}_{(s)}/In^{3+}$)
iii) Hydrogen evolution (HER, $H^{+}/H_{2(g)}$).

Particularly, the hydrogen evolution plays a diverse role according to the metal cathode. It is worthwhile to mention that, considering the metal cathode, the hydrogen overpotential changes indicate that indium reduction reaction on the Cu, Al, and Ti cathode happens without the typical bubbles of the parasitic hydrogen evolution. This

parasitic reaction starts at a more negative potential, as shown in Figure 9. Another proof of this phenomenon is observed with low current intensities for each peak, meaning a small indium reduction peak. In contrast, different behavior of hydrogen evolution is observed on AISI 316L and Ni cathode. In Figure 9, the hydrogen overpotential on the AISI 316L and Ni cathode starts around -0.75 and -0.65 V before the indium reduction peak, suggesting the co-presence of the hydrogen during the indium electrodeposition alter kinetic features illustrated on voltammograms. The parasitic hydrogen reaction also affects the intensities for each peak, overestimating its actual value, as can be observed in Figure 10d-e. Therefore, in the case of Cu, Al, and Ti cathode, the low hydrogen overpotential (more negative) permits indium discharge to occur before hydrogen evolution, while Ni and AISI 316L cathode present the opposite behavior where the hydrogen evolution takes place before the indium discharge altering charge-transfer phenomena.

Moreover, beyond the indium reduction/oxidation peak on the Cu cathode, Figure 10a shows other reactions. At -0.17 V, a single peak corresponds to the overlapping of Cu(II) and Cu(I) reduction reactions (Cu^{2+}/Cu^{1+} and Cu^{1+}/Cu^{0}), where the former is around -0.01 V, while the latter reaction appears close to -0.31 V vs SCE [183,184]. A similar overlapping is present on the stripping region and associated with the simultaneous indium and copper oxidation (Cu^{0+}/Cu^{1+}) followed by the subsequent peak formation of Cu^{1+}/Cu^{2+} at more positive potentials (Figure 10a). Ni cathode is also observed a stripping peak at the anodic region; however, the reason for this peak has been referred in literature to the desorption of indium adatoms from In-Ni physical mixture previously deposited [185,186] (Figure 10d). In general, applying enough anodic potential on all the metal supports (Cu, Al, Ti, Ni and AISI 316L), the indium layer formed during the reduction reaction can be reversibly stripped.

On the other hand, the scan rate variation implies different aspects of voltammograms. Irreversible features and kinetic parameters for the indium electrodeposition reaction have been determined by increasing the scan rate. Qualitatively, common characteristics are displayed on curves to describe irreversible or quasi-reversible aspects for the reduction reaction, such as the irregular stretching and the dependence of the peak current with the scan rate increases. Table 5 summarizes the most relevant values for all the voltammograms indicating potential and current densities values for the indium reduction and oxidation peaks. The maximum difference of peaks (ΔE_P) shows a value much higher than 220 mV, as well as a disproportion between cathodic and anodic current density (different from 1) that points out a non-reversible process controlled by slow heterogeneous electron transfer [171,173]. This phenomenon can be expressed as an irreversible process defined by the electron transfer process.

Table 5. Potential and current values for the cathodic and anodic peaks by using scan rates between 5 mV/s and 20 mV/s for the indium solution at pH 2.3 and 25 °C.

Electrode	**ν (mV/s)**	**$-J_{pc}$ (mA/cm²)**	**J_{pa} (mA/cm²)**	**$-E_{pc}$(V)**	**$-E_{pa}$(V)**	**$\lvert\Delta E_p\rvert$**
Cu	5	5.47	15.71	0.85	0.32	0.53
	10	6.02	19.25	0.87	0.24	0.63
	15	5.52	23.81	0.89	0.16	0.73
	20	6.73	26.94	0.90	0.11	0.80
Al	5	2.48	20.61	0.95	0.07	0.87
	10	2.62	22.54	0.97	0.08	0.89
	15	2.94	23.64	0.98	0.07	0.91
	20	3.02	22.94	1.03	0.11	0.92
Ti	5	1.15	12.94	0.87	0.26	0.61
	10	2.04	16.02	0.90	0.18	0.72
	15	3.08	23.76	0.93	0.06	0.87
	20	4.35	24.94	0.97	0.02	0.95
Ni	5	5.13	3.75	0.78	0.58	0.20
	10	7.05	4.51	0.88	0.56	0.32
	15	12.24	5.94	0.99	0.53	0.46
	20	17.82	7.97	1.10	0.51	0.59
AISI 316L	5	7.18	15.13	1.15	0.16	0.99
	10	13.78	16.17	1.39	0.15	1.24
	15	16.18	16.69	1.47	0.12	1.35
	20	17.21	17.71	1.51	0.09	1.42

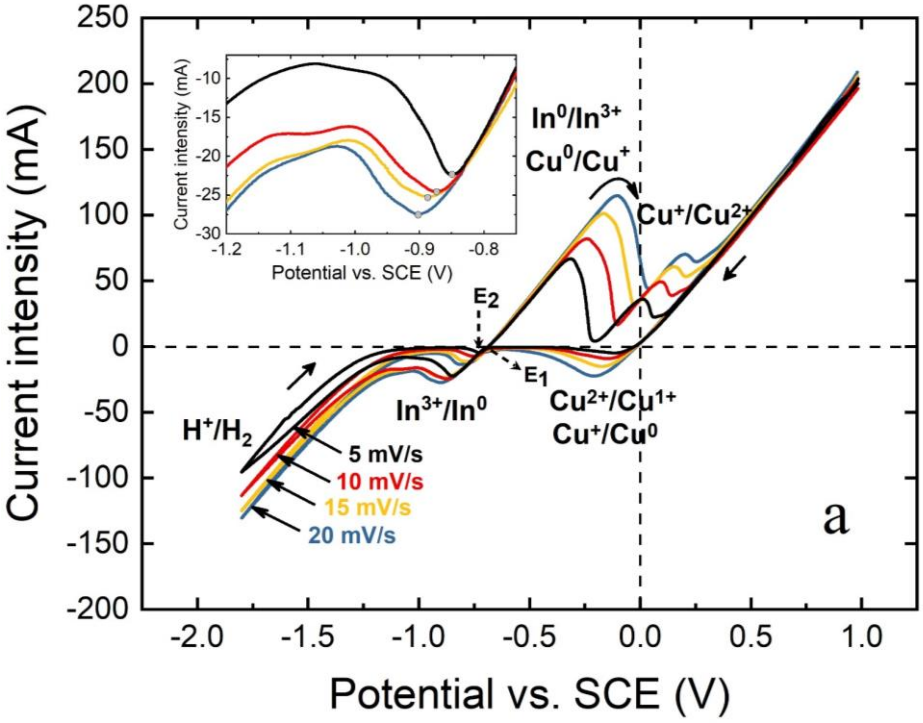
Current intensity (mA)
Potential vs. SCE (V)
In⁰/In³⁺
Cu⁰/Cu⁺
Cu⁺/Cu²⁺
E₂
E₁
In³⁺/In⁰
Cu²⁺/Cu¹⁺
Cu⁺/Cu⁰
H⁺/H₂
5 mV/s
10 mV/s
15 mV/s
20 mV/s
a

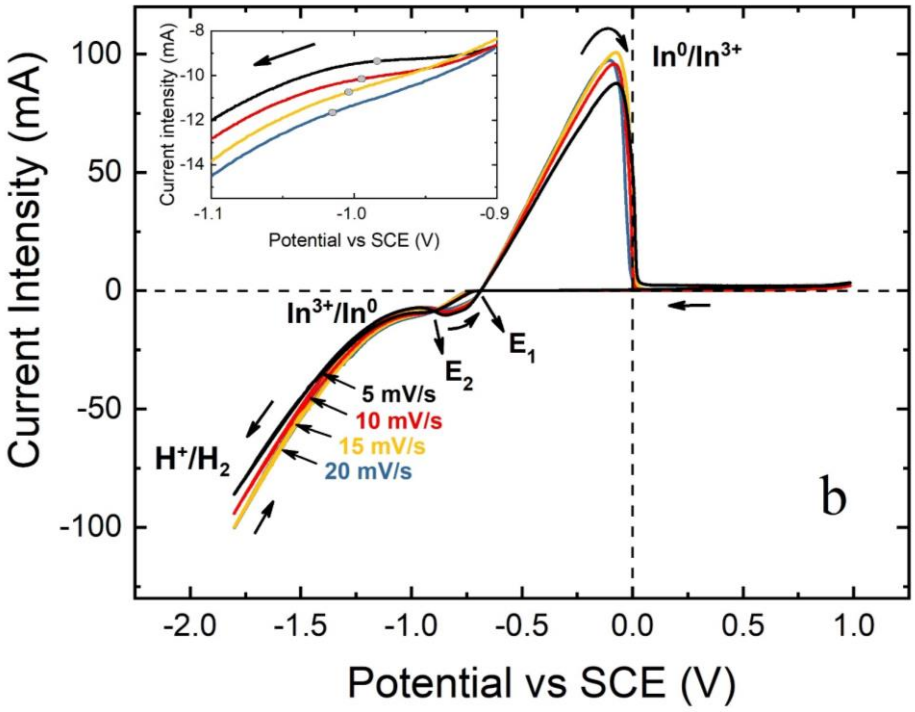
Current Intensity (mA)
Potential vs SCE (V)
In⁰/In³⁺
In³⁺/In⁰
E₂
E₁
5 mV/s
10 mV/s
15 mV/s
20 mV/s
H⁺/H₂
b

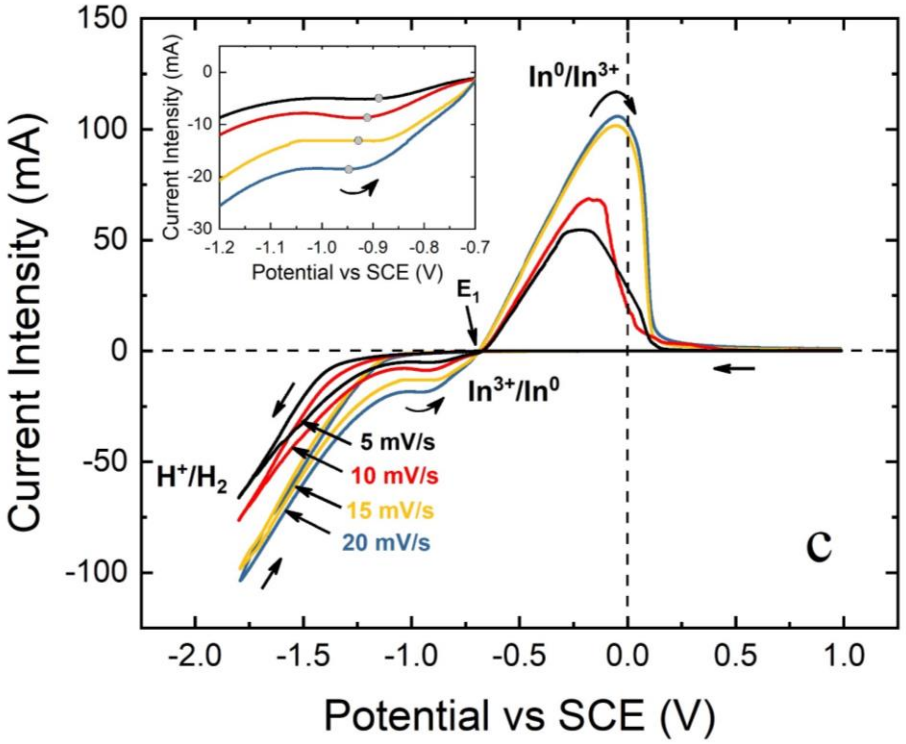
Current Intensity (mA)
Potential vs SCE (V)
In0/In3+
In3+/In0
E1
H+/H2
5 mV/s
10 mV/s
15 mV/s
20 mV/s
c

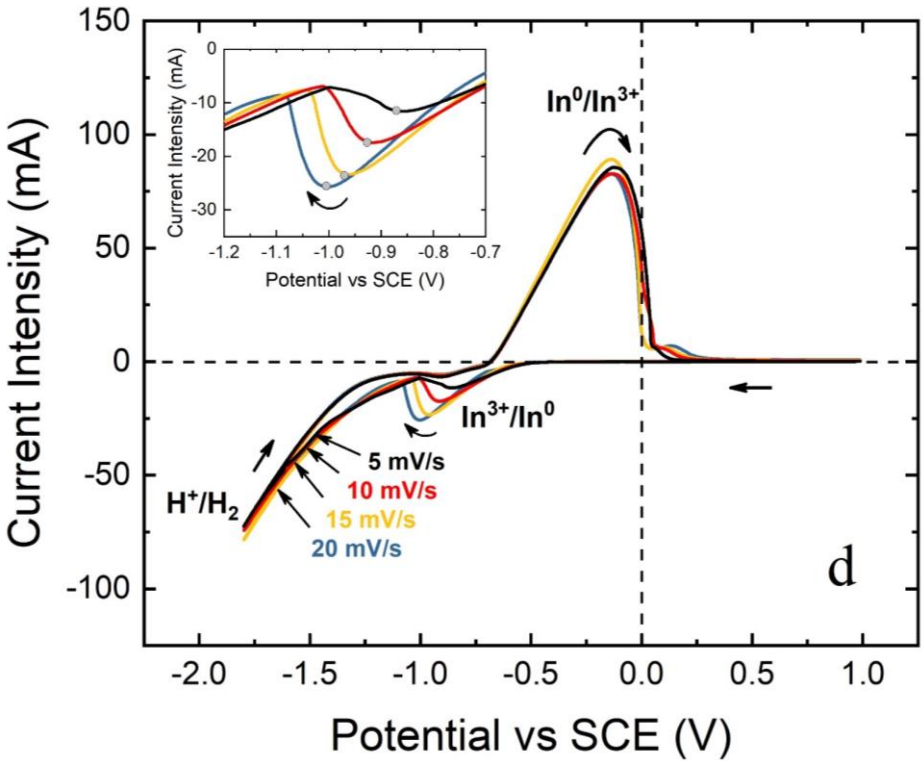
Current Intensity (mA)
Potential vs SCE (V)
In0/In3+
In3+/In0
H+/H2
5 mV/s
10 mV/s
15 mV/s
20 mV/s
d

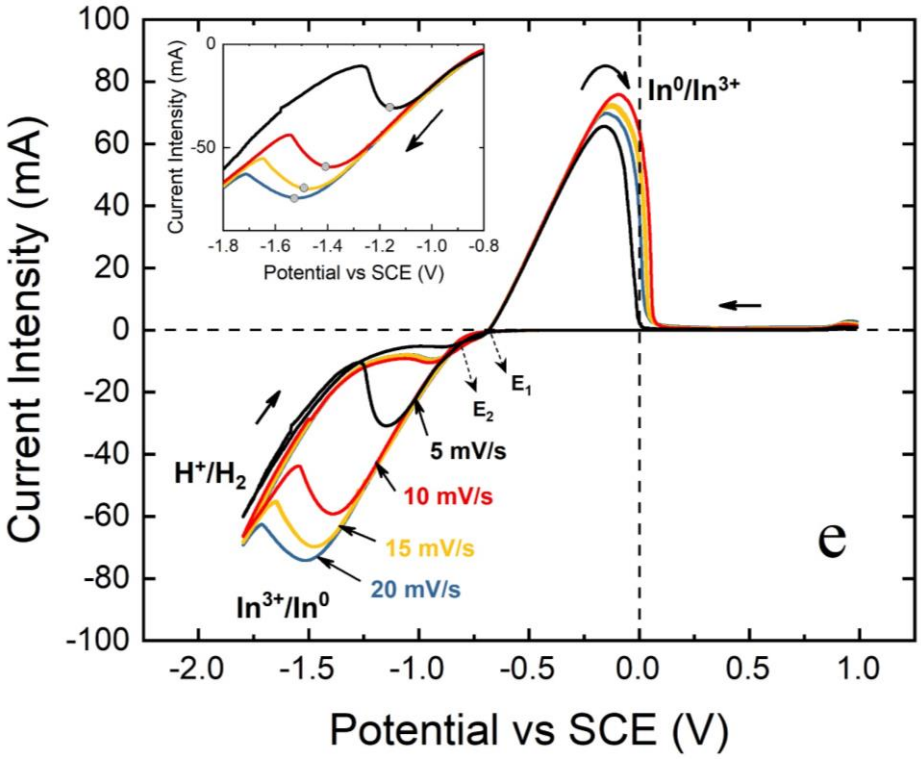

Figure 10. Cyclic voltammograms on a) Cu, b) Al, c) Ti, d) Ni and e) AISI 316L vs SCE using different scan rates (5, 10, 15 and 20 mV/s) at pH 2.3 and 25 °C. Inset: Magnification of the scan rate effect for the indium reduction peak.

During the voltammogram elaboration, two crossover points (E_1 and E_2) refer to equilibrium and nucleation potential, respectively. A close inspection on voltammograms shows that the E_1 point is firstly formed from 1 V vs SEC following the forward scanning. This intersection indicates the deposition or stripping threshold at which reaction begins (considering the sweep direction). Otherwise, the E_2 breaking point implies the starting potential for indium deposition with the nucleation process [174,187]. It is expected that E_1 matches on each metal cathode around -0.68 V vs SCE since this point corresponds with the thermodynamic equilibrium potential for In^{3+}/In^0 reaction calculated by known Nernst Equation [187]. However, a different approach can be seen in the Ni and AISI 316 L metal supports. In the former, the initial cathodic current flow is due to HER preventing the formation of the well-defined equilibrium potential for the indium reduction reaction. The latter, AISI 316L, suffers a similar phenomenon, but it seems that the hydrogen overpotential is high enough to allow a contemporaneous indium discharge and HER, and finally form the crossover point.

Regarding the E_2 point, different behaviors are observed on metal cathodes. The Cu cathode shows this point around -0.73 V vs SCE followed by the well-defined indium reduction peak (inset of Figure 10a). Correspondingly, AISI 316L and Al cathode also present a second-crossed point (E_2) on the voltammogram near -0.80 V and -0.87 V vs

SCE showing a nucleation potential much more negative than that obtained on Cu cathode. Nonetheless, a high overpotential for Al cathode hinders suitable diffusive conditions for the indium peak formation, leaving a small potential window to carry out only the indium deposition. Once the potential suppresses -1.0 V vs SEC, the reduction reaction of both indium and hydrogen, occurs contemporaneously, producing an inflection point instead of a peak. This behavior on the Al cathode is observed in the inset of Figure 10b.

In contrast, the AISI 316L cathode seems to have a behavior similar to that obtained on the Cu cathode; however, the low hydrogen overpotential (more positive), as shown in Figure 9, overlaps the real potential value for the E_2 point. In the case of Ni, this point is deprived since hydrogen discharge is much more intense on this cathodic surface. Although these cathodic surfaces favor the indium deposition (diffusion conditions for concentration gradient), the low hydrogen overpotential on Ni leads HER to increase charge transfer processes and shift crossover points (Figure 10d). Moreover, another notable observation occurs on the Ti voltammogram. A single crossover point (E_1) is shown without the formation of the indium current peak with the forward sweep potential. When the potential excesses -1.2 V vs SCE, indium discharge is accompanied by HER becoming a more favorable reaction as sweep potential reaches more negative values. Further, the reverse sweep potential forms a well-defined indium peak at around -0.9 V because an indium layer was previously discharged at more negative potentials and remained on the cathodic metal support. As reverse sweep potential turns to more positive, the hydrogen discharge overpotential is disfavored and the indium reduction peak is depicted. Then favorable diffusive conditions caused by the previous indium discharge allow the indium deposition without the HER occurrence (Figure 10c).

On the other hand, the low hydrogen overpotential on Ni and AISI 316 L cathode has altered the limiting potential and current of the indium reduction reaction, being a critical factor to carry out an accurate kinetic analysis. Initially, a comparative assessment of the effect of the indium reduction reaction and hydrogen discharge on Ni was carried out. In Figure 11a-c can be seen CV tests performed on Nickel support using a solution with/without indium sulfate, and an indium electrode with indium sulfate solution. In Figure 11a, the hydrogen discharge potential on Ni is about -0.65V vs SCE within a solution deprived of indium species. By drawing straight-line intersections (lines 1 and 2 with the abscissa) regarding both forward and reverse potential scanning, this potential is confirmed. Otherwise, a similar analysis is performed using an indium cathode into the electrolyte containing indium species (Figure 11b). Thus, the hydrogen discharge potential indicates a value around -1.25 V vs SCE (intersection of straight line 3 and the abscissa). Considering the indium reduction begins on indium cathode at a potential around -0.68 V vs SCE (intersection of straight-line number 4 with the abscissa), a significant overpotential window is evident between the indium reduction and HER on the indium cathode.

No overcrossing points are observed due to a low hydrogen overpotential (Figure 10d and Figure 11c) when the forward scanning returns at the switching potential (-1.8 V). The reverse scanning becomes less and less negative, and the indium layer, deposited on the nickel cathode, is progressively deprived of HER. Accordingly, the equilibrium potential could be found by drawing an intersection between a straight line at the beginning of stripping and the abscissa axis, giving rise to the potential close to -0.68 V. To sum up, this analysis confirms that the hydrogen evolution occurs first, before the indium reduction reaction, and its presence overlaps the overcrossing points and reduction peak on the Ni cathode.

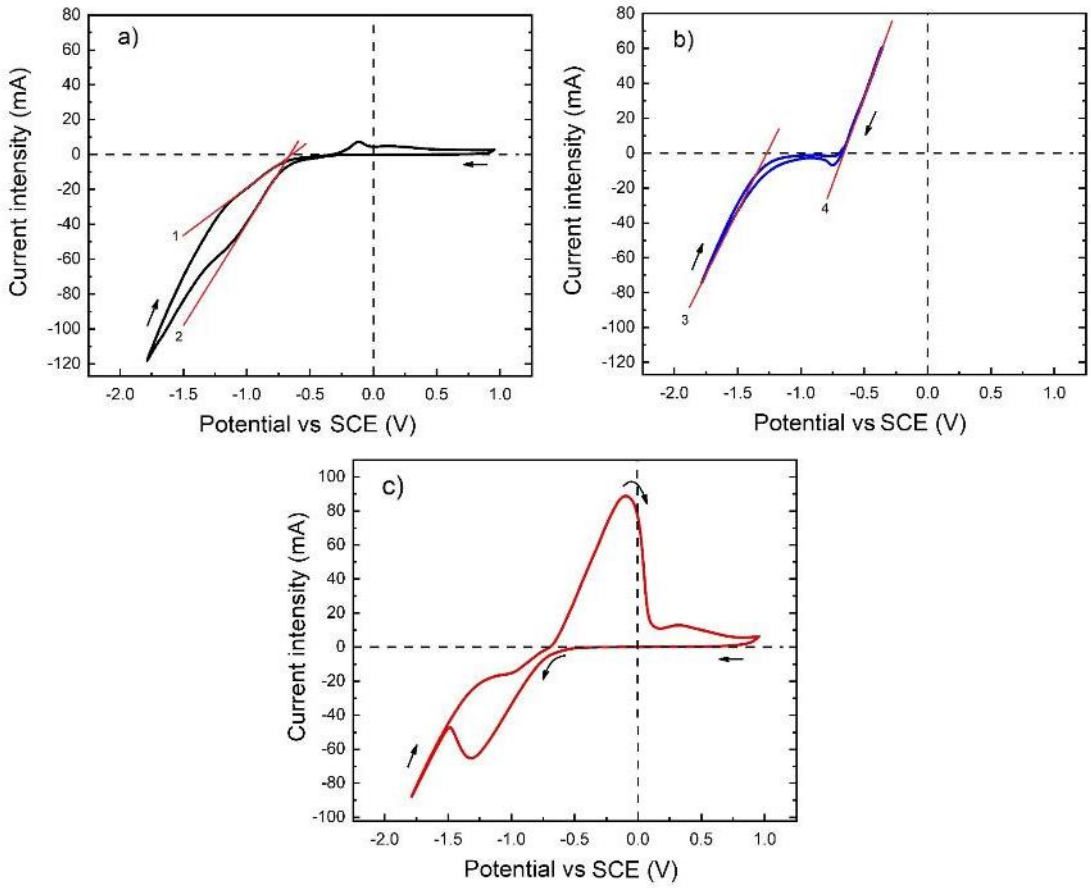

Figure 11. Cyclic voltammetry at 100 mV/s and 25 °C using: a) Ni electrode and the electrolyte without indium species; b) indium and c) Ni electrode with indium species into the electrolyte.

Figure 12 illustrates CVs for Ni and AISI 316L cathodes using sulfate electrolytes with and without indium species. These tests were carried out at different scan rates from 5 to 20 A/m^2 at pH 2.3 and room temperature. Based on these voltammograms, it is possible to indicate that the absence of the indium within the electrolyte leads to HER starts at around -0.65 and -0.75 V for Ni and AISI 316L cathodes, respectively (Figure 12a and b). Furthermore, Figure 12a shows that the hydrogen discharge for the Ni cathode,

without the indium inside the electrolyte, occurs before indium reduction and subsequently goes down after -0.65 V. Considering the indium sulfate into the solution, an indium layer takes place after the indium potential discharge is exceeded. When the indium layer covers the cathodic surface completely, it hinders the HER, producing a peak. Furthermore, a similar behavior was observed on the AISI 316L cathode in Figure 12b. However, in this case, the AISI 316L cathode suggests that both HER and indium reduction reactions start contemporaneously from -0.75 V. Anyway, this hydrogen evolution hinders the kinetic analysis of the indium reduction.

Increasing the scan rate, peaks shift towards more negative potentials and lower current intensities. This behavior is much more evident on AISI 316L than Ni cathode at low scan rates. The peak shifting could be attributed to faster hydrogen than indium discharge. The hydrogen evolution will be only hindered if the cathodic surface is completely covered by the indium deposit. From another point of view, the indium reduction reaction seems to be slower on the AISI 316L cathode with respect to what happens on Ni support, taking more time for covering the cathodic surface. Thus, the hydrogen evolution occurs longer, and consequently, the relative current peaks are higher on the AISI 316L cathode. In contrast, indium reduction on the Ni cathode seems to be a quicker reaction causing a lower hydrogen discharge. Using the same experimental conditions, the indium layer is entirely deposited faster on Ni than AISI 316L, causing the former cathode to present a lower hydrogen evolution; this means smaller current peaks in the voltammograms.

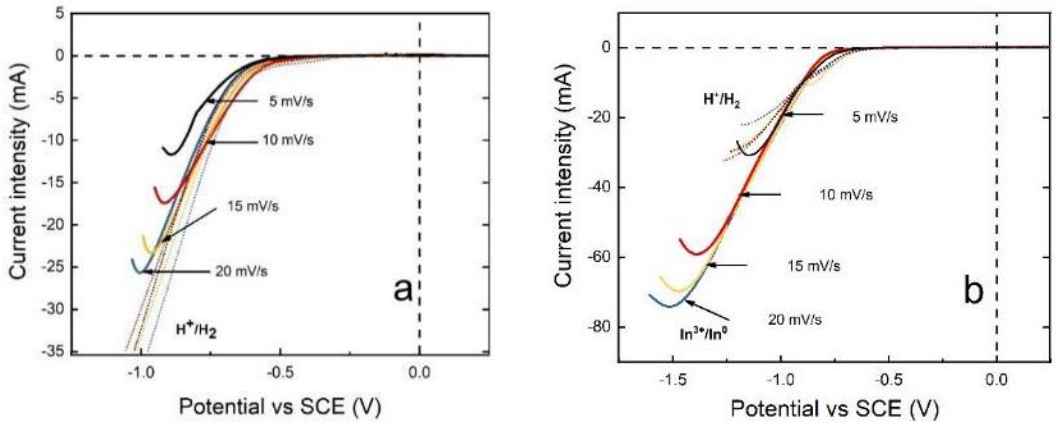

Figure 12. Comparison between the sulfate electrolyte containing supporting additives with (solid line) and without indium (dotted line) using metal cathode made of a) Ni and b) AISI 316L.

On the whole, it is evident that the HER is absent in Cu, Al, and Ti metal supports by a wide potential window. However, this parasitic reaction occurs at very low overpotentials on Ni and AISI 316L metal supports. The low overpotential of HER causes the overlapping of the indium reduction reaction on the CVs for both Ni and AISI 316L

supports. Thus, the cathodic peak formed on Ni and AISI 316L (Figure 10d and e, respectively) does not represent the unique cathodic phenomenon: a mix of both indium reduction and HER on each cathodic support. Therefore, an accurate kinetic study of indium reduction reaction on Ni and AISI 316L offers hardly representative outcomes, the fact that HER only occurs at very high cathodic overpotentials on Cu, Al and Ti cathodes has allowed to carry out the following kinetic analyses.

4.3. Nucleation stage for indium electrodeposition reaction on Cu, Al and Ti metal cathodes

Based on the previous results, Cu, Al and Ti cathodes were selected to perform a detailed kinetic study due to the absence of hydrogen discharge during the indium electrodeposition reaction. Figure 13 shows micrographs for indium reduction reaction on Cu, Al and Ti cathodes close to nucleation potential and at lower overpotentials than the E_2 point. These tests are also accompanied by composition analysis. When the E_2 point is set up around -0.78 V on the Cu cathode, the indium deposition denotes that indium grows as big and randomly distributed seeds (Figure 13a). However, at more negative potential (-0.90 V), nuclei are formed in a homogeneous distribution, as shown in Figure 13d.

Moreover, the Al cathode experiments a similar behavior around the nucleation overpotential near -0.92 V and the indium reduction at lower potential (-1.2 V) (Figure 13b-e). The respective micrographs suggest an analogous heterogeneity for the nuclei distribution with scarce indium nuclei on the Al surface at -0.92 V (Figure 13e). In contrast, Figure 13f at -1.2 V shows an abundant presence of small, well-formed indium deposits. Comparing previous results on the Ti cathode with those obtained on other metal supports show that the nucleation behavior occurs differently. By applying a constant potential at -0.8 V where there are no limiting currents (Figure 13c), the indium deposit does not occur, suggesting that the Ti cathodic surface demands a higher cathodic overpotential to start and fully carry out the indium reduction.

A reasonable explanation from the literature suggests that a direct deposition is achieved at higher cathodic overpotentials, where the nucleation step does not occur [175], passing to an kind of indium layer formation instead. According to this behavior, there is no reason to hesitate the indium deposit formation on the Ti cathode could be controlled by such a direct deposition forming small and well-distributed seeds only similar to a layer when potentials acquire very negative values on the metal surface (-1.3 V) (Figure 13f). Notably, the absence of E_2 point also suggests the diffusion conditions are favored at more negative overpotentials where simultaneous indium and HER discharge increases the limiting current. Hence, following the voltammogram, once the reverse sweep potential arrives at less negative overpotentials without HER, the formed

small and well-distributed seeds, that seems a layer, favor the diffusive conditions to depict the indium reduction peak.

On the other hand, it is well known that the bath content, type of metal cathodic support, and the applied overpotential can promote or inhibit the nucleation and subsequent growth process [188]. Thus, the metal cathodic support and the applied overpotential were analyzed for this study, leaving the bath content unchanged. Considering that different metal supports are characterized by an evident dissimilar anisotropic (adhesion surface energies, residual stress, etc.) and crystallographic properties, this latter factor also plays a relevant role in the first steps of nucleation [188]. A higher microstructural fitting could be achieved between the substrate and reduced species if they have the same or even similar lattices [188]. To the best of our knowledge, it is widely known that Cu and Al metal present a typical face-centered cubic (fcc) lattice, while a hexagonal lattice is associated with Ti metal. Thus more viable nucleation on Cu and Al cathodes is expected rather than on Ti cathode since indium metal is related to a body-centered tetragonal (bct) lattice, which is known as a slight distortion of fcc lattice [189]. Regarding the overpotential influence, a thermodynamic explanation is brought up. Nucleation can be modified by a *supersaturation* process [190], in which high overpotential allows that nuclei to be formed as small and highly distributed seeds. In contrast, low overpotentials favor bigger with a random distribution [190]. In the case of Al, the potential window to carry out the nucleation is smaller, while the deposit on Cu has a higher potential window that facilitates the indium nucleation. This behavior on Al cathode gives as a result nuclei no homogenous in both size and distribution. In fact, comparing both voltammograms, the second crossover (E_2) is different for Cu and Al metal supports, meaning that the E_2 for the Cu cathode is farther, and the Al cathode is closer, from HER. Thus, although nucleation can be explained by a *supersaturation* process (Cu cathode), higher overpotentials for the indium discharge alter the indium deposit formation.

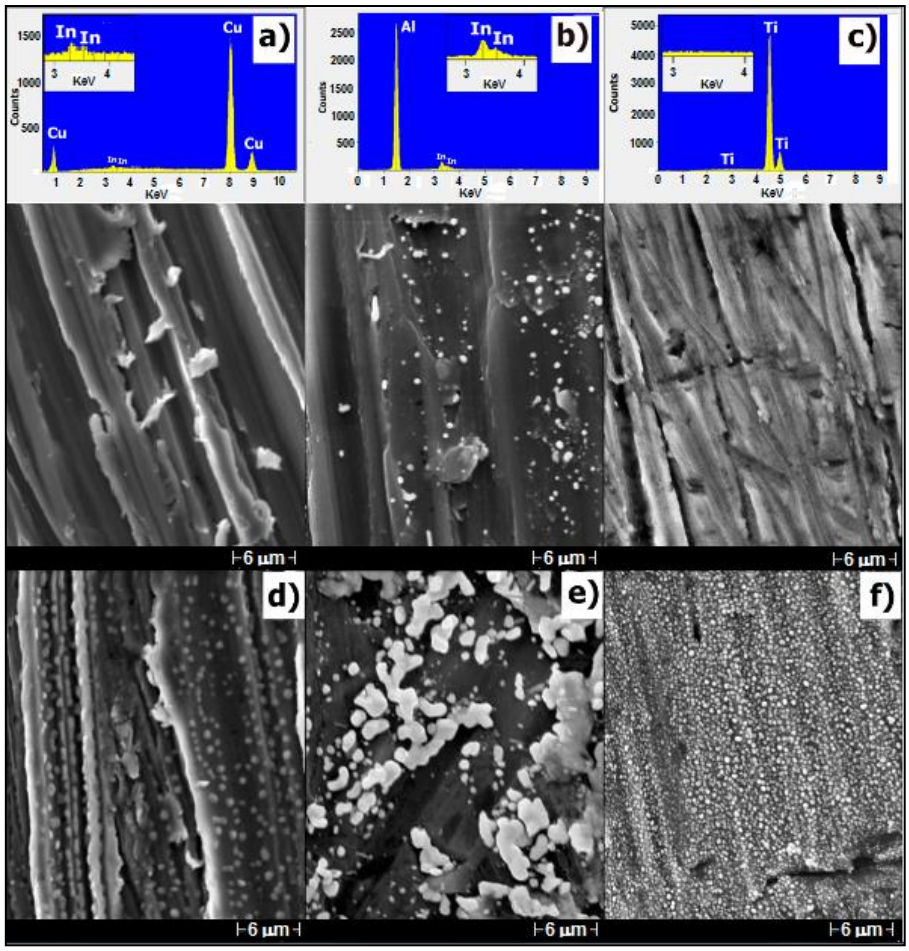

Figure 13. Potentiostatic study of the indium electrodeposition process near nucleation potentials and at more negative overpotentials for: Cu (a-d), Al (b-e) and Ti (c-f). An additional compositional analysis (EDS) has been supplied as an inset in the first stages of the indium discharge reaction (upper side).

4.4. Diffusion coefficient and heterogeneous electron transfer rate constant determination

Kinetic parameters herein are referred to Al, Ti and Cu cathodes since the HER absence avoids overlapping phenomena, allowing accurate analysis. Initially, CV and CA tests analyzed the indium diffusion coefficient. Based on the literature, equation 15 has been used for irreversible systems [191], where J_p, $[In^{3+}]_b$ and $\bar{n}$ are the current density peak (A/cm^2), the bulk concentration of indium (mol/cm^3) and the total number of electron involved in the electrochemical reaction, respectively. As previously reported, n corresponds to electron exchanged in the limiting step reduction reaction; α is the dimensionless charge transfer coefficient and ν is the scan rate. Prior to obtaining this coefficient, α values were firstly calculated by Eq. 11 from CV tests and reported in Table 6.

$$J_p = 0.496\ (\alpha n)^{0.5} \bar{n} \mathrm{F} [In^{3+}]_b \left(\frac{\nu \mathrm{F} D_o}{\mathrm{RT}}\right)^{0.5} \qquad (15)$$

The obtained diffusion coefficient is on average $4.6 \cdot 10^{-8}$ cm²/s (reported in Table 6). To verify this diffusion coefficient, CA tests were carried out and illustrated in Figure 14a and Figure 14b. The CA test was performed utilizing a sulfate solution at two different indium concentrations: 0.61 M and 0.05 M. Figure 14a shows the plot of the CD response in function of time, in which the diffusive regimen for indium at two different concentrations has been reported. Subsequently, data from CA tests were arranged and plotted according to the CD vs $t^{-1/2}$, as suggests the Cottrell law representation in Figure 14b.

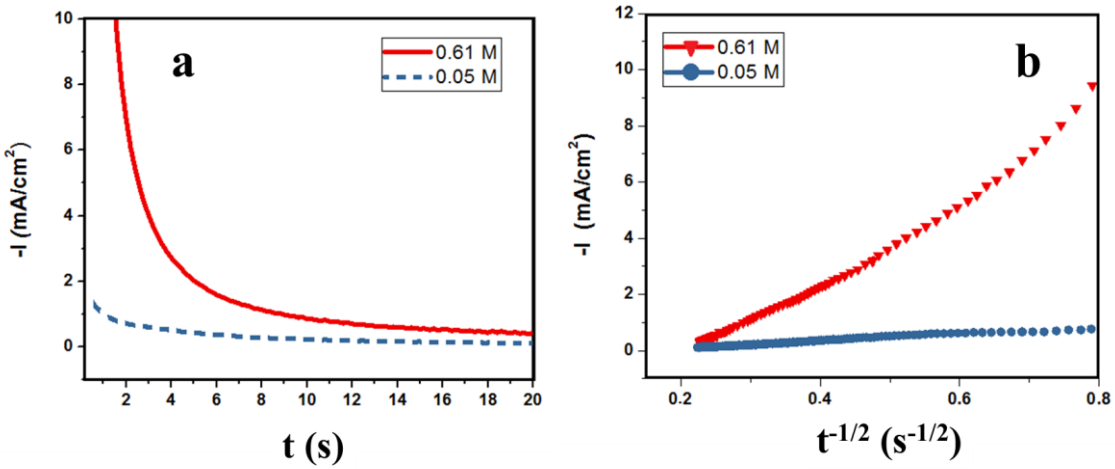

Figure 14. (a) Indium electrodeposition chronoamperogram at 25 °C on the copper support at -0.73 V vs SCE V by using different concentrations of indium sulfate (0.6 and 0.05 M In^{3+}), (b) Cottrell law representation to obtain the diffusion coefficient of In^{3+}.

Considering the diffusion coefficient calculated by the slope from the straight line, the obtained values correspond to $2.2 \cdot 10^{-8}$ cm²/s and $2.9 \cdot 10^{-8}$ cm²/s, when the concentration is 0.61 M and 0.05 M, respectively. A comparison between coefficient values obtained by CA tests and those calculated from the CV technique shows a suitable concordance, indicating that these results follow the diffusive phenomenon described by the widely known Cottrell's law (Eq. 16), as can be seen in Figure 14b.

$$\mathrm{J_d(t)} = \frac{\mathrm{nF} D_0^{1/2} [In^{3+}]_b}{\pi^{1/2} \mathrm{t}^{1/2}} \qquad (16)$$

Where $J_d(t)$ is the CD defined in function of time t. Based on the previously obtained values for the diffusion coefficient, an average value of $3.5 \cdot 10^{-8}$ cm²/s has been considered

for the following calculations. The diffusion coefficient is almost one order lower than those found in the literature for indium in chloride solutions [180]. The diffusion coefficient calculation is followed by the determination of α, and k_0 values for each voltammogram obtained at Al, Ti and Cu. Using Eq. 10,15,16, the average value for both α and k_0 for each electrode support after the nucleation process is shown in Table 6. The dimensionless α values are estimated to be around 0.11, 0.12 and 0.14, whereas k_0 values correspond to $5.4 \cdot 10^{-5}$, $6.1 \cdot 10^{-5}$ and $7.1 \cdot 10^{-5}$ cm/s for Al, Ti and Cu, respectively. A proper analysis of the above results indicates that the indium reduction reaction is controlled by a mixed process between electron transfer and mass transport, demonstrating that the suggested model and voltammograms (Figure 10a, 3b and 3c) suitably fit with irreversible features for indium reduction on the Al, Ti and Cu electrode support.

Table 6. Kinetic parameters for indium deposition using Al, Ti and Cu as electrodes by CV analysis.

Electrode	**ν (mV/s)**	**$E_{1/2}$ - E_{pc}(V)**	**α**	**k_0 (10^{-5} cm/s)**
Al	5	0.52	0.11 ± 0.3	5.4 ± 0.2
	10	0.54		
	15	0.54		
	20	0.57		
Ti	5	0.56	0.12 ± 0.2	6.1 ± 0.3
	10	0.55		
	15	0.49		
	20	0.48		
Cu	5	0.58	0.14 ± 0.2	7.2 ± 0.3
	10	0.56		
	15	0.53		
	20	0.50		
D_0($1 \cdot 10^{-8}$ cm^2/s)			4.6[a]	
			2.5[b]	

[a] *by CV (on average)*
[b] *by CA (on average)*

4.5.Roughness factor and exchange current density

The roughness factor is widely used to calculate the real surface area in function of capacitive behavior between the surface electrode and boundaries of the double layer. This estimation is helpful to evaluate the cathodic surface participation and subsequently perform Tafel analysis. To carry out the roughness factor estimation, LSV was performed in a potential range between -0.2 and -1.8 V for Al, Ti and Cu, at different scan rates. The real surface was calculated on each linear sweep voltammogram from the same non-faradic regions. In this case, metal surface supports were not intensively pretreated in order to have cathodic metal surfaces similar to those used normally for

electrowinning. In that region, the charge transfer process does not occur. Thus, it is possible to determine the roughness factor.

In practice, as scan rate changes, a capacitive current (i_c) is formed, and its progressive increase facilitates the calculation of that factor. The latter behavior presumes that there is a partially accessible surface area influenced by surface defects (porosity, cracks and grains boundaries limiting) that allows cations transfer conditions. Therefore, this internal surface area is increasingly excluded from the electrochemical response as the rapid interaction arises at very high scan rates. However, it shows a more relevant role at low scanning rates. The exclusion of the internal one at high scan rates has been associated with limiting ionic phenomena of the double layer charging process [192,193]. The surface area participation in the electrochemical response can be plotted as the scan rate in function of the current, where the output is a two-slope straight line. Such linearity occurs at two different scan rates (low and high scan rates), where the relationship of this slopes can be understood like the morphology factor μ (Eq.17), in terms of internal (C_i, due to rugosity and porosity) and total (C_t) capacity involved in the system [194].

The related literature shows that the morphology factor indicates a numerical value from 0 to 1 [15], where values closer to one means a higher internal capacity influence. Nevertheless, another interpretation of the morphological factor is presented in this investigation. Considering the roughness factor (φ) from Eq. 18, this parameter relates the total and geometrical capacity, where C_g is the geometrical capacitance defined as the difference between the total and the internal capacity. This ratio is controlled by the above-mentioned effect of the cathodic surface at a low and high scan rate. Therefore, based on these considerations, the total and geometrical capacity ratio proposes a relationship between the capacity of all microscopic and macroscopic regions on the cathodic surface.

$$\mu = \frac{C_i}{C_t} \tag{17}$$

$$\varphi = \frac{C_t}{C_g} \tag{18}$$

Figure 15 shows the change of capacitive currents at different scan rates (5,10, 15, 20, 50, 100, 200, 250 and 300 mV/s) from non-faradic regions on Cu, Ti and Al cathodes. By performing these plots from the LSV technique, it is possible to calculate the φ value. As was above-mentioned, a two-slope straight line for each cathode is shown at low and high scan rates. Hence, both C_g and C_t can be subtracted from the respective slope, while the φ value is obtained after dividing those values using Eq. 18. In Table 7, it can be seen all results regarding φ values for Cu, Ti and Al metal supports.

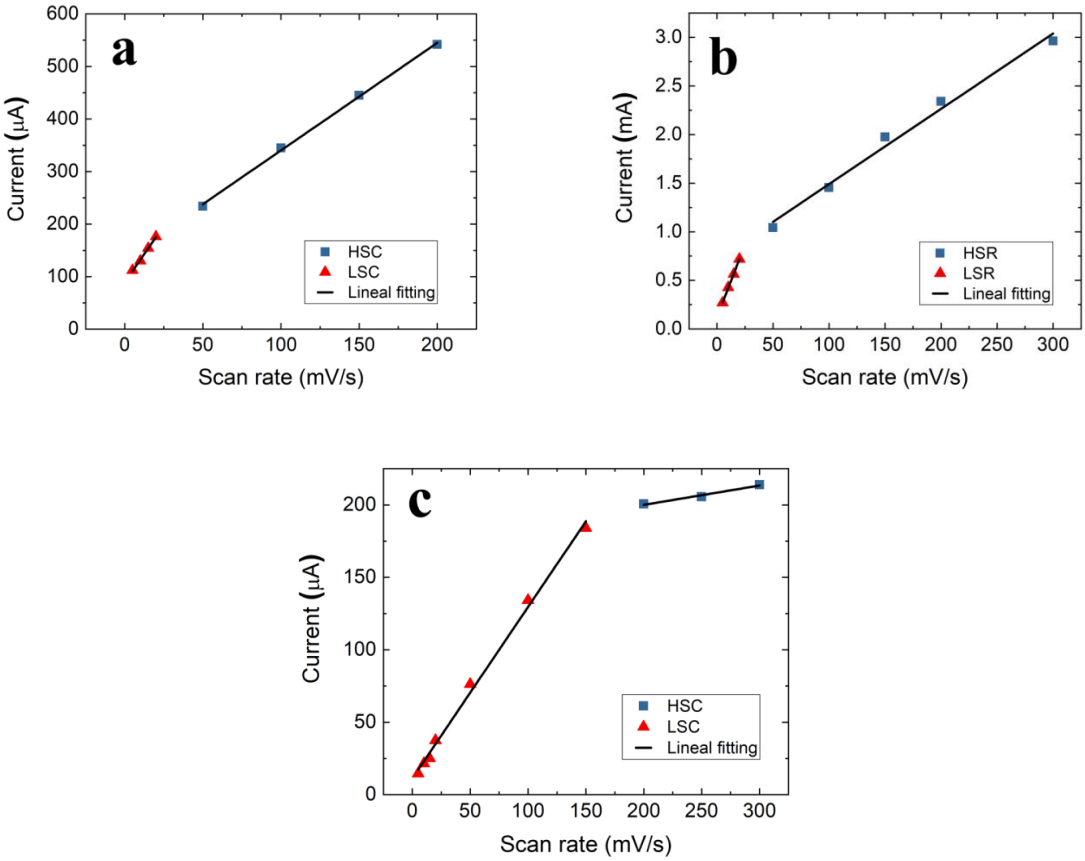

Figure 15. Change of capacitive currents in function of low and high scan rates from the non-faradic region of LSV tests on different cathodic support: a) Cu, b) Ti and c) Al.

Considering φ values, it is possible to highlight that Al cathode describes a higher roughness factor than Ti and Cu cathodes. This result means that the real surface area has a higher significance on the Al cathode, whereas the lowest influence of this parameter is observed at copper support. In addition, SEM micrographs for each metal agree with the numerical values for the roughness factor, as shown in Figure 16a-c. The Al cathode shows a local surface significantly altered by defects roughness, porosity and cracks, which is much lower for Ti and Cu cathode.

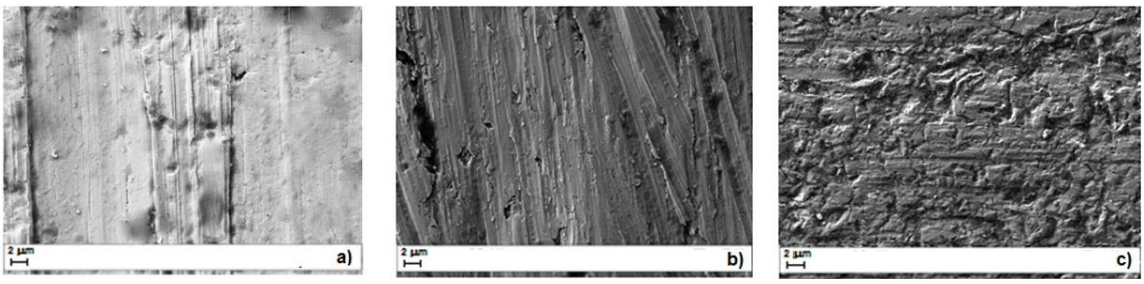

Figure 16. SEM micrographs for metal surface: a) Cu, b) Ti and c) Al cathode.

The calculated real electrode area allowed to estimate, considering the ohmic resistance compensation, the α and i_0 value using the Butler-Volmer simplified equation (Eq. 19a), also called in the logarithmic form Tafel's equation (Eq. 19b). By performing a cathodic polarization and plotting the overpotential vs log(i), as can be seen in Figure 17 for Cu, Ti and Al cathodes, it is possible to obtain the slope of each curve. In other words, pondering the slope from each curve and the respective y-axis intercept, α and i_o values are obtained.

$$i_c = i_o exp\left[-\frac{\alpha n F}{RT}\eta_c\right] \tag{19a}$$

$$\eta = \frac{RT \cdot 2.3}{\alpha n F}\log(i) - \frac{RT \cdot 2.3}{\alpha n F}\log(i_o) \tag{19b}$$

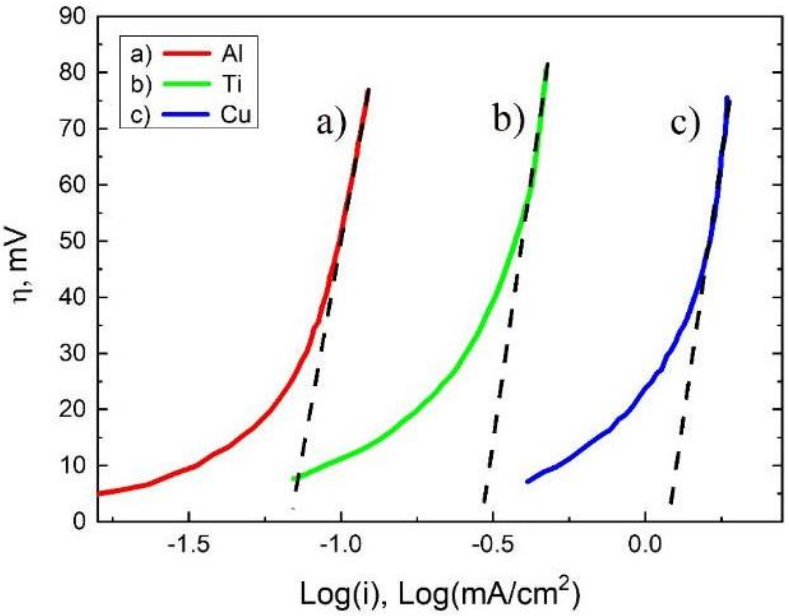

Figure 17. Cathodic polarization curves of a) Cu, b) Ti and c) Al cathode using a sulfate electrolyte to obtain the α and i_o value from Tafel's plot.

The obtained α values by the Tafel equation were compared with those previously calculated by the CV technique, reported in Table 6, indicating a suitable agreement. Based on the exchange current density, the indium discharge on copper cathode exhibits a higher electrocatalytic response with a value of 1.20 mA/cm² than Ti and Al cathodes with 0.30 and 0.075 mA/cm², respectively. This behavior suggests a lower electrocatalytic response for the same reaction at the same experimental conditions. In Table 7, the obtained α and i_0 values, the charge-transfer stage resistance (R_{ct}) and Tafel slopes can be seen.

On the one hand, The R_{ct} depicts an inverse function with the i_0 value [171], meaning that if the low overpotential regime is considered in this work, different R_{ct} values are expected as an intrinsic response of the material support at similar conditions of the indium electrodeposition. In this sense, a lower resistance is presented on the Cu cathode, followed by Ti and Al cathodes corresponding to 2.4, 5.3 and 10.4 Ω, respectively. Another relevant analysis has been supplied by the Tafel's slope, whose values are around 380 mV/decade for all metal supports, except Al cathode with 370 mV/decade. Since the slopes have a similar value, it is suggested that the indium electrodeposition reaction in an aqueous solution follows the same mechanism. Moreover, taking into account the published literature, both Markovoc in 1965 and Walsh in 1978 [14,182] indicated that the limiting step corresponds to In^{3+}/ In^{2+} (slowest step) when it is used a low regime of current densities and pH around 2.2. Thereby, their Tafel slopes and α values around 350 mV/decade and 0.15 are in concordance with the above results presented in this investigation.

Table 7. Summary of morphological and kinetic parameters for Cu, Ti and Al cathode supports in the sulfate solution.

	Metal surface		
	Cu	**Ti**	**Al**
Roughness factor (φ)	2.1	3.8	8.8
α	0.15	0.15	0.16
i_0 (mA/cm^2)	1.20	0.30	0.075
R_{ct} (Ω)	2.4	5.3	10.4
Tafel slope (mV/dec)	380	380	370

Chapter 5: **AISI 316L cathode**

5.1.Introduction

The indium electrowinning process is influenced by both the operative conditions (CD, electrolyte composition, pH and temperature) and the metal support. This chapter individuates the most relevant effects on the deposit's productivity, energy consumption, and deposit quality. Initially, the electrolyte was prepared on the basis of preliminary tests. Those preliminary experimentations were carried out to define a representative starting point and achieve the following optimization analysis. At room temperature, the starting condition was defined at 40 g/L of In^{3+}, 10 g/L aluminum sulfate, 10 g/L sodium sulfate at pH 2.0. The assessments are performed varying CD, electrolyte composition and pH. A synergic analysis of the effect of operative conditions on the indium electrowinning outputs is performed. This chapter also includes morphological and crystallographic characterization for the indium deposits.

5.2.Effect of CD on the indium electrowinning

To analyze the CD effect on indium electrowinning, the starting operative conditions were initially defined at 40 g/L of In^{3+} at room temperature and 10 g/L aluminum and 10 g/L sodium sulfate as supporting electrolytes, while the pH value was established at 2.0 after adding 20 g/L boric acid into the solution. Figure 18 shows the indium electrowinning working between 25 and 300 A/m^2 CD. In this figure, changing the CD, cell voltage, CE and SEC were evaluated. The rise of CD indicates an evident decrease in the CE values. This behavior is mainly attributed to the parasitic HER at the metal cathode.

As CD increases, the hydrogen evolution is more evident with bubbles formation covering the cathodic surface entirely [169,170,195–197]. HER is caused by a progressive overpotential increase on the metal cathodic support that triggers and becomes a parasitic reaction. This parasitic characteristic is due to a contemporaneous occurrence with indium reduction reaction. HER negatively alters the CE and limits indium deposition, favoring the bubbles' formation preferentially at high CD values [169,170,195–197]. In fact, using 25 A/m^2 CD, the process achieves 35% CE, as shown in Figure 18, while the progressive CD increase decreases the CE at 8% CE. Another consequence of this behavior is reflexed on the cell voltage increase. Once HER strongly occurs, the cathodic and anodic overpotential also increases [169,195,198,199]. A similar trend is also observed for SEC. The lowest consumption is only achieved at 25 A/m^2 with a value close to 7 kWh/kg, while it drastically increases above 35 kWh/kg, as CD rises.

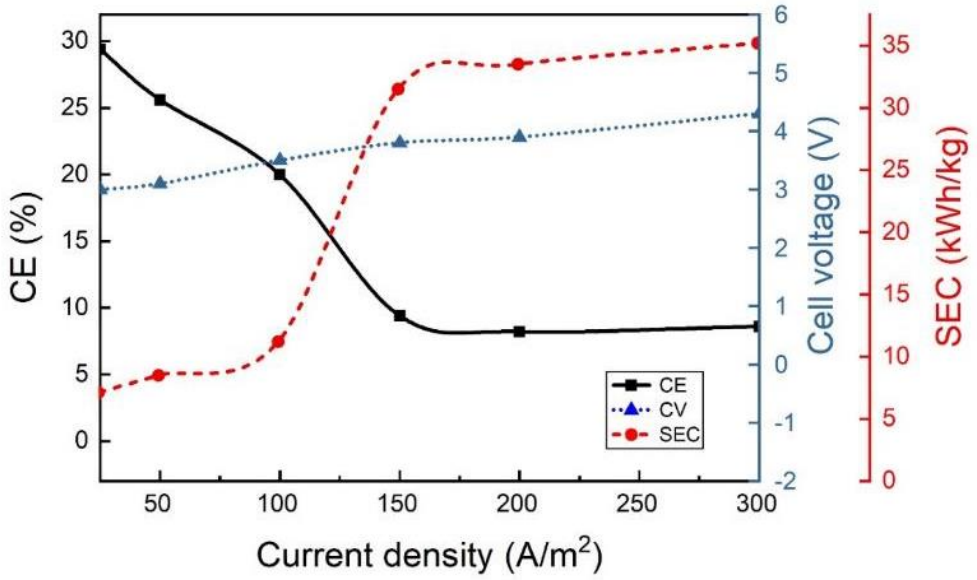

Figure 18. CD effect on the CE, cell voltage and SEC for the indium electrowinning using the starting solution containing 40 g/L In^{3+}, 10 g/L $Al_2(SO_4)_3$ and 10 g/L Na_2SO_4 at pH 2.0 and 25 °C.

Further changing CD, the deposit quality is altered. A macroscopic magnification of indium deposits shows a brilliant surface without dendritic structures at low CD values. After CD increases above 100 A/m², dendritic structures appear and become abundant (Figure 19). The starting of the dendritic structure formation is attributed to highly intensified current lines, mainly around the cathodic edge, which is well known as the "edge effect". Once the dendrite grows, it follows the current lines between the cathodic and anodic surfaces, self-feeding and subsequently growing. These dendrites are undesirable for the electrowinning process since SEC raises and short circuits can happen if dendrites reach to touch the anodic surface.

Another effect of high CDs on the deposit morphology involves the formation of round cavities or holes. Once the hydrogen overpotential is excessed on the AISI 316L cathode, bubbles are formed and attached to the surface. Considering a bubble, the overpotential is highly intensified at its border, generating irregular deposit growth and leaving a rounded-like hole once the bubble collapses or comes off. Figure 19 shows macrographs of the dendritic growth of indium on the AISI 316L cathode at different CDs. As CD increases (100, 200 and 300 A/m²), the formation of dendrites is much more evident and abundant at 300 A/m², when HER is more intensive. These figures also are related to the previous inefficient CE and SEC outcomes due to the intense HER at high CDs. This dendritic growth is a critical problem in the electrowinning process.

Figure 19. Dendritic growth as CDs increases from 100 to 300 A/m² using a sulfate electrolyte and the AISI 316L cathode.

5.3. Indium deposits obtained at high current densities

In Figure 20a-b, micrographs of the indium deposit at 50 and 300 A/m² are shown, respectively. A detailed observation of indium deposits suggests that grain in microstructure increases in size by increasing CD. A lamellar microstructure is observed in both micrographs, suggesting a progressive growth in layers. The high CD also produces irregular grains formation, as seen in Figure 20b.

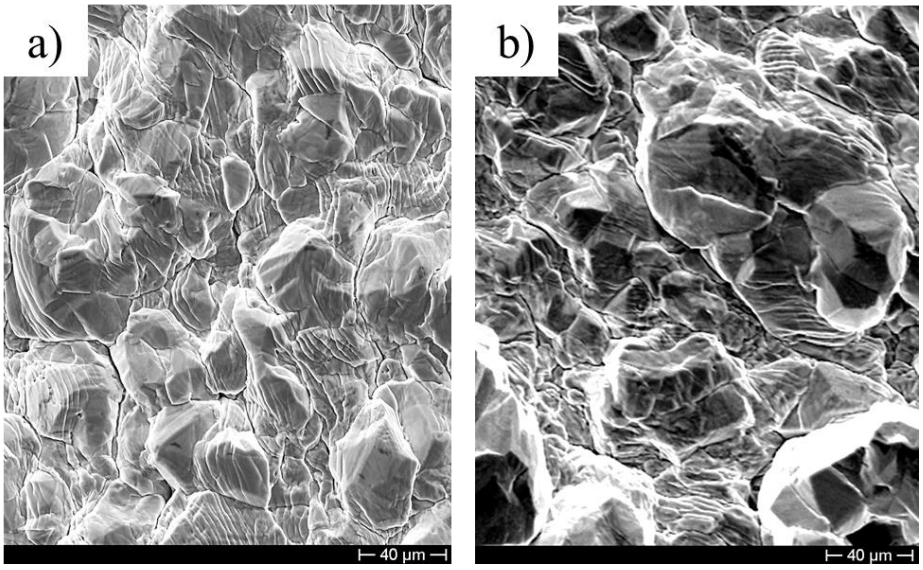

Figure 20. Morphological comparison between deposits obtained at a) 50 A/m² and b) 300 A/m² using the starting solution containing 40 g/L In^{3+}, 10 g/L $Al_2(SO_4)_3$ and 10 g/L Na_2SO_4 at pH 2.0 and room temperature.

In the case of supporting compounds, gelatin from porcine skin was initially tested to attempt to hinder the dendritic growth. These compounds are well known because of their isolating features. Since they are organic compounds virtually insoluble and non-conductors, once electrolyte is prepared with these supporting compounds, their

objective is to avoid or at least diminish the dendrites formation. This assessment was performed using a CD at 200 A/m^2 and electrolytes containing 0.02 g/L and 0.06 g/L porcine skin. Micrographs using these electrolytes can be seen in Figure 21a-b. The gelatin addition changes the gain size of the deposit, passing from around 40 μm to less than half of this size. Although the pork skin makes more refined grains, the morphology remains unchanged.

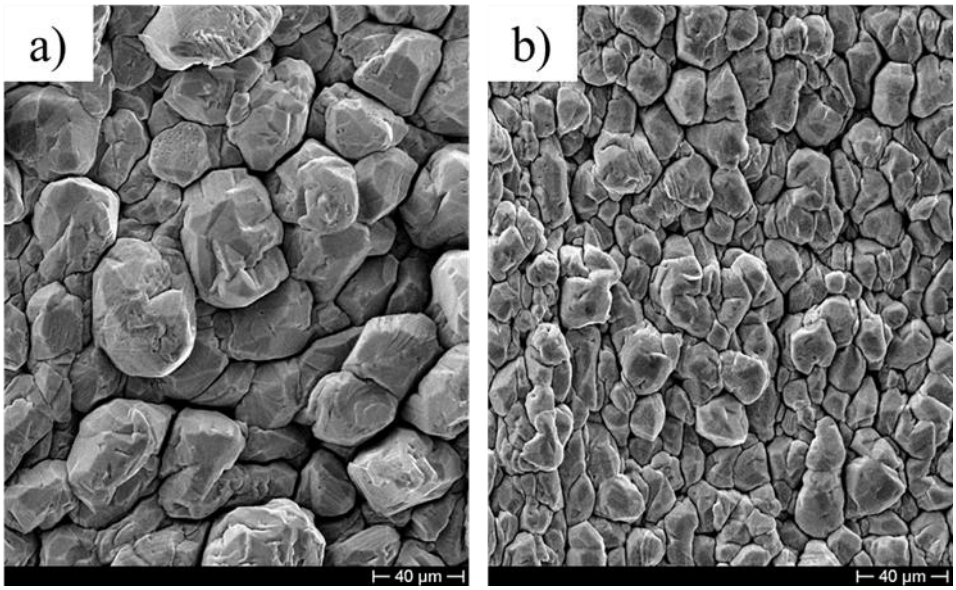

Figure 21. Effect of gelatin from porcine skin on indium deposit morphology with a) 0.02 g/L and b) 0.06 g/L at 200 A/m^2 within an electrolyte containing 40 g/L In^{3+}, 10 g/L $Al_2(SO_4)_3$ and 10 g/L Na_2SO_4 at pH 2.0.

In Figure 22, it can be seen the experimental campaign at high CD (300 A/m^2) in order to analyze the temperature effect on the indium electrowinning. Increasing temperature, both conductivity and mobility of ions into the electrolyte are altered, favoring the mass transport towards the cathodic surface of both indium and hydrogen. At the same CD, the temperature positively affects cell voltage, CE, and SEC. The increase of temperature mainly decreases the resistance overpotentials, and it seems that the indium reduction is more favored than HER. Thus, electrowinning was performed to illustrate this aspect into a sulfate solution at different temperatures (5, 25 and 40 °C). The sulfate solution, in this opportunity, contained 60 g/L of In^{3+}, 30 g/L Na_2SO_4, 20 g/L $Al_2(SO_4)_3$, 20 g/L of H_3BO_3, while the pH value was maintained close to 2.0. As shown in Figure 22, increasing from 5 to 40 °C, the CE increases from 24% to 33%, respectively. Regarding SEC, the temperature increase makes it drop from approximately 12 to 8.5 kWh/kg. The temperature variation indicates a favorable effect at 300 A/m^2 contributing to the rise of CE, despite HER and some small dendrites, as shown below.

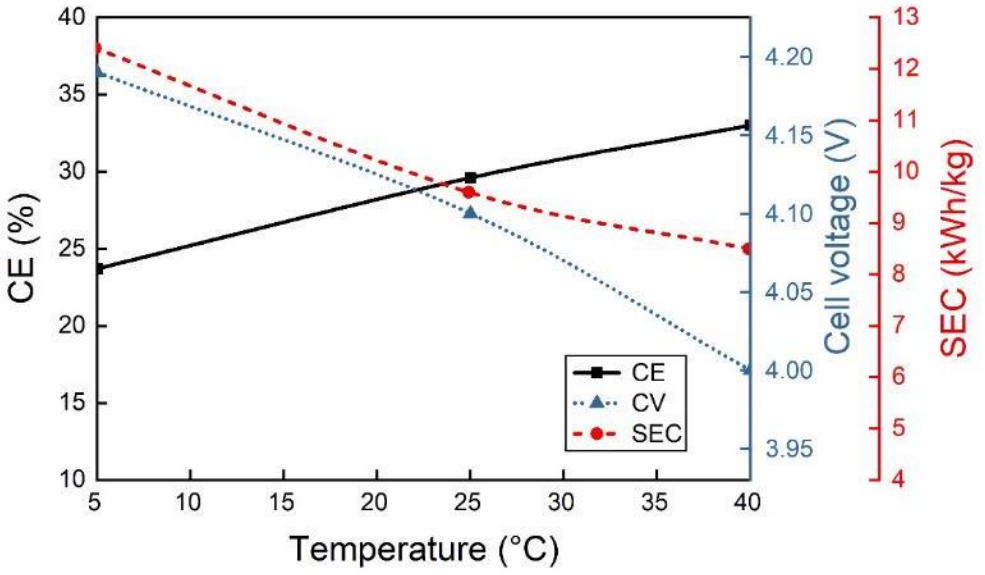

Figure 22. Effect of temperature at high current density (300 A/m²) on CE, cell voltage and SEC for the indium electrowinning using a solution with 60 g/L of In^{3+}, 20 g/L H_3BO_3, 20 g/L $Al_2(SO_4)_3$ and 30 g/L Na_2SO_4.

Figure 23 shows the indium deposit micrographs obtained at 40 °C and 300 A/m². These micrographs show rounded cavities and dendritic structures (Figure 23a), which are the HER footprints on indium morphology. Furthermore, Figure 23b reveals rounded cavities and the starting of dendritic structures around. In Figure 23c, the lamellar microstructure can be reached at high magnifications with the characteristic layers-like formation. Based on these findings, it is possible to claim that the high CDs accelerate the HER generating surface defects (dendrites and holes), but by increasing the temperature to 40 °C, the indium reduction reaction in such CD value can occur.

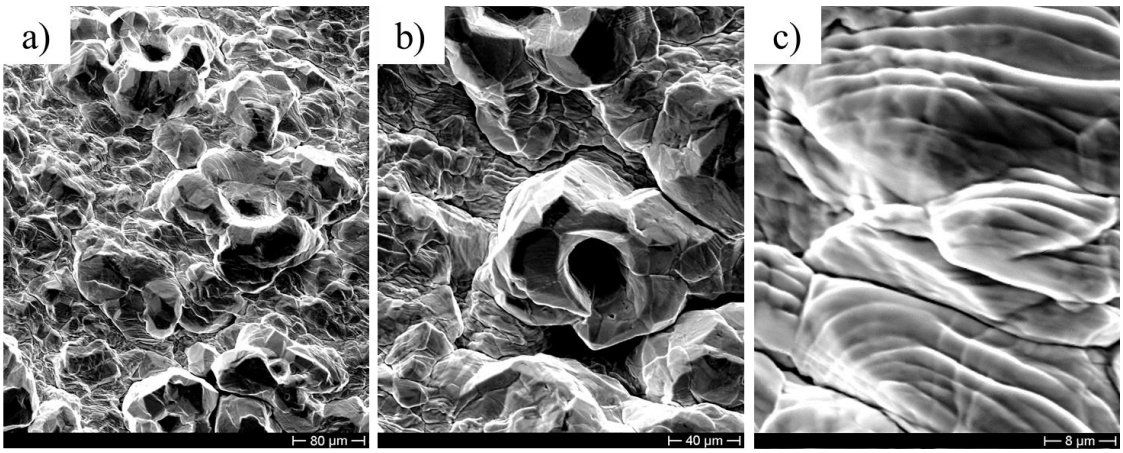

Figure 23. SEM micrographs of indium deposit obtained at 40°C and 300 A/m² at different magnifications.

5.4.Influence of the indium concentration

The influence of the indium concentration into the electrolyte was evaluated in terms of cell voltage, CE and SEC. The other operative parameters remained unaltered at room temperature, 25 A/m^2 CD and pH of 2.0. Figure 24 shows the indium concentration effect at 30, 40, 50 and 60 g/L In^{3+}. This figure shows that the CE value increases as indium concentration increases. This behavior indicates around 18 % CE at 30 g/L In^{3+}, while reaches to 48% CE at 60 g/L. Conversely, cell voltage and SEC show a progressive decrease as indium concentration rises. In fact, at 30 g/L In^{3+}, those parameters are around 4.5 V and 17.1 kWh/kg, respectively. However, when the In^{3+} concentration in the electrolyte increases at 60 g/L, CE and SEC increasingly fall at about 3.3 V and 4.3 kWh/kg, respectively.

Based on these results, the low indium concentration is not convenient for electrowinning. The low concentration of bearing-species can cause both increases of both resistive and concentration overpotential components, inducing conditions for HER or even promoting the formation of unstable species (hydroxides and sulfates) [157,200,201]. Therefore, the exhausted electrolytes represent an improper condition for the indium electrowinning. Thus, it is suggested that indium concentration should be maintained at values higher than or equal to 60 g/L In^{3+}.

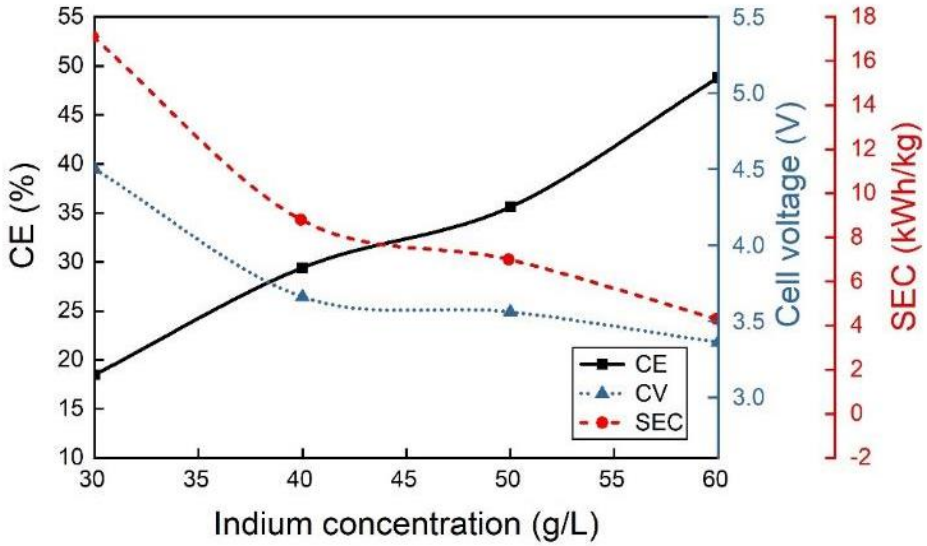

Figure 24. Effect of the indium concentration on CE, cell voltage and SEC using a sulfate electrolyte composed of 20 g/L H_3BO_3, 10 g/L $Al_2(SO_4)_3$ and 10 g/L Na_2SO_4 at 25 A/m^2, pH 2.0 and room temperature.

Figure 25 shows SEM micrographs of the deposited samples at low and high indium concentrations. In both cases, the size and shape of grains are not well defined. However, the deposit at high concentration shows a microstructure like overlapped layers (Figure 25c-d). This growth is also known as lamellar growth, and it is more evident at high magnifications. In agreement with the CD effect, the dendritic structure does not occur at 25 A/m^2 even if the indium concentration is adjusted at 40 g/L; however, the deposit aspect is quite irregular using that latter concentration.

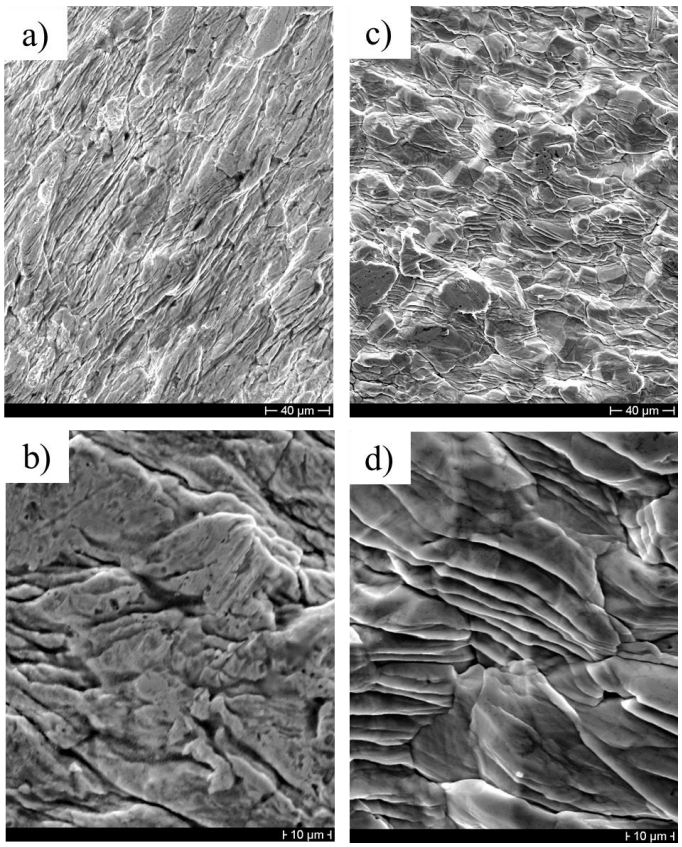

Figure 25. SEM micrographs at different magnifications of indium deposits obtained at 25 A/m^2, (a- b) 40 g/L and (c-d) 60 g/L indium, respectively.

5.5.Effect of supporting salt in the electrolyte

The deposit quality is considered a consequence of the electrowinning process. The composition of the electrolyte has a significant effect on indium deposition. In the literature, some authors have mentioned the insulating influence of adding organic components into the electrolyte [202]. These compounds hinder the dendrites formation on deposits due to local inhibitions of the overpotential close to edges.

Other inorganic supporting compounds have been identified as inorganic salts, whose primary function is to alter both conductivity and final aspect of deposit.

Different supporting compounds (boric acid, aluminum and sodium sulfate) were used in this investigation to evaluate their effect on the indium electrowinning (CE, SEC and deposit quality). The deposit quality was studied according to its morphology and crystallography. The starting electrolyte above used (60 g/L In^{3+}, 20 g/L H_3BO_3, 10 g/L $Al_2(SO_4)_3$ and 10 g/L Na_2SO_4) was considered the starting solution, and each inorganic compound was changed one at a time.

In Figure 26, the variation of the aluminum sulfate concentration was considered fixing the composition from 0 to 30 g/L. The presence of aluminum sulfate within the sulfate electrolyte shows a slight change for the cell voltage remaining on average around 3.1 V. However, CE and SEC are notably influenced by this compound at 20 g/L with a value of 5.2 kWh/kg. The other concentrations indicate lower CE and higher SEC outputs, suggesting that the proper condition is 20 g/L aluminum sulfate concentration.

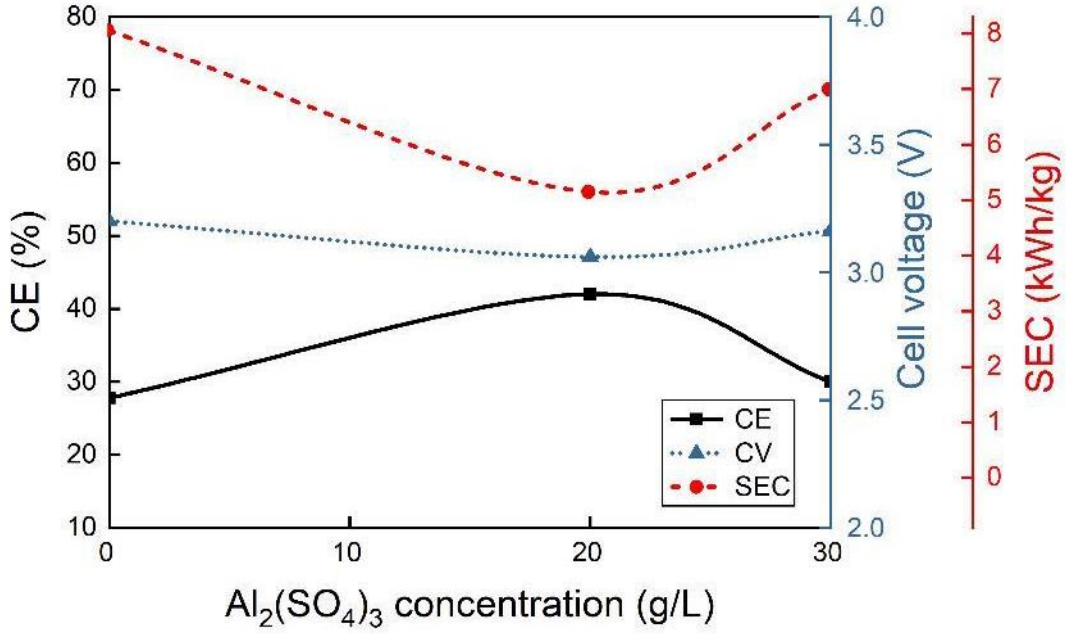

Figure 26. Effect of the aluminum sulfate addition on indium electrowinning using a sulfate electrolyte containing 60 g/L In^{3+}, 20 g/L H_3BO_3 and 10 g/L Na_2SO_4 at 25 A/m², pH 2.0 and room temperature.

Figure 27a-c shows indium deposits obtained by varying the aluminum sulfate at 0, 20 and 30 g/L, respectively. An analysis of all three deposits highlights a slight effect on the grain shapes till the aluminum sulfate reaches 20 g/L. Deposits obtained without and 20 g/L of aluminum sulfate (Figure 27a and Figure 27b) present grains size on average very similar, around 40 μm. Additionally, the former concentration shows grains with well-marked polygonal shapes and a subtle plate-like growth. The increase of aluminum sulfate at 30 g/L proposes a drastic change in the grain morphology. This morphology seems to be highly compact, where a lamellar microstructure is widely evident on the

grain surface. In general, the lamellar microstructure is present on each sample; however, it is much evident as aluminum sulfate rises.

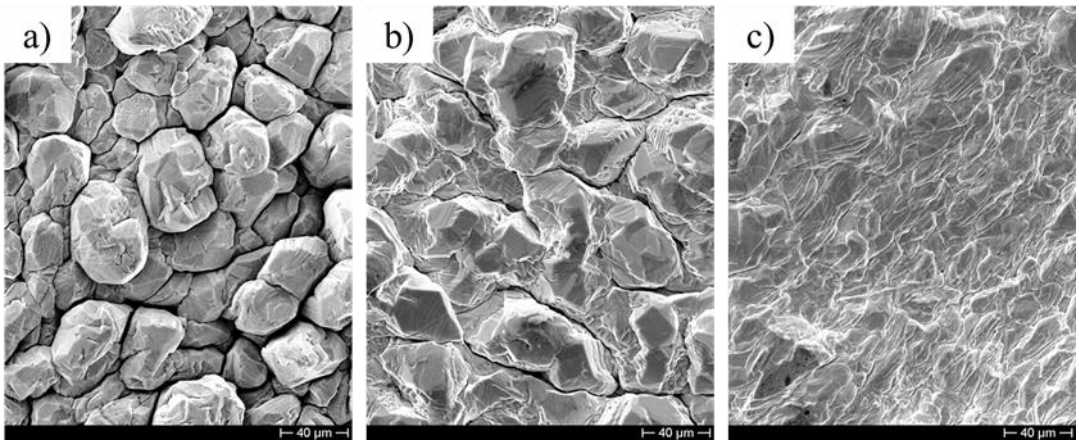

Figure 27. SEM micrographs of indium deposit at 25 A/m² varying the aluminum sulfate at a) 0, b) 20 and c) 30 g/L into 60 g/L In^{3+}, 20 g/L H_3BO_3 and 10 g/L Na_2SO_4 at 25 A/m², pH 2.0 and 25 °C.

Figure 28 shows the cell voltage, CE and SEC variation of indium electrowinning as the sodium sulfate content is changed from 10 to 40 g/L in the sulfate-based solution at 25 A/m² pH 2.0 and room temperature. Based on these results, cell voltage slightly varies, but this parameter decreases as sodium sulfate increases. Nonetheless, the CE value enhances up to around 40% at 30 g/L sodium sulfate. Further, SEC drops at 30 g/L sodium sulfate, while the other concentrations show higher output in SEC.

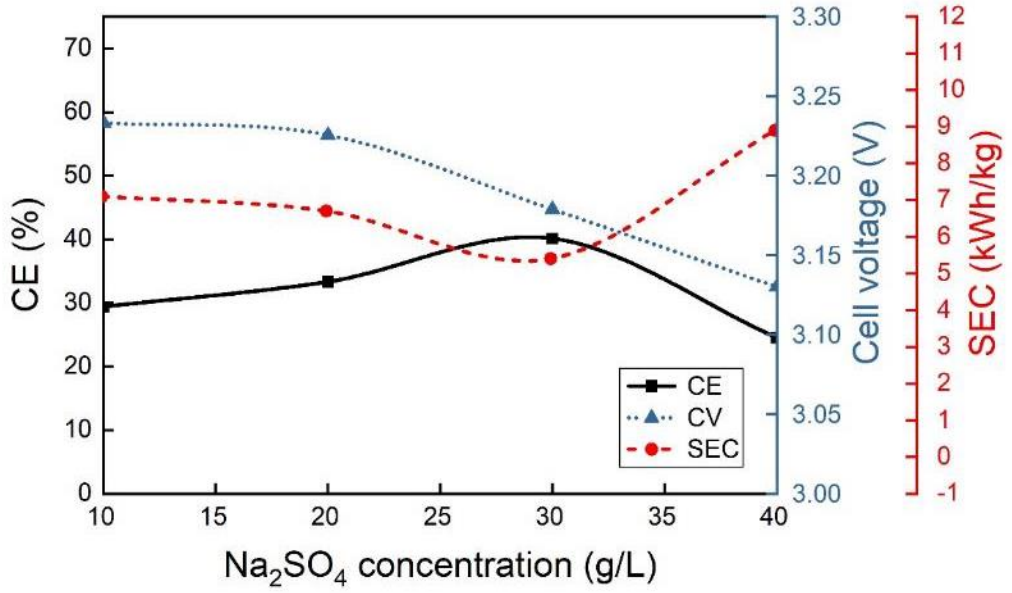

Figure 28. CE, cell voltage and SEC for the indium electrowinning changing the sodium sulfate concentration within 60 g/L In^{3+}, 20 g/L H_3BO_3 and 10 g/L $Al_2(SO_4)_3$ at 25 A/m², pH 2.0 and 25 °C.

In Figure 29, it can be seen the micrographs for deposits obtained at 10, 20 and 30 g/L sodium sulfate, pH 2.0 and room temperature. The micrographs show slight changes in the deposit microstructure. In fact, a regular microstructure is characterized by grain size smaller than 40 μm on average. Although the growth is chaotic and randomly oriented, the grain edges are well-defined. A growth of plate-like grains is observed for each sodium sulfate concentration being more evident at 30 g/L.

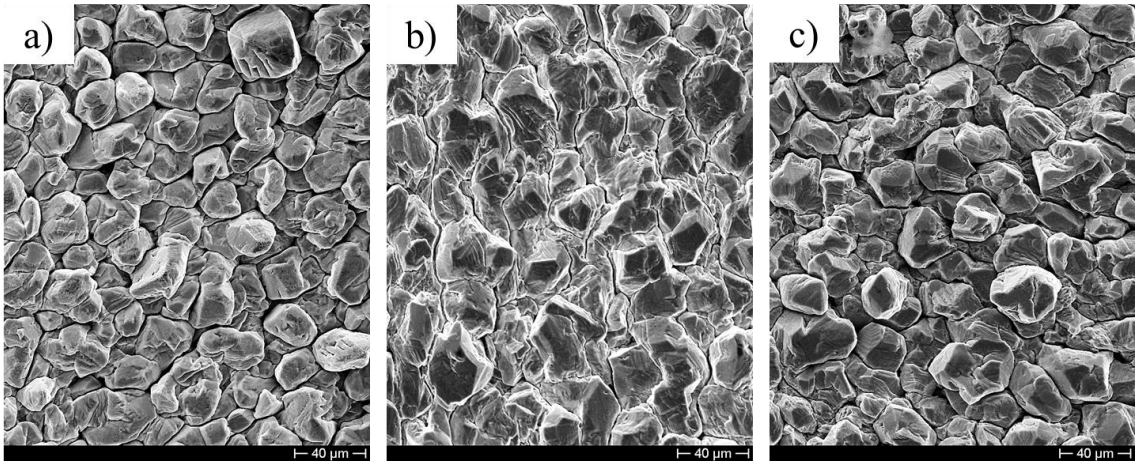

Figure 29. SEM micrographs of the indium deposits influenced by the sodium sulfate concentration at a) 10 g/L b) 20 g/L; and c) 30 g/L within an electrolyte containing 60 g/L In^{3+}, 20 g/L H_3BO_3 and 10 g/L $Al_2(SO_4)_3$ at 25 A/m², pH 2.0 and 25 °C.

The supporting salts effect was evaluated by XRD analysis are performed, considering indium deposits obtained with the electrolytes proposed in Table 8. These assessments were carried out at different sodium and aluminum sulfate, where indium and boric acid content were unchanged.

Table 8. Sulfate solutions containing different sodium and aluminum concentrations for the XRD analysis.

	Concentration (g/L)			
Solution	**In^{3+}**	**$Al_2(SO_4)_3$**	**Na_2SO_4**	**H_3BO_3**
a	60	10	10	20
b	60	30	10	20
c	60	10	40	20

As shown in Figure 30, the three XRD patterns illustrate a tetragonal crystalline structure related to indium identified with the crystallographic open database (C.O.D, 1538014). The crystallographic orientation is related to a characteristic peaks (101), (002)

and (110) before 40° (2θ), being the preferential peak (101) for all the studied compositions. Further secondary orientations are present at higher angles (2θ), with lower intensities. Although XRD patterns suggest a slight change as the composition varies, the substantial difference is defined in the power of the preferential orientation at 101, once 40 g/L sodium sulfate is used (Figure 30c).

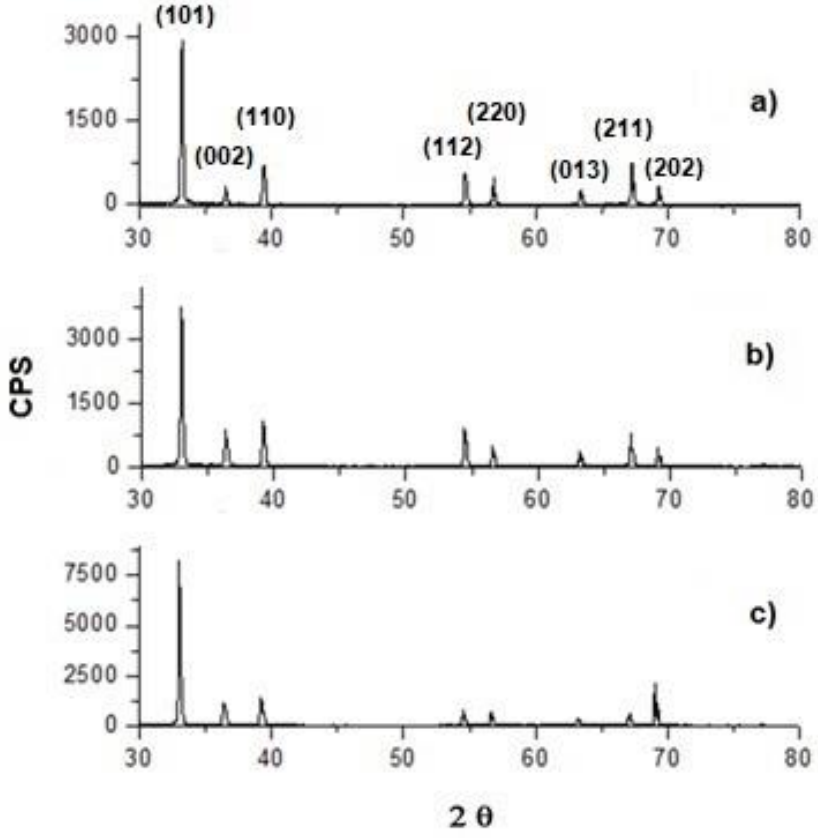

Figure 30. XRD patterns for indium deposits were performed using solutions containing a) the sulfate solution (blank), b) high aluminum sulfate (30 g/L) and c) sodium sulfate (40 g/L) concentration at pH 2.0 and 25 °C.

The boric acid also is considered in this investigation, evaluating different concentration levels (0, 10 and 20 g/L) and observing its effect on the indium electrowinning process. This procedure was performed using the same starting electrolyte at room temperature and pH 2.0, as shown in Figure 31. That figure shows the variation of cell voltage, CE and SEC, as boric acid is added into the sulfate electrolyte. When electrolyte contains 20 g/L boric acid, only a maximum of around 43 % CE is observed with the lowest cell voltage and SEC close to 3 V and 4.8 kWh/kg, respectively. The other conditions present worse electrowinning outputs, such as around 30% CE and 6.8 kWh/kg in the absence of boric acid. From literature, the boric acid effect into sulfate solutions has been discussed, indicating that this compound leaves protons

in the diffusion layer on the cathode once dissociation is reached. Such proton release transfers at more negative potentials the reduction region [203–205]. Based on this evidence and the results presented, there is no reason to hesitate about the importance of boric acid on the indium electrowinning on AISI 316L, showing a CE and SEC improvement using 20 g/L boric acid.

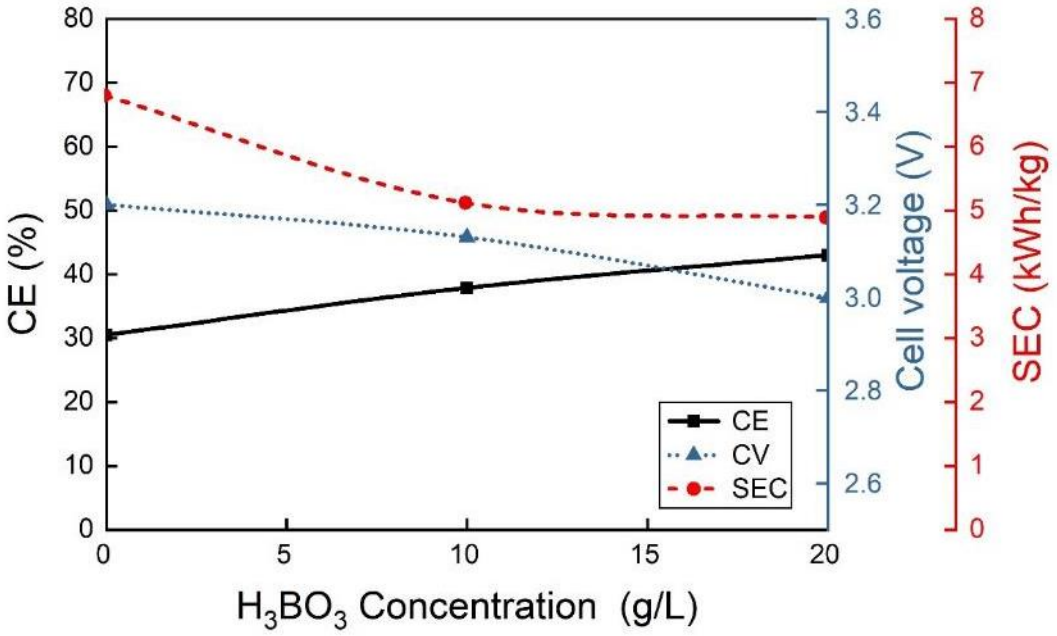

Figure 31. Effect of different boric acid concentrations on the CE, cell voltage, and SEC within an electrolyte containing 60 g/L In^{3+}, 10 g/L $Al_2(SO_4)_3$ and 10 g/L $Na_2(SO_4)_3$ at 25 A/m², pH 2.0 and 25 °C.

Figure 32a-c shows the morphology change of indium deposits with different boric acid concentrations (0, 10 and 20 g/L). The obtained morphologies present slight changes. It only can be seen large grains with irregular shapes. Those grains, in fact, lamellar growth. Based on these results, it is clear that boric acid has a more significant influence on CE and SEC than deposit morphology using AISI 316 as a cathode.

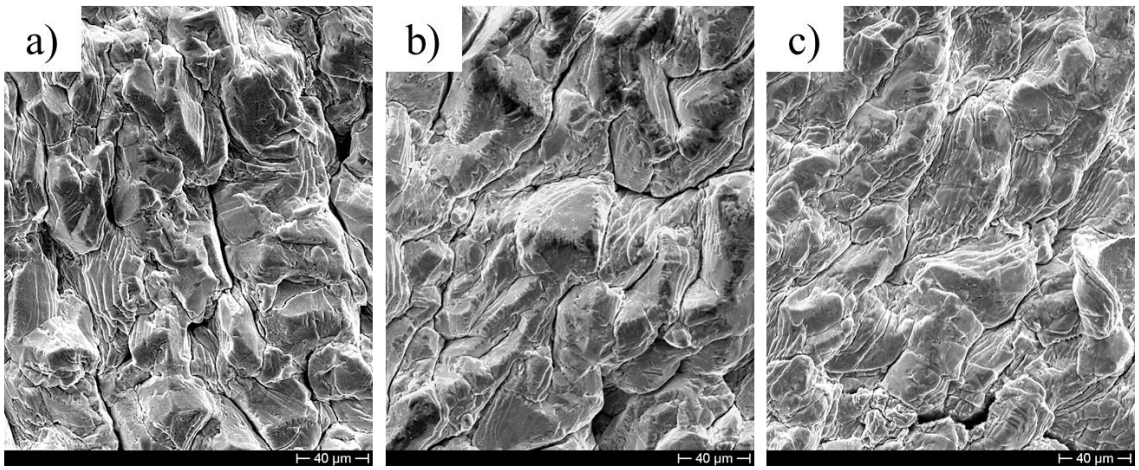

Figure 32. Micrographs for indium deposits varying the boric acid concentration at 0, 10 and 20 g/L.

5.6.The pH effect on the indium electrowinning process

The stability region for In^{3+} is theoretically defined until pH 3.0 in the potential-pH equilibrium diagram (Pourbaix diagram) for the indium-water system (Figure 33). However, indium tends to form indissoluble hydroxides after exceeding pH values around 3, impeding stable conditions for electrowinning, including the electrolyte preparation. Further, pH can be increased near the cathodic surface during electrowinning, facilitating indium hydroxide precipitation. The pH turns out to be a relevant parameter to guarantee stable conditions for the electrolyte containing indium species and maintain a regular hydrogen ions concentration.

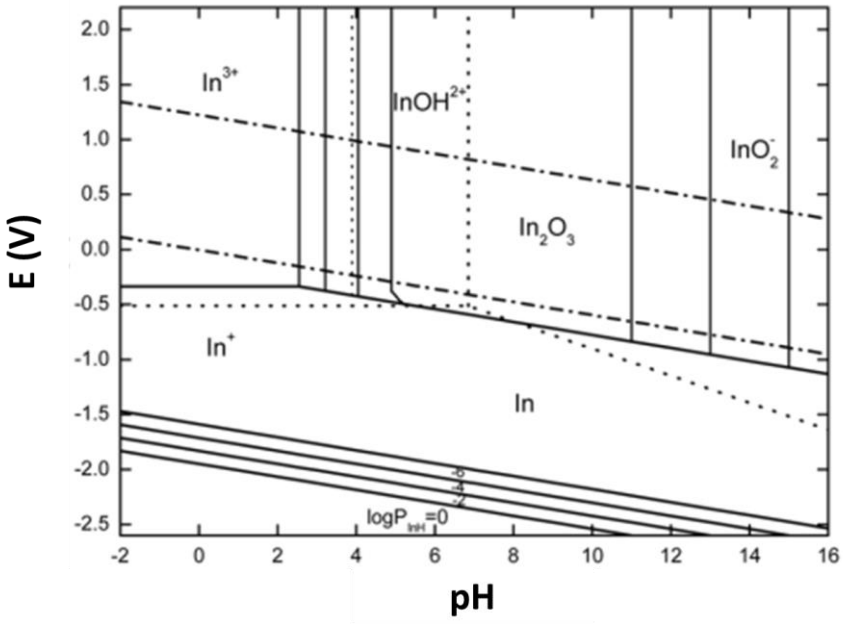

Figure 33. Potential-pH equilibrium diagram for the In-H_2O system at 25 °C [181].

The pH effect on the indium electrowinning using the starting sulfate solution at room temperature and 25 A/m² has been depicted in Figure 34. In this figure, as pH changes in a range from 1 to 2.7, it is observed that pH slightly affects cell voltage; however, it is more notable on CE and SEC at pH around 2.3. A reasonable explanation for the low CEs below pH than 2.3 could be attributed to the limiting adsorption step of HER at low pH values on the cathodic surface. In the literature, HER has been explained to occur in different mechanisms: Heyrovsky−Volmer (HV), Tafel−Volmer (TV), Heyrovsky−Tafel (HT), and Heyrovsky−Tafel−Volmer (HTV) [206]. Although it has been suggested that pH slightly affects the water electrolysis, experimental evidence indicates that the desorption step is the limiting step shifting the theoretical expected Tafel slopes at high CD, when adsorption is the determining step [169,207]. To sum up, if the HV model is excluded, CE is not modified by pH unless the desorption step (Tafel reaction) is the limiting step. Other authors have proved that pH can influence the water electrolysis at less negative potentials in particular conditions, low pH and low CD (< 2 and < 500 A/m²) [169]. Considering the experimental conditions, the pH around 2.3 improves the indium reduction, although the parasitic HER is present anyway. On the other hand, the exceeding pH value beyond 2.7 exacerbates the production of indium hydroxides near the electrode surface, causing those hydroxides either being attached to the deposit or impoverishing the indium content's electrolyte. Accordingly, the indium reduction reaction is negatively altered by pH, and it is reflexed on the decline of electrowinning outputs.

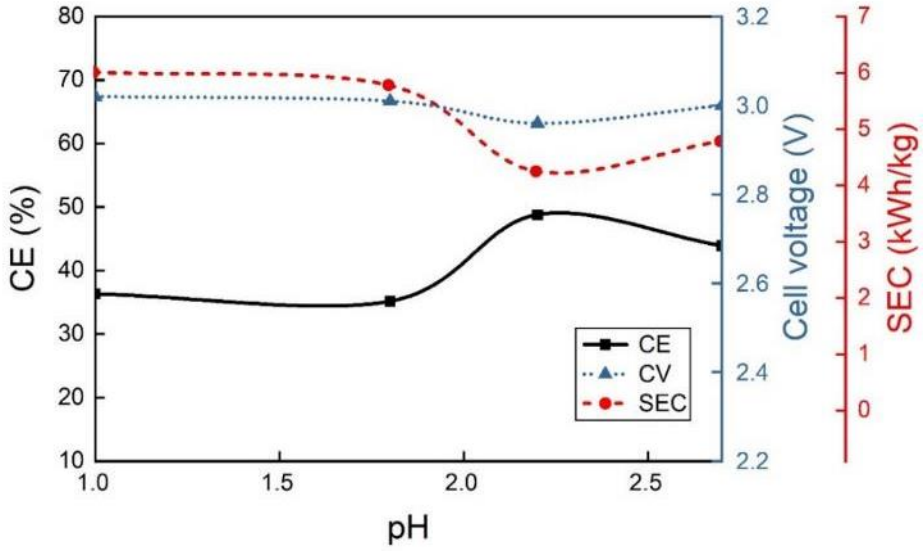

Figure 34. Effect of pH on CE, cell voltage and SEC for the indium electrowinning at room temperature, 25 A/m² and using a sulfate electrolyte (60 g/L In^{3+}, 20 g/L H_3BO_3, 10 g/L $Na_2(SO_4)$ and 10 g/L $Al_2(SO_4)_3$ at 25 A/m² and 25 °C).

5.7.Synergy effect of optimized parameters

To gain a better insight into the influences of different parameters on the CE and the deposit quality. Low CDs is the condition that offers the highest CE values. However, the indium electrowinning process requires a proper balance between high CE and low SEC. Based on the above assessments, the CD at 25 A/m^2 shows the best results and is selected to carry out the electrowinning process on the AISI 316L cathode. Regarding the electrolyte composition, the increase of indium sulfate at 60 g/L causes a rise in CE. In addition, a similar effect is obtained with boric acid, sodium and aluminum sulfate at 20, 30 and 20 g/L, respectively. In the case of pH value, it is defined at 2.3 without exceeding 2.7 to avoid indium precipitation. Since the previous operative parameters achieve high CE and low SEC, they are considered the optimized conditions for the indium electrowinning on the AISI 316L cathode (electrolyte containing 60 g/L In^{3+}, 20 g/L H_3BO_3, 30 g/L Na_2SO_4, 20 g/L $Al_2(SO_4)_3$ at 2.3 pH and 25 A/m^2).

At this point, an additional test varying the temperature is considered to evaluate the variation of electrowinning outputs. Figure 35 shows the temperature effect at three different values: 15, 25 and 40 °C. Under the optimized conditions, cell voltage and SEC decrease as temperature increases, being the best condition at 40 °C with a CE around 80%, while lower temperature only causes a negative outcome for both CE and SEC. This behavior could be attributed to an expected ions mobility. Initially, increasing temperature could suggest a detrimental effect on the electrowinning process due to the HER occurrence. Instead, a better result (high CE and low SEC) could be obtained by increasing temperature. In fact, indium electrowinning is highly dependent upon temperature. Therefore, the temperature at 40 °C affects more indium reduction than hydrogen discharge using the AISI 316L metal support for the electrowinning process.

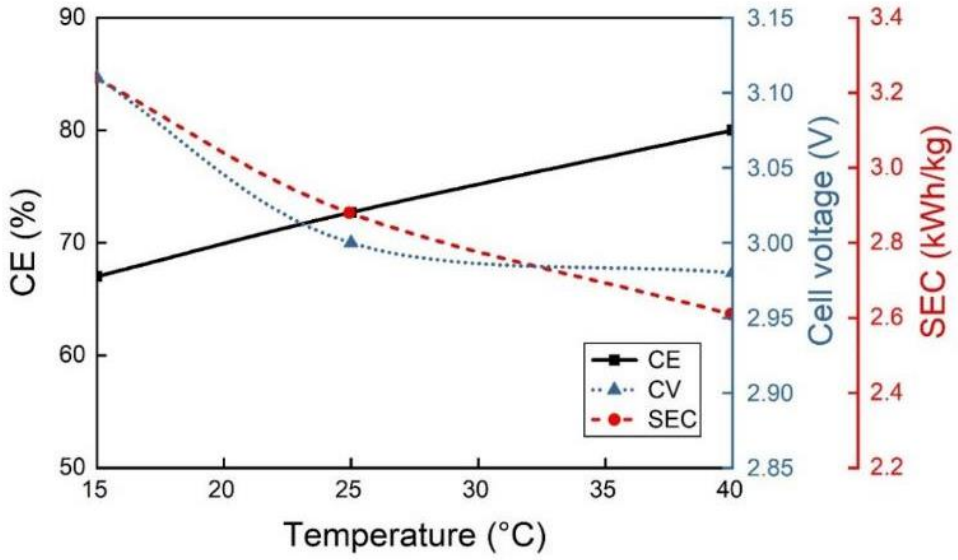

Figure 35. Effect of temperature on cell voltage, CE and SEC using the optimized conditions on the AISI 316L cathode at 25 A/m^2.

Figure 36 highlights the indium deposit obtained using optimized operative conditions. This morphology suggests a very compact microstructure, where grains present an irregular but smoothed morphology. A lamellar-like microstructure is observed at higher magnifications. Further, little holes are identified due to a slight HER (Figure 36b).

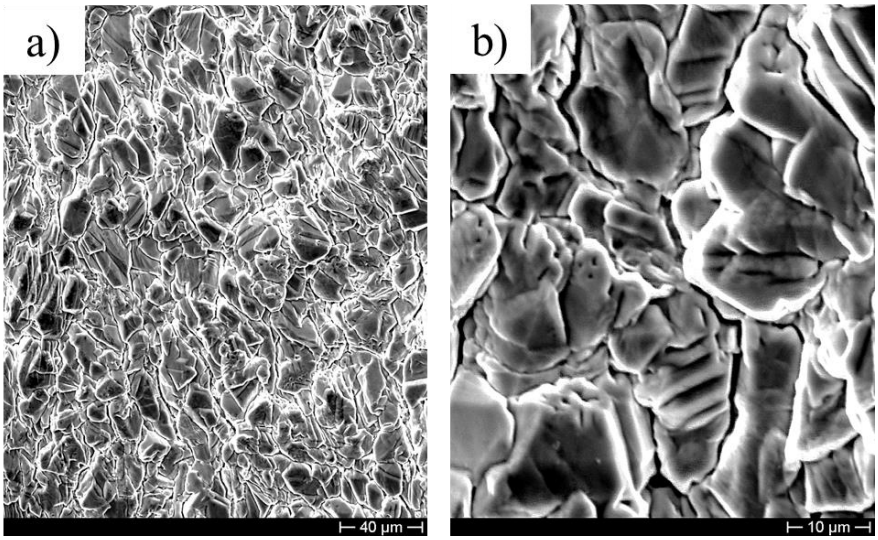

Figure 36. Indium deposit SEM micrographs at a) low and b) high magnification, using the optimized operative parameters on the AISI 316L cathode at 40 °C.

5.8.Current density analysis using optimized operative conditions

Optimized conditions were achieved at 25 A/m^2, as above shown. To prove if the balance between high CE values and low SEC is maintained for the indium electrowinning process, it was decided to increase the CD values. Figure 37 shows electrowinning outputs at different CDs using optimized operative conditions and AISI 316L as metal cathode support. These results indicate that CE can be higher than 80% at 25 A/m^2 and 40 °C. However, CE values progressively fall as CD increases to obtain around 27 % at 200 A/m^2. The cell voltage decreases, passing from 2.2 V to 4.5 V in the maximum CD level. However, HER rapidly increases SEC. For example, SEC drops as CD increases since the cathodic surface is progressively covered by hydrogen bubbles, suggesting higher energy requirements to carry out the indium deposition. Based on these findings, it is possible to claim that the maximum CE, where SEC value is low, can be reached at 25 A/m^2 using AISI 316L as metal support.

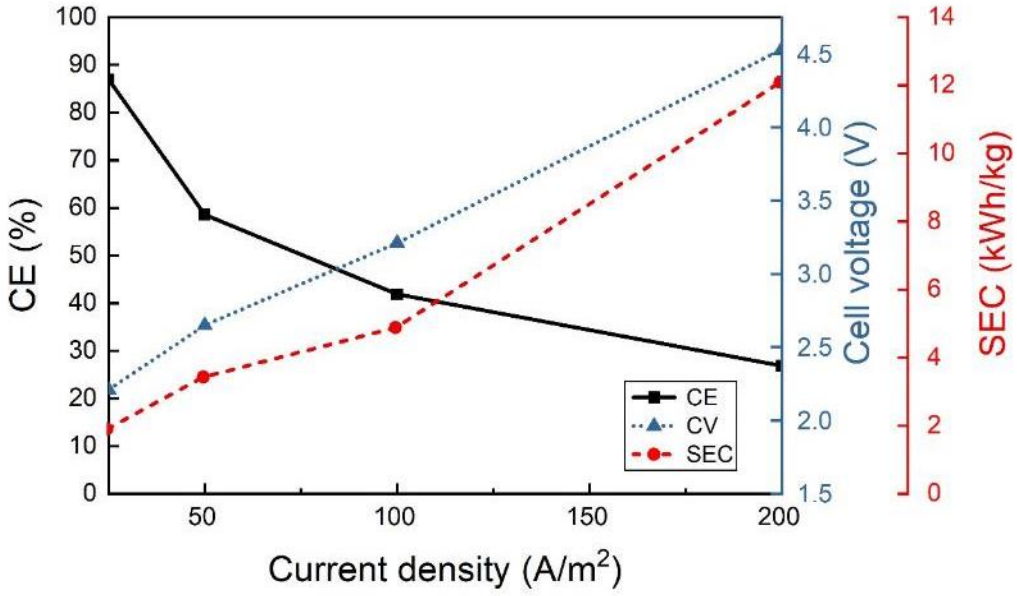

Figure 37. CD effect for indium electrowinning using the optimized electrolyte (60 g/L In^{3+}, 20 g/L H_3BO_3, 30 g/L Na_2SO_4, 20 g/L $Al_2(SO_4)_3$) at 2.3 pH and 40 °C.

The microstructure of all deposits obtained by different CDs (25, 50 and 100 A/m^2) are presented in Figure 38. These figures show that grains grow as CD increases. Figure 38a has a microstructure that is small and compact. Instead, in Figure 38b and Figure 38c, micrographs are very similar regarding the size and shape of grains. Both deposits have elongated and rounded cavities due to both deposit growth and HER, respectively. Despite the similarity, Figure 38c presents a less-compact morphology. At high CD, the microstructure increases in size, showing a more homogenous shape.

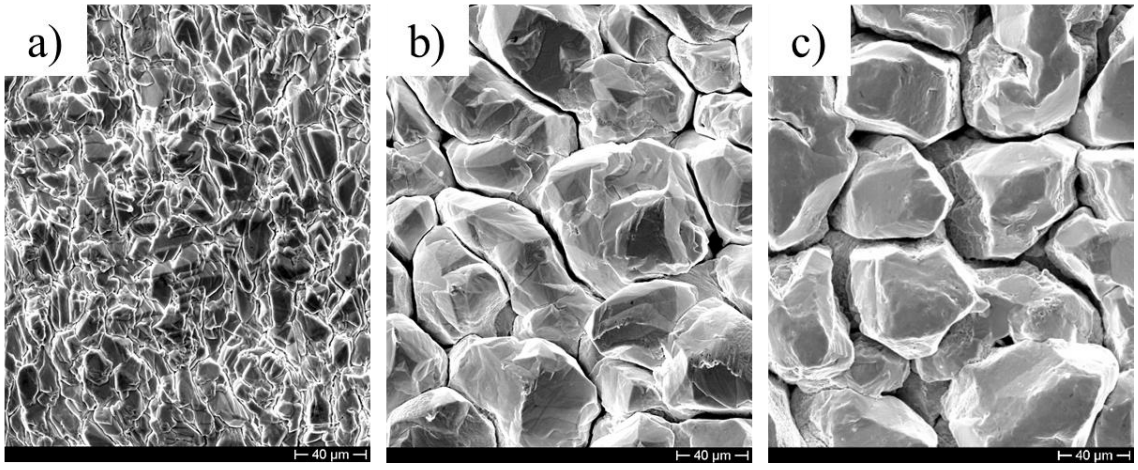

Figure 38. SEM micrographs for indium deposit using the optimized conditions at a) 25, b) 50, c) 100 A/m^2 at 40°C.

The crystallographic patterns for each indium deposit as CD changes were also examined, as shown in Figure 39. In this figure, it presents the typical indium crystallographic patterns, but they change in two aspects: First, intensity for each preferential peak decreases as CD rises; however, orientations (101), (002) and (110) can be seen even at higher CDs, while the secondary peaks are almost illegible at 200 A/m^2. Normally, the crystallographic features analyzed from XRD patterns can be related to both the height and the full width at half maximum of a peak (FWHM) [208]. Taking into account the three main peaks from diffractograms, it is possible to observe that, increasing CD, the peaks' intensity diminishes. An opposite trend is observed in the case of FWHM values, these values increase as CD rises. Thus, it is possible to suggest that the crystalline features for the indium deposits decrease, increasing the CD (Figure 40).

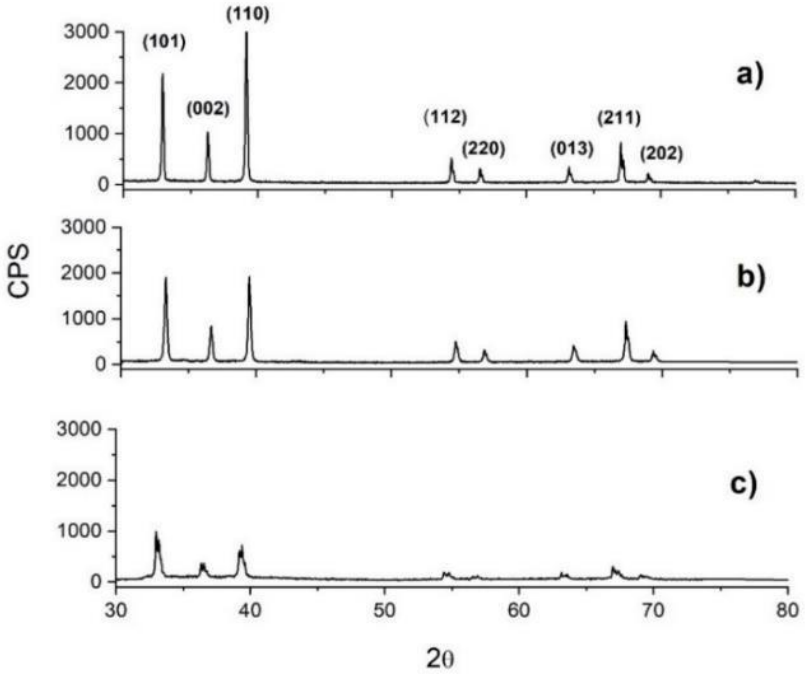

Figure 39. XRD patterns for the indium deposits at a) 25, b) 50 and d) 100 A/m^2 using the optimized conditions at 40 °C and pH 2.3.

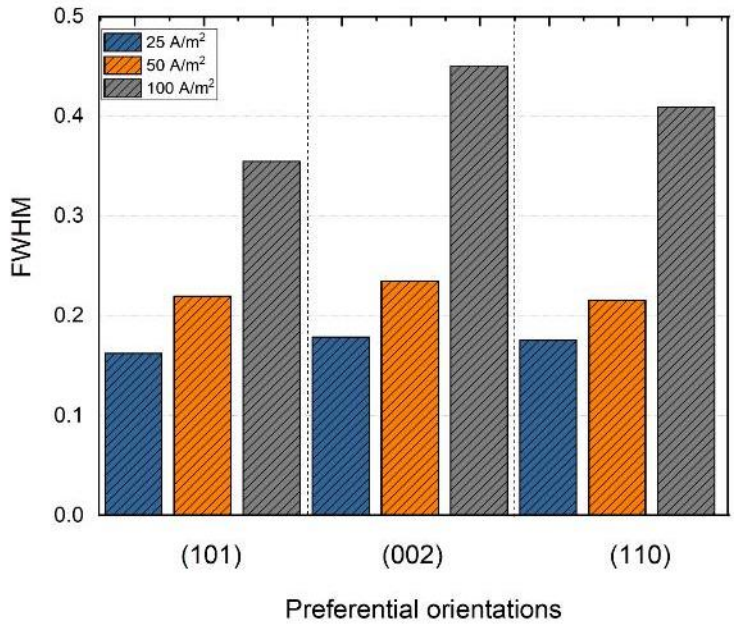

Figure 40. FWHM Analysis at the three main peaks (101), (002) and (110) for diffractograms for indium deposits obtained, changing the CD between 25 and 100 A/m².

Chapter 6: **Nickel cathode**

6.1.Introduction

Based on preliminary results, the nickel cathode was selected to carry out the indium electrowinning [149]. Those results showed that working at 25 A/m^2, Ni cathode can achieve around 94% and 1.7 kWh/kg using an electrolyte containing 70 g/L In^{3+}, 5 g/L H_3BO_3, 20 g/L $Al_2(SO_4)_3$ and 30 g/L Na_2SO_4 at pH 2.3 and 40 °C. Since the Ni cathode showed relevant electrowinning outputs at 25 A/m^2, it was initially decided to optimize the indium electrowinning process varying the CD, electrolyte composition, pH and temperature. The main aim of this optimization is to reach high productivity and low energy consumption (high CE and low SEC), together with a good aspect deposit. Furthermore, the obtained indium deposits also were analyzed by morphological and crystallographic characterization tests.

6.2.CD effect on the indium electrowinning

The indium electrowinning process on Ni cathode is evaluated considering the CD effect from a starting solution containing 70 g/L In^{3+}, 5 g/L H_3BO_3, 30 g/L Na_2SO_4, 20 g/L $Al_2(SO_4)_3$ at 40 °C and pH 2.3. That process has shown relevant CE and SEC outputs at 25 A/m^2 [149]. Figure 41 shows electrowinning outputs tested by changing CD from 25 to 200 A/m^2 and maintaining temperature and pH at 40 °C and 2.3, respectively. The CE achieves values above 95% from 25 to 80 A/m^2. However, it falls fast once CD rises, reaching 40% at 200 A/m^2. Conversely, both cell voltage and SEC depict the opposite behavior, maintaining low values up to 80 A/m^2 and increasing for the highest CD.

This behavior is attributed to the overvoltage growth resulting from hydrogen bubbles' formation on the electrode surface. An intense gas layer is observed at high CDs like on the AISI 316L cathode. This situation is hardly observed at lower CDs, where no bubbles on the cathodic surface suggest a lower hydrogen evolution. At CDs higher than 80 A/m^2, HER starts randomly on the cathodic surface, with tiny bubbles, whereas a progressive HER generates an abundant bubble presence, as it experimented at 200 A/m^2. A significant change is also observed for SEC; it keeps unchanged almost at 1.9 kWh/kg between 25 and 80 A/m^2 CD, and subsequently increases around threefold (6.1 kWh/kg) at 200 A/m^2. Based on these results, the first suggestion could be to increase the CD to improve the indium recovery; nonetheless, this route causes cell overpotential increases and triggers HER and its respective effects. Thereby, a good agreement between CE and SEC is required for such long-lasting processes. That agreement consists of high productivity and low energy consumption. Although the indium electrowinning on Ni cathode achieves high CE and low SEC at low CDs up to 80 A/m^2, because of the HER inhibition, the opposite scenario is observed at higher CDs, describing low CEs and

high SEC values. Hence, working on Ni cathode, the most suitable CD is 80 A/m², combining relevant CE rates and insignificant HER.

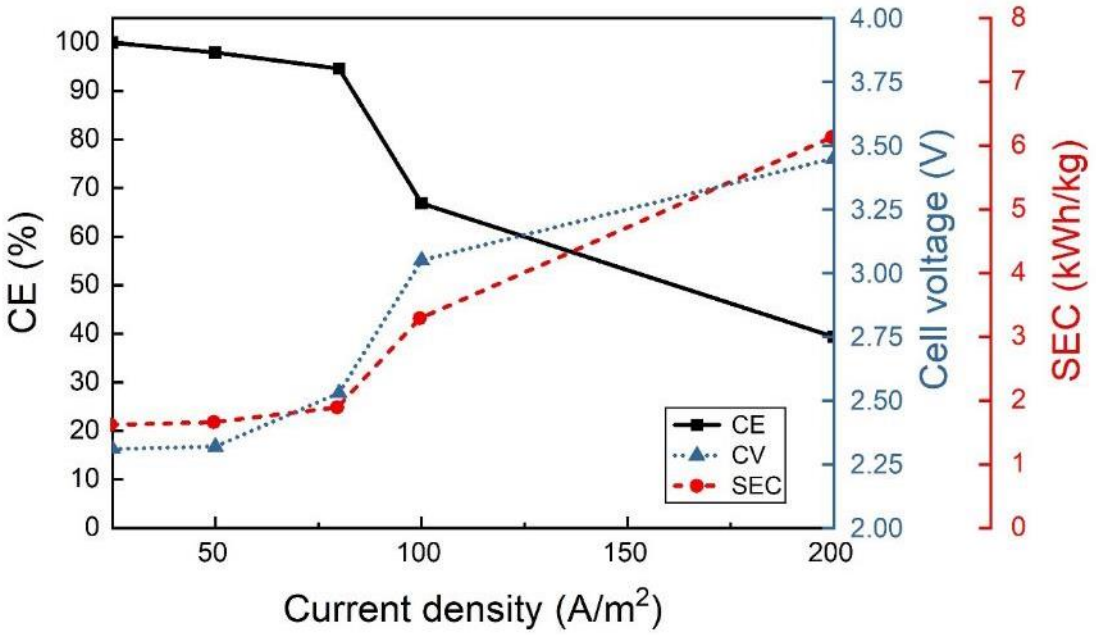

Figure 41. Influence of the current density on the cell voltage, CE and SEC for the indium electrowinning process using an electrolyte containing 70 g/L In^{3+}, 5 g/L H_3BO_3, 30 g/L Na_2SO_4, 20 g/L $Al_2(SO_4)_3$ at 40 °C and pH 2.3.

The deposit quality has been evaluated regarding the final aspect of indium deposits and crystallographic features. Figure 42 shows the morphology of indium deposits at different CDs (25, 80 and 100 A/m²). The grain size observed in these micrographs indicates a slight change as the CD increases. In Figure 42a, grains exhibit a regular polygonal-like well-defined shape with sizes around 250 μm at 25 A/m², while the indium deposit depicts a finer and compact structure at higher CDs (Figure 42b-c). SEM micrographs show grain size does not follow a trend, indicating smaller grain sizes at 80 A/m² with respect to 25 A/m², but they look larger at 100 A/m². The deposit obtained by 100 A/m² (Figure 42c) shows a surface altered by holes, some due to HER. Well-formed rounded cavities are associated with hydrogen bubble formation, while those elongated ones describe the grains boundary after deposit growth.

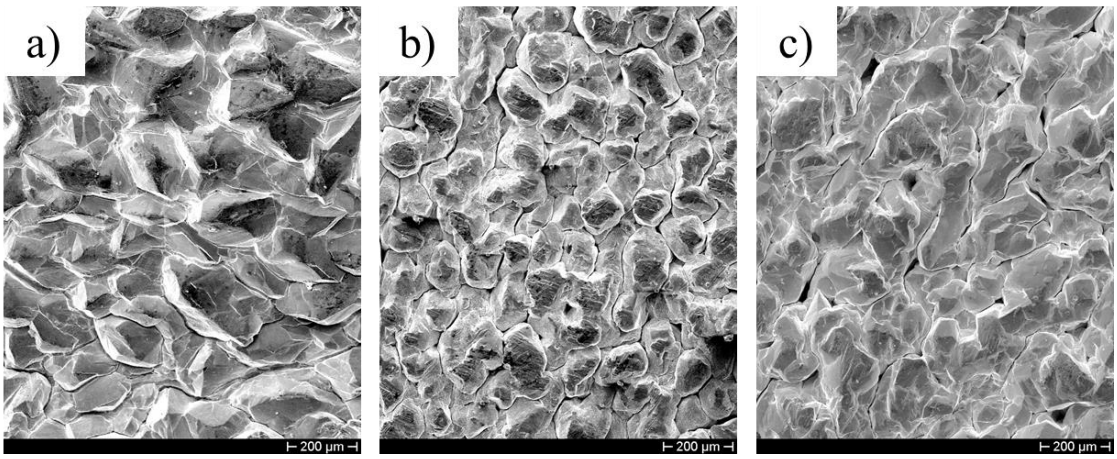

Figure 42. Morphology of indium deposits obtained by a) 25, b) 80 and c) 100 A/m².

Figure 43 shows the XRD patterns for indium deposits obtained at different CDs (25, 80 and 100 A/m².). From the literature, it has been suggested that less-intensive peaks can be observed in XRD patterns as CD increases [209,210]. Nonetheless, in our case, XRD patterns do not present a significant change. In fact, in general terms, they are similar, but it is possible to highlight that, working at 100 A/m², preferential orientation changes from (101) to (110), while (002) and the second orientation planes at angles higher than 50° (2θ) are represented by less intense peaks.

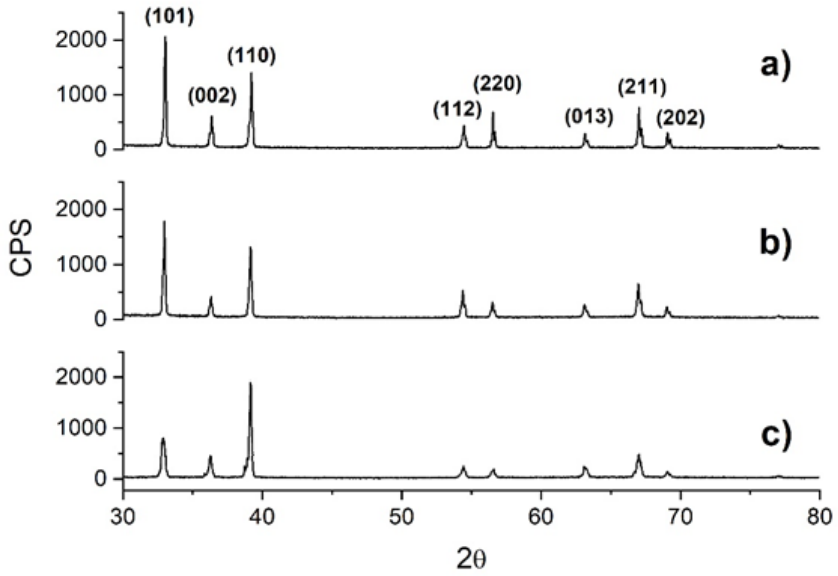

Figure 43. XRD pattern of indium deposits obtained on Ni electrode by different CDs: a) 25, b) 80 and c) 100 A/m².

6.3.Indium concentration effect

The availability of indium species within the electrolyte represents a relevant aspect to avoid the typical resistance effects in the electrowinning cell. As indium concentration decreases, it is expected that overpotential will be intensified due to the concentration and ohmic overpotential. Hence a working concentration range should be suggested, in which indium ions must be reintegrated to maintain stable both CE and SEC. Figure 44 shows the CE behavior as the indium concentration changes from 70 to 51 g/L at 80 A/m^2, 40 °C and pH 2.3. CE falls after concentration is lower than 65 g/L In^{3+}, CE shifts from 98% to 40% when the indium depletion increases and the concentration reaches about 51 g/L. Based on these results, electrowinning outputs slightly vary from 70 g/L and 65.36 g/L, whereas lower concentrations lead CE to drop significantly. Thus, CE for the indium electrowinning can remain above 95% using 80 A/m^2 CD if indium concentration into electrolyte is held above 65 g/L. A proper explanation about CE decreasing is related to indium depletion. The solution progressively is becoming poor in indium species during electroreduction. This depletion also occurs while contemporaneously hydrogen concentration rises from the anodic reaction of water hydrolysis. The increase of hydrogen concentration is easily demonstrated in the experimental tests due to a pH variation towards more acidic pH values (from 2.3 to 1.6).

The lack of enough indium species available within the electrolyte leads cell potential to rise as a result of resistive phenomena on the cathode (cathodic ohmic and concentration overpotential components). This situation promotes that the hydrogen evolution increasingly competes against the indium reduction reaction, favoring less-indium ions can be reduced. Since CE is affected by the indium concentration decrease, a simple analysis indicates that lower indium concentration into the electrolyte, higher cell voltage and SEC. That behavior is also demonstrated in Figure 44, where SEC changes from around 2.5 to 3.1 kWh/kg as indium concentration decreases.

Furthermore, SEM micrographs of indium deposits obtained using enriched and exhausted electrolytes can be seen in Figure 45. At low magnifications (Figure 45a-c), indium deposits obtained using an enriched electrolyte exhibit a homogeneous morphology; however, the size and shape of grains are hardly defined. In the case of the exhausted electrolyte, a morphology with round cavities because of HER is observed in Figure 45c. On the other hand, a microstructure based on a lamellar formation can be seen in both deposits at higher magnifications (Figure 45b-d). In addition, no dendritic microstructures were formed in this experimentation, even if the electrolyte contained a low indium concentration. Since indium depletion is a factor that can promote dendritic formation because of the increase of resistance and concentration overpotentials, it is recommended to maintain indium concentration above 65 g/L.

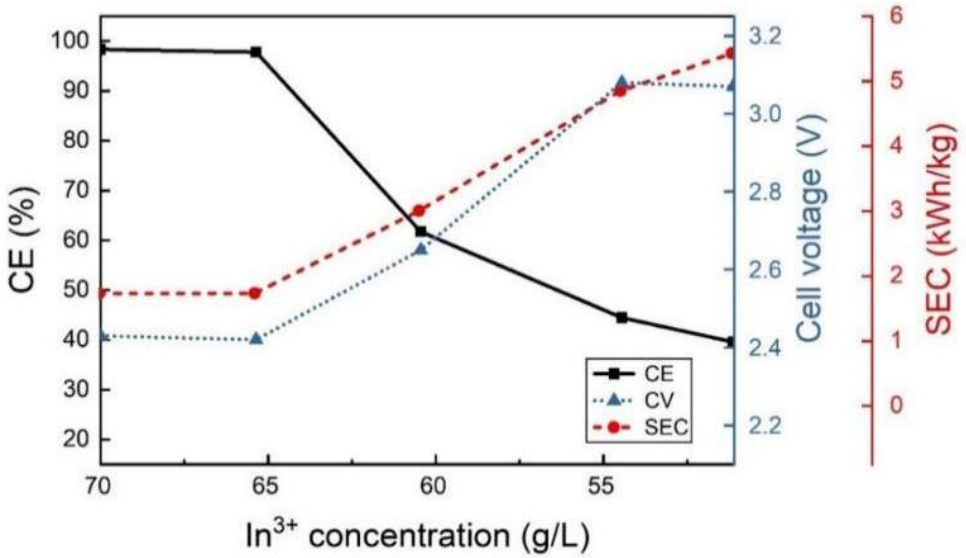

Figure 44. Effect of In^{3+} concentration on CE, cell voltage and SEC using a sulfate electrolyte at 40 °C, 2.3-pH value, and 80 A/m² for a length of 22 h (Initial concentration: 70 g/L In^{3+}).

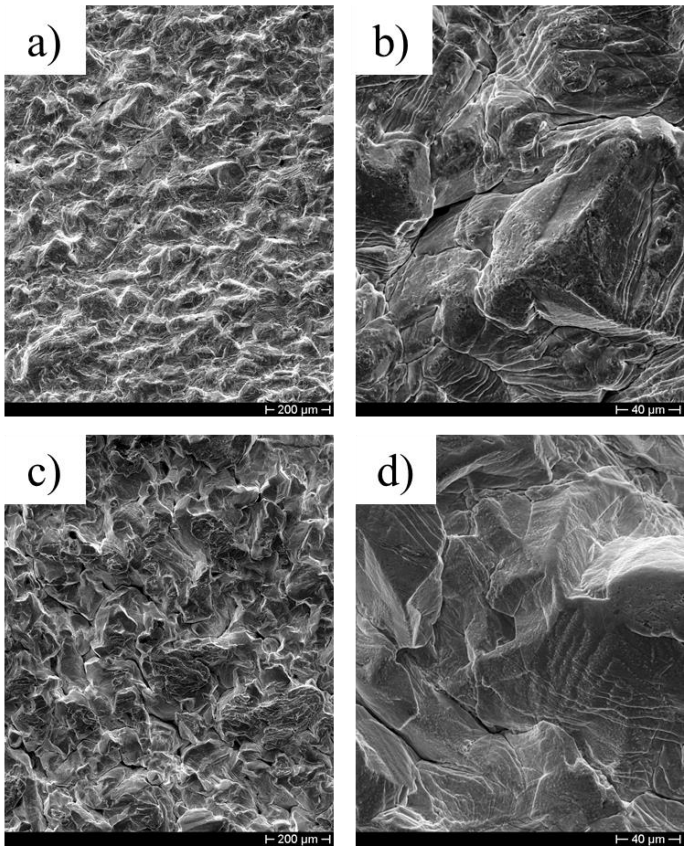

Figure 45. SEM micrographs of indium deposits under the optimized condition at 40 °C, 2.3-pH value, and 80 A/m² for a duration of 22 h with: a-b) enriched (70 g/L In^{3+}) and c-d) exhausted (55 g/L In^{3+}) indium solution.

6.4. pH effect on the indium electrowinning

The pH effect was analyzed using the Pourbaix diagram for indium in an aqueous solution at 25 °C (Figure 33). In this diagram, a working area until a pH 3.0 is delimited to avoid the precipitation of indium hydroxides ($InOH_3$). In Table 9, it can be seen the pH variation using a sulfate electrolyte (70 g/L In^{3+}, 5 g/L H_3BO_3, 20 g/L $Al_2(SO_4)_3$ and 30 g/L Na_2SO_4) and keeping unchanged operative parameters such as CD and temperature at 80 A/m^2 and 40 °C, respectively. The use of a pH equal to 2.3 allows reaching a maximum CE of around 98%, while other pH values supply CEs higher than 46%. High hydrogen concentrations in the electrolyte (more acidic conditions) causes poor CEs. In the literature, it has been highlighted that low pH values cannot affect the water electrolysis if working at high CD values; however, it has been shown that at low CD values, the HER can be influenced [169]. First, HER overpotential shifts towards less cathodic potentials, which is also explained as decreasing the activation overpotential [211]. Therefore, when the indium reduction occurs at very acidic pH values, hydrogen evolution is discharged contemporaneously to the indium reduction. This behavior renders HER a parasitic reaction for the indium reduction, worsening electrowinning outputs. Furthermore, increasing pH beyond 2.7 disfavors the indium reduction since indium hydroxide precipitation is triggered and progressively increases, giving rise to both lowering indium species and decreasing CE [161].

Another finding of the indium hydroxides production is associated with local pH rise near the cathodic surface. In the literature, the formation of hydroxides is considered an inhibiting reaction that hinders metal deposition [161]. Some supporting additives have been related to avoiding or regulating the hydroxide formation even in acidic media near the cathodic surface [202–204,211,212]. Based on this, pH variation alters SEC outputs around 5.6 kWh/kg at the most acidic state, whereas it indicates 4.5 kWh/kg at the most alkaline condition. The optimum condition reaches 1.66 kWh/kg at pH 2.3. Therefore, pH is a sensitive parameter for indium electrowinning, indicating optimum results in CE and SEC around a pH value of 2.3. In addition, the anodic water oxidation reaction should be also considered on the pH change in the electrowinning cell. The disbalance reaction between the hydrogen production at the anode and consumption on the cathodic surface occur. This disbalance is the main cause of the electrolyte acidification at the end of the process, reaching pH values below 1.6.

Table 9. Variation of CE, cell voltage and SEC changing the pH value (1.5, 2.3 and 2.7) for indium electrowinning at 80 A/m² and 40 °C with a duration of 22 h.

pH	Cell voltage (V)	CE (%)	SEC (kWh/kg)
1.5	2.84	35.72	5.57
2.3	2.43	94.58	1.79
2.7	2.95	45.85	4.50

Figure 46 shows XRD patterns of indium deposits performed at three different pH values a) 1.5, b) 2.3 and c) 2.7. The crystallographic tetragonal structure for indium deposits is associated with the pattern C.O.D. 1539229. A description of the preferential orientation shows three peaks at 2θ = 32.96°, 36.39° and 39.10°, which are associated with planes (101), (002) and (110). At higher 2θ-angles, five secondary peaks are related to the planes (112), (220), (013), (211) and (202). Changing the pH value to 1.5, the diffractogram shows a slight decrease in power for all peaks, except (110), which remains highly intense. Varying the pH value from 1.5 to 2.7, the relative intensity of the main peaks can change, as well as the preferential orientation.

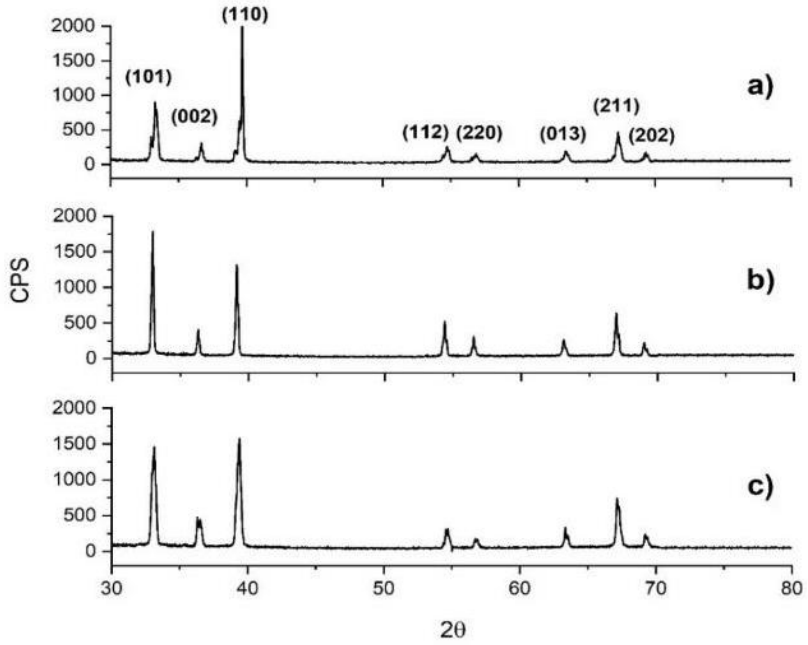

Figure 46. XRD patterns for indium deposits varying the pH value: a) 1.5; b) 2.3 c) 2.7 using a sulfate electrolyte containing 70 g/L In^{3+}, 5 g/L H_3BO_3, 20 g/L $Al_2(SO_4)_3$ and 30 g/L Na_2SO_4 at 40 °C for 22 h.

6.5. Temperature effect

Figure 47 illustrates the study of the temperature on the indium electrowinning using the sulfate solution at two different temperature levels (25 and 40 °C) and CD (50 and 80 A/m^2). The results indicate that temperature highly affects CE values, increasing to 98% at the two selected CDs. At room temperature, the lowest CD allows obtaining around 77% CE. The temperature accelerates the kinetic processes and improves the diffusion conditions. It seems that a slight increase in temperature (40 °C) is enough to enhance electrowinning outputs working at 50 and 80 A/m^2. A reasonable explanation is attributed to lessening the overpotential cell components (concentration, ohmic and activation), which have a higher contribution to increasing the overpotential cell at room temperature. On average, the cell voltage at 50 A/m^2 and 25 °C varies from 3.2 V to 2.3 V when the temperature increases to 40 °C. In the case of SEC values, they depict a relevant difference with a maximum of 3.6 kWh/kg at 80 A/m^2, falling to a minimum of 1.7 kWh/kg at 40 °C. A similar trend is also observed working with 50 A/m^2. Thus, from Figure 47, it is possible to mention that keeping the CD value constant, the temperature significantly influences the electrowinning outputs. The temperature effect is more important with the CD increase.

SEM micrographs of indium deposits obtained on Ni cathode at 80 A/m^2 and different temperatures, 25 °C (Figure 48a-c) and 40 °C (Figure 48d-f), can be seen in Figure 48. Temperature seems to influence slightly the grain size of deposits. Performing electrowinning at 25 °C, the obtained deposit appears to have a lower homogeneity than that observed on the deposit at 40 °C (Figure 48a and Figure 48d, respectively). Anyway, the temperature range does not show notable differences in the shape of grains that at low magnifications appear all rounded. Instead, grains in Figure 48d seem to have a more randomly distribution. Micrographs at higher magnifications show lamellar growth (Figure 48b and Figure 48e).

Further, although there are no remarkable changes in Figure 48c and Figure 48f, the morphology of deposits shows crystallites and growth in layers. Those crystallites, also known as nucleation seeds, are homogeneously dispersed on the indium deposit. The morphological results also were assisted by the crystallographic analysis.

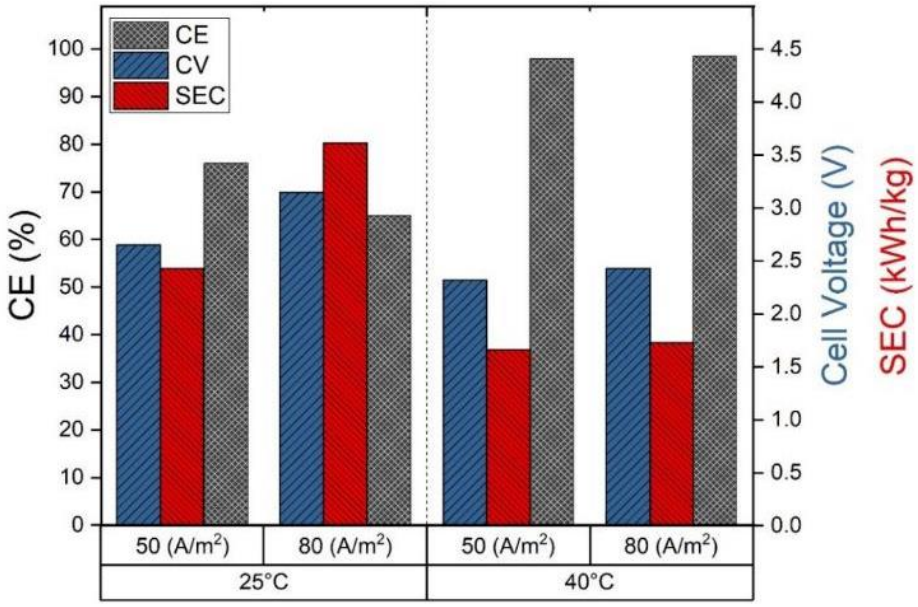

Figure 47. Effect of temperature on cell voltage, CE and SEC of the indium electrowinning using different current densities (50 and 80 A/m²) within the sulfate electrolyte (70 g/L In^{3+}, 5 g/L H_3BO_3, 20 g/L $Al_2(SO_4)_3$ and 30 g/L Na_2SO_4) at pH 2.3 for 22 h.

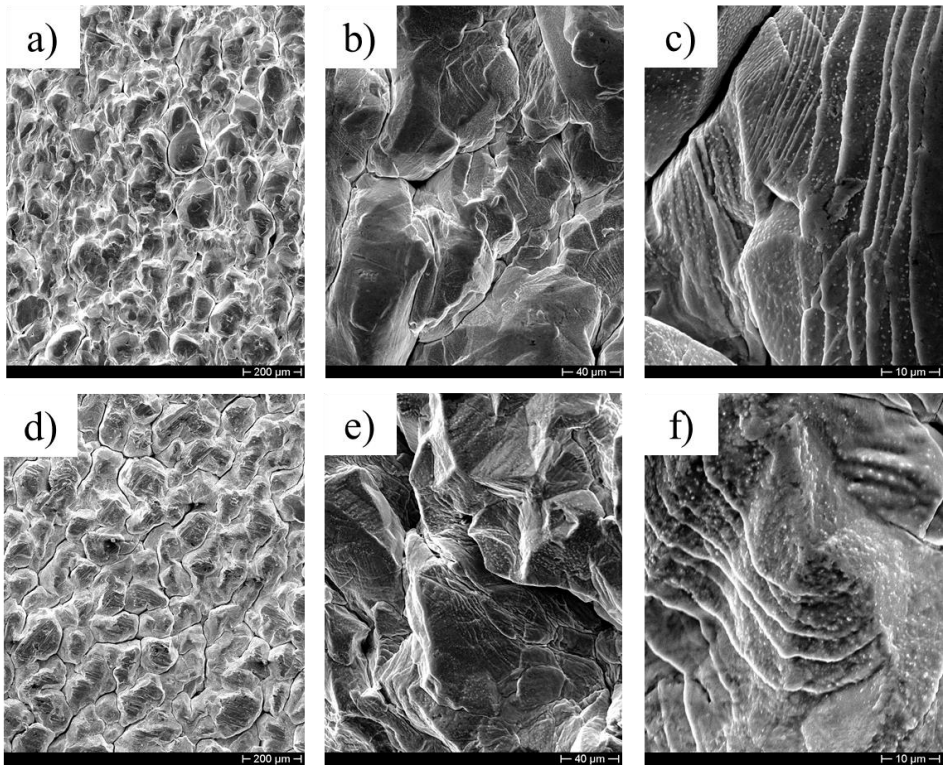

Figure 48. Microstructure of indium deposit obtained on Ni cathode at different magnifications using the sulfate electrolyte at pH 2.3, 80 A/m² and 22 h and varying temperature at: a-c) 25 °C and d-f) 40 °C.

The crystallographic analysis using XRD tests on the indium deposits obtained on the Ni electrode is reported in Figure 49. These analyses were performed on the obtained deposits at 80 A/m^2. At 25°C, the indium deposit shows the typical XRD pattern for indium, where the first three peaks before 40°(2θ) correspond to (101), (002) and (110), while the rest appertains to (112), (220), (013), (211) and (202). Fixing the temperature at 40 °C, diffractograms show a decrease of intensity; nonetheless, the preferential orientation remains unchanged. Generally, the crystallographic features analyzed from XRD patterns can be associated with both the height and the full width at half maximum of a peak (FWHM) [208]. Thus, considering the same equipment and operative conditions for both tests, except temperature, the intensity change is attributed to the temperature effect. Taking into account the three main peaks from diffractograms, it is possible to observe that, increasing temperature, the peaks decrease. The FWHM for the (101) and (002) peaks remain almost unchanged, except for the (110) peak (Figure 50).

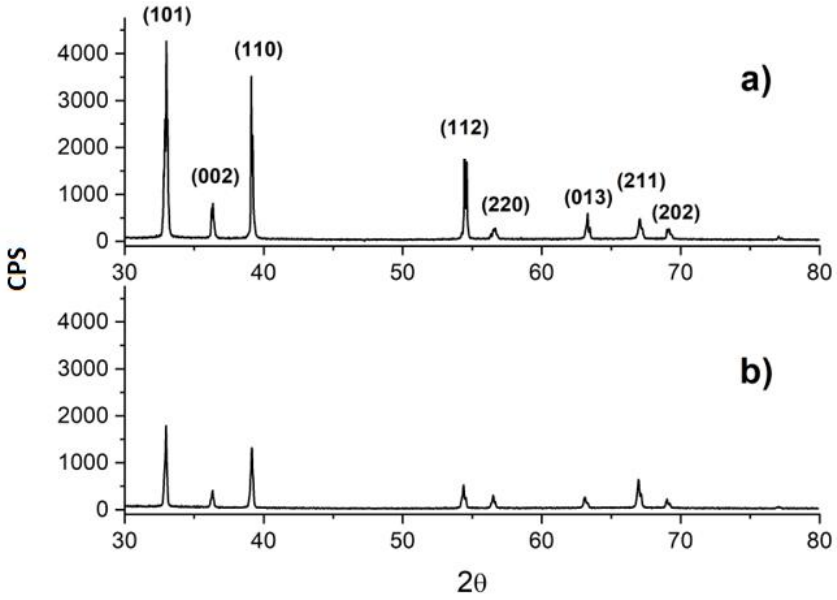

Figure 49. Effect of temperature on the indium deposit diffractograms obtained using the Ni electrode with 80 A/m^2 CD, at a) 25 °C and b) 40 °C.

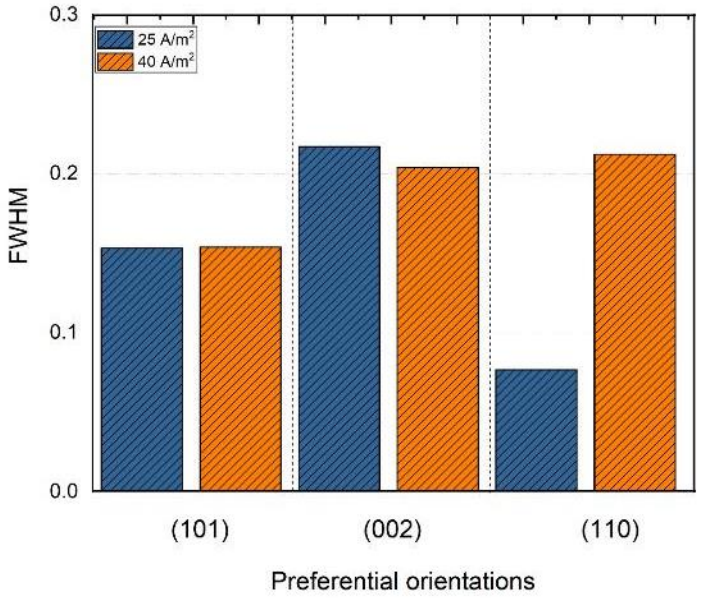

Figure 50. Analysis of FWHM at the three main peaks (101), (002) and (110) for indium deposit diffractograms obtained by changing the temperature values.

6.6. Supporting reagent effect on the indium electrowinning

Considering the analysis above, the best operative conditions to carry out indium electrowinning on Ni cathode are 80 A/m^2, 40 °C and pH 2.3. These conditions using a sulfate electrolyte (70 g/L In^{3+}, 5 g/L H_3BO_3, 20 g/L $Al_2(SO_4)_3$ and 30 g/L Na_2SO_4) allowed to obtain after 22 h around 98% and 1.7 kWh/kg of CE and SEC, respectively. However, one of the most important aims in the electrowinning process is to reach high productivity with low energy consumption. Since CE and SEC are negatively affected as CD increases, changes in the electrolyte composition are required. Therefore, it was then proposed to carry the indium electrowinning process establishing 100 A/m^2 as CD at 40 °C and pH 2.3 and varying the composition of supporting reagents (aluminum and sodium sulfate, and boric acid).

6.6.1. Effect of aluminum sulfate

The composition influence on the indium electrowinning process was initially considered by changing the aluminum sulfate concentration into the starting sulfate solution. The cell voltage, CE and SEC for the indium electrowinning has been evaluated by varying the aluminum sulfate concentration, as shown in Figure 51. By using Ni cathode, a gradual increase of aluminum sulfate causes a decrease in CE. This decrease represents about 32% CE, and it is much lower, when 40 g/L $Al_2(SO_4)$ is added. On the

contrary, if this compound is suppressed from the electrolyte, CE remains around 80% with low cell voltage and SEC values.

Regarding SEC, higher consumption values are observed when electrolyte contains the highest concentration of aluminum sulfate, indicating around 3.7 kWh/kg. With the absence of this compound, this output achieves around 2.6 kWh/kg. The presence of aluminum sulfate suggests an overpotential increase of the electrowinning cell, and therefore it does not improve electrowinning outputs on Ni cathode.

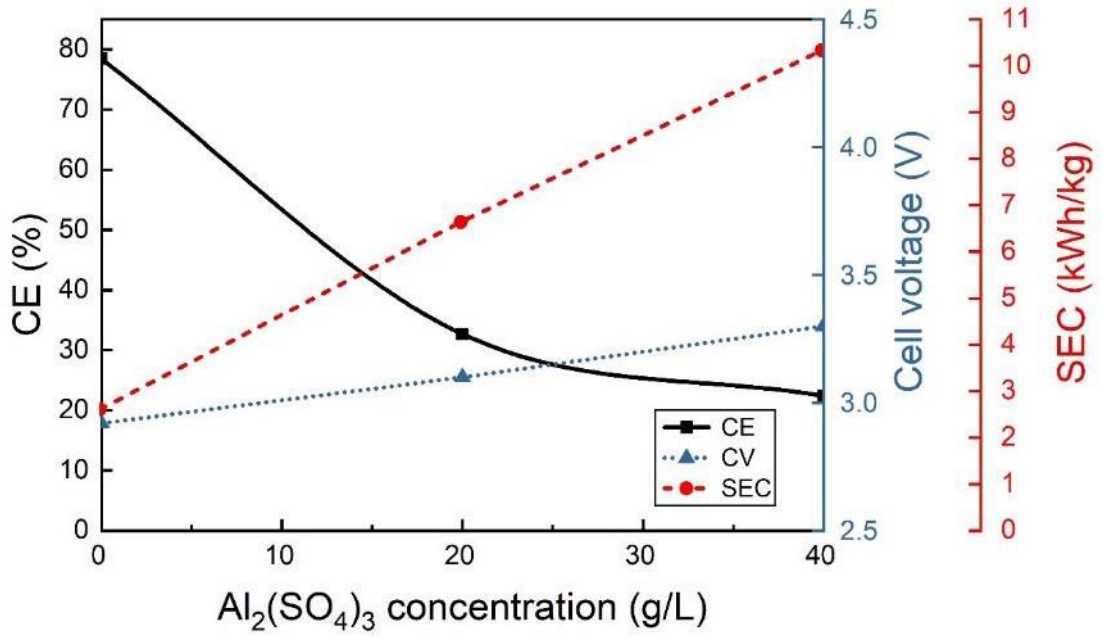

Figure 51. Effect of aluminum sulfate on CE, cell voltage and SEC for the indium electrowinning process using a sulfate electrolyte (70 g/L In^{3+}, 40 g/L H_3BO_3, 30 g/L Na_2SO_4) with different aluminum sulfate concentrations (0, 20 and 40 g/L) at 40 °C and 2.3-pH value.

The contribution of aluminum sulfate corresponds to the deposit quality improvement. Figure 52 shows the morphology of indium deposits affected by the aluminum sulfate variation from 0 to 40 g/L. Micrographs show abundant holes on the surface. These defects are much more intense without aluminum sulfate in the electrolyte (Figure 52a). While this compound increases, rounded cavities are apparently lowered (Figure 52b), showing a significant change at 40 g/L $Al_2(SO_4)_3$ (Figure 52c). Diffractometric patterns for each indium deposit at different aluminum sulfate concentrations can be seen in Figure 53. From these patterns, it is noted that the preferential orientation is (101) peak at 0 and 40 g/L $Al_2(SO_4)_3$, but at 20 g/L, the preferential orientation is instead related to the (110) peak. Additionally, some particular increases in the intensity are also depicted in secondary peaks at (112) and (013) for 0 and 40 g/L $Al_2(SO_4)_3$, respectively. Considering morphological changes, aluminum

sulfate shows deposit quality improvements. However, the main goal of electrowinning points out high CE and low SEC. Therefore, to carry out the indium electrowinning on the Ni cathode at 100 A/m^2, pH 2.3 and 40 °C, it is not recommended to use aluminum sulfate as a supporting reagent.

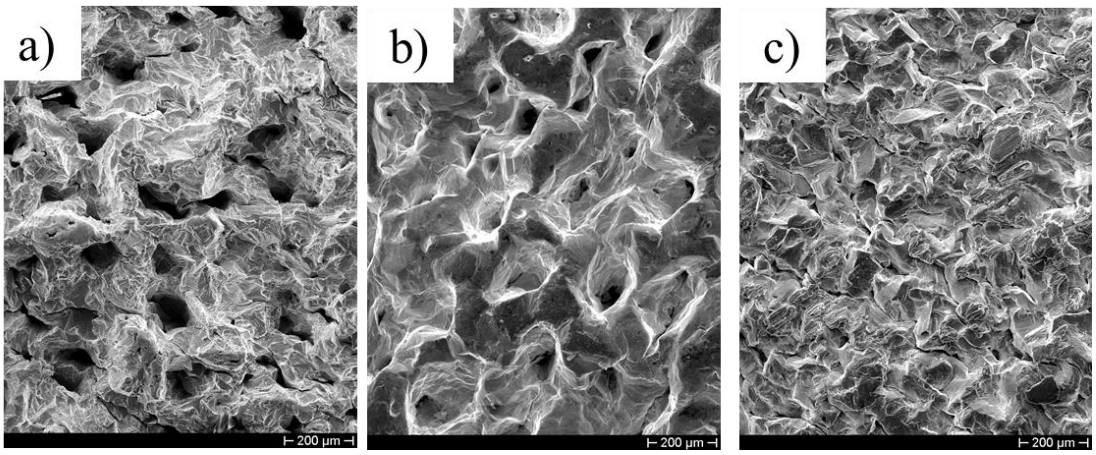

Figure 52. Morphology of indium deposits varying aluminum sulfate concentration: a) 0, b) 20 and c) 40 g/L $Al_2(SO_4)_3$ into a sulfate electrolyte.

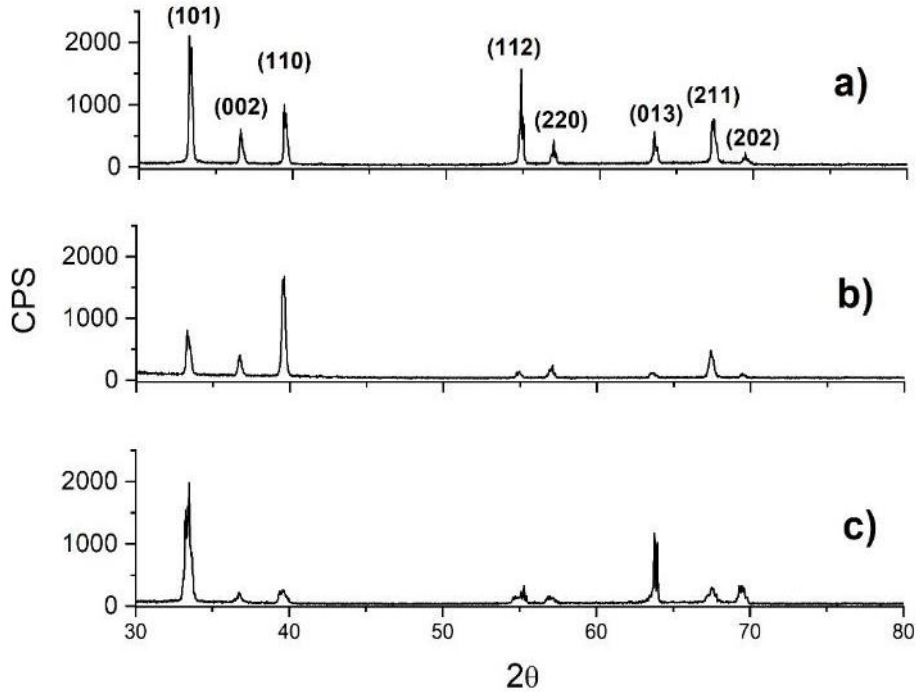

Figure 53. XRD patterns for indium deposits performed using different aluminum sulfate concentrations: a) 0, b) 20 and c) 40 g/L.

6.6.2. Effect of sodium sulfate

Figure 54 shows the change of cell voltage, CE and SEC as sodium sulfate increases. Using a sulfate electrolyte containing 70 g/L In^{3+} and 40 g/L H_3BO_3, the starting CE is around 73%. While increasing sodium sulfate concentrations can be achieved more than 80% CE. This positive effect also is observed in cell voltage and SEC, where these outputs reach around 2.9 V and 2.6 kWh/kg, respectively. The lack of this compound in the solution indicates that overpotentials (mainly resistance) increase cell voltage and SEC values. Therefore, the sodium sulfate contribution during the indium electrowinning is required.

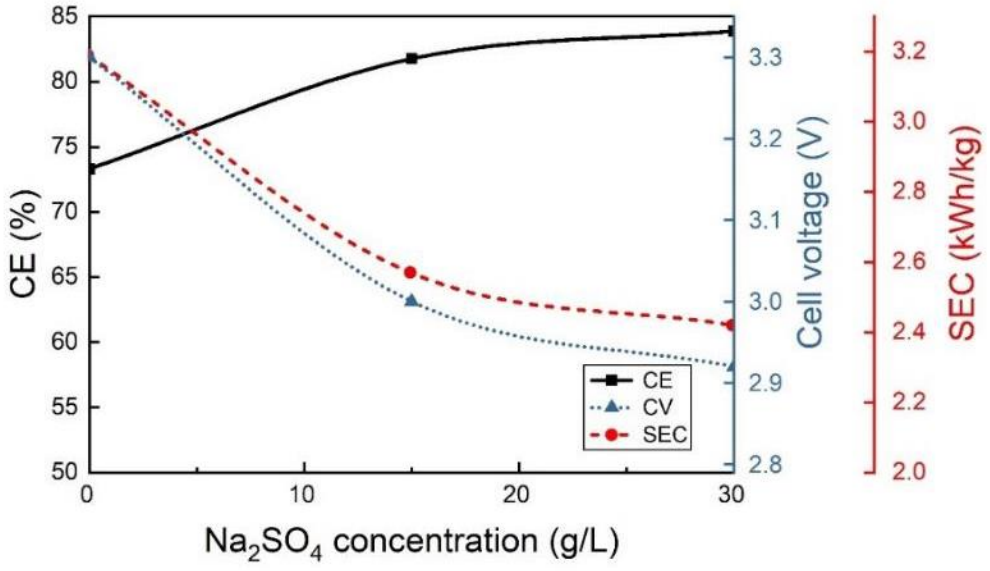

Figure 54. Influence of sodium sulfate on CE, cell voltage and SEC by using a sulfate electrolyte (70 g/L In^{3+}, 40 g/L H_3BO_3) and different sodium sulfate contents (0, 15 and 30 g/L) at 100 A/m², 40 °C and pH value 2.3.

Figure 55 highlights the morphology of the indium deposit using different sodium sulfate concentrations. The absence of this supporting salt favors the formation of dendritic structures on the deposit (Figure 55a). They trigger energy consumption and put at risk the electrowinning process by eventual short circuits. The edge effect, produced by the continuous flow of current lines from cathodic to the anodic surface, can be intensified by irregular deposit growths causing those dendrites.

Furthermore, the aspect of indium deposit in Figure 55b-c shows a more flattened surface at sodium sulfate concentrations. A porous morphology is observed in each micrograph. But it is much more evident the porous morphology when 30 g/L sodium

sulfate is added. Based on these results, sodium sulfate can improve the electrowinning performance according to CE and SEC; however, the deposit aspect is modified.

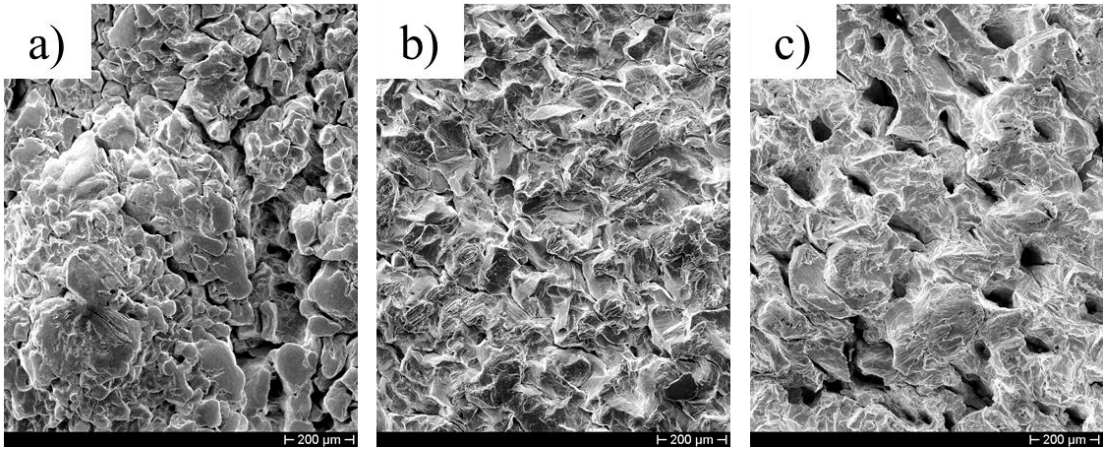

Figure 55. Morphology of indium deposits varying sodium sulfate concentration a) 0, b) 15 and c) 30 g/L into the sulfate electrolyte at 40 °C and pH 2.3.

On the other hand, Figure 56 shows XRD patterns for indium deposits using the sulfate electrolyte with different sodium concentrations (0, 15 and 30 g/L). The sodium sulfate favors indium deposits with much more defined crystalline phases. In Figure 56, the diffractograms' peak intensity increases as Na_2SO_4 concentration increases.

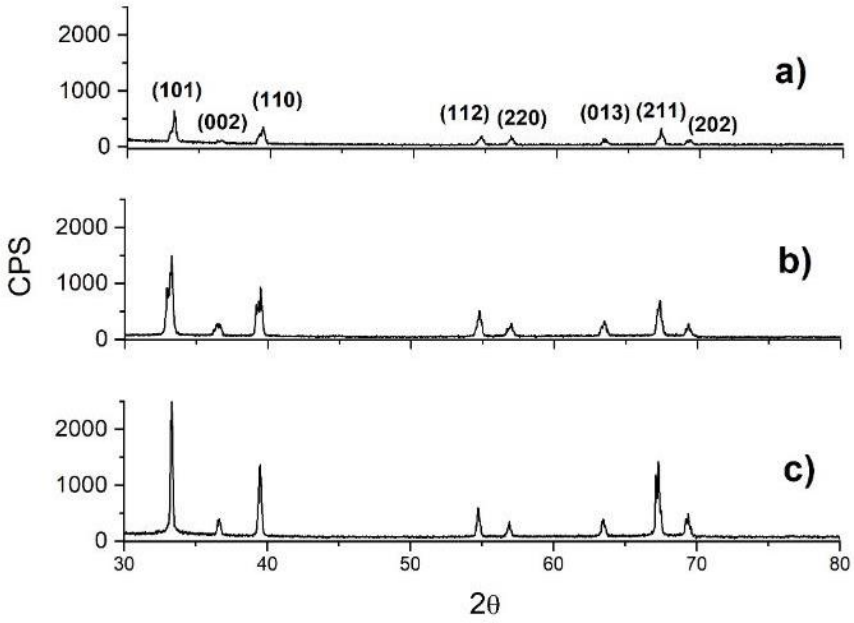

Figure 56. XRD patterns for indium deposits preformed using the sulfate electrolyte (70 g/L In^{3+} and 40 g/L H_3BO_3) at 40°C, pH 2.3, 100 A/m² and different sodium sulfate concentrations: a) 0, b) 15 and c) 30 g/L.

6.6.3. Boric acid effect

Figure 57 shows the effect of boric acid on indium electrowinning, establishing three concentrations (0, 20 and 40 g/L). From this figure, CE is positively affected by boric acid, increasing from 60% to 83% when H_3BO_3 rose from 0 to 40 g/L, respectively. Cell voltage shows a progressive fall reaching about 2.85 V at 40 g/L. Since this test is maintained constant CD at 100 A/m^2, it could be expected that this supporting agent helps to lessen the overpotential cell. Apart from this, boric acid notably affects the cell voltage overpotential in the electrowinning process. The latter is corroborated in pioneer reports where boric acid plays a relevant role against the hindering of the parasitic hydrogen evolution reaction during the electrodeposition [203,205,213]. It has been also explained that boric acid into electrolyte works like a proton source, which could even control the increase of the local pH near the cathodic surface [203]. Consequently, the previous behavior also facilitates diminishing SEC outputs, occurring a progressive drop from 3.4 kWh/kg (boric acid absence) up to 2.4 kWh/kg once the concentration reaches the maximum value (40 g/L), as shown in Figure 57.

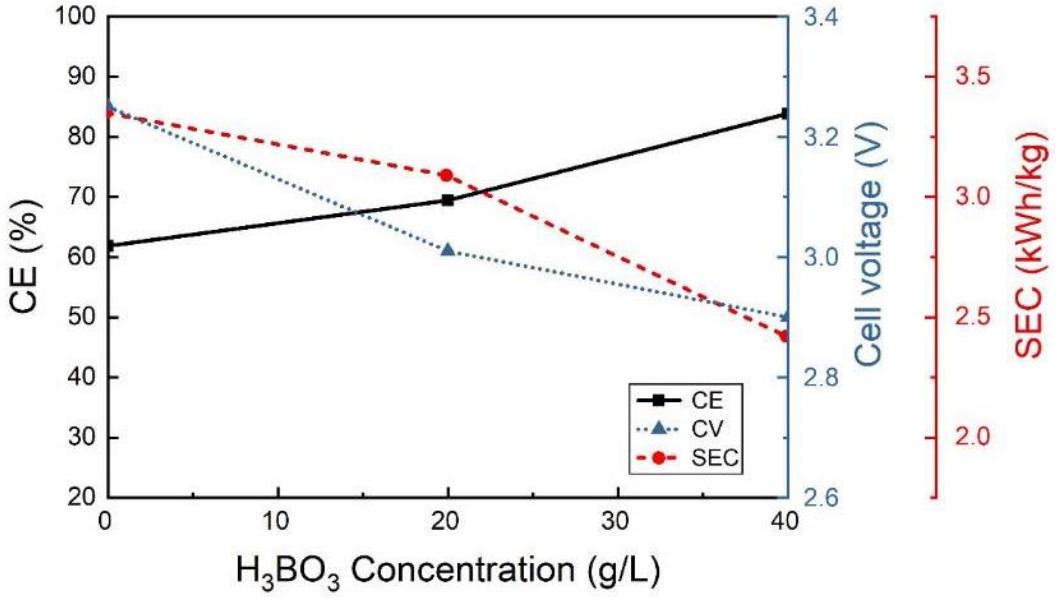

Figure 57. Analysis of the boric acid effect by using different concentrations (0, 20 and 40 g/L) on CE, cell voltage and SEC. An electrolyte containing 70 g/L In^{3+} and 30 g/L Na_2SO_4 for indium electrowinning at 100 A/m^2, 40 °C and pH 2.3 was used.

Morphology of indium deposits obtained with different boric acid concentrations, while the other operative parameters kept unchanged (40 °C and 2.3-pH value) can be seen in Figure 58. The indium deposit morphology changes remarkably as the boric acid concentration rises. The lack of boric acid in the electrolyte favors that the indium deposit

looks much more compact, where grain bounders are hardly identified. However, as boric acid increases, grain boundaries are clearer. Indeed, this reagent allows obtaining well-defined polygonal grains with a bright appearance (from a macroscopic point of view). In addition, the HER effect can be seen observed on all micrographs; however, it is much more evident on the highest boric acid concentration, forming rounded cavities (Figure 58c). If the latter deposit is compared to their electrowinning outputs, a disagreement could be suggested due to the apparent HER; nonetheless, a detailed inspection of Figure 58c shows elongated cavities that indicate an incomplete coalescence. Thus, a notable grains' growth is highlighted in this deposit (at least larger than the other deposits). Although this morphology could appear much more porous and less compacted than those in Figure 58a and Figure 58b, the correspondence with high CEs (83%) and low SEC (2.4 kWh/kg) indicates using 40 g/L boric acid benefits efficiency outcomes. This concentration hardly benefits the final aspect of deposits; however, boric acid at 40 g/L reaches high CE with low SEC values. Therefore, the indium electrowinning performed using a Ni cathode shows the best performance with an electrolyte containing 70 g/L In^{3+}, 30 g/L Na_2SO_4 and 40 g/L H_3BO_3 at 40 °C and pH 2.3.

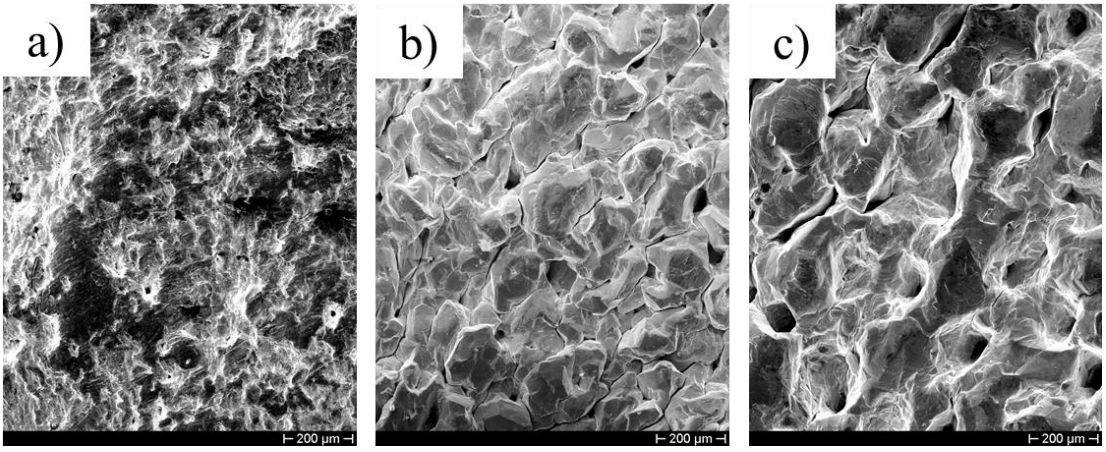

Figure 58. Morphology of indium deposits varying boric acid concentration a) 0, b) 20 and c) 40 g/L into a sulfate electrolyte (70 g/L In^{3+} and 30 g/L Na_2SO_4) at pH 2.3 for a length of 22 h.

On the other hand, SEM micrographs were also accompanied by XRD characterization, as shown in Figure 59. From a comparison among the XRD results, the boric acid has no substantial influence on the crystallographic features of deposit or any variation of the oriental preferential peak. The (101) peak is the preferential peak on all diffractograms.

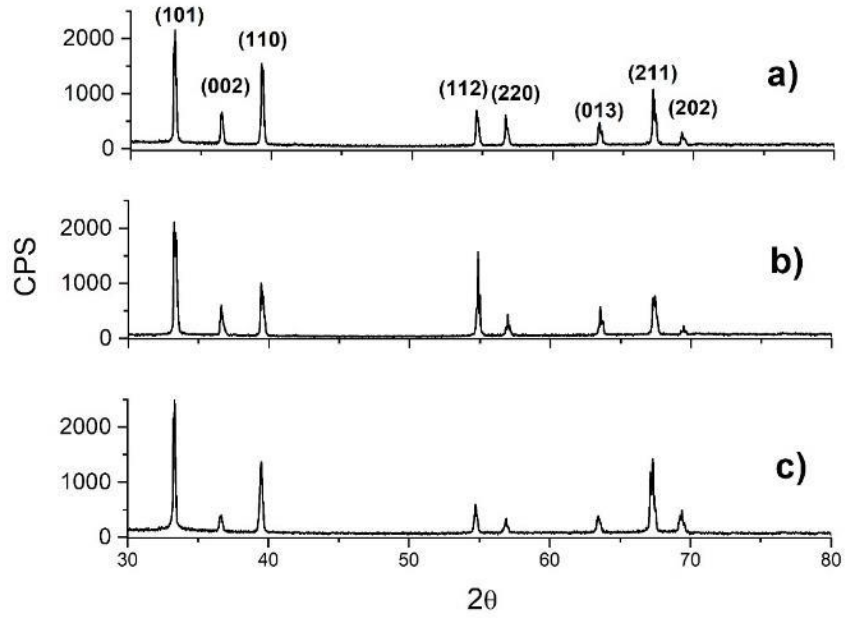

Figure 59. XRD test for indium deposits obtained varying boric acid concentrations: a) 0, b) 20 and c) 40 g/L.

Chapter 7: **Copper cathode**

7.1. Introduction

This chapter individuates the most relevant effects on productivity, energy consumption, and deposit quality using copper as metal support. An electrolyte composition containing 140 g/L $In_2(SO_4)_3$, 5 g/L H_3BO_3, 20 g/L $Al_2(SO_4)_3$ and 30 g/L Na_2SO_4) was previously utilized using 25 A/m^2 CD, 2.3 pH, 40 °C temperature [149]. The results indicate that the Cu cathode hardly can work at 25 A/m^2 at those operative parameters. Therefore, the optimization of the indium electrowinning process was carried out using the same metal support and varying the operative conditions (CD, electrolyte composition, temperature and pH) to improve CE and SEC. Finally, morphological and crystallographic features of the obtained indium deposits also were tested by XRD and SEM techniques.

7.2. Current density effect on the indium electrowinning

Figure 60 shows the change of CE, cell voltage and SEC as CD values increase from 25 to 200 A/m^2 at 40 °C and pH 2.3 in a sulfate solution containing merely 70 g/L In^{3+}. The CE output shows the highest value at 25 A/m^2, and it progressively decreases as CD grows, reaching 30 % at 200 A/m^2. In the case of the cell voltage and SEC, the tendency is to increase being much more intense for SEC values. The former rises roughly 700 mV in the entire CD range (starting from around 2.8 mV), while the latter increases from 3.4 to 8.2 kWh/kg. The progressive HER is a factor that promotes the growth of the overpotential cell, and consequently, SEC increases as well. Without any supporting compound, this parasitic reaction notably affects the CE responses from 50 A/m^2, which is more evident at higher CD values. Given that 56 % CE was the maximum value obtained using the copper cathode without any supporting additive, the following tests are focused on the CE and SEC improvement.

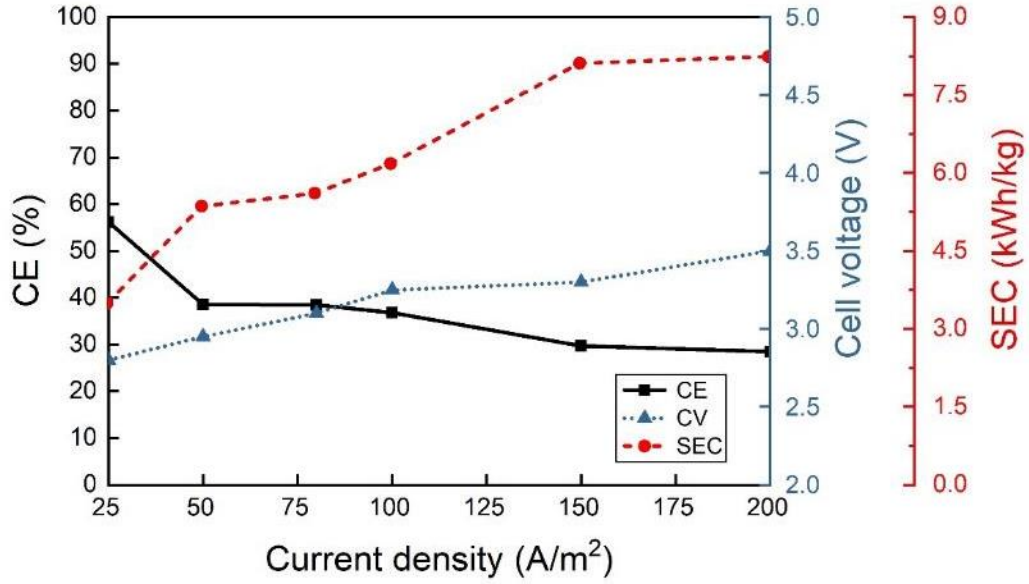

Figure 60. Influence of the CD (25, 50, 80, 100, 150 and 200 A/m²) on the indium electrowinning process using a sulfate electrolyte containing 70 g/L In^{3+}, 40 °C and pH 2.3.

7.3. The boric acid effect at 25 A/m²

The low CE and high SEC values obtained in the experimental campaign varying CD led to focus the attention on the electrolyte composition at 25 A/m², at which is reached the best CE and SEC outputs. Thus, boric acid effect within a sulfate electrolyte (70 g/L In^{3+}) at 40 °C and pH 2.3 was evaluated, as shown in Figure 61. By adding 20 or 40 g/L H_3BO_3, the CE value is enhanced above 90% in both cases, while the cell voltage and SEC values have a contrary effect. In that way, cell voltage decreases from around 2.9 V to 2.1 V, while SEC shifts from 3.4 to 1.6 kWh/kg. The boric acid has a remarkable impact on the performance of the indium electrowinning process, increasing CE rates and decreasing SEC values.

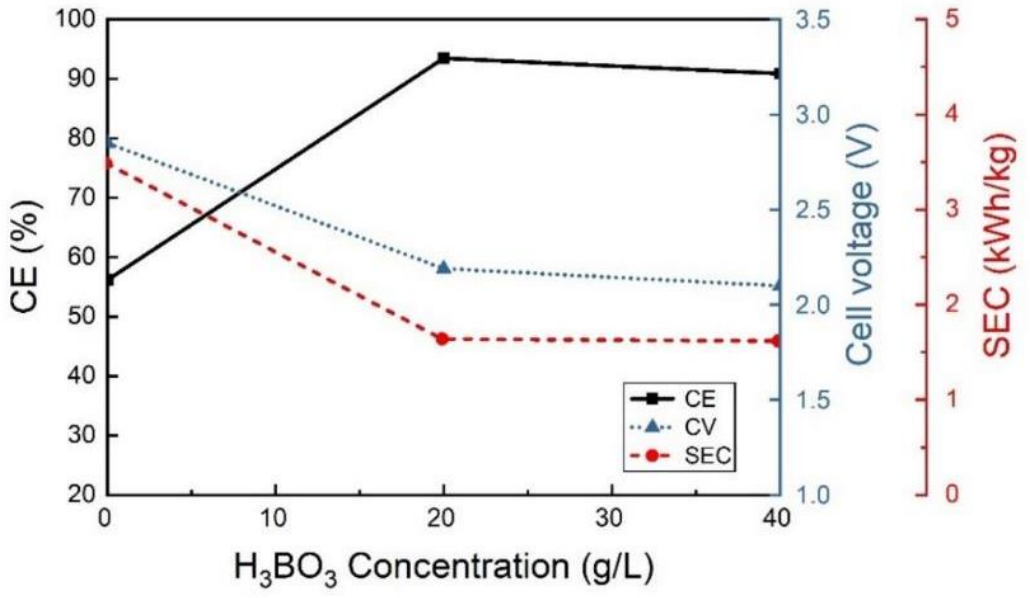

Figure 61. Effect of boric acid concentrations from 0 to 40 g/L on the indium electrowinning using a sulfate electrolyte composed of 70 g/L In^{3+} at 25 A/m², 40 °C and pH 2.3.

7.4. Current density effect using 20 g/L H_3BO_3

Since 20 g/L H_3BO_3 reached more than 90% CE, it was proposed the necessity of testing the CD effect using a sulfate electrolyte with that composition. Figure 62 illustrates the CD effect on CE, cell voltage and SEC for the indium electrowinning process considering an electrolyte containing 70 g/L In^{3+} and 20 g/L H_3BO_3 at 40 °C and pH 2.3. The boric acid increases notoriously the CE at both 25 and 50 A/m² compared with those obtained in Figure 60. At CD values higher than 50 A/m², the CE falls at about 22% at 200 A/m². Furthermore, cell voltage starts at 2.2 V and grows to 3.7 V at 200 A/m².

Analyzing SEC, a quick increase stands out from a minimum of around 1.64 kWh/kg at 25 A/m², followed by a sharp SEC value of about 12 kWh/kg. Based on the literature, boric acid has been described as a supporting compound capable of tackling the hydrogen evolution, leaving protons in the cathodic diffusion layer, and decreasing the incidence of hydrogen absorption on the surface. As a consequence, a reasonable working potential window at more negative potentials can be reached [203–205]. Another advantage obtained with the boric acid into electrolyte is the local pH regulation, working as a proton supplier on the cathodic surface that hinders the intense HER [203–205]. Since a higher CE and lower SEC values could be obtained at 50 A/m² only by adding boric acid, this CD is thus chosen to continue evaluating the indium electrowinning process.

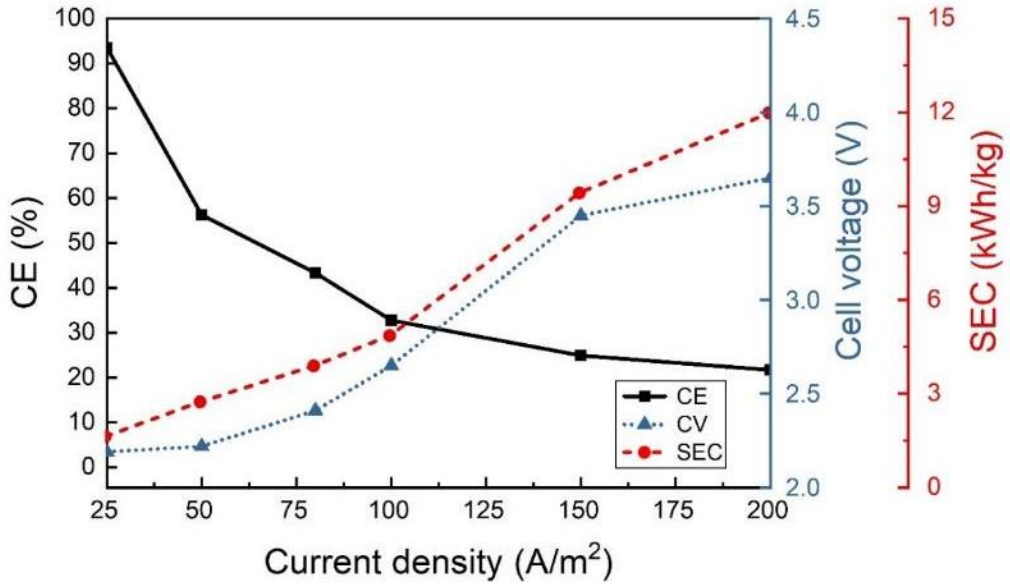

Figure 62. Effect of the CD on CE, cell voltage and SEC using a sulfate electrolyte containing 70 In^{3+} g/L and 20 g/L H_3BO_3 at 40 °C and pH 2.3.

7.5. Sodium sulfate effect at 50 A/m^2

The sulfate solution (70 g/L In^{3+} and 20 g/L H_3BO_3) at 50 A/m^2 CD, 40 °C and pH 2.3 was used to evaluate the sodium sulfate effect on indium electrowinning (Figure 63). This figure shows a negative effect on CE, cell voltage and SEC as Na_2SO_4 increases. The maximum CE value is obtained without sodium sulfate (around 56%) and dropping subsequently below 50% when the concentration is 30 g/L. Moreover, cell voltage remains on average constant during all experimental campaigns. However, the addition of sodium sulfate proposes a cell voltage diminishing around a potential difference of 30 mV.

Regarding SEC, this value increases once the sodium sulfate concentration rises. This compound usually is employed in literature to improve the conductivity of electrolytes or even the deposit quality [149–151]. However, the combination of 20 g/L H_3BO_3 with any Na_2SO_4 concentration is not enough to increase the CE. Therefore, the experimentation changing sodium sulfate concentration was newly carried out but using 40 g/L of boric acid into the sulfate electrolyte.

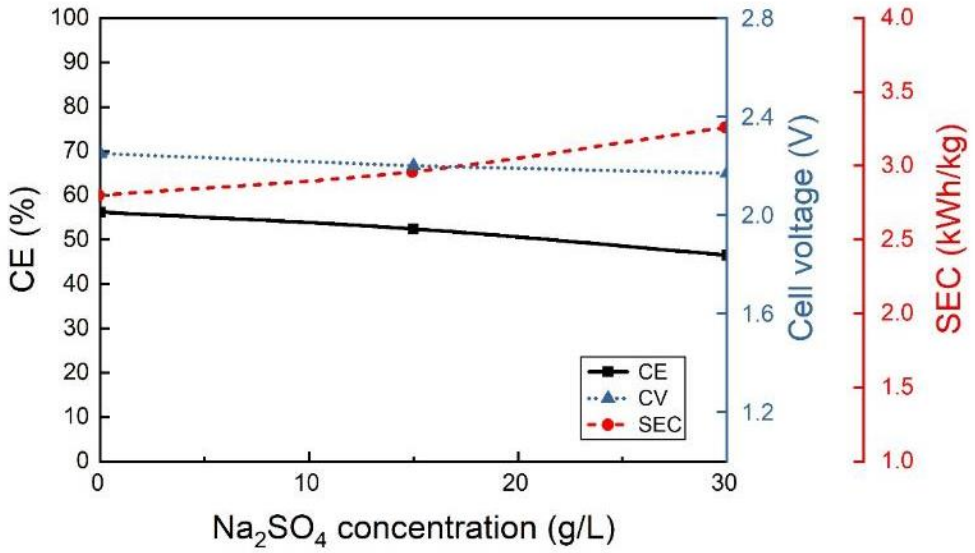

Figure 63. Variation of CE, cell voltage and SEC in the indium electrowinning at different sodium sulfate concentrations. I was used a sulfate electrolyte composed of 70 g/L In^{3+} and 20 g/L H_3BO_3 at 50 A/m², 40 °C and pH 2.3.

The indium electrowinning process was then evaluated by changing the sodium sulfate using an electrolyte containing 70 g/L In^{3+} and 40 g/L H_3BO_3 at 50 A/m², 40 °C and pH 2.3, as shown in Figure 64. The results show that the indium electrowinning is efficient on Cu cathode at 50 A/m², once the electrolyte contains 40 g/L boric acid and 30 g/L sodium sulfate, achieving close to 80 % CE.

Regarding cell voltage, it keeps almost unchanged at about 2.3 V, while a significant decrease of SEC, as the sodium sulfate concentration increases, is observed in Figure 64. At 30 g/L Na_2SO_4, SEC value reached 2.1 kWh/kg. The electrolyte composition is a sensitive factor in indium electrowinning. As can be seen above, it is possible to achieve high CE and low SEC values on the Cu cathode at 50 A/m², 40 °C and pH 2.3, combining boric acid and sodium sulfate at 40 and 30 g/L, respectively. Therefore, the indium electrowinning using Cu cathode can be performed at 25 A/m² to reach more than 90% CE using the indium sulfate electrolyte with 20 g/L H_3BO_3. Likewise, it is possible to use sulfate solution with 40 g/L H_3BO_3 and 30 g/L Na_2SO_4 at 50 A/m² to achieve about 80% CE.

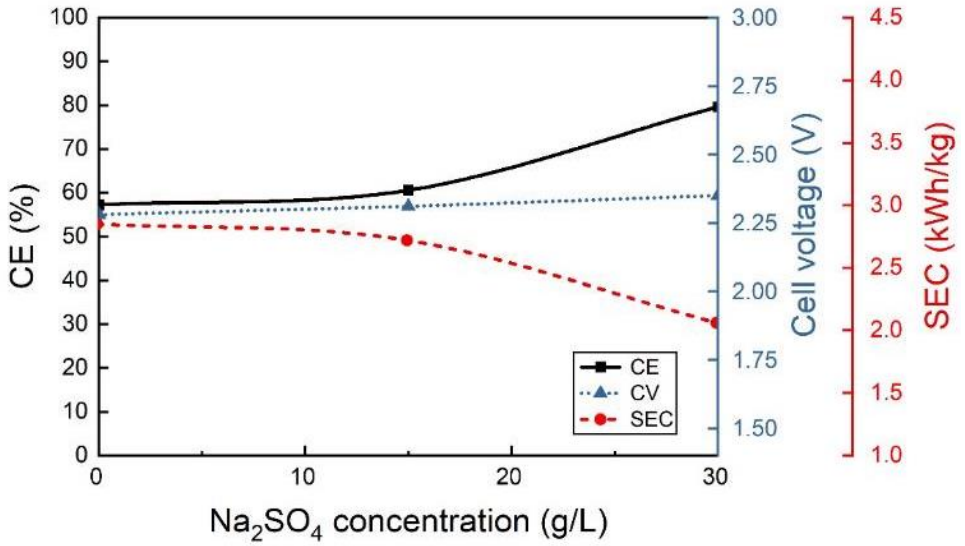

Figure 64. Variation of CE, cell voltage and SEC in the indium electrowinning at different sodium sulfate concentrations into a sulfate electrolyte composed of 70 g/L In^{3+} and 40 g/L H_3BO_3 at 50 A/m², 40 °C and pH 2.3.

7.6. Aluminum sulfate effect at 50 A/m²

Figure 65 shows the aluminum sulfate influence on CE, cell voltage and SEC during the indium electrowinning process using a sulfate electrolyte containing 70 g/L In^{3+}, 40 g/L H_3BO_3 and 30 g/L Na_2SO_4. Another compound like aluminum sulfate causes a significant drop of CE from 80% to 40% when 30 g/L $Al_2(SO_4)_3$ are added. Conversely, an adverse effect on cell voltage and SEC is obtained. First, aluminum sulfate increases the cell voltage about 3.3 V. As this compound rises into the electrolyte, the bubble formation is evidenced. Thus, aluminum sulfate causes an adverse effect on cell voltage, CE and SEC and, accordingly, increases HER. In the case of SEC, it is also verified a drastic SEC rise reaching almost 5.8 kWh/kg. Based on these outcomes, the electrolyte for the indium electrowinning on the Cu cathode must be deprived of aluminum sulfate. This salt significantly alters the indium reduction reaction, triggering the hydrogen reduction reaction.

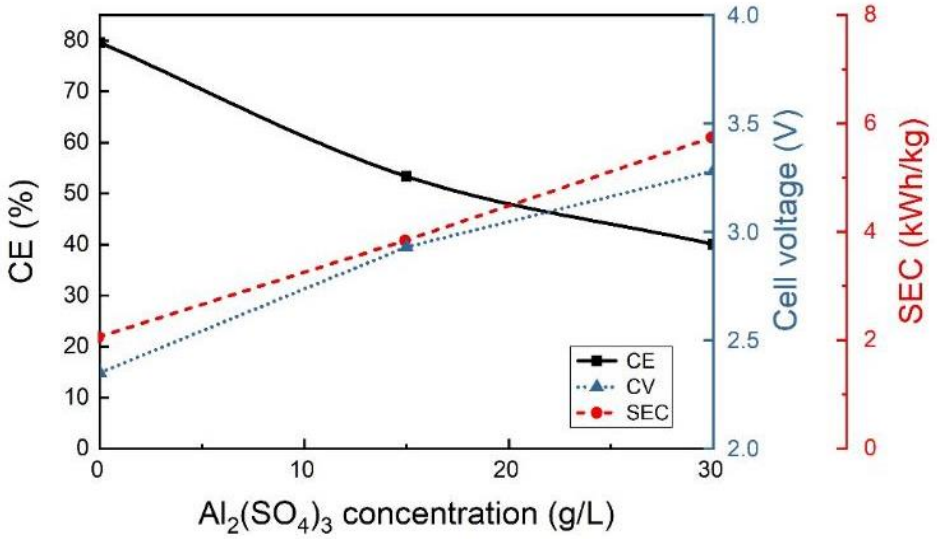

Figure 65. Effect of the aluminum sulfate concentration from 0 to 30 g/L on CE, cell voltage and SEC using a sulfate electrolyte containing 70 g/L In^{3+}, 40 g/L H_3BO_3 and 30 g/L Na_2SO_4 at 50 A/m^2, 40 °C and pH 2.3.

7.7. Effect of pH and temperature

The examination of operative conditions for the indium electrowinning on Cu has indicated the need to use an electrolyte containing 70 g/L In^{3+}, 40 g/L H_3BO_3 and 30 g/L Na_2SO_4 at 50 A/m^2. However, the pH and temperature effect should also be studied to evaluate any change concerning cell voltage, CE and SEC. These results are gathered in Table 10. The pH variation indicates a remarkable effect on both CE and SEC. Initially, low pH values (1.5) suggest more hydrogen ions in the solution than those at higher pH values. Thus, high hydrogen concentrations (low pH) cause a competing behavior between hydrogen and indium reduction reactions, hindering an effective indium discharge on the metal support. This competition is translated into degenerating the expected electrowinning outputs.

On the other hand, high pH values also indicate a negative effect on the indium electrowinning. At pH 2.7, the electrolyte is very close to unstable chemical conditions. From Pourbaix diagram for the indium in an aqueous solution, the indium ions form indissoluble hydroxides after pH 3.0 (Figure 33). Apart from this chemical threshold, when the indium reduction reaction occurs, pH is locally increased, altering the chemical equilibrium surroundings, consequently triggering the formation and precipitation of indium hydroxides. Therefore, working at pH 2.3, the indium electrowinning is performed without the risk of promoting unstable conditions for the electrolyte. Since pH can locally be increased near the cathodic surface, pH 2.3 is widely distant from the chemical limit for forming insoluble hydroxides. By using the above-mentioned

operative conditions at pH 2.3, high CE and low SEC can be obtained without traces of precipitated hydroxides throughout the process.

Table 10. pH effect on the indium electrowinning outputs. The electrolyte was composed of 70 g/L In^{3+}, 40 g/L H_3BO_3 and 30 g/L Na_2SO_4 at 50 A/m², 40 °C and pH 2.3.

pH	Cell voltage (V)	CE (%)	SEC (kWh/kg)
1.5	2.93	10.87	18.86
2.3	2.92	79.59	2.56
2.7	2.36	43.57	5.43

In the case of the temperature, Figure 66 shows the temperature evaluation on CE, cell voltage and SEC for the indium electrowinning. Varying the temperature (25, 40 and 60 °C), CE increases as temperature increases, indicating that it is possible to achieve about 90 % at 60 °C. The other temperatures only reach lower values, such as about 80% and 70% for 40 and 25 °C, respectively. On the contrary, cell voltage increases at room temperature roughly to 3.1 V, while SEC decreases at 3.2 kWh/kg. The lowest cell voltage and SEC values can be obtained at 60 °C to be close to 2.5 V and 2.0 kWh/kg, respectively.

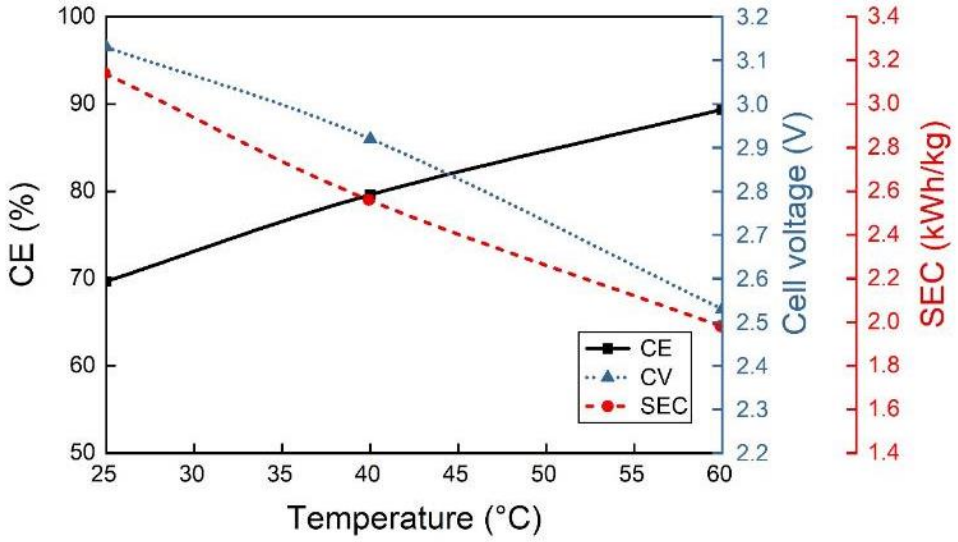

Figure 66. Temperature effect on the indium electrowinning. The electrolyte was composed of 70 g/L In^{3+}, 40 g/L H_3BO_3 and 30 g/L Na_2SO_4 at 50 A/m² and pH 2.3.

7.8. Morphological analysis for the indium deposits at diverse operative conditions

Figure 67 shows SEM micrographs at two magnifications using a sulfate solution containing 70 g/L In^{3+} at different CDs (25, 50, 100 and 150 A/m^2). A trend of growth is observed as CD increases. The indium deposit obtained at 25 A/m^2 shows small and round grains (Figure 67a). The deposit looks more compact, with grains tightly together at a higher magnification. Additionally, a lamellar microstructure is observed on most grains (Figure 67e). As CD increases, grain size rises. Figure 67b and Figure 67c show similar morphologies and size; nonetheless, the former particularly shows an abundant presence of nucleation seeds combined with lamellar microstructures. Although the deposit at 100 A/m^2 has a grain size on average similar to that obtained at 50 A/m^2, its smoother aspect is highlighted. Anyway, this indium deposit seems less compact than that at 50 A/m^2.

These two deposits obtained at 50 and 100 A/m^2 reveal at higher magnifications interesting morphologies (Figure 67f and Figure 67g). The former shows a junction growth (Figure 67f), while the latter is featured by well-defined polygonal grain boundaries. Also, it is possible to identify a step-growth (Figure 67g). Furthermore, when CD is increased at 150 A/m^2, the average grain size exceeds 40 μm, and the morphology is much less compact. Although elongated cavities are evident, suggesting a significant growth, round holes are also identified because of HER (Figure 67c-d). In Figure 67h, the micrograph of indium deposit obtained at 150 A/m^2 indicate some lamellar microstructures on grain edge along with nucleation seed everywhere. In addition, some well-defined polygonal grains with large sizes (> 40 μm) can be seen.

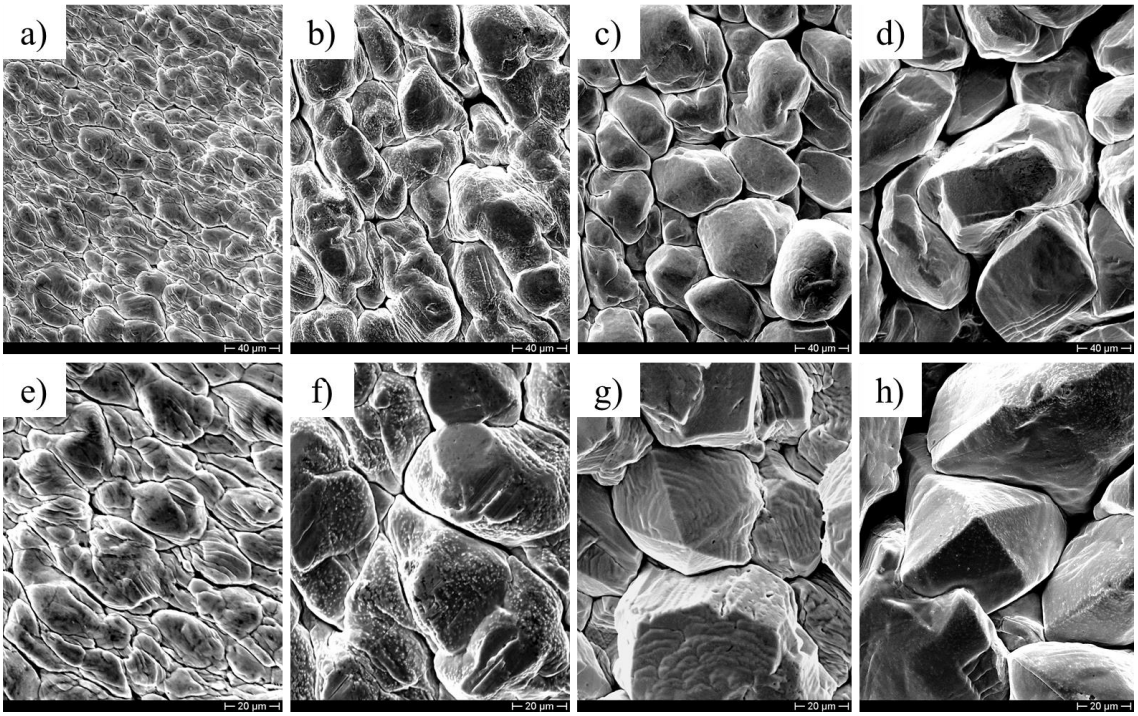

Figure 67. SEM micrographs for indium deposits using a sulfate electrolyte containing 70 g/L In^{3+}, 40 °C, pH 2.3 and using different CDs: a-e) 25, b-f) 50, c-g) 100 and d-h) 150 A/m^2.

The deposit morphologies obtained from an electrolyte containing 70 g/L In^{3+} and 20 g/L H_3BO_3 and different CDs are presented in Figure 68. The boric acid within the electrolyte suggests notable grain growth. Comparing the morphology and shape obtained without (Figure 67a-e) and with boric acid (Figure 68a-e) shows a significant increase in grains size. In Figure 68a, deposit morphology shows very close grains with lamellar microstructure on all deposits. The latter statement is confirmed in Figure 68e. At 50 A/m^2, the indium deposit presents grains covered by nucleation seeds, as appeared in Figure 67b without boric acid concentration. As CD increases, grain shapes of indium deposits depict polygonal grains with a very well-defined edge, that is more evident in Figure 68g-h. Also, indium deposits form well-delineated step-like grains, as shown in Figure 68h.

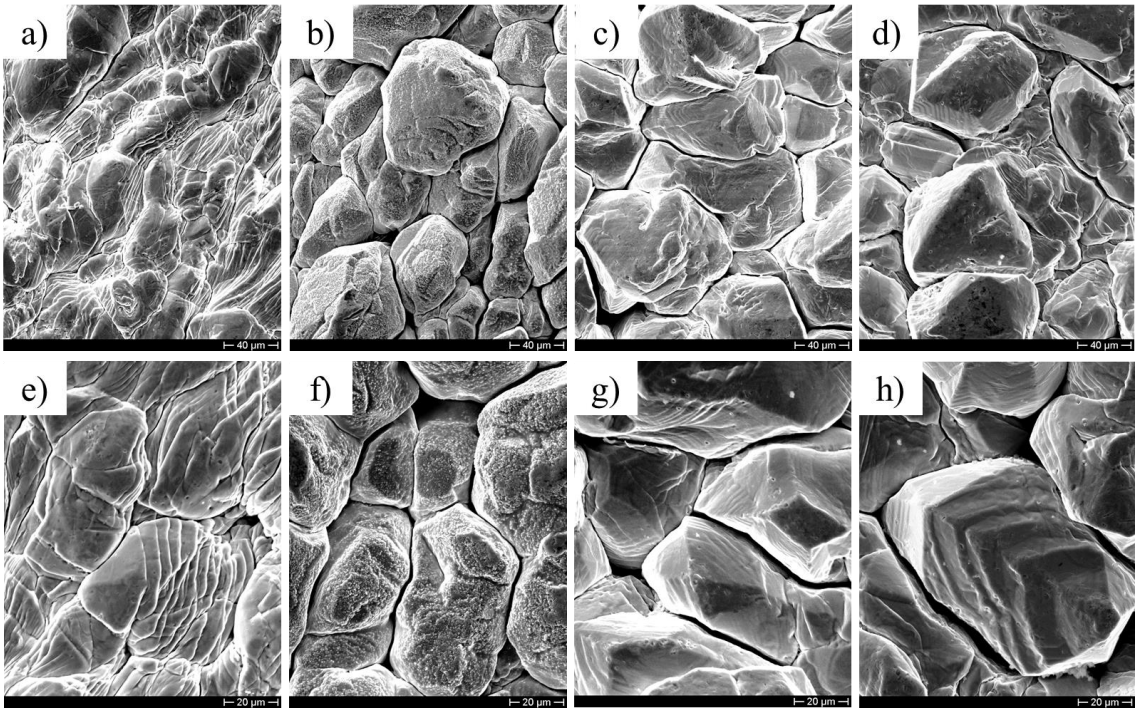

Figure 68. SEM micrographs for indium deposits using CDs at a-e) 25, b-f) 50, c-g) 100 and d-h) 150, respectively. The employed electrolyte was composed of 70 g/L In^{3+} and 20 g/L H_3BO_3 at 40 °C and pH 2.3.

Using Cu as metal support, the indium electrowinning at 25 A/m2 reaches more than 90% CE and around 1.5 kWh/kg SEC, changing the starting operative conditions. Since the main objective in the indium electrowinning process is to improve the productivity and lower energy consumption at high CD, the electrowinning process on the Cu support was undertaken at 50 A/m^2 CD, even if CE and SEC outputs can slightly decrease (79.6 % and 2.6 kWh/kg, respectively). Figure 69 shows SEM micrographs for indium deposit obtained at 50 A/m^2 using an electrolyte containing 70 g/L In^{3+} and varying the boric acid concentration. Micrographs indicate a notable change in the grain morphology rather than size. Without the boric acid into the electrolyte, the growth without any additive contribution forms large grains with round and poor-defined edges.

Nevertheless, despite a random morphology, grains grow irregularly where different heights create a complex morphology of elongated cavities. Anyway, the whole surface is covered by nucleation needs and lamellar microstructures (Figure 69a-d). The boric acid addition of 20 g/L suggests slight changes regarding morphology; however, the lamellar morphology is less notable, but nucleation seeds are highly distributed (Figure 69b-e). Mainly, it can be seen in Figure 69e, grains highly covered by nucleation seeds that form a like-layer close to the edge, followed by the entire grain surface. On the contrary, adding 20 g/L more of boric acid (Figure 69c), a very well-defined

microstructure is obtained with a polygonal-like morphology, also is possible to distinguish traces of step growths. The latter can be seen in detail in Figure 69f.

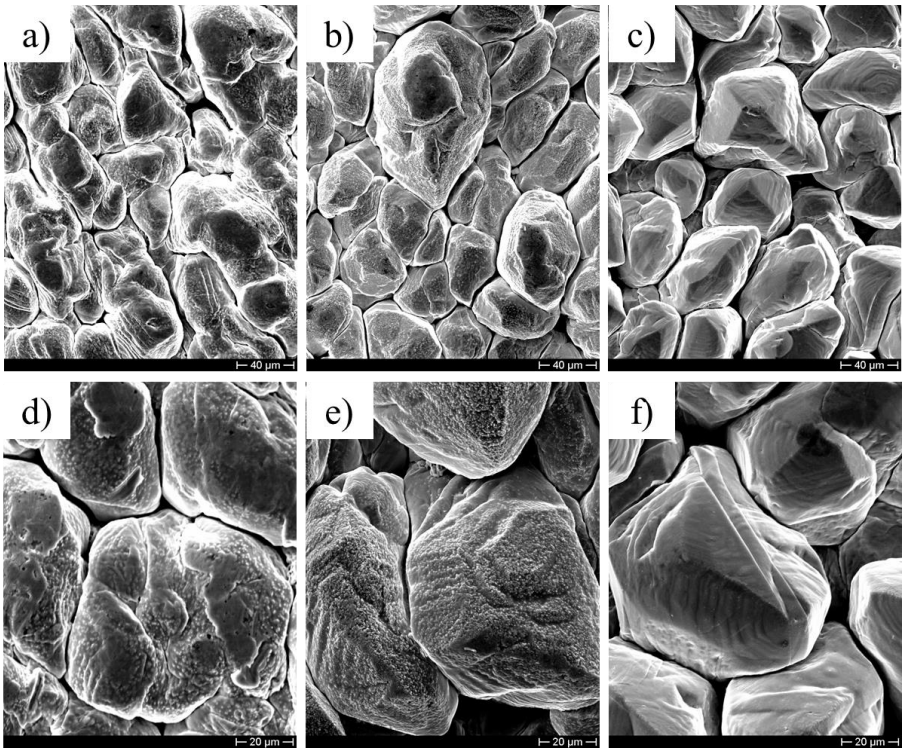

Figure 69. SEM micrographs for indium deposits obtained at 50 A/m², pH 2.3, at 40 °C and deposition time of 22 h varying the boric acid concentration a-d) 0, b-e) 20, c-f) 40 g/L in a sulfate electrolyte containing 70 g/L In^{3+}.

In Figure 70, it is shown the sodium sulfate effect on the indium electrowinning using an electrolyte containing 70 g/L In^{3+} and 40 g/L H_3BO_3. The sodium sulfate shows a slight modification of indium deposit morphology. All deposits exhibit well-defined shapes with polygonal grains. Moreover, the aluminum sulfate slightly affects the morphology, similar to sodium sulfate.

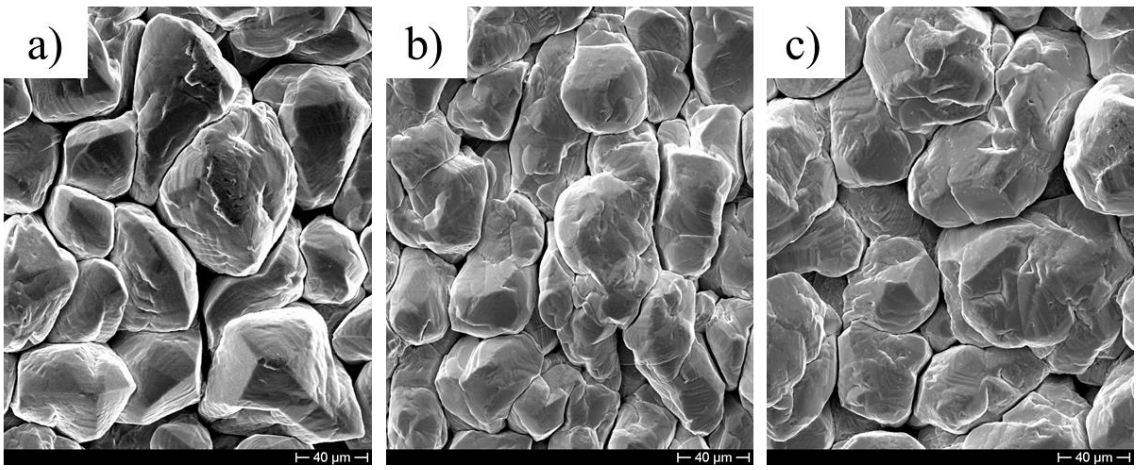

Figure 70. SEM micrographs for indium deposits obtained at 50 A/m², pH 2.3, 40 °C for 22 h varying the Na_2SO_4 concentration a) 0, b) 15, c) 30 g/L in a sulfate electrolyte containing 70 g/L In^{3+} and 40 g/L H_3BO_3.

The pH influence on the indium deposit morphology is observed in Figure 71. The fixed operative conditions were a sulfate electrolyte containing 70 g/L In^{3+}, 40 g/L H_3BO_3 and 30 g/L Na_2SO_4 at 40 °C. The morphology of indium deposits is affected by the pH change. Elongated grains with sizes smaller than 40 µm were highlighted with a compact aspect (Figure 71a). The pH increase induces a dramatic change in the indium microstructure. At a pH value of 2.7, the deposit seems to have a finer microstructure, where grains are not well-defined (Figure 71c). In fact, the deposit has a like-dendrites microstructure; nonetheless, it is much more compact than that obtained at pH 1.5. Now, a test performed at pH 2.3 shows a morphology where grains have well-defined edges and morphologies (Figure 71b). Thus, electrowinning outputs and indium deposit morphology working on the Cu cathode is clearly affected by the pH of the electrolyte.

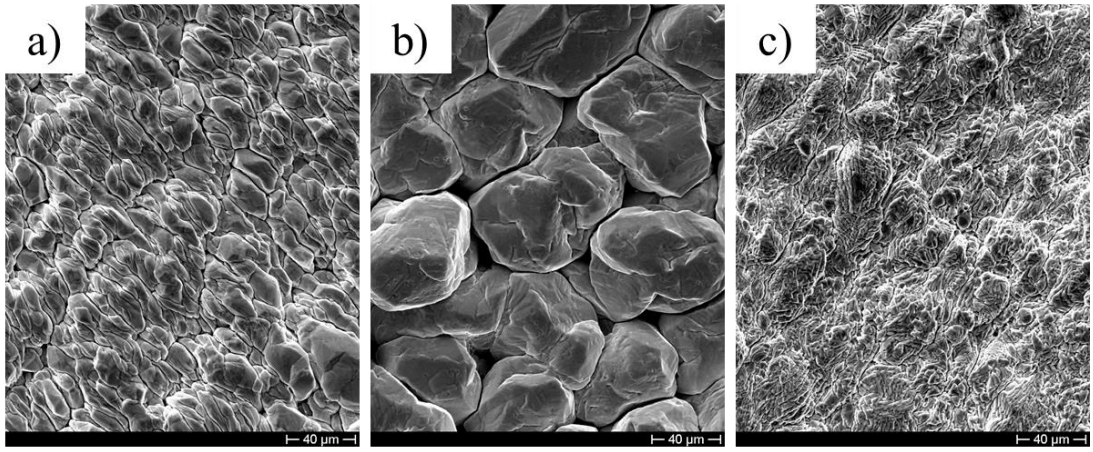

Figure 71. Effect of pH at a) 1.5, b) 2.3 and c) 2.7 for indium electrowinning process using a sulfate solution containing 70 g/L In^{3+}, 40 g/L H_3BO_3 and 30 g/L Na_2SO_4 at 40 °C and 50 A/m².

Another processing parameter important during the indium electrowinning is temperature. Figure 72a-c shows indium deposit morphology obtained after varying temperatures at 25, 40 and 60 °C, respectively. The tests were performed using a sulfate solution containing 70 g/L In^{3+}, 40 g/L H_3BO_3 and 30 g/L Na_2SO_4 and 50 A/m^2 CD. A slight change of morphology is observed for the indium deposits obtained by using three different temperatures. These deposits present compact morphologies with grains higher than 40 μm, covered by lamellar structures.

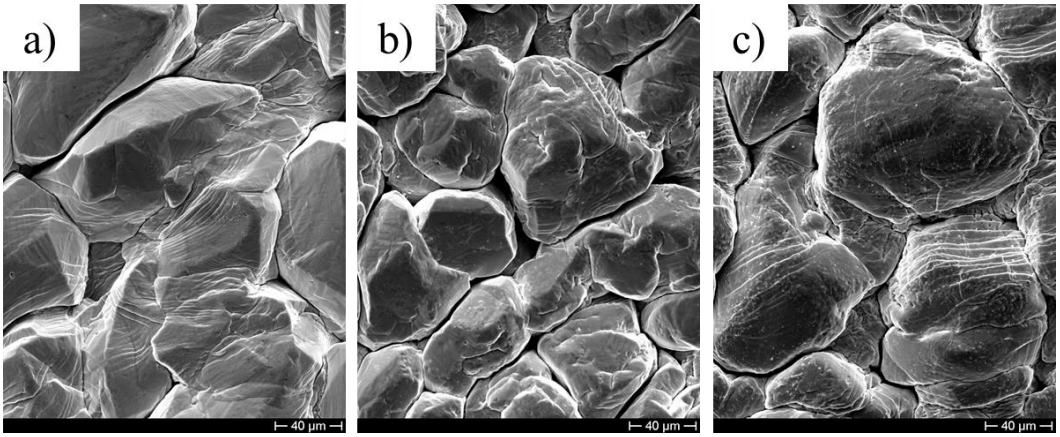

Figure 72. Effect of temperature on the indium electrowinning at a) 25, b) 40 and 60 °C using a sulfate solution containing 70 g/L In^{3+}, 40 g/L H_3BO_3 and 30 g/L Na_2SO_4 and pH 2.3.

7.9. XRD analysis for the indium deposits at diverse operative conditions

Figure 73a-d shows diffractograms for indium deposits obtained varying the CD between 25 and 200 A/m^2. As CD value increases, the pattern's intensity of indium deposits decreases. The latter is only observed progressively from 25 to 200 A/m^2. Furthermore, at 150 A/m^2, the preferential orientation is that of the (002) plane (Figure 73d), which presents broadening peaks with low intensities. These diffractograms suggest the crystallinity of indium deposits decreases as CD increases (Figure 74).

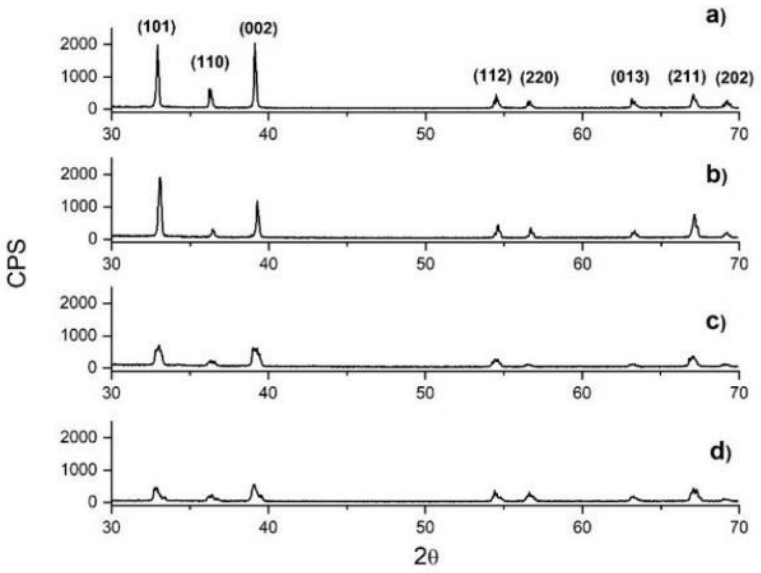

Figure 73. Diffractograms for indium deposits obtained using a sulfate electrolyte containing 70 g/L In^{3+} and 20 g/L H_3BO_3 at 40 °C, pH 2.3 and changing the CD: a) 25, b) 50, c) 100, d) 200 A/m^2.

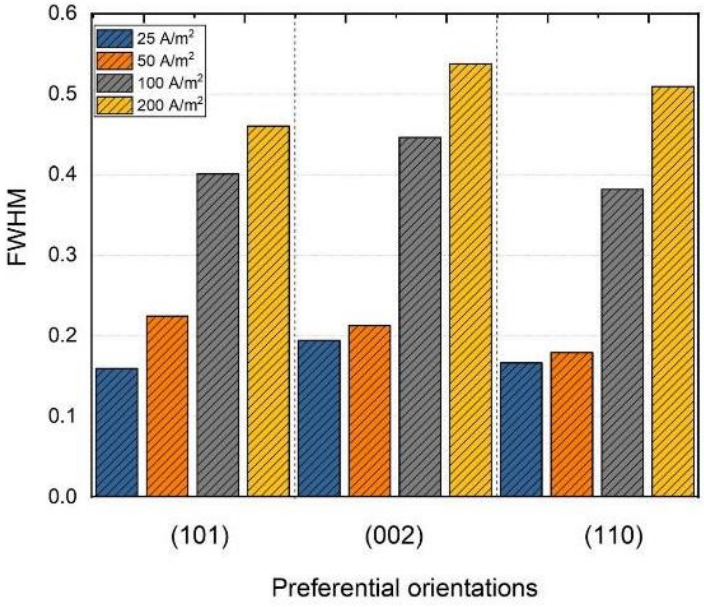

Figure 74. Analysis of FWHM at the three main peaks (101), (002) and (110) for indium deposits diffractograms obtained by changing the CD between 25 and 200 A/m^2.

XRD tests were also used to evaluate indium deposits obtained by different electrolyte compositions. In Figure 75, it can be seen diffractograms from indium deposits obtained using an electrolyte content of 70 g/L In^{3+}, pH 2.3, 40 °C and different boric acid concentrations. Those diffractograms show that the plane (101) is the preferential orientation, but less for that one at 20 g/L H_3BO_3. Slight crystallographic variations were observed by increasing the H_3BO_3 content. On the other hand, by adding into the electrolyte (70 g/L In^{3+}, 40 g/L H_3BO_3.) further concentrations of sodium sulfate

(Figure 76) and aluminum sulfate (Figure 77), different changes on diffractograms are highlighted. First, the sodium sulfate (0,15 and 30 g/L) into the electrolyte brings an intensity increase of the (101) peak when the solution contains 30 g/L Na_2SO_4. It seems the crystallinity features of the indium deposit are improved. In contrast, in the case of the aluminum sulfate, peaks' intensities are progressively decreased, suggesting a crystallinity decrease. The electrolyte containing high aluminum sulfate shows small and broadened peaks (Figure 77c).

Moreover, Figure 78 and Figure 79 present diffractograms for indium deposits obtained at different pH and temperature values, respectively. As previously treated, the low pH value influences the hydrogen evolution, causing small and broadened peaks, whereas slight changes are observed at higher pH values. Furthermore, the temperature exhibits similar behavior, which means a significant decrease of the diffractograms' intensity occurs, as temperature increases. In fact, peaks look more broadened and smaller at 60 °C, suggesting a diminishing of the deposit crystallinity.

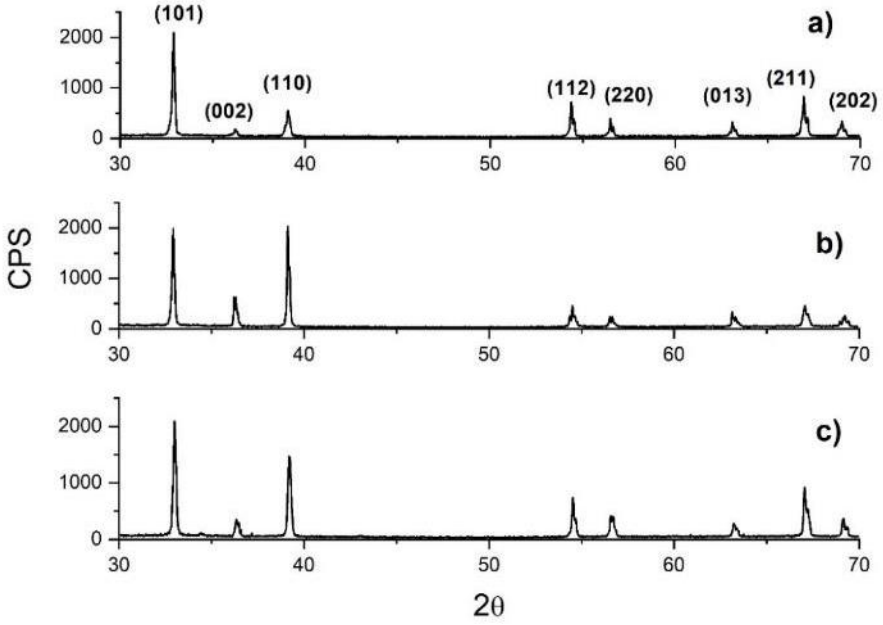

Figure 75. XRD patterns for indium deposits obtained using a sulfate electrolyte containing 70 g/L In^{3+} and boric acid concentration a) 0, b) 20 and c) 40 g/L at 25 A/m², pH 2.3 and 40 °C for 22 h.

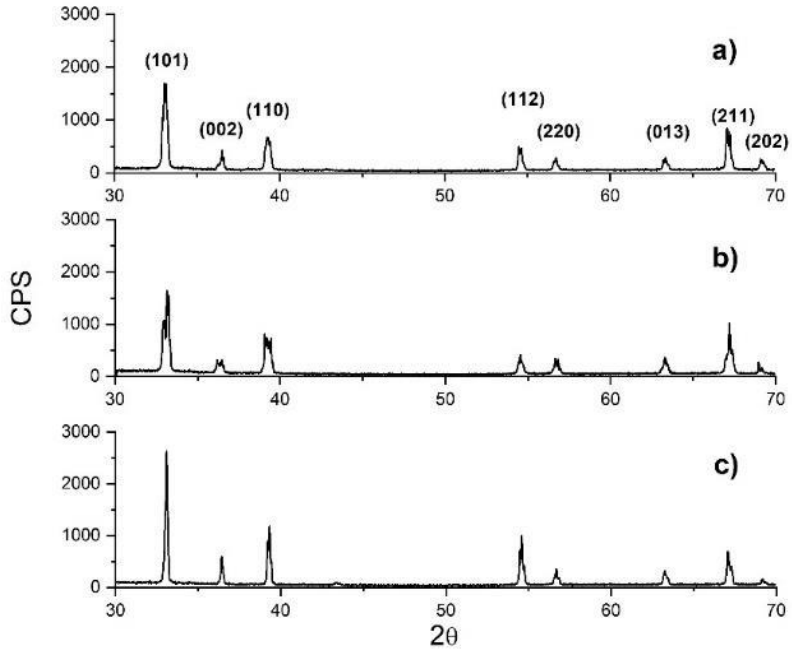

Figure 76. XRD patterns for indium deposits obtained varying sodium sulfate concentration: a) 0, b) 15 and c) 30 g/L in the sulfate electrolyte containing 70 g/L In^{3+} and 40 g/L H_3BO_3 at 50 A/m², pH 2.3, 40 °C for 22 h.

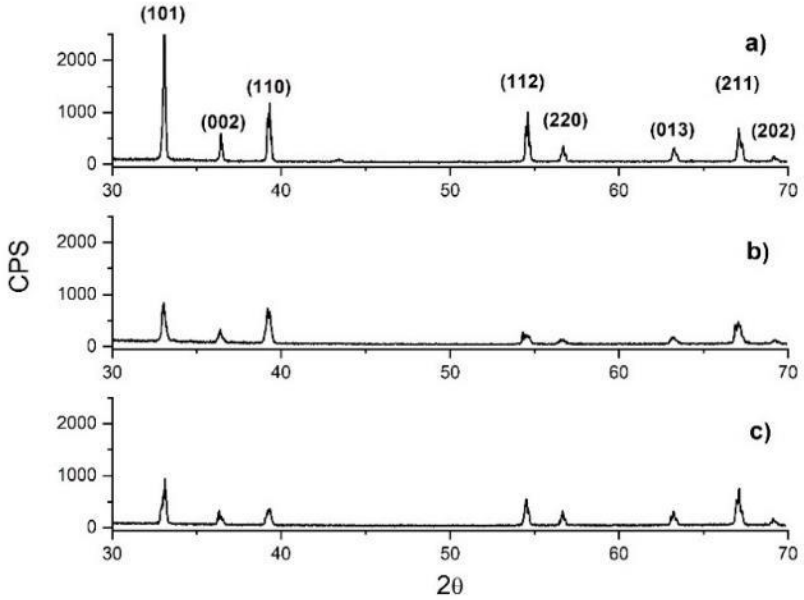

Figure 77. XRD patterns for indium deposits obtained using different aluminum sulfate concentrations a) 0, b) 15 and c) 30 g/L at 50 A/m², pH 2.3 for 22 h. The sulfate electrolyte contains 70 g/L In^{3+}, 40 g/L H_3BO_3 and 30 g/L Na_2SO_4.

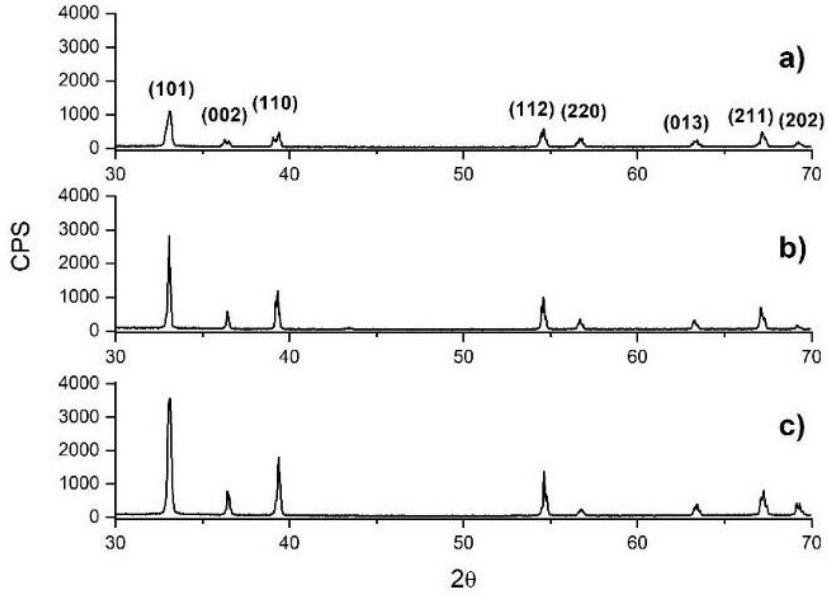

Figure 78. XRD patterns for indium at pH value of a) 1.5, b) 2.3 and c) 2.7. The sulfate solution contained 70 g/L In^{3+}, 40 g/L H_3BO_3 and 30 g/L Na_2SO_4 at 40 °C and 22 h as processing time.

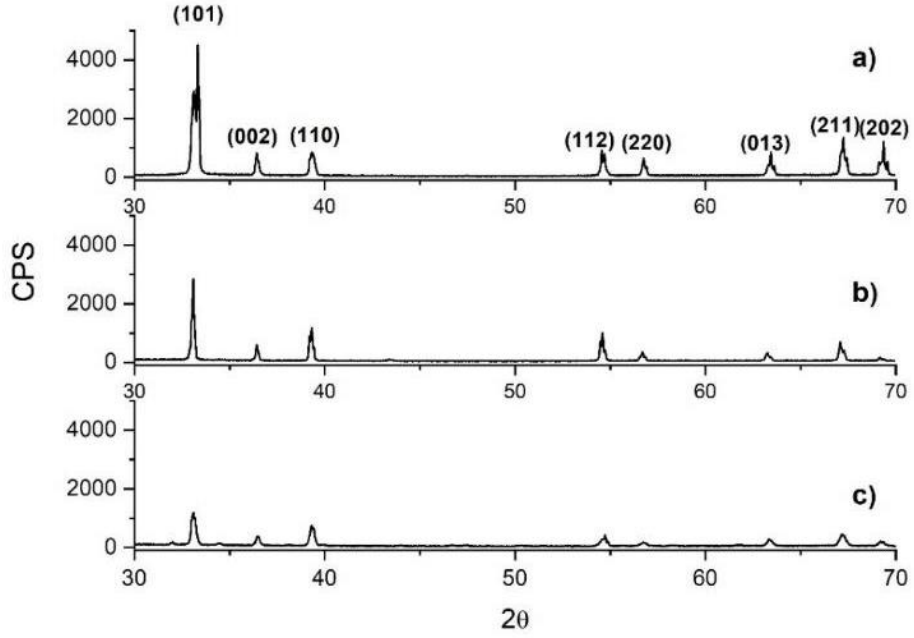

Figure 79. XRD patterns for indium deposits using a sulfate electrolyte containing 70 g/L In^{3+}, 40 g/L H_3BO_3 and 30 g/L Na_2SO_4 at 50 A/m^2, pH 2.3, deposition time of 22 h and changing temperatures at a) 25, b) 40 and c) 60 °C.

Chapter 8: **Titanium cathode**

8.1. Introduction

The indium electrowinning was carried out using titanium as metal support. The initial experimental conditions were taken from preliminary results [149]. In that work, the indium electrowinning was performed at 25 $A/m^{2,}$ obtaining 85% and 2.36 kWh/kg as CE and SEC, respectively. The operative conditions were defined at pH 2.3 and 40 °C using an electrolyte containing 140 g/L $In_2(SO_4)_3$, 5 g/L H_3BO_3, 20 g/L $Al_2(SO_4)_3$ and 30 g/L Na_2SO_4. Since those operative conditions gave relevant values in productivity and energy consumption at 25 A/m^2, it was decided to increase the CD values and determine the optimal conditions for the indium electrowinning. Therefore, in this chapter, the indium electrowinning process was carried out using the Ti cathode. To determine the best operative conditions of the process, different CD, pH and temperature values were evaluated to achieve high CE and low SEC outputs. Also, the low adhesion conditions between the metal support and the indium deposit led to assessing the etched surface's effect using HF. The morphology and crystallinity features of the obtained indium deposits were carried out.

8.2. Influence of boric acid and sodium sulfate on the indium electrowinning at 25 A/m^2

The boric acid has been mentioned in literature as a weak acid capable of hindering the hydrogen reduction reaction on the cathodic surface through the proton generation within the cathodic diffusion layer and controlling local pH variations near the cathodic surface [203,205,213]. In the case of Na_2SO_4, conductivity improvements and final aspect modification have been some of the reasons to use it [148,151].

The boric acid effect on CE and SEC at 25 A/m^2 is shown in Figure 80. The addition of boric acid at 25 A/m^2 using the Ti cathode seems not to significantly influence the electrowinning outputs since remain around 93% CE and 1.65 kWh/kg on average regardless of concentration used. Working without boric acid and different sodium sulfate concentrations, both CE and SEC keep unchanged above 94% and 1.6 kWh/kg, respectively (Figure 81). Such behavior suggests that the diverse overpotential cell are relatively negligible that the indium electrowinning at 25 A/m^2 using the Ti cathode can work without supporting additives. However, the used CD is relatively low for an industrial application in terms of productivity.

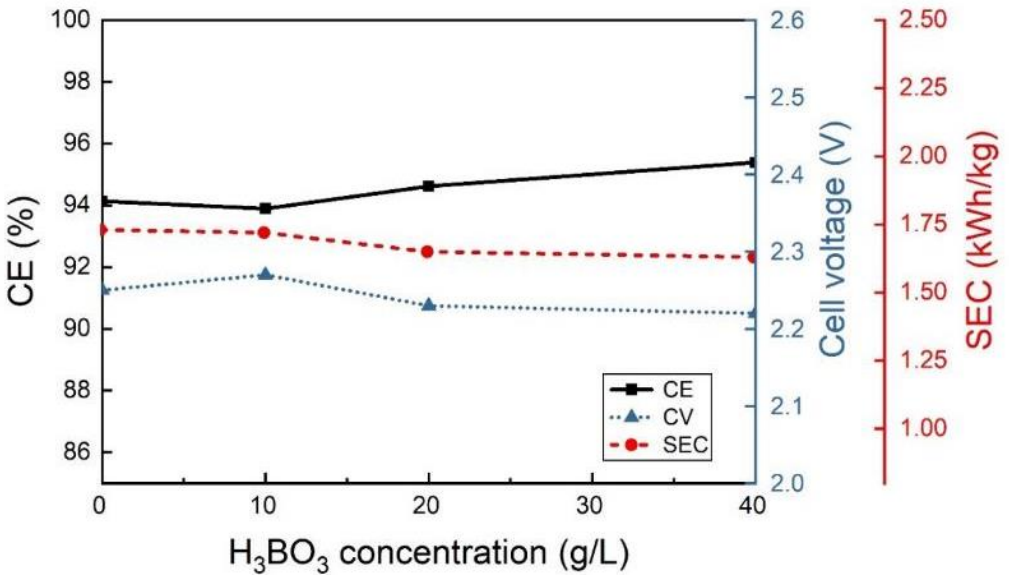

Figure 80. Effect of CE, cell voltage and SEC on the indium electrowinning as boric acid concentration is modified (0, 10, 20 and 40 g/L) at 25 A/m², 40 °C and pH 2.3.

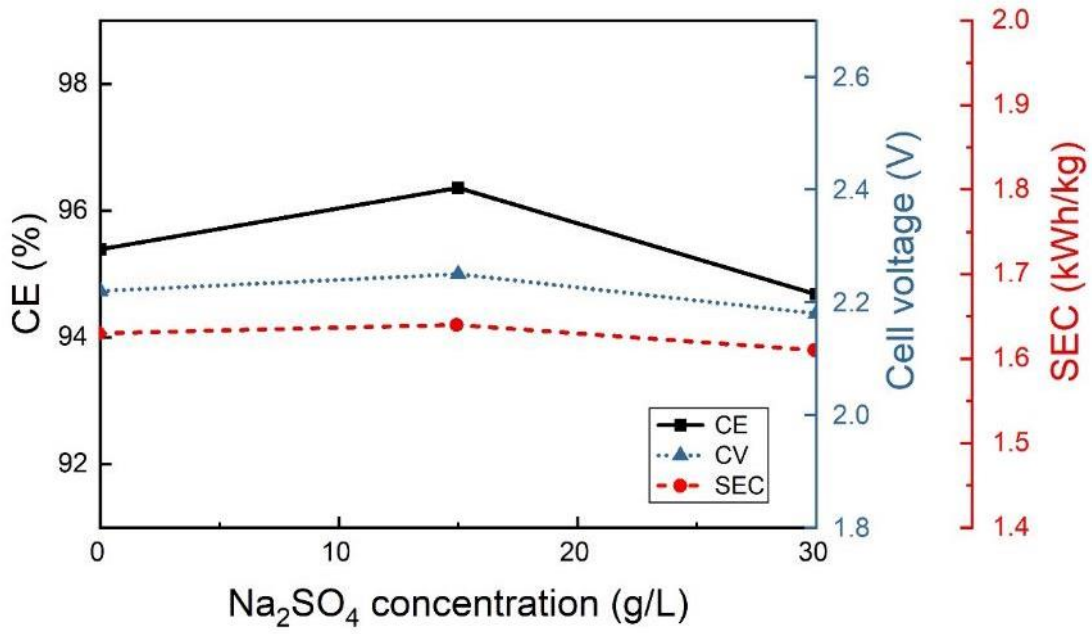

Figure 81. Influence of the sodium sulfate concentration at 0, 15 and 30 g/L on CE, cell voltage and SEC for the indium electrowinning at 25 A/m², 40 °C and pH 2.3.

8.3. Effect of the current density on the indium electrowinning

An experimental campaign was performed to analyze the CD effect using a solution containing 70 g/L of In^{3+} at pH 2.3 and 40 °C, as can be seen in Figure 82. The investigated CDs were 25, 50, 80, 100, 150 and 200 A/m². By Increasing CD, CE shows a constant trend up to 80 A/m², where a CE value above 90% is reached. Once CD exceeds this value, CE drops rapidly, reaching about 38% at 200 A/m².

Cell voltage and SEC follow an opposite behavior, increasing progressively as CD increases. At 200 A/m², these outputs are close to 3.4 V and 6.1 kWh/kg, respectively. The sharp fall after 80 A/m² has been attributed to cathodic overpotential phenomena exacerbated by HER. The parasitic HER competes with the indium reduction reaction, and the former becomes increasingly dominant. In particular, high CD values HER is strongly produced, giving rise to undesirable electrowinning outputs. Based on these results, it seems that 80 A/m² is the CD value to undertake the indium electrowinning. However, this investigation aims to high productivity and low energy consumption using high CD values. Therefore, the 100 A/m² CD was selected to achieve better electrowinning outputs. The electrowinning tests at 100 A/m² evaluated the effect of electrolyte composition, pH, temperature and the etched surface pretreatment on CE, cell voltage and SEC.

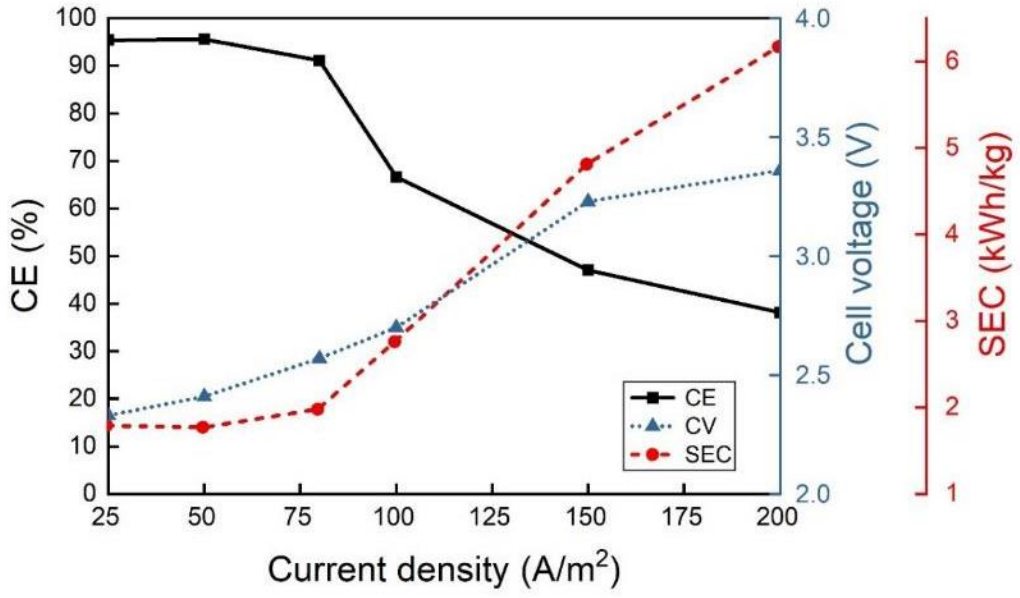

Figure 82. Analysis of current density effect (from 25 to 200 A/m²) on CE, cell voltage and SEC at 40 °C and pH 2.3.

8.4.Comparative effect of boric acid and sodium sulfate on the indium electrowinning 100 A/m^2

Table 11 shows the indium electrowinning outputs for cell voltage, CE and SEC at 100 A/m^2, 40 °C and pH 2.3. The results indicate that boric acid and sodium sulfate have a detrimental effect. In fact, only two remarkable results were obtained: i) without any additive compound and ii) adding 40 g/L H_3BO_3. The former electrolyte condition supplies about 67% CE and 2.8 kWh/kg SEC, while the increase of boric acid concentration at 40 g/L enhances CE that reaches around 83.5 %, while SEC is about 2.5 kWh/kg. The cell voltage shows a slight change using both compounds contemporaneously and 40 g/L H_3BO_3. Results indicate values close to 3 V. One relevant result is observed after this experimentation, indicating that boric acid and sodium sulfate together disfavor the electrowinning outputs for the indium recovery. Based on these considerations, it is convenient to use only 40 g/L H_3BO_3 into the electrolyte to improve the electrowinning process.

Table 11. Comparative analysis of boric acid and sodium sulfate effect on the indium electrowinning at 100 A/m^2, 40 °C and pH 2.3.

H_3BO_3 (g/L)	**Na_2SO_4 (g/L)**	**Cell voltage (V)**	**CE (%)**	**SEC (kWh/kg)**
0	0	2.70	66.61	2.76
0	15	3.10	25.79	8.52
0	30	3.08	33.16	6.50
40	0	3.01	83.51	2.52
40	15	3.12	69.60	3.11
40	30	3.07	23.69	9.10

8.5.Effect of pH on the indium electrowinning process at 100 A/m^2

From the previous outcomes, the pH change of indium electrolyte (70 g/L In^{3+} and 40 g/L H_3BO) at 40 °C and 100 A/m^2 was evaluated, as shown in Table 12. The maximum CE is reached at pH values close to 2.3, confirming the previous results obtained on other metal cathodes. At this pH condition, CE and SEC are about 83.5% and 2.5 kWh/kg, respectively. In the literature, it has been explained that pH effect on water electrolysis [169]. It has been claimed that HER at low pH values cannot be affected if working at high CD values; however, it has been shown that the HER can be promoted at low CD values [169]. Considering this report, the low CE and high SEC reported in Table 12 could be explained by the HER at low pH values (1.5 pH).

On the contrary, at higher pH values than 2.7, the formation of insoluble indium hydroxides is a real risk to the electrowinning process, causing adverse responses for CE and SEC. The formation of hydroxides coincides with the thermodynamical limits evidenced on the potential-pH diagram for the indium and water system at 25 °C (Figure 33). Thus, it is recommended to carry out the indium electrowinning using pH values close to 2.3 in order to achieve reasonable outputs in terms of CE and SEC.

Table 12. Influence of different pH values on the indium electrowinning using an electrolyte containing indium sulfate and boric acid at 100 A/m² and 40 °C.

pH	Cell voltage (V)	CE (%)	SEC (kWh/kg)
1.5	3.5	55.40	4.44
2.3	3.0	83.51	2.52
2.7	3.3	48.39	4.77

8.6. Comparative analysis at high current densities varying boric acid concentration

To reach interesting values of CE and SEC around 67% and 2.8 kWh/kg, respectively, operative conditions such as electrolyte containing 70 g/L In^{3+} and 100 A/m² were considered. In contrast, increasing CD to 150 A/m², those outputs are negatively affected, arriving at 47.02 % and 4.81 kWh/kg (Table 13). The latter indicates that rising CD only causes detrimental results on CE and SEC for the indium electrowinning. Thus, based on the previous results, 40 g/L boric acid was added to compare results obtained using 100 and 150 A/m². The boric acid addition improves in both cases CE and SEC, but the SEC is much higher than those tests performed at 150 A/m². Anyway, considering the balance between CE and SEC, the CD at 100 A/m² can be considered the most proper CD to carry out the indium electrowinning on the Ti cathode.

Table 13. Influence of the boric acid on the indium electrowinning process varying the CD between 100 and 150 A/m² at 40 °C and pH 2.3.

H_3BO_3 (g/L)	CD (A/m²)	Cell voltaje (V)	CE (%)	SEC (kWh/kg)
0	100	2.70	66.61	2.76
0	150	3.23	47.02	4.81
40	100	3.08	83.51	2.52
40	150	3.41	63.47	3.76

8.7.Effect of the pretreated titanium cathode on indium electrowinning

At low CDs, the indium deposit on Ti support remains attached. Nevertheless, once the indium electrowinning process is held at higher CDs (> 100 A/m^2), the deposit quality is altered by a swelling phenomenon causing the deposit detachment from the cathodic surface. Such swelling phenomenon is also observed in the literature for the indium electrorefining process using Ti support as a metal cathode [151]. Although the swelling phenomenon on the indium deposit is not highlighted in that work, it is possible to suggest, based on our findings, that this swelling is due to the internal stress of the deposit. As CD increases, current lines become more intense on the cathode edge. In fact, in those places, the formation of dendritic morphologies increases.

The literature about metallic films deposition using amorphous substrates has shown the deposit swelling and detachment from cathode [214]. Considering the nature of our deposits and electrolysis conditions, the swelling phenomenon could be due to low adhesion conditions between the deposit and Ti surface. Therefore, it was decided to use 1 M hydrofluoric acid (HF) solution for 30 s to eliminate the possible presence of surface residues. This pretreatment attempted to increase the roughness and the physical contact between the deposit and metal surface. Figure 83 shows a qualitative comparison of quality deposits without and with etching. Figure 83a-c shows swelled indium deposits at different CDs. Notably, at 200 A/m^2 current lines form dendritic morphologies at the edge of the cathodic surface. Once the cathodic surface is undergone etching pretreatment, the swelling phenomenon is highly hindered (Figure 83d-f). Nonetheless, the dendritic morphology close to the edge is anyway present at 200 A/m^2 due to the high overpotential achieved at that current density.

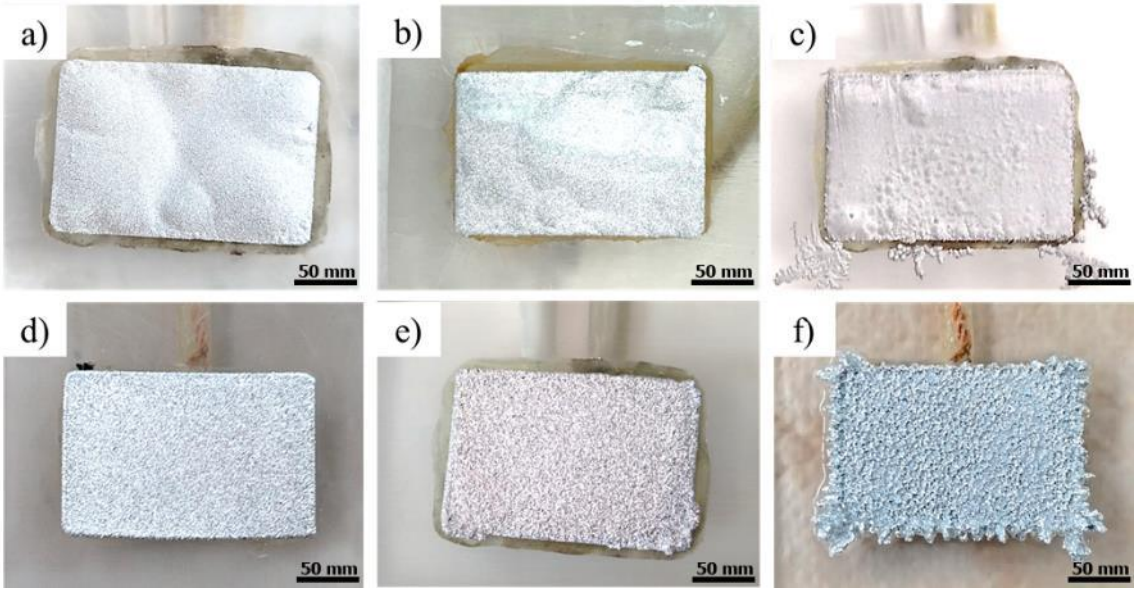

Figure 83. Aspect of the indium deposits without (a-c) and with (d-c) the etching on the Ti surface at different current densities: a-d) 100, b-e) 150 and c-f) 200 A/m^2.

The influence of etched cathodic support on electrowinning outputs was studied, as shown in Table 14. By using 1M HF to etch the Ti surface for 30 seconds, the indium electrowinning process has a better performance. Thus, a remarkable CE value of about 81% at 150 A/m^2 represents an improvement in the efficiency of 36%, which is more than that obtained without the etching pretreatment (43.85% CE) at the same conditions. In the case of 100 and 200 A/m^2, CE and SEC improvements are also achieved at both CDs higher 70% and lower 3.5 kWh/kg, respectively. More in detail, the etched cathode improved the indium electrowinning at 100 A/m^2 CD increases CE values from 63 to 78%, while at 200 A/m^2 CD, CE increases from 38 to 71%. On the other hand, relevant decreases of about 56% SEC are observed at both 150 and 200 A/m^2, with respect to those SEC values obtained with unmodified cathodes. The former CD drops close to 3.1 kWh/kg, while the latter decrease at 3.4 kWh/kg.

If the Ti cathode works without the etching, the best electrowinning outputs are obtained by adding 40 g/L boric acid into the sulfate electrolyte at 100 A/m^2. In contrast, the indium electrowinning can be carried out at 150 A/m2 with high CE and low SEC for the etched Ti cathode. Thus, the modified cathodic surface achieves efficiently more indium mass deposited on the cathode at the end of the process using higher CDs. In other words, the etched Ti cathode is required to improve the contact between the deposit and cathodic surface. In consequence, a reasonable balance between CE and SEC values working at higher CD (≥100 A/m^2) is reached. Therefore, since the main aim of in investigation points out achieving interesting high CE and low SEC values, a conservative analysis could suggest that the best performance for the indium electrowinning occurs working with Ti cathode at 100 A/m^2 CD and 40 g/L H_3BO_3. Nonetheless, the etched cathodic surface of titanium can utilize higher CE values without supporting reagents in the electrolyte. Although a slight SEC increase was reported, the etching pretreatment on the Ti surface makes the electrowinning process more practical and versatile since it only requires an electrolyte containing indium sulfate.

Table 14. Effect of the etching pretreatment on the indium electrowinning performance. The sulfate solution (70 In^{3+} g/L) and CD values between 100 and 200 A/m^2 at 40 °C and pH 2.3 were used. The etching pretreatment was performed by 1 M HF for 30 s.

Pretreatment	CD (A/m^2)	Cell voltage (V)	CE (%)	SEC (kWh/kg)
-	100	2.48	63.04	2.76
Etching	100	3.10	77.68	2.79
-	150	3.45	43.85	5.51
Etching	150	3.22	81.05	3.11
-	200	3.36	38.13	6.17
Etching	200	3.51	71.79	3.43

8.8.Temperature effect on the indium electrowinning

Figure 84 shows the effect of indium electrowinning outputs as temperature changes. From this figure, no matter the selected CD, a slight increase in CE is evident as temperature rises. However, at 150 A/m^2, the CE value was higher than that at 200 A/m^2. A brief explanation of the change in CE as temperature increases could be related to variation in ions mobility in the electrolyte. As was previously mentioned, increasing temperature, the CE of the indium reduction is positively affected. In this investigation, the etched Ti cathode, utilizing optimized electrolyte composition, is evaluated by different values of both CD and temperature. From experimental results, at 150 A/m^2 CD and room temperature, the electrowinning process obtains about 79% CE. While a CE close to 81% is achieved with a temperature increase at 40 °C. This CE value is slightly improved at 60 °C, showing around 86%. However, performing the electrowinning process at 200 A/m^2, the maximum CE is reached about 76% at room temperature.

Comparing cell voltage reported from both tests, at 150 and 200 A/m^2, a constant fall occurs as temperature increases, which is expected taking into account that temperature minizine resistive phenomena inside the electrolyte. In all cases, cell voltage at 200 A/m^2 is clearly larger than 150 A/m^2 since higher CDs involve higher cell overpotentials. Thus, when the temperature rises from 25 to 60 °C, this parameter goes from 3.6 to 3.4 V at 150 A/m^2, while at 200 A/m^2, cell voltage changes from 4.0 to 3.5 V. As a result of cell voltage, SEC also decreases as temperature increases. In fact, increasing temperature from 25 and 60 °C at 150 A/m^2 saves about 19% of energy consumption, whereas working at 200 A/m^2, the energetic saving indicates 11% among the same temperature range. Based on these findings, better electrowinning outputs are obtained by increasing temperature at 60°C using both 150 and 200 A/m^2. Nonetheless, the former CD value achieves notable results in productivity and energy consumption.

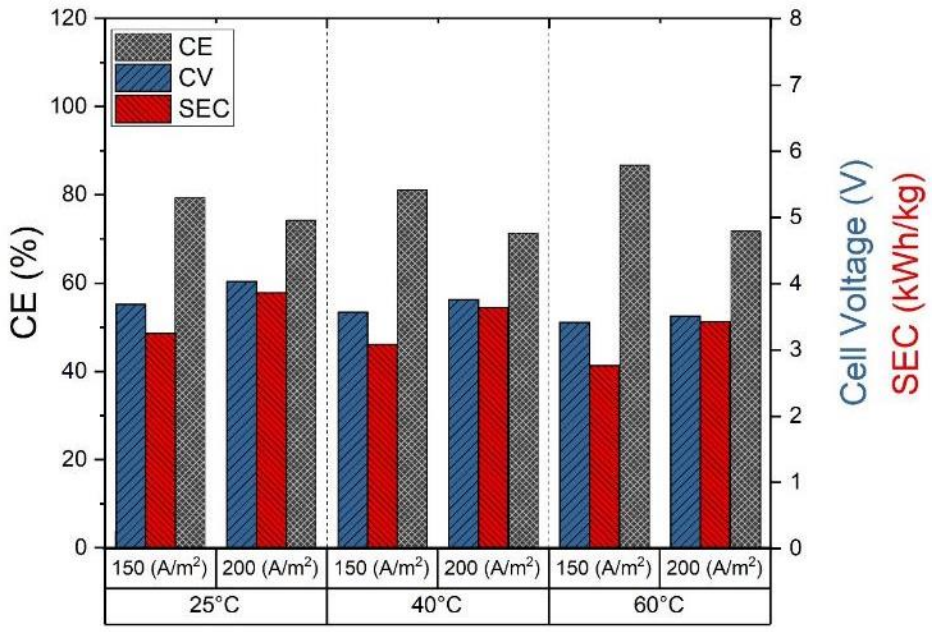

Figure 84. Effect of temperature (25, 40 and 60 °C) on the indium electrowinning using the etched Ti cathode, electrolyte containing 70 In^{3+} g/L at 150 and 200 A/m² as current density.

8.9.SEM characterization of indium deposits obtained on the Ti cathode

In Figure 85, it is shown SEM micrographs for indium deposits obtained at different CDs, while other operative conditions were kept unchanged (70 g/L In^{3+}, pH 2.3, temperature 40 °C and deposition time of 22 h). From micrographs, the CD increase has a relevant impact on the morphology of the indium deposit. A flattened morphology is observed at a low CD of 25 A/m² (Figure 85a). As CD increases, grains grow (Figure 85b-c). Thus, the deposit appearance is homogeneous and well defined. Still, it should be emphasized that the grains are bigger at higher CDs, and therefore deposits are less compact compared to those obtained at lower CDs. At 25 A/m², the deposit shows a disproportional growth, which could be seen better at high magnifications (Figure 85d). Unlike the microstructure obtained at 25 A/m², the indium deposit obtained at 100 A/m² does not show a similar microstructure. Instead, it is possible to observe nucleation seeds well-distributed on the whole surface at higher magnifications. These nucleation seeds represent the nucleation points where the grains will grow (Figure 85e).

As CD increases at 150 A/m², grains grow in size, surpassing more than 40 μm on average. The morphology shows an irregular growth on the grain boundary (Figure 85c), which is expected in electrowinning at high CDs. Once the CD increases, the deposit grows initially near grain boundaries since they are considered low energy points for nucleation [215]. However, this growth is irregular and alters the polygonal morphology of grains, as shown in Figure 85c. Another distinctive morphology at that CD is the step-growth that is much more evident at higher magnifications (Figure 85f).

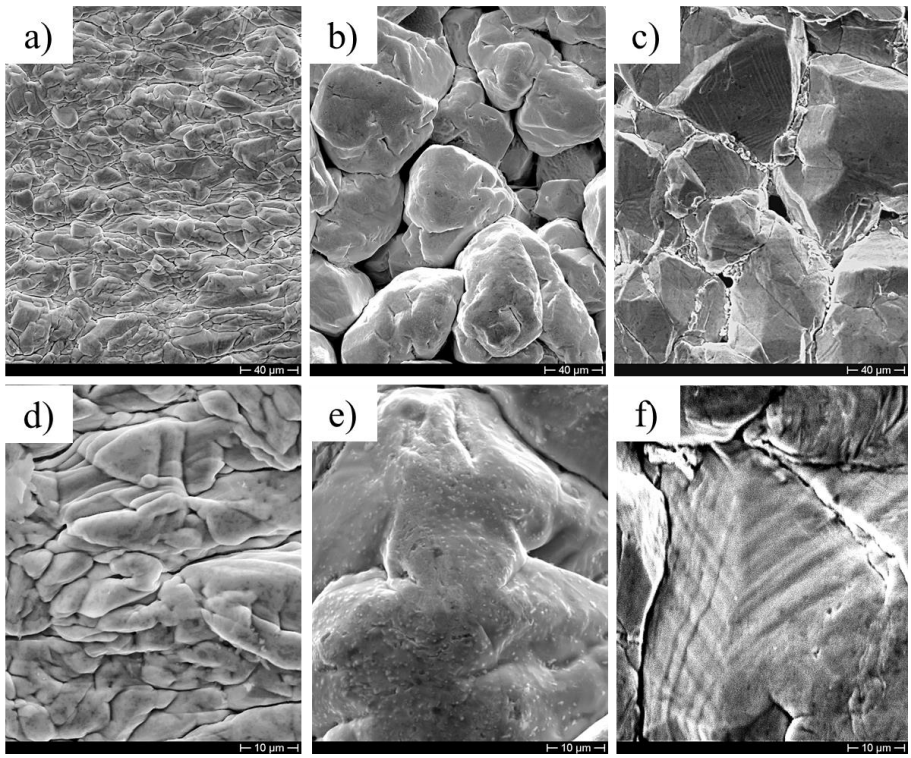

Figure 85. SEM micrographs for indium deposits obtained using a sulfate solution of 70 g/L In^{3+}, pH 2.3 at 40 °C and deposition time of 22 h. The SEM micrographs are presented varying the CD: a-c) 25 A/m², b-e) 100 A/m², c-f) 150 A/m².

The previous assessment was repeated, integrating different boric acid concentrations into the electrolyte. The micrographs of those deposits are shown in Figure 86. These morphologies follow a trend like Figure 85, that is, grain size increases as CD rises. Moreover, the grains size is much larger in Figure 86 b-c at 100 and 200 A/m², respectively. Regarding the morphology, micrographs show no significant changes with boric acid. Nonetheless, lamellar morphologies are evident in both Figure 86d and Figure 86e. At 150 A/m², the grain size of the deposit is much more prominent than those obtained at lower CDs. In addition, hole or round cavities also indicate the HER at high CD values.

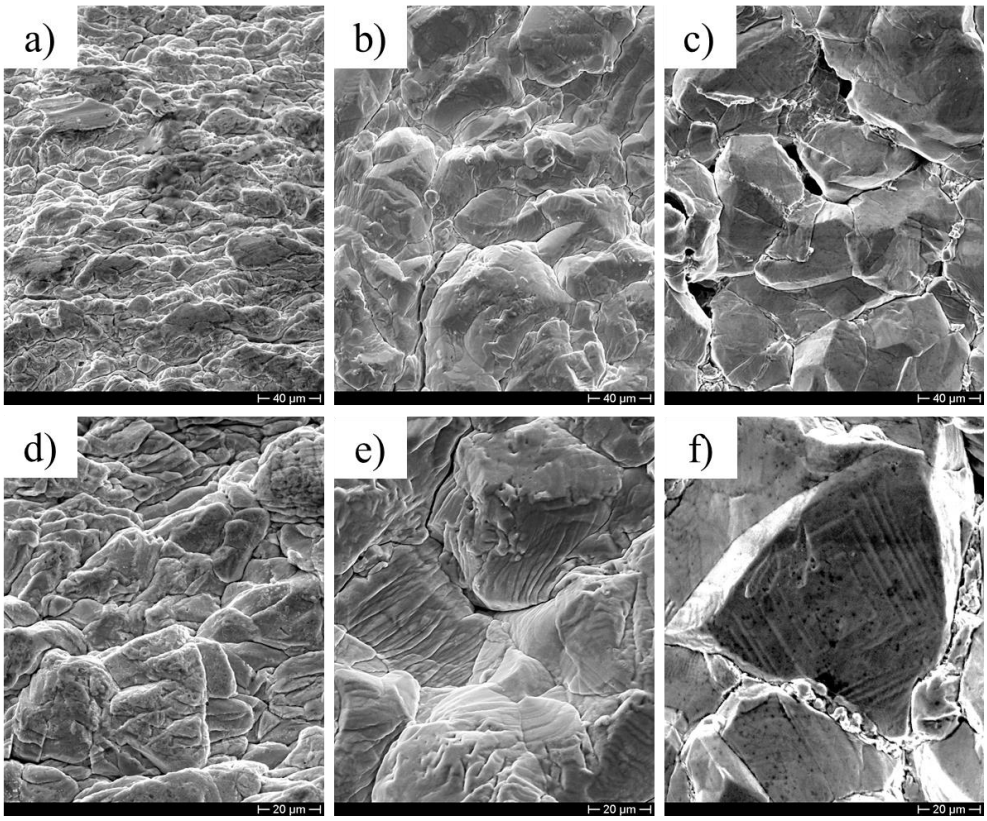

Figure 86. SEM micrographs for indium deposits obtained by using an electrolyte containing 70 g/L In^{3+}, 40 g/L H_3BO_3, pH 2.3, temperature at 40 °C and working time of 22 h. The SEM micrographs are presented varying the CD: a-d) 25 A/m², b-e) 100 A/m², c-f) 150 A/m².

By changing the pH within the electrolyte (Figure 87), the indium deposit obtained at pH 1.5 show smaller size grains (Figure 87a) than those obtained at pH 2.3 and 2.7 (Figure 87b and Figure 87c, respectively). However, deposits morphology is very similar despite the pH level, indicating that this parameter slightly affects the morphology. Micrographs show a lamellar microstructure at higher magnifications at pH 2.3 (Figure 87e), whereas it is not observed on the indium surface at pH 1.5 (Figure 87d). Considering pH 2.7, the surface is covered by brilliant little points, known as nucleation seeds (Figure 87f), which are well-distributed on the whole deposit. At this pH condition, grain size is significantly larger compared to the other studied pH values.

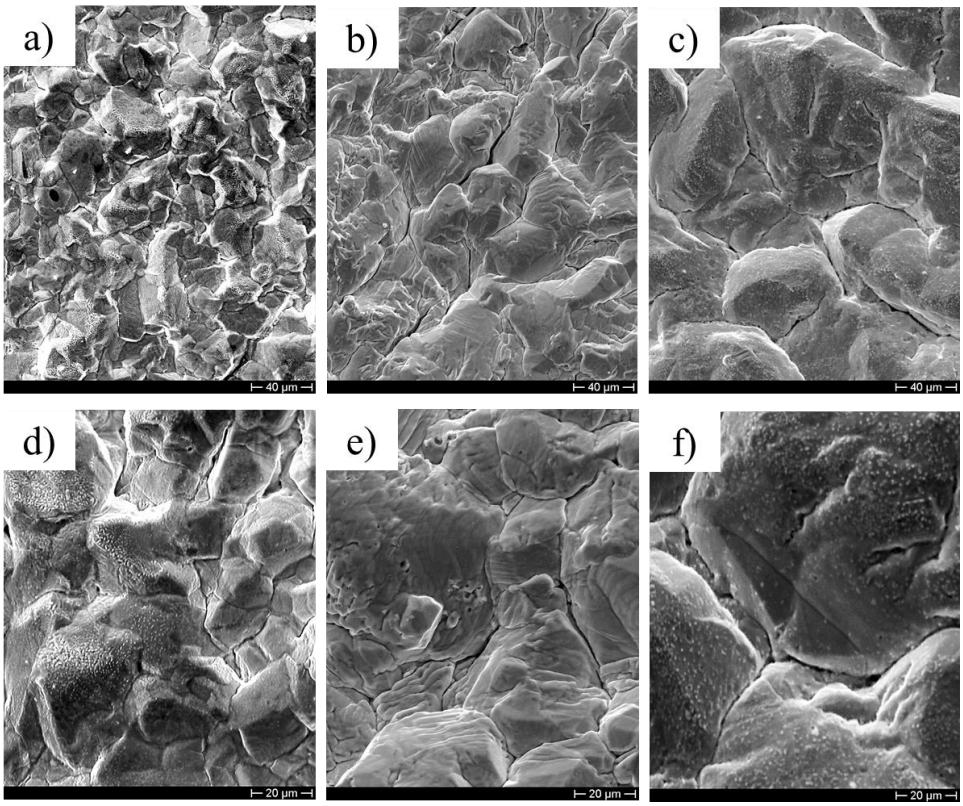

Figure 87. SEM micrographs for indium deposits obtained from a solution containing 70 g/L In^{3+}, 40 g/L H_3BO_3, temperature at 40 °C, 100 A/m² and deposition time of 22 h. The SEM micrographs are presented varying the pH value: a-d) 1.5, b-e) 2.3 and c-f) 2.7.

In Figure 88, it can be observed the indium deposit morphology obtained by using an electrolyte containing 70 g/L In^{3+}, 30 g/L Na_2SO_4 and pH 2.3 at 40 °C. The Na_2SO_4 into the electrolyte can alter the deposit morphology. At low CDs, the surface appearance is represented by stacked-like grains with a lamellar structure on the whole deposit. If the grain size of deposits performed at 25 and 100 A/m² is qualitatively compared, the deposit obtained at lower CD shows grain sizes smaller than those found at 100 A/m² (Figure 88a-b). Otherwise, Figure 88b-d depicts micrographs of the indium deposit obtained at 100 A/m² at different magnifications. Grain sizes surpass 40 µm with a smooth morphology. These conditions promote grains larger in size. Additionally, the HER incidence also leaves some tiny round holes, while high overpotentials exacerbate the formation of irregular deposits at the grain edge.

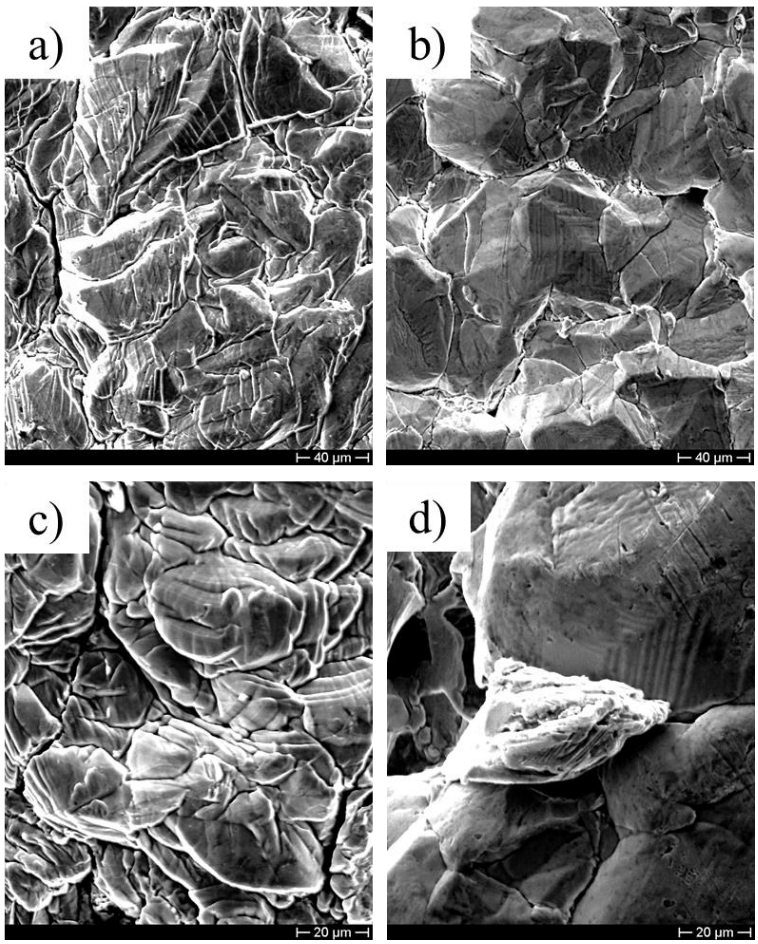

Figure 88. SEM micrographs for indium deposits obtained using an electrolyte containing 70 g/L In^{3+}, 30 g/L Na_2SO_4 at pH 2.3, 40 °C and deposition time of 22 h. The SEM micrographs are presented varying the CD: a-c) 25 A/m² and b-d) 100 A/m².

Since the swelling phenomenon and HER occur at CD higher than 80 A/m², the Ti cathodic surface was etched with 1 HF for 30 s before each assessment. The morphology of indium deposits obtained at 100 and 200 A/m² was evaluated (Figure 89). Figure 89a-c shows the indium morphology using a 100 A/m2 CD at different magnifications. The morphology is homogeneous and compact. In fact, grain boundaries are hardly recognizable on the deposit at lower magnification (Figure 89a). Similar behavior is illustrated increasing CD at 200 A/m² (Figure 89d-f). Although the deposit morphology, at low magnifications, looks very compact, some bigger grains are highlighted from the surface. Anyway, the microstructure still has a lamellar structure on grains at high magnifications (Figure 89c), while the morphology at 200 A/m² showed the step-growth on grains (Figure 89f). In both micrographs, notable round holes are attributed to HER (Figure 89b-e). This characteristic is also common for all the deposits obtained at high CDs. They have larger dimensions and are well distributed when the indium electrowinning is performed at 200 A/m².

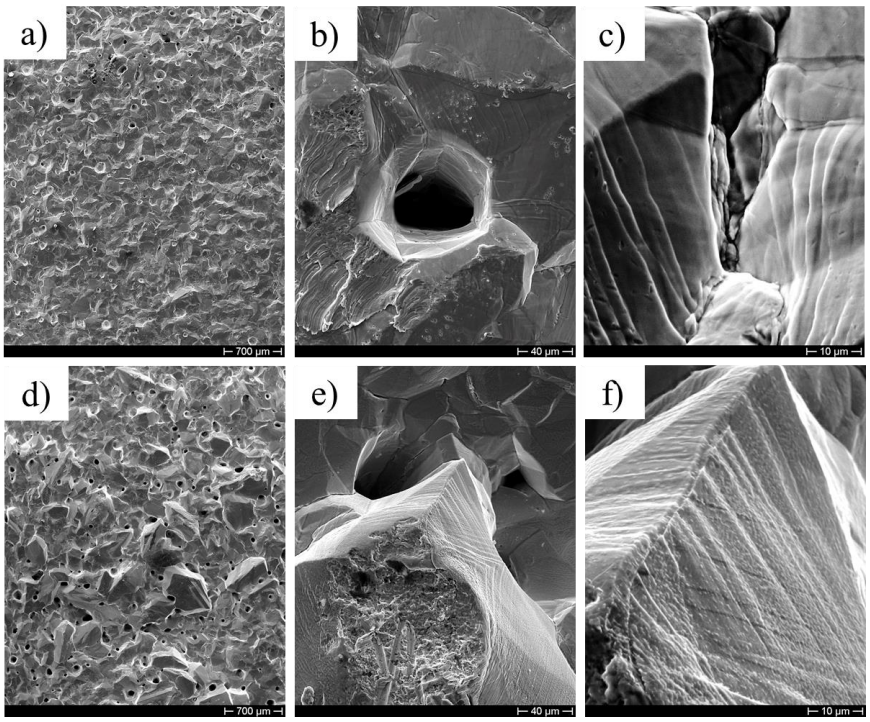

Figure 89. SEM micrographs of indium deposits obtained at 70 g/L In^{3+} at pH 2.3, 40 °C, deposition time of 22 h and different CDs: a-c) 100 A/m² and d-f) 200 A/m². The Ti cathode was etched by 1M HF.

Figure 90 shows the morphology of indium deposits obtained at different temperatures (25, 40 and 60 °C) using a CD at 150 and 200 A/m². The upper and below figures correspond to the CD at 150 and 200 A/m², respectively. At 150 A/m² CD, an intense hydrogen evolution at room temperature is observed due to a morphology full of holes (Figure 90a), while the temperature increase maintains a more compact microstructure (Figure 90c). The HER is present during all the experimental campaigns due to high CDs, but the temperature increase allows bubbles to move, collapse, or detach faster. Similar behavior is also observed considering 200 A/m² CD, but it is much more intense than that at 150 A/m². Further, the morphology is highly altered at room temperature, showing cavities with diameters higher than 200 µm (Figure 90d). Likewise, the deposit aspect resembles burnt and breakable due to the high overpotential at room temperature.

Since the temperature can modify resistive phenomena in the bath, it can alter the mobility for both indium and hydrogen ions or even accelerate the collapse of bubbles. Its contribution is definitely positive for the indium morphology and aspect, as corroborated in Figure 84. On the whole, increasing temperature makes it possible to increase CE and SEC values and improve the deposit aspect for the indium electrowinning.

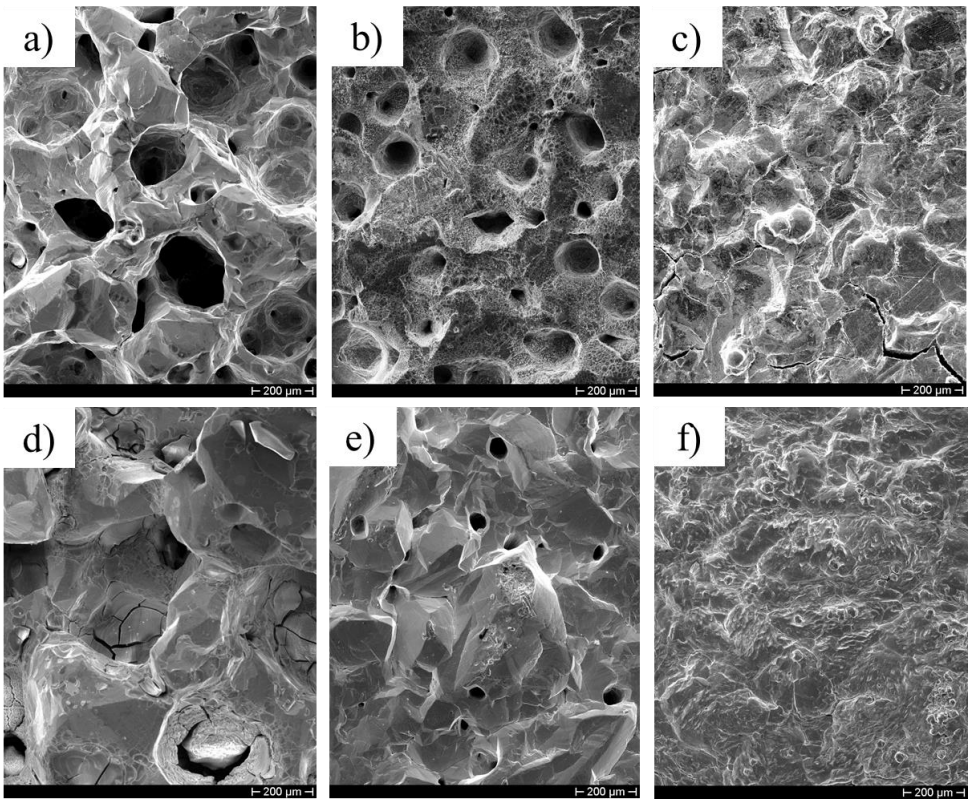

Figure 90. Morphology of indium deposit obtained by using an etched Ti cathode, 70 g/L In^{3+} and pH 2.3 for 22 h. Temperatures were varied at a-d) 25, b-e) 40 and c-f) 60 °C. Also, the CD was changed: the upper (a-c) and below (d-f) figures correspond to the CD at 150 and 200 A/m^2, respectively.

8.10. XRD analysis of indium deposits obtained on Ti cathode

XRD tests analyzed indium deposits changing the CD value. In general, all diffractograms present the characteristic peak related to the preferential orientation ((101), (002) and (110)). These preferential orientations are placed on the left side of the diffractograms. Other peaks with a lower intensity related to (112), (220), (013), (211) and (202) are placed on the right side of the diffractograms, considered as secondary peaks.

In general, the diffractograms' intensity decreases progressively as CD increases for an electrolyte containing 70 g/L In^{3+} (Figure 91) and another one with 70 g/L In^{3+} and 40 g/L H_3BO_3 (Figure 92). Regardless of peak height succession, this analysis shows that the peak (101) is always the main preferential orientation and the most intense at each CD.

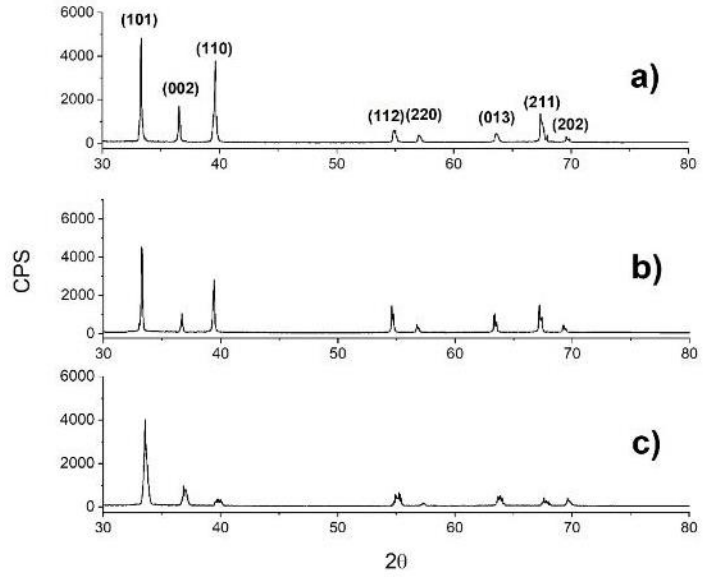

Figure 91. Diffractograms for indium deposits obtained by using an electrolyte containing only 70 g/L In^{3+} at pH 2.3, 40 °C and different CDs: a) 25, b) 80 and c) 100 A/m^2.

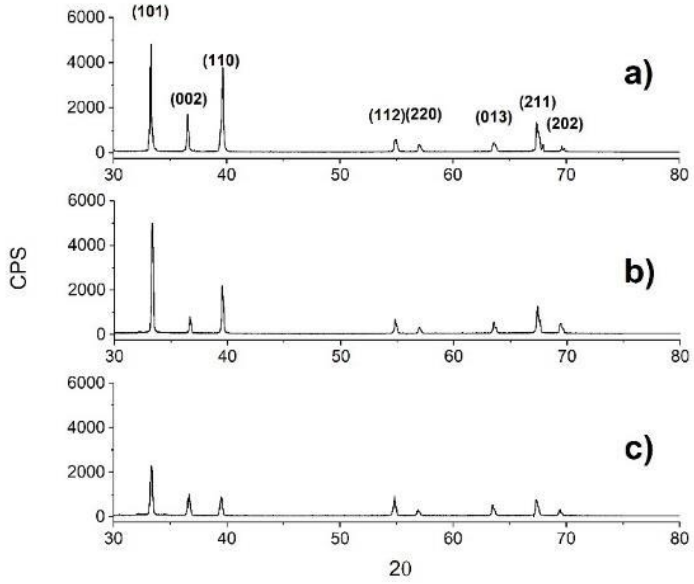

Figure 92. Diffractograms for indium deposits obtained by using an electrolyte containing 70 g/L $In^{3+}$and 40 g/L H_3BO_3 at pH 2.3, 40 °C and different CDs at a) 25, b) 100 and c) 150 A/m^2.

The addition of sodium sulfate into the electrolyte (Figure 93) shows an intensity decrease of XRD patterns, except for the (002) peak. At 100 A/m^2, it seems that the (002) peak increases more in intensity than that at 25 A/m^2.

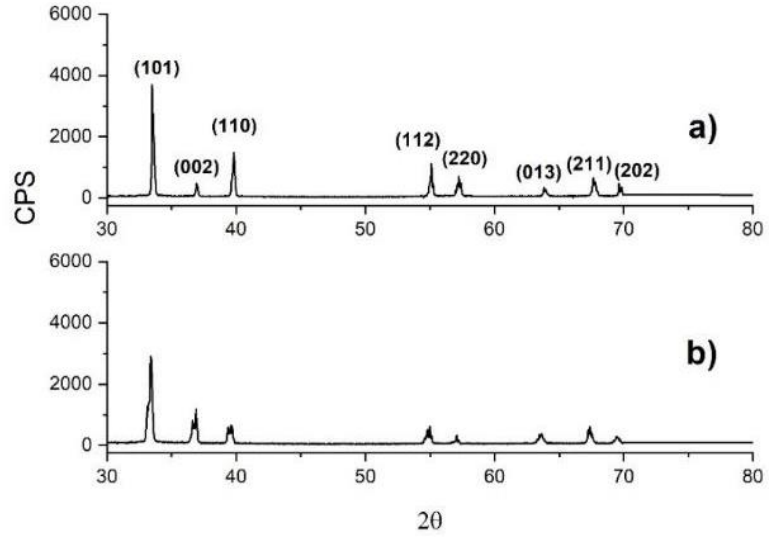

Figure 93. Diffractograms at a) 25 and b) 100 A/m² of indium deposits using a sulfate electrolyte containing 70 g/L In^{3+} and 30 g/L Na_2SO_4, pH 2.3, 40 °C for a period of 22 h.

Finally, deposits obtained at different temperatures (25, 40 and 60 °C) using the etched Ti cathode at 200 A/m² were evaluated by XRD assessments, as shown in Figure 94a-c. It is observed a progressive decrease of the peak intensity as temperature rises. Although the orientation (002) seems to keep the same intensity at 25 and 40 °C (Figure 94b), the pattern' intensity follows a drastic fall and the broadening of peaks at 60 °C. This behavior could suggest a diminishing of crystallinity features of the indium deposit.

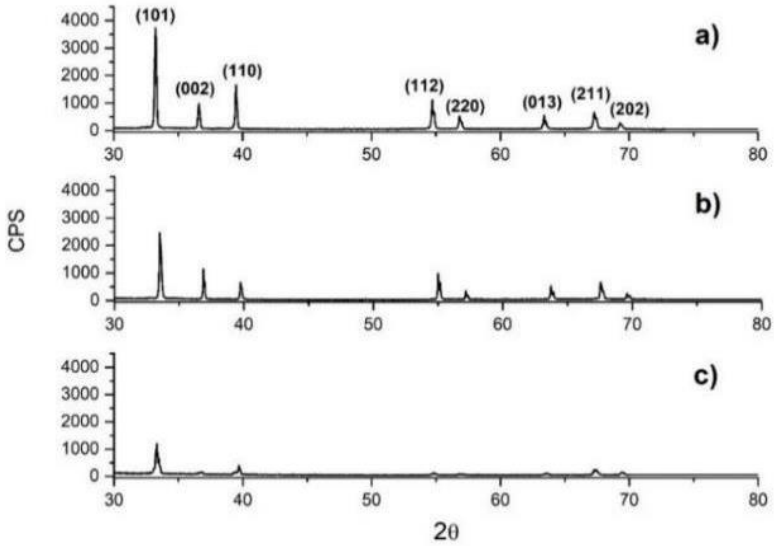

Figure 94. Diffractograms of indium electrowinning performed at different temperatures a) 25, b) 40 and c) 60 °C using an etched Ti cathode at 200 A/m² and a sulfate electrolyte containing 70 g/L In^{3+} at pH 2.3 for 22 h.

Chapter 9: **Aluminum cathode**

9.1.Introduction

The study of the indium electrowinning using aluminum as cathodic support is initially carried out considering the results from previous work [149]. In that work, the indium electrowinning was performed using the Al cathode and an electrolyte containing 140 g/L $In_2(SO_4)_3$, 5 g/L H_3BO_3, 20 g/L $Al_2(SO_4)_3$ and 30 g/L Na_2SO_4, pH 2.3, 25 A/m^2 and 40 °C. From those results, Al support was suggested not to be a suitable metal to run the electrowinning process. However, considering the kinetic analysis, the absence of hydrogen evolution reaction in a wide potential range and their electrochemical responses could be capitalized in the indium electrowinning at different operative conditions. Therefore, this chapter is focused on optimizing the indium electrowinning using the Al cathode at different conditions (CD, electrolyte composition, temperature and pH). Also, the effect of the etched cathodic surface is part of the analysis to improve electrowinning outputs. The obtained deposits of indium were also evaluated using morphological and crystallographic assessments.

9.2.Current density effect on the indium electrowinning

Figure 95 illustrates cell voltage, CE and SEC changes varying the CD in a range between 50 and 200 A/m^2 using a sulfate electrolyte containing only 70 In^{3+} g/L at 40 °C and pH 2.3. High CE outputs can be obtained at low CD values around 100% below 80 A/m^2. However, the CD value at 100 A/m^2 achieves a significant CE of around 87%. This result shows that the Al cathode can work at 100 A/m^2. Once CD is adjusted at higher CD than 100 A/m^2, CE falls drastically below 50 %. This scenario suggests that at CDs higher than 100 A/m^2, progressive HER can hinder the indium electrowinning.

At the same operative conditions, increasing CD implies a progressive cathodic polarization that produces a competing state between indium and hydrogen reduction. Although the indium reduction is the preferential reaction at low CD values, hydrogen reduction increasingly occurs as CD increases. This rection is notoriously perceived after 100 A/m^2 with abundant bubble formation. Regarding cell voltage and SEC, both parameters rocket after 100 A/m^2. In the beginning, cell voltage and SEC are around 2.3 V and 1.6 kWh/kg; nevertheless, they exceed significantly those starting values showing a maximum of about 3.3 V and 5.3 kWh/kg at 200 A/m^2 for cell voltage and SEC, respectively.

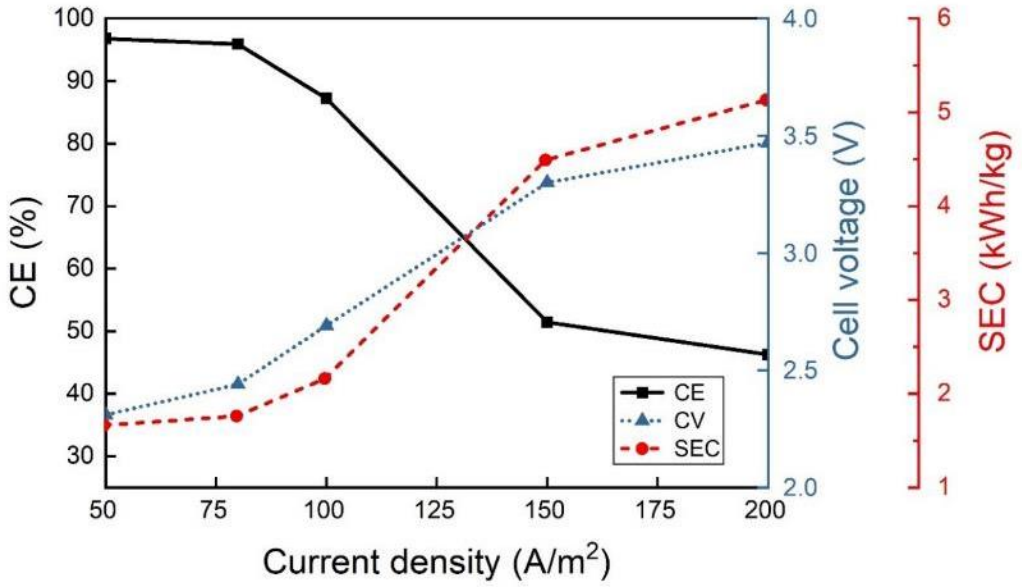

Figure 95. Analysis of CE, cell voltage and SEC of the indium electrowinning varying CD from 50 to 200 A/m² using a sulfate electrolyte containing 70 g/L In^{3+} at 40 °C and pH 2.3.

9.3.Effect of boric acid and sodium sulfate

Considering the electrolyte composition, boric acid and sodium sulfate have been used to investigate their effect on indium electrowinning. In previous results, the CD change indicated that a remarkable performance was achieved working with aluminum as metal support at 100 A/m². Based on those findings, boric acid and sodium sulfate were considered to improve the indium electrowinning process at 150 A/m². Figure 96 shows the boric acid influence (concentration range between 0 and 40 g/L) on cell voltage, CE and SEC maintaining unchanged operative conditions such as the sulfate electrolyte containing 70 g/L In^{3+}, CD at 150 A/m², 40 °C and pH 2.3. The boric acid hinders the electrowinning process when CE decreases from around 52% to 39%. Although in this experimental array, cell voltage varies slightly, suggesting an average value around 3.3 V, while a different behavior is observed for SEC. As boric acid concentration increases, SEC raises from around 4.5 kWh/kg at 0 g/L H_3BO_3 to 6.1 kWh/kg at 40 g/L H_3BO_3.

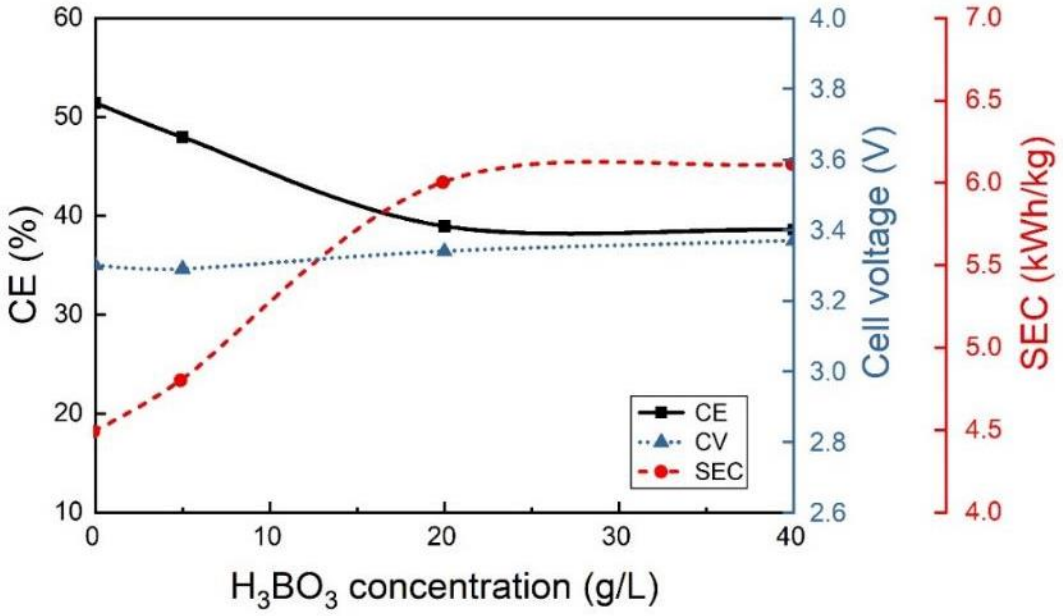

Figure 96. Influence of different boric acid concentrations on CE, cell voltage and SEC at 150 A/m², 40 °C and pH 2.3.

On the other hand, sodium sulfate is varied from 0 to 30 g/L in an independent assay maintaining the other operative conditions (Figure 97). The rise of sodium sulfate shows a comparative effect to the boric acid one. This behavior means a detrimental influence of CE decreasing to 39% at 40 g/L Na_2SO_4. A comparable trend was also depicted by SEC rising from 4.4 to 6.9 kWh/kg at 0 g/L and 30 g/L Na_2SO_4, respectively. CE and SEC outputs were not improved by integrating both boric acid and sodium sulfate into the electrolyte. Therefore, modifying the sulfate electrolyte seems not to have a markable effect when the Al cathode is used as cathodic support. Accordingly, another strategy was proposed to work at 150 A/m² and achieve high CE and low SEC values.

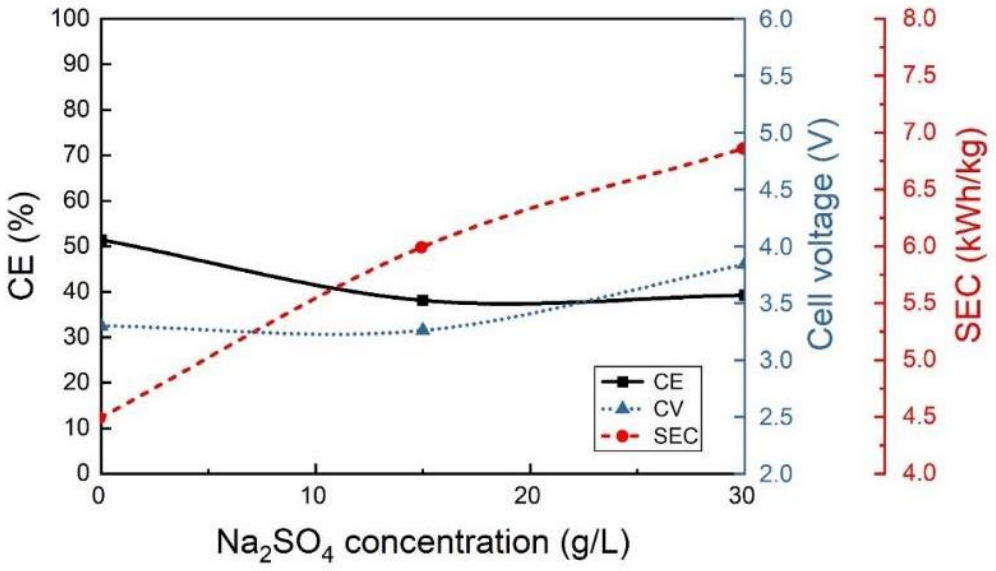

Figure 97. Influence of different sodium sulfate concentrations on CE, cell voltage and SEC at 150 A/m², 40 °C and pH 2.3.

9.4. Surface pretreatment of aluminum cathode

Another strategy to achieve a good relationship between CD and SEC was to modify the cathodic surface. The cathodic surface of aluminum was undergone etching pretreatment with 1 M HF. When Al cathode is used as cathodic support in the indium electrowinning, deposits suffer a swelling phenomenon at high CDs similar to that observed on the Ti cathode. Therefore, the etching pretreatment is proposed to eliminate residues from the surface (oxides, oils and dirt) and consequently increase the roughness and deposit-surface adherence. The swelling phenomenon has been attributed to internal stress of the deposit and the absence of adhesion conditions on the metal surface. At the beginning of the process, indium layers are formed on the cathodic surface when nucleation occurs. At this point, no swelling is present on the metal deposit. However, the indium deposit swells as the electrowinning process draws on. Since current lines are dominant on the cathode edge, it could be suggested that the stress state of the deposit starts from hereon. Clearly, adhesion conditions of the metal surface and a growing deposit exacerbate a progressive detachment of the indium metal from the cathodic surface.

If the CD increases, the hydrogen overpotential triggers, and the hydrogen evolution will make part of the process. An intense gas layer forms on the surface at high CDs, accelerating this physical removal. In literature, some works suggest that low adhesion conditions, internal stress and operative conditions can cause and accelerate the detachment [214].

Based on these findings, the etching pretreatment with HF remove residues from the surface, consequently increasing roughness and deposit-surface adherence. Figure 98 highlights the macrostructural change of indium deposit at 100, 150 and 200 A/m^2 without (a-c) and with (d-f) etching pretreatment. Figure 98a-c shows an evident swelling on deposits being much more intense as CD increases. As aforesaid, it seems that deposits are well attached to the cathodic edge, which is reasonable due to the intense current lines from the anodic surface. The swelling is almost negligible once the etching is performed on the Al cathode (Figure 99d-f). This change suggests that HF cleans the cathodic surface, improving the physical contact between the deposit and the metal surface. Then, since the swelling phenomenon can be hindered even at 200 A/m^2 (Figure 98c-f), this pretreatment was integrated into the electrowinning process to reach CE, SEC improvements using CD values higher than 80 A/m^2.

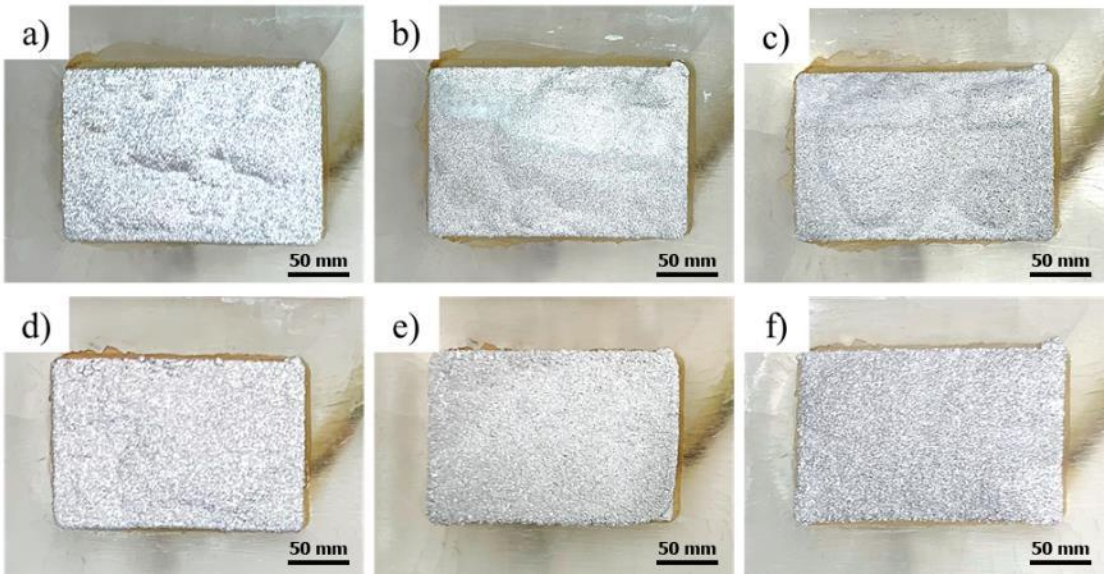

Figure 98. Comparative analysis of indium deposits obtained at 100, 150 and 200 A/m^2 considering the cathodic surface of aluminum (a-c) without and (d-f) with 1M HF etching pretreatment at 40 °C and pH 2.3. The sulfate electrolyte was composed of 70 In^{3+} g/L.

Figure 99 shows the indium electrowinning process varying the CD from 100 to 200 A/m^2 at 40 °C and pH 2.3. This assessment used a sulfate electrolyte containing only 70 In^{3+} g/L and a cathodic surface etched by 1M HF. Comparing results from Figure 95, it is possible to establish that a reasonable CE and SEC can be obtained at 100 A/m^2 without the fluoric acid pretreatment. Once CD increases, those values drop. If the aluminum cathodic surface is etched with 1M HF, CE and SEC can be improved working at 100 and 150 A/m^2. The former CD is increased from 87% to 92% CE, while the latter CD is rose from around 46% to 87% CE (Figure 99). In terms of SEC obtained with and without etching, a remarkable decrease of SEC is observed at 150 A/m^2 with the etched Al

cathode, consuming almost twice less (2.72 kWh/kg) than the process without the cathodic pretreatment. The increase of cell voltage without and with etching pretreatment can be seen in Figure 95 and Figure 99, respectively. The overpotential cell increase is expected when the CD increases. Regardless of the etching pretreatment, high CDs unavoidably will promote high overpotentials and the parasitic HER.

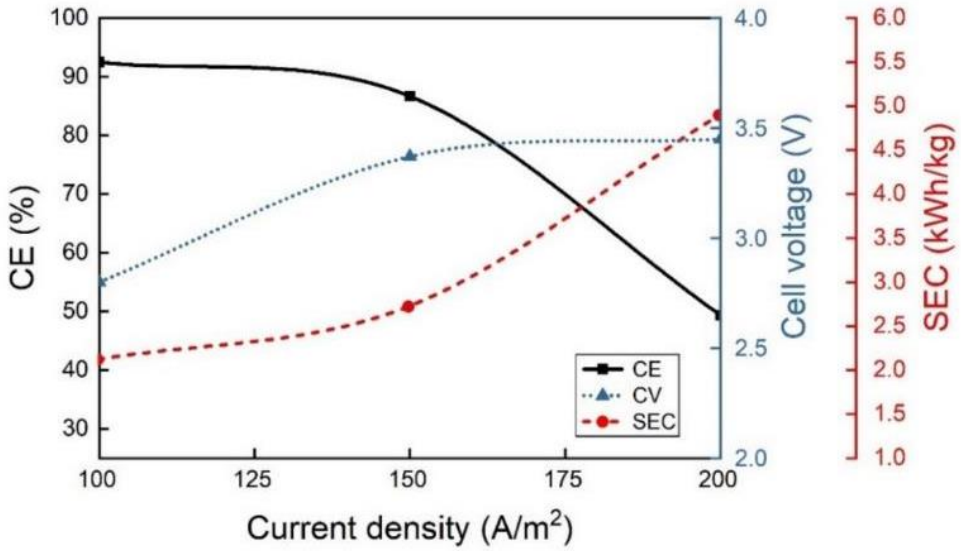

Figure 99. Influence of CD between 100 and 200 A/m² on the indium electrowinning process at 40 °C, pH 2.3 and the etched Ti support.

Further assessments were proposed to evaluate if the electrolyte composition could still influence the performance of the indium electrowinning using the etched cathode. Table 15 shows the independent effect of 40 g/L H_3BO_3 and 30 g/L Na_2SO_4 on cell voltage, CE and SEC at 40 °C and pH 2.3 using the etched Ti cathode. Even at the optimized conditions, those additives negatively affect both CE and SEC. Although cell voltage keeps on average unchanged, the best condition for carrying out the indium electrowinning at 150 A/m² remains under the following conditions: sulfate electrolyte containing 70 g/L In^{3+}, etching pretreatment on the Al cathode, 40 °C and pH 2.3.

Table 15. Effect of boric acid and sodium sulfate on CE, cell voltage and SEC at 40 °C, pH 2.3 and 150 A/m². The etched Ti support was used.

H_3BO_3 (g/L)	Na_2SO_4 (g/L)	Cell voltage (V)	CE (%)	SEC (kWh/kg)
0	0	3.37	86.66	2.72
40	0	3.35	34.69	6.76
0	30	3.38	49.18	4.81

9.5. Effect of pH and temperature

Table 16 shows the pH effect using an electrolyte containing only indium sulfate at 40 °C, pH 2.3 and the pretreated cathode. The electrolyte was tested using different pH values (1.5, 2.3 and 2.7). The maximum pH value was defined at 2.7 based on the thermodynamically potential-pH diagram for indium and water system at 25 °C (Figure 33). The best outputs can be achieved at pH 2.3, confirming the previous results obtained. At low pH values, the solution is very acidic, favoring much more the hydrogen discharge reaction than the indium one. At pH values higher than 2.7, the formation of indium hydroxides is very likely since pH is locally increased near the cathodic surface. Although the anodic half-reaction produces H^+ ions and decreases the pH electrolyte during the entire test duration, hydroxides formation can occur at the first stages of the process, destabilizing the electrolyte in indium species and increasing the overpotential cell. This hydroxide formation, anyway, decreases the CE and increases the SEC (Table 16).

Table 16. Effect of pH variation on CE, cell voltage and SEC using a sulfate electrolyte containing 70 In^{3+} g/L at 40 °C, 2.3 pH, and 150 A/m^2 CD. The etched Ti support was used.

pH	Cell voltage (V)	CE (%)	SEC (kWh/kg)
1.5	3.34	27.76	8.40
2.3	3.37	86.66	2.72
2.7	3.33	55.26	4.23

Considering the influence of temperature (25 and 40 °C) and CD (150 and 200 A/m^2) and a pretreated cathode, the variation of cell voltage, CE and SEC can be seen observed in Figure 100. It could be acceptable to assume that temperature decreases the cell voltage, as it increases. One of the most reasonable explanations is that overpotential cell diminishes (mainly resistance and activation overpotential). Furthermore, the temperature increase modifies the electrolyte conductivity. Although temperature influences the ions' mobility in the solution, it is observed that the indium reduction reaction occurs more preferentially than the HER. In that way, increasing temperature improved both CE and SEC values. Now, concerning the experimental results, the best CE highlights at 150 A/m^2 and 40 °C closer to 87% CE, while using other temperature and CD values, CE reaches hardly values around 63%. Thus, maintaining the unchanged temperature at 40 °C, the indium electrowinning should be carried out at 150 A/m^2 CD, while working at room temperature, both CE and SEC reach lower values.

More in detail, at 150 A/m^2, the CE reaches 56% at 25 °C, while is around 87% CE at 40 °C. In contrast, at room temperature, SEC values are about 4.6 kWh/kg, decreasing

significantly near 2.7 kWh/kg at 40 °C. In the case of 200 A/m² CD, the productivity decreases as temperature increases. To sum up, it is evident that the temperature increases diminish the overpotential at the metal support. The beneficial effect is very significant at 150 A/m2, suggesting that the indium electrowinning using the Al cathode should be carried out at 40 °C.

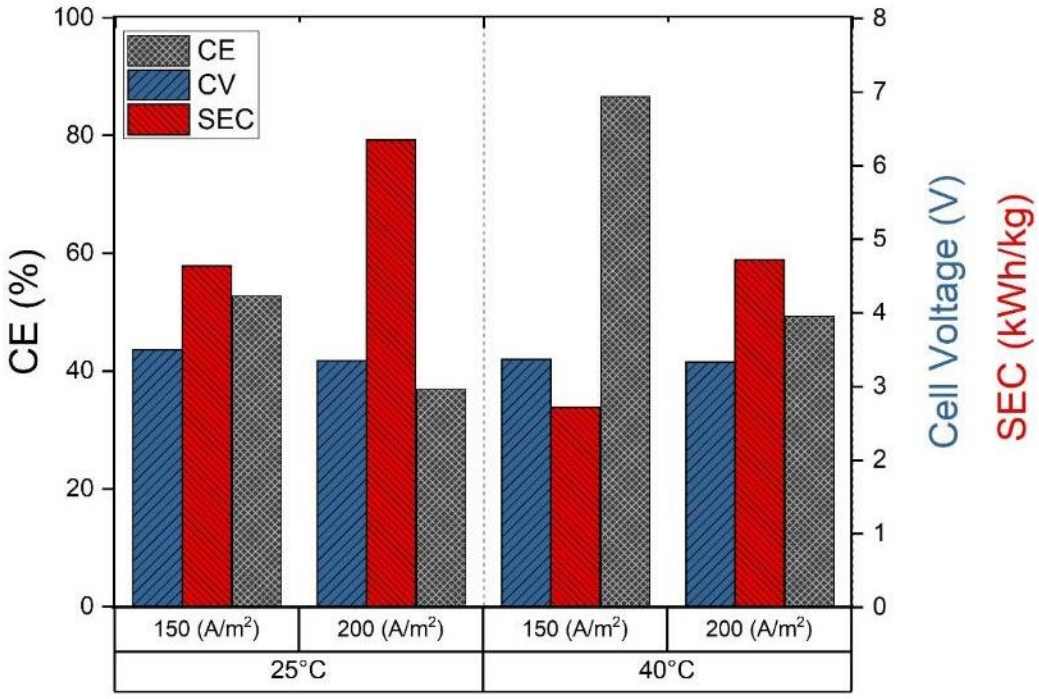

Figure 100. Influence of temperature (25 and 40 °C) and CD (150 and 200 A/m²) using a pretreated Al cathode on the CE, cell voltage, SEC within a sulfate electrolyte containing 70 g/L In^{3+} at pH 2.3.

9.6. SEM analysis of indium deposits obtained on the aluminum cathode

Figure 101 shows SEM micrographs at low and high magnifications of indium deposits obtained at different CDs (50, 100, 150 and 200 A/m²) and 40 °C and pH 2.3 using a sulfate electrolyte containing 70 In^{3+} g/L. At low magnification, micrographs at 50 and 100 A/m² show a similar morphology (Figure 101a-b), While CD increases at 150 and 200 A/m² grains are more prominent and well-defined (Figure 101c-d). Further, micrographs reveal notable features with different CDs. For instance, nucleation seeds are well distributed on the whole surface of the indium deposit at 50 A/m² (Figure 101 e). Elongated nucleation seeds that grow at the grain boundary can be seen (Figure 101e). Moreover, lamellar structures and well-defined polygonal microstructures are shown in Figure 101g-h, respectively.

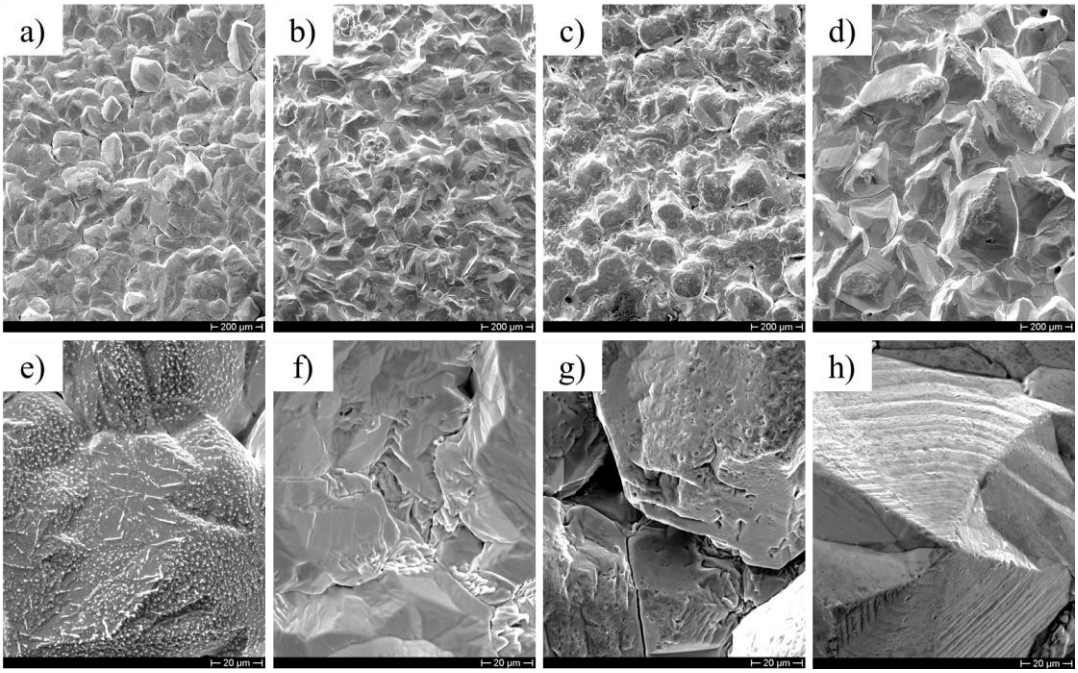

Figure 101. SEM micrographs for indium deposits using different CDs: a-e) 50, b-f) 100, c-g) 150 and d-h) 200 A/m² at 40 °C and pH 2.3 using a sulfate electrolyte containing 70 g/L In^{3+}.

The influence of the different concentrations of boric acid (0, 20 and 40 g/L) into the sulfate electrolyte can be seen in Figure 102. The boric acid absence shows an irregular morphology, as was above mentioned. The boric acid addition generates similar morphologies featured by grains with very well-defined polygonal shapes (Figure 102b-c). Further, it is possible to observe a step-growth (Figure 102e) and a well-defined polygonal microstructure (Figure 102c).

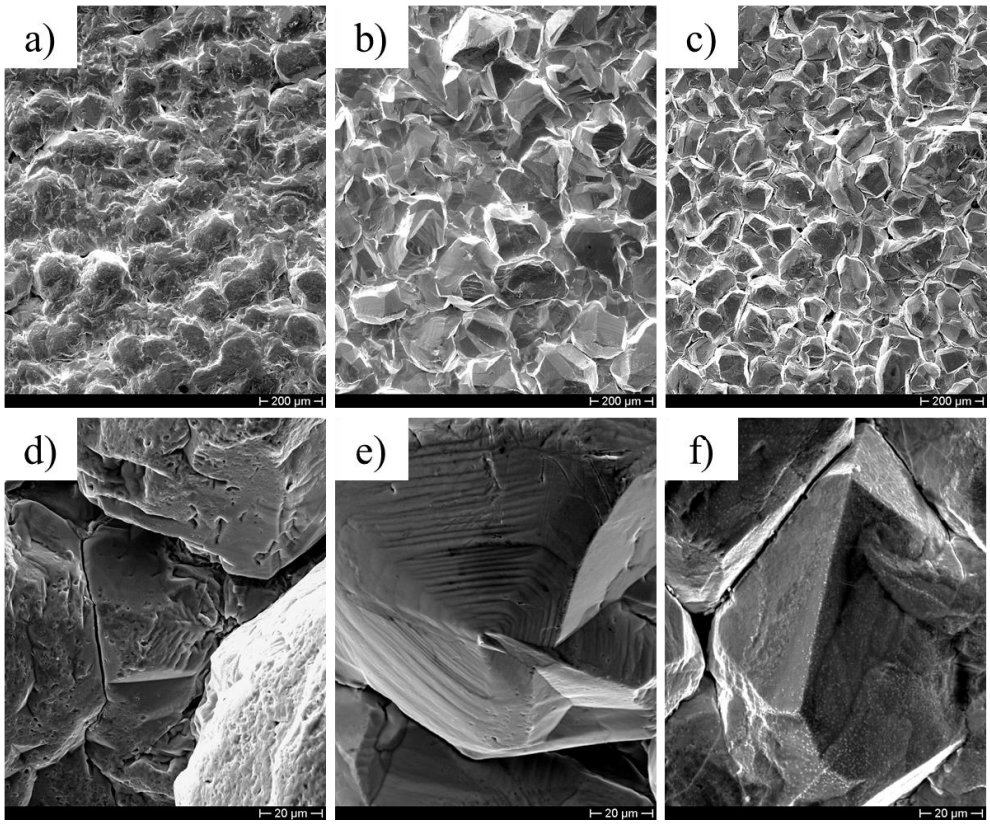

Figure 102. SEM micrographs for indium deposits obtained at 150 A/m², pH 2.3, temperature at 40 °C and deposition time of 22 h varying the boric acid concentration (0, 20, 40 g/L) in a sulfate electrolyte containing 70 g/L In^{3+}.

The indium morphologies obtained varying the sodium sulfate concentration were observed in Figure 103. Without sodium sulfate, a like-flattened morphology is marked with some irregular growths of small grains. But at 15 g/L Na_2SO_4, grains show an irregular morphology with a grain size close to 200 µm. The deposit aspect is much more irregular at 30 g/L Na_2SO_4 (Figure 103c). The sodium sulfate addition produces very-well defined polygonal grains (Figure 103e-f).

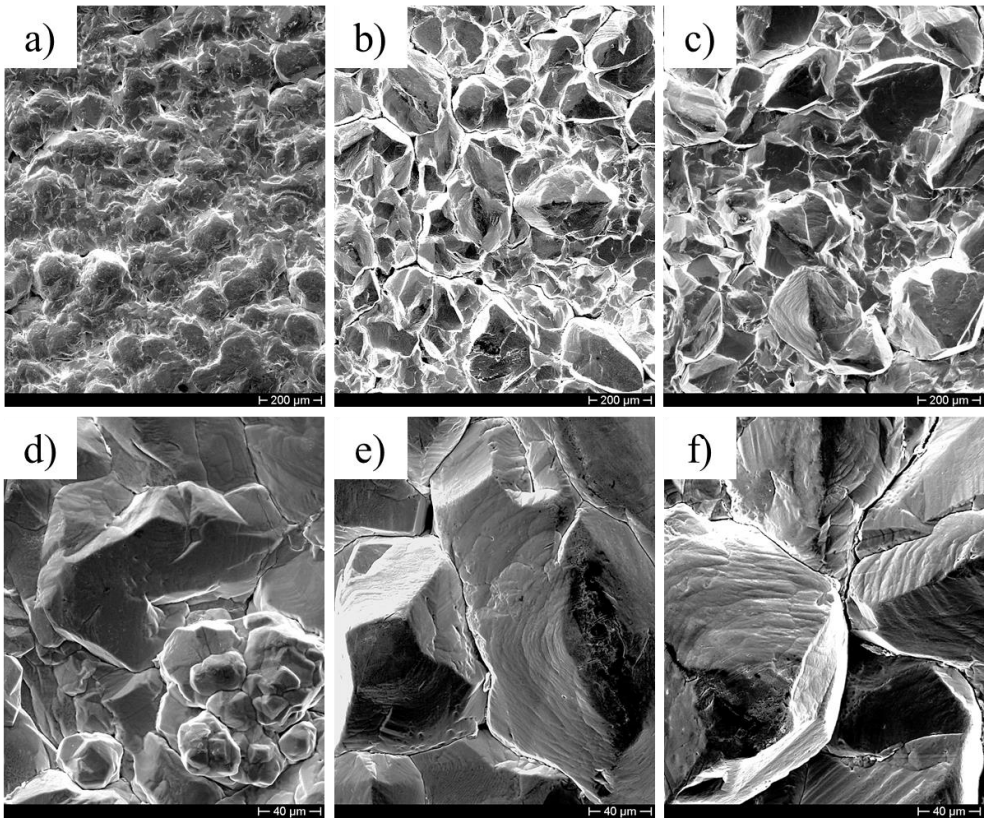

Figure 103. SEM micrographs for indium deposits obtained at 150 A/m², pH 2.3, temperature at 40 °C and deposition time of 22 h varying the sodium sulfate concentration (0, 15, 30 g/L) in a sulfate electrolyte containing 70 g/L In^{3+}.

Figure 104 shows SEM micrographs of indium deposits obtained at different CDs between 100 and 200 A/m² using an etching pretreatment on the cathodic surface at 40 °C and pH 2.3. The indium electrowinning was performed on the etched Al cathode; otherwise, deposits remain hardly attached to the metal surface. Then, the etching improved the roughness of the Al cathode to increase the adhesion between the indium deposit and the cathodic surface. This pretreatment lessened the swelling phenomenon, allowing the Al cathode to work efficiently at CDs lower or equal to 150 A/m².

In the morphology case, the microstructure suffers changes regarding the grain shape (Figure 104a-c). A compact and flattened microstructure is observed at 100 and 150 A/m². Nonetheless, when the CD is fixed at 200 A/m², the morphology is more affected by HER. Thus, the etching treatment improves the adhesion between deposit and surface, but round holes can appear at high CDs. Those holes are easily observed at high magnifications (Figure 104e-f).

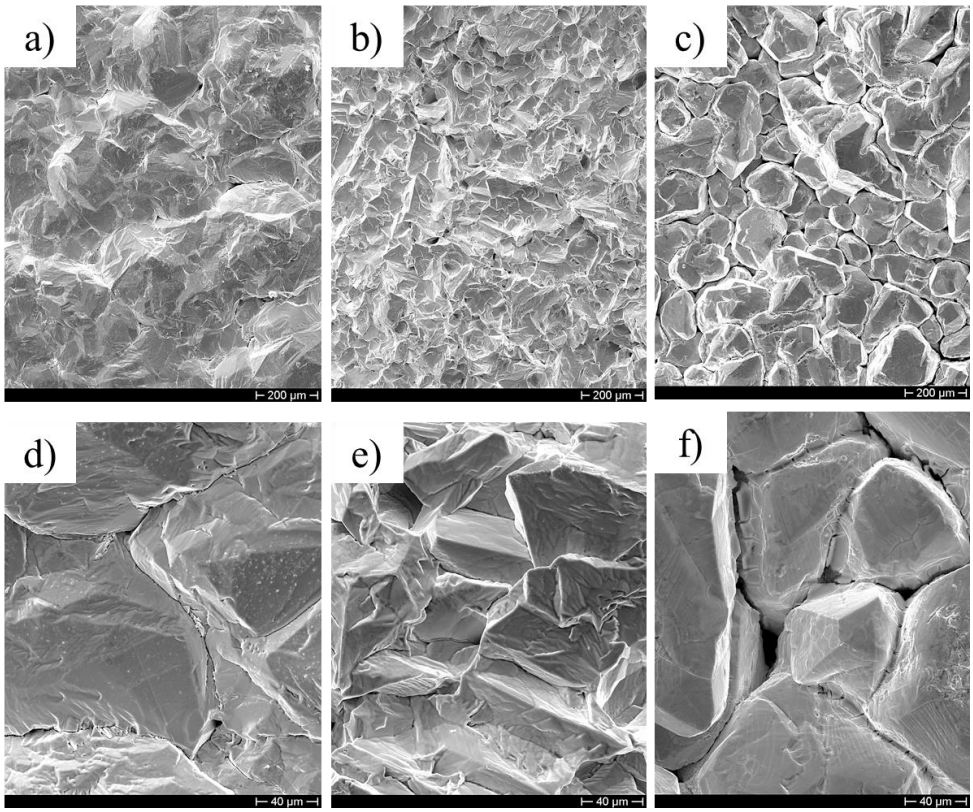

Figure 104. SEM micrographs for indium deposits obtained at different CDs (100, 150 and 200 A/m^2), pH 2.3, temperature at 40 °C and deposition time of 22 h in a sulfate electrolyte containing 70 g/L In^{3+}. It was used the etched cathodic surface.

The indium electrowinning process was conducted at 200 A/m2 using two temperatures (25 and 40 °C). The cathodic surface was etched by using 1 M HF for 30 s. At room temperature and 40 °C, the morphology of indium deposits is very similar with well-defined polygonal grains (Figure 105a-b). At higher magnifications, that observation can be confirmed, but also it is possible to mention a random distribution (Figure 105c-d). Comparing the grain size of indium deposits at different temperatures show that those obtained at 40 °C are slightly larger than those obtained at room temperature.

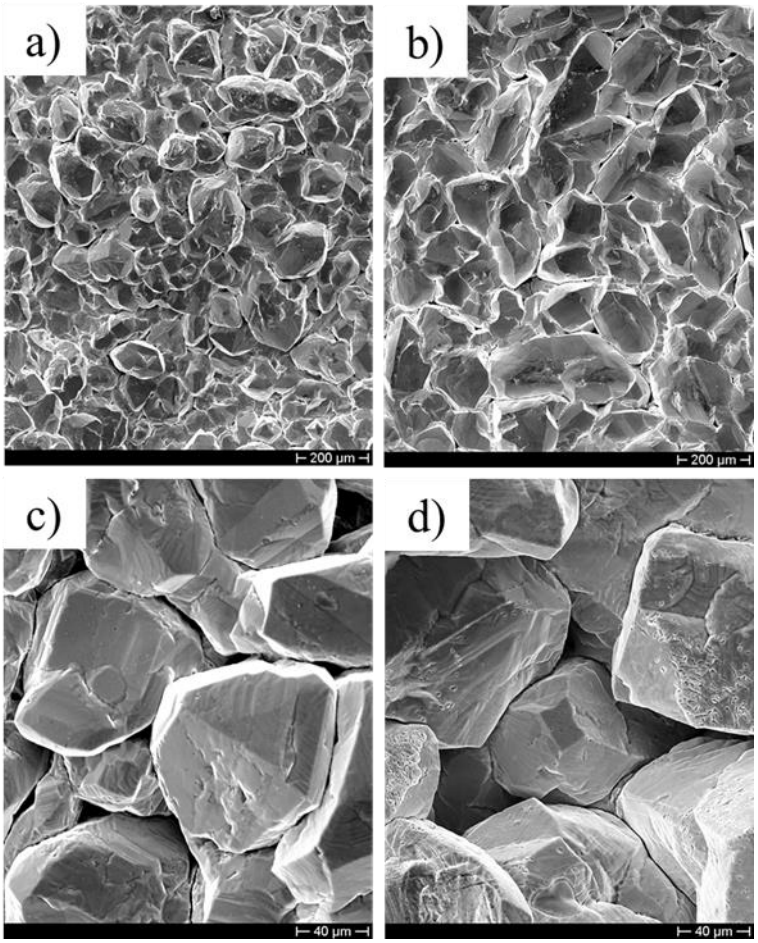

Figure 105. SEM micrographs for indium deposits obtained at different temperatures (25 and 40 °C), 200 A/m², pH 2.3 and deposition time of 22 h into a sulfate electrolyte containing 70 g/L In^{3+}. It was used the etched cathodic surface.

9.7. XRD analysis of indium deposits obtained on the aluminum cathode

The best electrowinning outputs were achieved at 150 A/m² CD. The effect of supporting additives (boric acid and sodium sulfate) on the deposit crystallinity was analyzed. Three main peaks before 45° (2θ) and secondary peaks with lower intensity after that angle can be seen in diffractograms of the indium deposits. Figure 106 depicts XRD patterns for indium deposits obtained from a sulfate electrolyte with 70 In^{3+} g/L and several boric acid concentrations (0, 20 and 40 g/L) at 40 °C and pH 2.3. Working at 150 A/m² and using different concentrations of boric acid, the preferential orientation in each XRD pattern is held at the (101) peak. Both (002) and (110) peaks progressively increase as boric acid increases. In the case of secondary peaks, it is observed that boric acid shows insignificant changes.

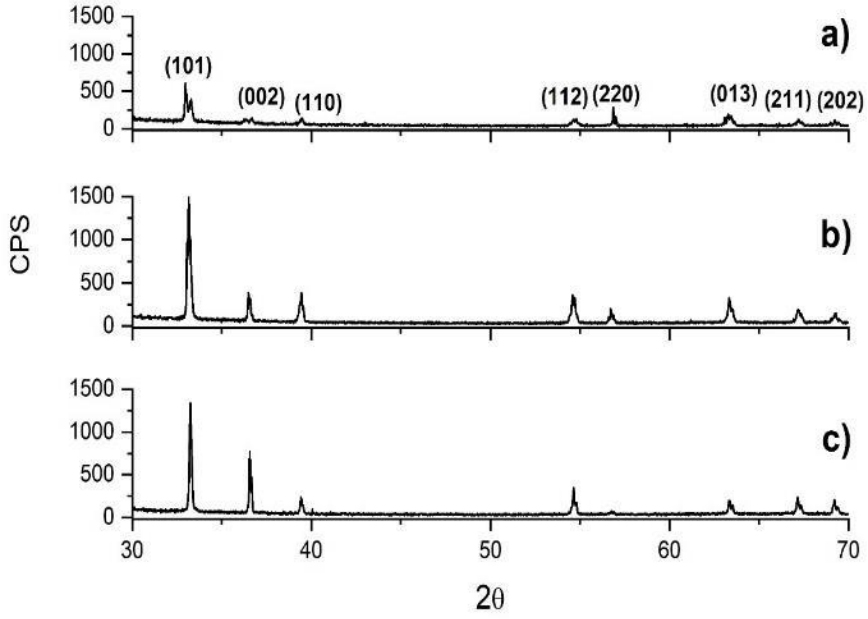

Figure 106. XRD pattern of indium deposits obtained using a sulfate solution containing 70 g/L In^{3+}, 150 A/m², 40 °C and pH 2.3 for a length of 22 h. The different concentrations of boric acid were a) 0, b) 20 and c) 40 g/L.

When different concentrations of sodium sulfate (0, 15 and 30 g/L) are added into the sulfate electrolyte (70 In^{3+} g/L), a growth of (002) and (110) peak is observed (Figure 107). It seems that sodium sulfate can increase the patterns' intensity. However, beyond the secondary (013) peak, the sodium sulfate addition shows no significant changes in the crystallinity.

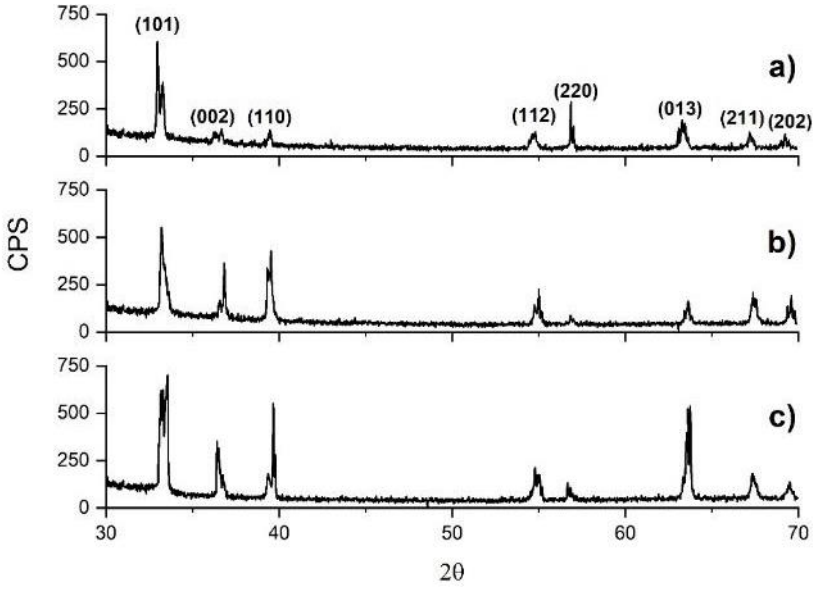

Figure 107. XRD pattern of indium deposits obtained using a sulfate solution containing 70 g/L In^{3+}, 150 A/m², 40 °C and pH 2.3 for a length of 22 h. The different concentrations of sodium sulfate were a) 0, b) 15, and c) 30 g/L.

In Figure 108 A, diffractograms obtained using different CDs (100, 150, and 200 A/m^2), with electrolyte containing 70 g/L In^{3+}, not etched surface, at 40 °C and pH 2.3 are shown. By increasing CD from 100 to 200 A/m^2, it is observed that the preferential orientation is the (101) peak. Particularly, at 100 A/m^2 CD, the (101) and (110) peak highlight, while both (002) and (110) peaks disappear at 150 A/m^2 CD. In the case of 200 A/m^2 CD, three main peaks are visible. Further, secondary peaks also show a random change. In addition, an increase in the height of secondary peaks at 100 A/m^2 can be identified at (112), (220) and (013) peaks, while the intensity decreased is markedly observed for those at 150 A/m^2.

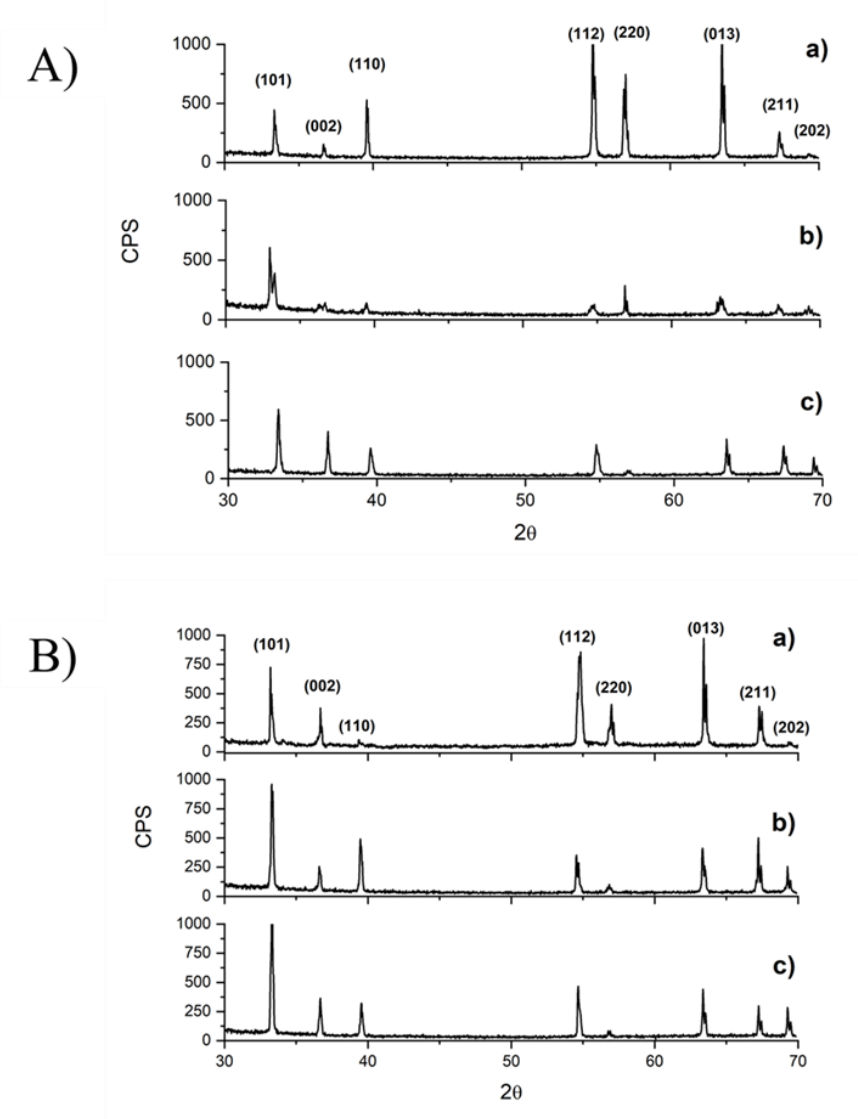

Figure 108. Diffractogram of indium deposits obtained at 70 In^{3+} g/L, pH 2.3, 40 °C for 22 h. The employed CD corresponds to a) 100, b) 150 and d) 200 A/m^2. The upper figure (A) is related to the deposits obtained from the Al cathode without etching, while the lower figure (B) is for those obtained from the Al cathode with etching.

Considering Figure 108 B, diffractograms for indium deposits obtained using an electrolyte containing 70 g/L In^{3+}, 40 °C and pH 2.3. The indium electrowinning was performed using an etched Al metal support. As CD increases, the (101) peak becomes progressively more intense, whereas those (002) and (110) peaks do not follow a specific trend. Instead, secondary peaks (after 40° (2θ)) decrease in intensity when CD reaches 150 and 200 A/m². In comparison, the etching pretreatment reveals an increase in the preferential orientations (101), (002) and (110), and some secondary peaks mainly at 150 A/m² (Figure 108 A and B).

It is worthwhile to mention that the best conditions for carrying out the indium electrowinning in terms of CE and SEC were determined at 150 A/m², the etched cathode and an electrolyte containing only indium sulfate. But the effect of boric acid and sodium sulfate was also tested at 40 and 30 g/L, respectively (Figure 109). The crystallinity of indium deposits changes as electrolyte composition varies. Although the boric acid does not directly influence electrowinning outputs, it increases the patterns' intensity of indium deposits. In contrast, sodium sulfate negatively affects both the process performance and the crystallographic features of the deposit.

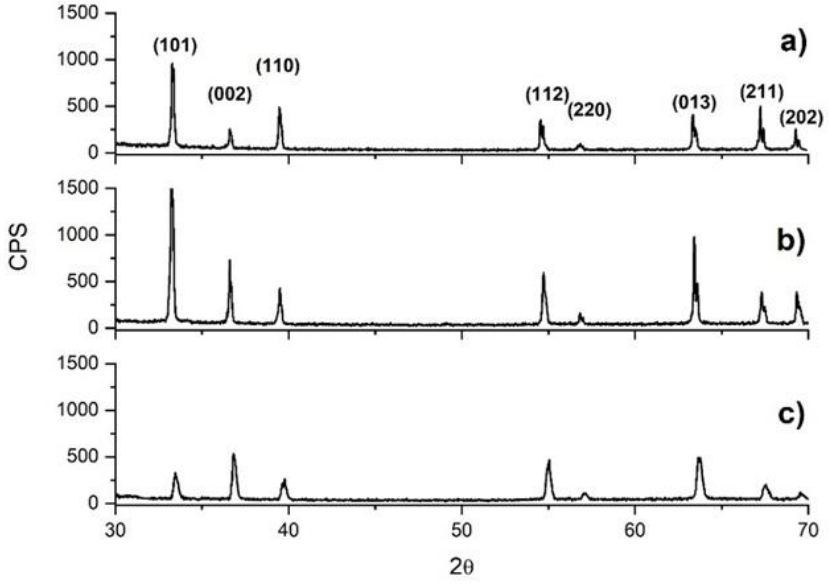

Figure 109. XRD pattern of indium deposits obtained using a sulfate solution containing 70 g/L In^{3+}, 150 A/m², 40 °C and pH 2.3 for a length of 22 h. The etched Al support and different supporting additives: a) blank, b) 40 g/L H_3BO_3 and c) 30 g/L Na_2SO_4, were utilized.

The XRD analysis for deposits obtained at different temperatures, etched cathodic surface, pH 2.3 and 40 °C can be seen in Figure 110. The increase in temperature causes a sequential decrease of XRD patterns. This intensity decrease is progressive and much more evident for the experimental condition at 60 °C. In fact, at 60 °C, the XRD pattern has small and broadened peaks. Based on these findings, it is possible to indicate that the temperature cannot alter the preferential orientation, but it changes the crystallinity of deposits.

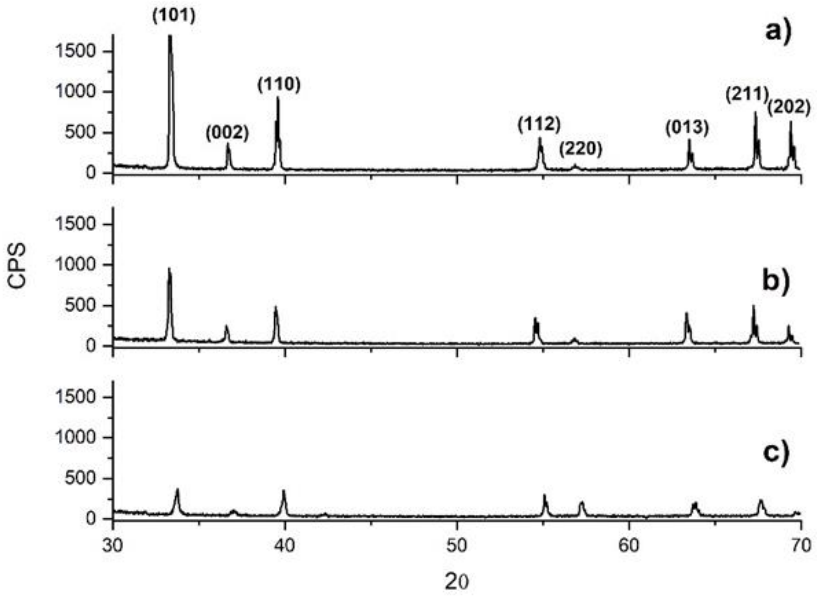

Figure 110. XRD patterns of indium deposits obtained using a sulfate solution containing 70 g/L In^{3+}, 150 A/m^2 CD and pH 2.3 for a length of 22 h. The etched Al support and different temperatures: a) 25, b) 40 and c) 60 °C, were utilized.

Chapter 10: **Comparative analysis for the electrowinning outputs performed on different metal supports varying operative conditions**

The study of operative conditions of the indium electrowinning suggests that electrolyte composition, CD, pH and temperature play a significant role in reaching the maximum efficiency and minimum energy consumption. Furthermore, it has been noted that the best operative conditions and the metal support can influence the process performance. Thus, the assessments entailed the independent analysis of different metals (AISI 316L, Cu, Ni, Ti and Al) considering the cell voltage, CE and SEC as electrowinning outputs. Such outputs were studied varying the operative conditions (CD, electrolyte composition, temperature and pH). This chapter compares the most relevant electrowinning outputs using different CD and electrolyte compositions at different metal supports.

Figure 111 shows CE values of the indium electrowinning utilizing different metal supports and electrolytes in a CD range between 25 and 200 A/m^2. The best CE values are mainly obtained at 25 A/m^2 for these five metal supports. However, working with Ni, Ti and Al cathode, it is possible to achieve CEs above 93% when CD is adjusted at 80 A/m^2. At 200 A/m^2, AISI 316L and Cu cathode achieve the lowest CE value. In the case of Al and Ti cathodes, CE values at 80 A/m^2 achieve above 90% and drop subsequently below 50% when is employed the maximum CD value (200 A/m^2) (Figure 111).

On the other hand, it is worthwhile to highlight that good results at 100 A/m^2 on Al cathode or even at 80 A/m^2 on Ti cathode suggests that the performance on these metals is slightly influenced by the electrolyte composition (supporting reagents) since their tests were carried out only with the presence of 70 g/L In^{3+}. Conversely, the electrolyte composition does affect the Ni cathode performance, which reaches around 98% at 80 A/m^2 with the assistance of boric acid, sodium and aluminum sulfate. A similar dependence is observed for AISI 316L and Cu cathode showing the maximum CE at 25 A/m^2. Therefore, optimizing operative parameters in the indium electrowinning is required to achieve a proper balance between high CE and low SEC, implying high productivity and low energy consumption.

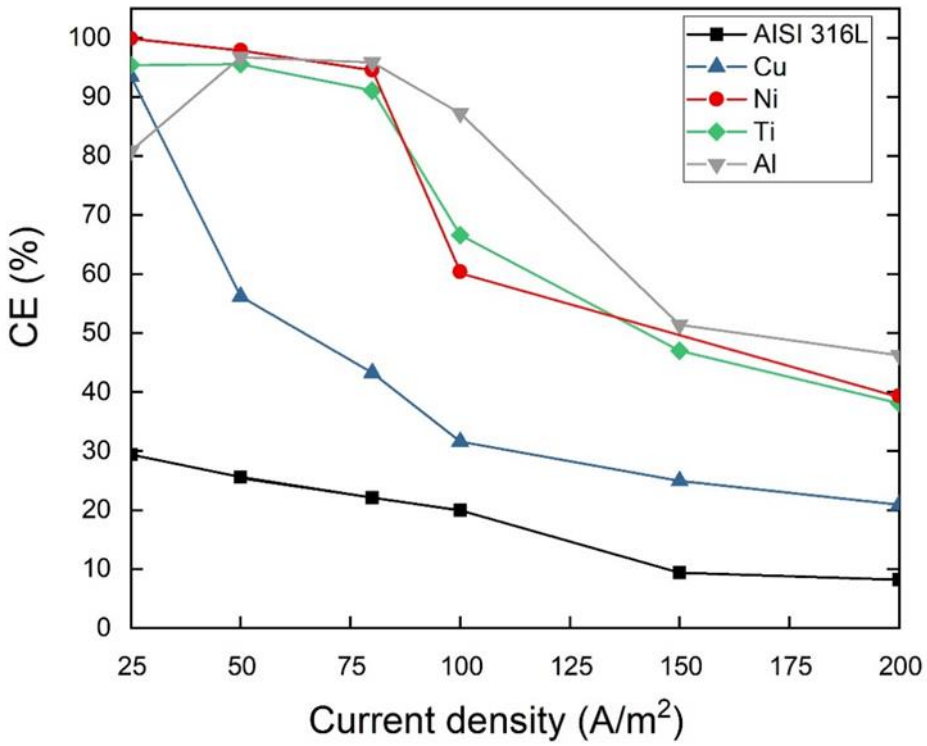

Figure 111. Variation of CE at different CD values (25, 50, 80, 100, 150 and 200 A/m²) using different metal supports (AISI 316L, Ni, Cu, Al and Ti). Initial electrolyte composition for each metal support: AISI 316L (40 g/L In^{3+}, 20 g/L H_3BO_3, 10 g/L $Al_2(SO_4)_3$, 10 g/L Na_2SO_4), Ni (70 g/L In^{3+}, 5 g/L H_3BO_3, 20 g/L $Al_2(SO_4)_3$ and 30 g/L Na_2SO_4,), Cu (70 g/L In^{3+} and 20 g/L H_3BO_3), Ti (70 In^{3+} g/L) and Al (70 g/L In^{3+}).

Prior to discussing the optimization conditions and the respective electrowinning outputs for indium recovery, it is necessary to analyze the effect of CD on SEC to enhance the relationship between productivity and energy consumption (Figure 112). Considering the AISI 316L cathode, when CD varies from 25 to 200 A/m², SEC changes from 7 to 33 kWh/kg, indicating the highest values in energy consumption. On the contrary, the other cathodes start from SEC values lower than 2.5 kWh/kg at 25 A/m², and as CD increases, the SEC grows progressively. Regarding the Cu cathode, after CD exceeds 25 A/m², SEC quickly increases, reaching around 11 kWh/kg at 200 A/m². This behavior differs from those observed on Ni, Ti and Al. Using those cathodes, SEC obtains values around or even lower than 2 kWh/kg from 25 to 80 A/m². If CD keeps increasing, in all the three cases, SEC increases gradually, maintaining the energy consumption at values lower than about 6 kWh/kg at 200 A/m². At that CD, the Al support reports the lowest SEC, showing 5.13 kWh/kg. Furthermore, it is necessary to highlight that Ni, Al and Ti work efficiently until CD equals 80 A/m², giving high CE and low SEC values. Thereby, the indium electrowinning on each metal support requires optimization, as above-mentioned, in order to work at higher CD but maintain a reasonable balance between CE and SEC outputs.

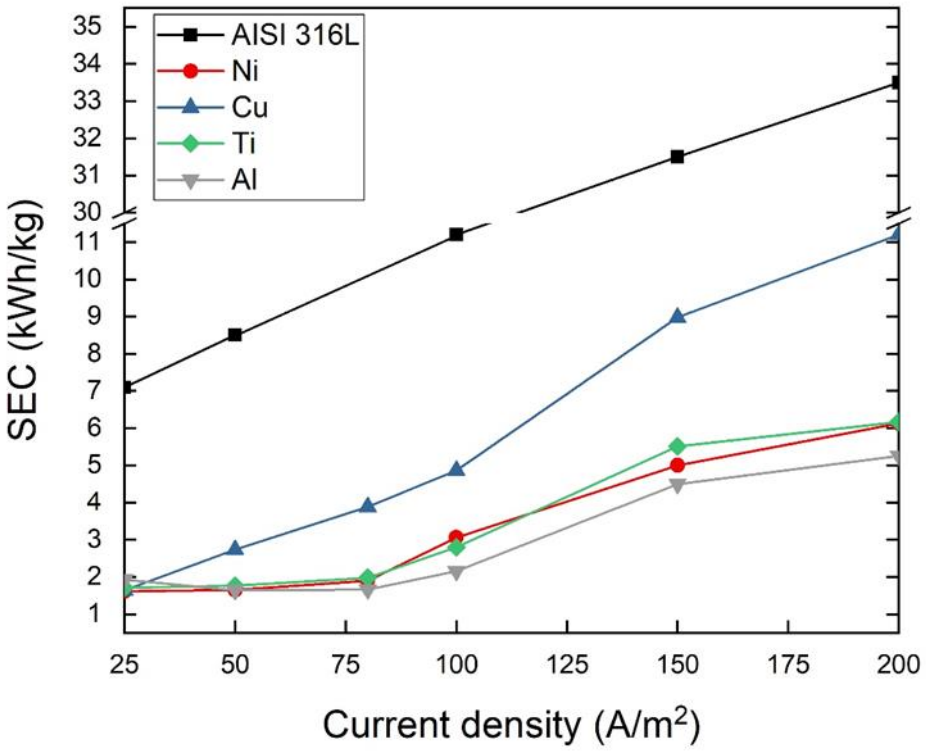

Figure 112. Variation of SEC at different CD values (25, 50, 80, 100, 150 and 200 A/m²) using different metal supports (AISI 316L, Ni, Cu, Al and Ti). Initial electrolyte content according to metal support: AISI 316L (40 g/L In^{3+}, 20 g/L H_3BO_3, 10 g/L $Al_2(SO_4)_3$, 10 g/L Na_2SO_4), Ni (70 g/L In^{3+}, 5 g/L H_3BO_3, 20 g/L $Al_2(SO_4)_3$, 30 g/L Na_2SO_4,), Cu (70 g/L In^{3+} and 20 g/L H_3BO_3), Ti (70 g/L In^{3+}) and Al (70 g/L In^{3+}).

Both SEC and the indium recovery are herein considered influencing parameters to propose cost-benefit estimations. Thus, the CD is varied to individuate the condition, where indium can be highly recovered using lower energy consumption and reasonable economic costs. Figure 113 illustrates the relationship between SEC and the indium recovery for each metal support at different CD values. These results clearly show that the indium recovery increases until a determined CD maintains a low SEC. Exceeding that CD, while SEC grows much faster than indium recovery trend indicating a higher energy consumption.

Firstly, both AISI 316L and Cu cathodes describe a significant SEC increase as CD rises. Notably, the AISI 316L cathode reaches the lowest values for indium recovery, and the SEC grows much faster than any other metal support. In the case of Cu metal, it also shows a disbalance between CE and SEC, being 25 A/m² the most appropriated CD to carry out the indium electrowinning. Secondly, Ni, Ti and Al describe attractive results (high CE and low SEC) working below 80 A/m². But the Al cathode can work at a higher CD (100 A/m²). Thus, based on the operative conditions for the indium electrowinning,

Ni, Ti and Al cathode can admit higher CD values before the electrowinning outputs sharply fall.

Concerning those previous results, metal supports strongly contribute to the indium electrowinning performance, as shown in Figure 113. Metal supports like AISI 316L and Cu suggest a higher hydrogen overpotential that only leaves to efficiently works at 25 A/m^2; once the CD increases, the hydrogen evolution reaction is progressively triggered and intensified, favoring the hydrogen discharge rather than indium reduction. On the other hand, the behavior of Ni, Ti and Al cathodes shows that hydrogen evolution is electro catalyzed only at higher CDs than 80 A/m^2. However, after 100 A/m^2, the indium electrowinning is less and less efficient, meaning the progressive predominance of HER, and consequently consuming more energy.

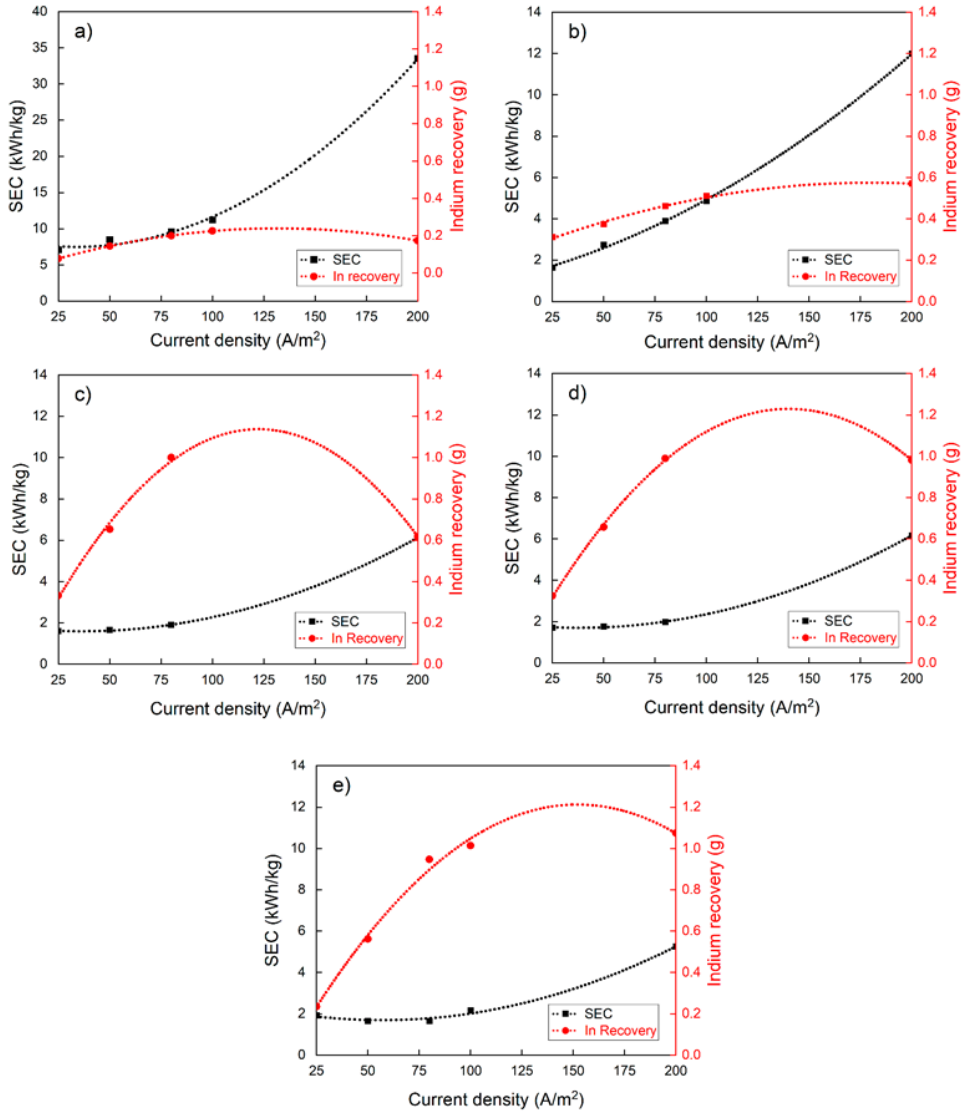

Figure 113. Comparison of SEC and the indium productivity as weight in grams with a duration of 22h for each test at different CDs using a) AISI 316L, b) Cu, c) Ni, d) Al and e) Ti supports. Electrolyte content changes according to metal support: AISI 316L (60 g/L In^{3+}, 40 g/L H_3BO_3, 20 g/L $Al_2(SO_4)_3$, 30 g/L Na_2SO_4), Cu (70 g/L In^{3+}, 20 g/L H_3BO_3), Ni (5 g/L H_3BO_3, 30 g/L Na_2SO_4, 20 g/L $Al_2(SO_4)_3$), Ti (70 g/L In^{3+}) and Al (70 g/L In^{3+}).

Apart from productivity, CE and SEC, an economic analysis regarding the energetic cost is carried out to evaluate what metal presents the best profits. In Figure 114, an economic analysis of the energy cost vs different CDs is shown using AISI 316L, Cu, Ni, Ti and Al as metal cathodes and the initial operative conditions for each one. Based on those results, the energetic cost shows that Al support exhibits a minimum cost visibly formed at 80 A/m^2, whereas Ti and Ni indicate their minimum costs at lower CDs (Figure 114a). The minimum cost to carry out the indium electrowinning using AISI 316L and Cu cathodes is observed at 25 A/m^2. As more CD is applied, the indium electrowinning using those cathodes is more costly (Figure 114b). To sum up, the CD increase implies that the electrowinning process is more expensive and economically unaffordable. Therefore, the best scenario is represented by the high CE, low SEC, where this balance means reasonable energy costs.

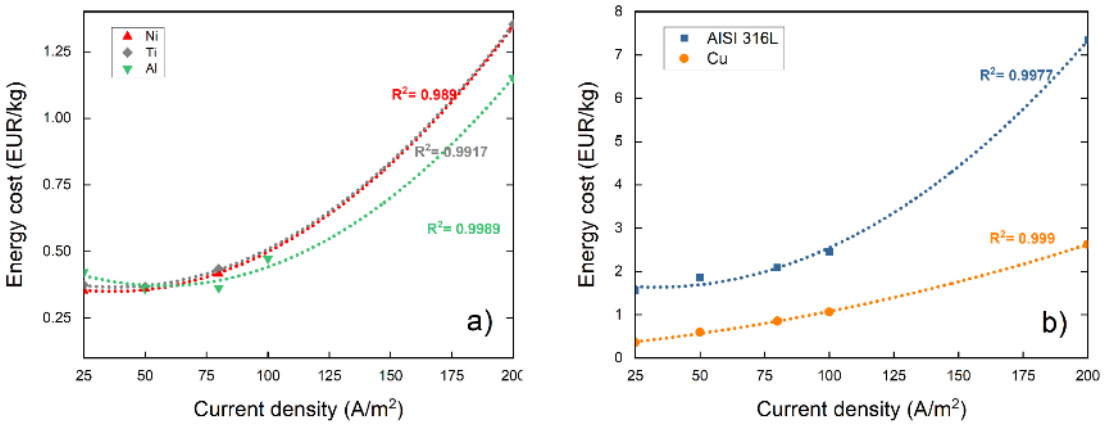

Figure 114. Mathematical representation of the energy cost for indium production via electrowinning at different CD and metal supports: a) Ni, Ti and Al, and b) AISI 316L and Cu cathodes. The balance was carried out by following the energy price for the European Union in the first half of 2021 [216].

An empirical equation for each metal cathode is observed in Eq. 20-24, where *y* represents the energy cost in EUR/kg and *x* the CD (A/m^2). Further, results for both Ni and Ti cathodes at 100 A/m^2 were not considered in the analysis due to the lack of fit. This misfit is caused by the intense HER that hinders the indium electrowinning.

$$y = 2.1 \cdot 10^{-4}x^2 - 1.1 \cdot 10^{-2}x + 1.87 \quad (20)$$

$$y = 3.5 \cdot 10^{-5}x^2 + 5.0 \cdot 10^{-3}x + 0.23 \quad (21)$$

$$y = 3.7 \cdot 10^{-5}x^2 - 2.7 \cdot 10^{-3}x + 0.40 \quad (22)$$

$$y = 3.7 \cdot 10^{-5}x^2 - 2.8 \cdot 10^{-3}x + 0.43 \quad (23)$$

$$y = 3.8 \cdot 10^{-5}x^2 - 4.3 \cdot 10^{-3}x + 0.50 \quad (24)$$

Furthermore, according to the electro-recovery literature, the minimum points in Figure 114, where indium recovery and energy consumption are efficiently balanced, are recognized as the theoretical place to undertake an affordable indium electrowinning process. However, those theoretical points should be optimized for each cathode to work at the highest possible CD. In Table 17, it can be seen the CE and SEC values obtained from optimized operative conditions (CD, temperature, pH and electrolyte composition) in each cathodic support. Moreover, it is important to highlight that operative conditions and their results analyzed in Figure 111 and Figure 112 can be improved to achieve better CE and SEC outputs.

Initially, focusing on the indium electrowinning outputs for AISI 316L, Cu and Ni cathodes, CE reaches values in each case similar or greater than 80%, preparing the electrolyte with boric acid, sodium sulfate, or aluminum sulfate. This improvement is achieved since those salts work like supporting agents, enhancing the working conditions for the indium electrowinning. In consequence, a proper electrolyte has demonstrated, in this investigation, the capacity of decreasing resistive phenomena. These conditions improve CE values due to the overpotential lessening. Thus, Cu and Ni supports can work at CDs higher than those reported in Figure 111. Furthermore, this means that it is possible to work at 50 A/m^2 obtaining around 80% CE, in the case of the former cathode, while the latter reaches 84% CE at 100 A/m^2. Both Cu and Ni cathodes achieved those outputs using in both cases an electrolyte containing 70 g/L In^{3+}, 40 g/L H_3BO_3 and 30 g/L Na_2SO_4. Otherwise, using AISI 316L as metal support, it is only possible to work at 25 A/m^2, reaching more than 90% CE if electrolyte contains 60 g/L In^{3+}, 20 g/L H_3BO_3, 20 g/L $Al_2(SO_4)_3$ and 30 g/L Na_2SO_4.

Concerning Ti and Al cathodes, improvements in CE and SEC are achieved after the cathodic surface is undergone the etching pretreatment with 1M HF. This etching pretreatment reaches CE values around 86% with electrolytes containing only indium sulfate at a CD equal to 150 A/m^2. Nevertheless, the indium electrowinning on the Ti cathode requires maintaining the temperature at 60 °C. Unlike the other three metal supports, Ti and Al do not show dependence on supporting agents; instead, they negatively affect the electrowinning outputs. In short, based on the optimized results, these two cathodic supports can be considered metal supports with the best indium electrowinning performance.

Table 17. Optimized operative conditions for each metal support in the indium electrowinning process (AISI 316L, Cu, Ni, Ti and Al) from sulfate solutions.

Metal	Electrolyte (g/L)	T (°C)	CD (A/m^2)	Cell voltage (V)	CE (%)	SEC (kWh/kg)
AISI 316L	60 In^{3+}, 20 H_3BO_3, 20 $Al_2(SO_4)_3$, 30 Na_2SO_4	40	25	2.3	93.86	1.71
Cu	70 In^{3+}, 40 H_3BO_3, 30 Na_2SO_4	60	50	2.9	79.59	2.56
Ni	70 In^{3+}, 40 H_3BO_3, 30 Na_2SO_4	40	100	2.9	83.88	2.42
Ti*	70 In^{3+}	60	150	3.4	86.40	2.76
Al*	70 In^{3+}	40	150	3.3	86.66	2.72

**Etched surface*

To compare the effectiveness of the optimized operative conditions, electrowinning outputs before and after the optimization procedure were analyzed, as shown in Figure 115. In Figure 115a, the obtained CE for each cathode after the optimization shows a significant increase near or even above 80%. Although the best result seems to be associated with the AISI 316L around 94% CE, following the explanation above proposed, the best CE outcomes are, in fact, obtained for Ti and Al cathodes. Both cathodes can work at 150 A/m^2 improving productivity with relatively low SEC values. Regarding SEC, it is possible to claim that the optimized conditions favor the indium electrowinning. Both Ti and Al cathodes show low SEC values working at 150 A/m^2 after the optimization test. Furthermore, the energy cost also suffers a serious change once those optimized conditions are implemented. From an energetic point of view, the cost is decreased in each metal support adopting the optimized operative conditions (Figure 115c). A remarkable improvement is observed for the AISI 316L, passing from 1.6 to 0.4 EUR/kg. Apparently, it could be indicated that this cathode shows relevant increases in CE, decreases in SEC and energy cost. However, it is first necessary to consider that AISI 316L is optimized at a CD value of 25 A/m^2. Therefore, the energy requirement is lower; accordingly, lower productivity is then reported than those cathodes that work at higher CDs.

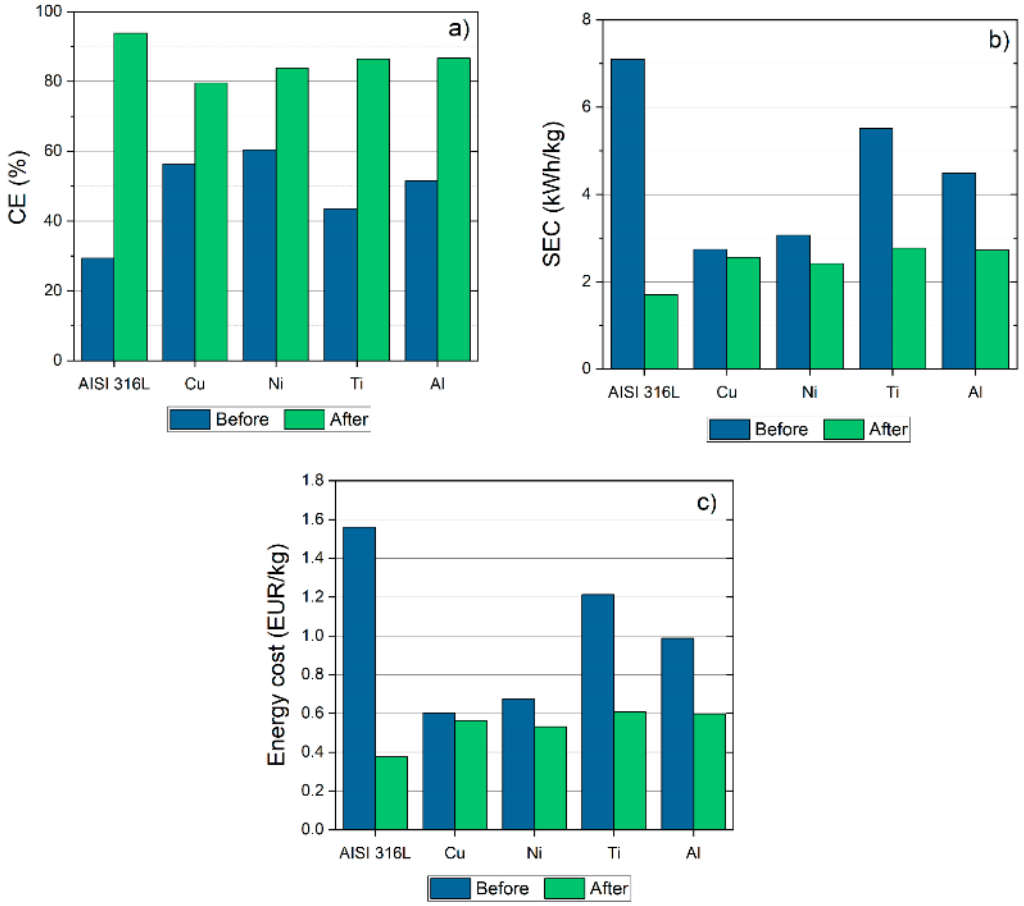

Figure 115. Comparison of indium electrowinning outputs a) CE b) SEC and c) energy cost, before and after optimizing operative conditions for AISI 316L, Cu, Ni, Ti and Al cathode from sulfate solutions. The indium and the electricity prices were found in [216,217]**.**

Figure 116 presents the normalized profit and cost a day with respect to the AISI 316 L cathode. This analysis is held from an energetic point of view, without considering other typical fixed expenses at higher productive scales like facilities, workers, supplies, taxes etc. Figure 116a shows the profit and cost a day for the indium electrowinning for different metal supports normalized to AISI 316L. As above mentioned, it seems that AISI 316L could offer the best improvement in the indium electrowinning. However, the best profit is highlighted by Ti, followed by Al cathode. Ti and Al cathodes respectively show 7 and 6 more times profit than the AISI 316L cathode. In other words, the AISI 316L cathode requires much more time to obtain the same profit as Ti and Al cathodes, which is inconvenient at a higher productive scale. Therefore, Ti and Al cathodes work more effectively and efficiently than the AISI 316L cathode.

A contrary result is observed from the normalized expenses, indicating that those cathodes have a higher energy consumption than AISI 316L. However, this result is clearly expected since Ti and Al cathode work at higher CD values (150 A/m^2). The process has to deal with high overpotentials and proportional energy consumption at

high CDs. Based on these results, the indium electrowinning with more efficiency and reasonable energy consumption can be carried out by Ti and Al cathodes.

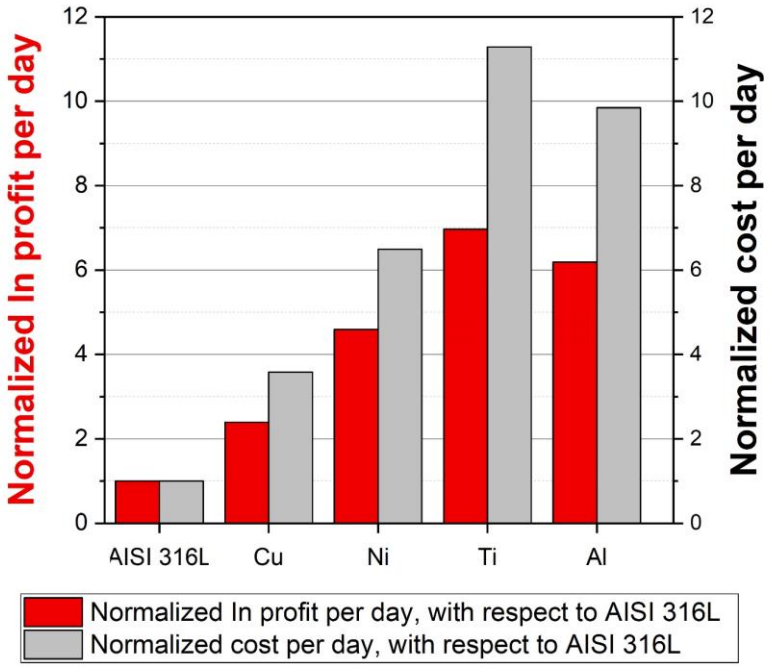

Figure 116. Analysis of a) normalized profit and b) cost with respect to the AISI 316 L cathode per day.

On the other hand, concerning the deposit morphology, some remarkable features are observed on the deposit morphology, using AISI 316L cathode at 25 A/m^2. The deposit shows lamellar growth, as shown (Figure 25d). Also, it is possible to observe the influence of sodium and aluminum sulfate (Figure 27b and Figure 29c). Likewise, the Cu cathode shows notable morphologies, only changing the CD. The operative conditions obtain a step-growth and very well-defined polygonal morphologies (Figure 67). The latter is also more evident in Figure 68, where different CD and 20 g/L H_3BO_3 were used to carry out the indium electrowinning process. In the case of the deposits obtained using Ni cathode, morphology also shows a lamellar growth, where layer by layer forms the deposit (Figure 45 and Figure 48).Furthermore, very well-defined grains were also shown in the indium electrowinning on Ti at 150 A/m^2 (Figure 85c-f). Indeed, polygonal morphologies with step-growths can be seen. Additionally, irregular aggregates at the grain edge are formed because of the high overpotential and HER occurrence (Figure 86c-f and Figure 88b-d).

It was verified for Ti and Al cathodes the swelling phenomenon mainly at high CDs, which has not occurred on the other metal supports. Two different hypotheses were suggested: i) the influence of the metal cathode support on the first layer of indium deposit that could create stresses at the interface between support and indium deposit,

ii) hydrogen atoms absorption in the crystal lattice of indium in substitutional positions that could create stress in the deposit. Nevertheless, none of them is satisfying, at least for the present experiments. Thus, further studies are required to understand that phenomenon. However, this problem was solved by etching the cathodic surface with HF solution and this suggests that the deposit was effectively stressed.

Conclusions

The present investigation studied the indium reduction reaction from sulfate solutions using different metal cathodic supports and operative conditions. Considering that the global indium demands for high-tech devices unavoidably propose a shortage scenario, secondary sources, mainly ITO-LCD waste, become attractive resources for indium valorization. Further, electrowinning displays a notable methodology capable of achieving indium recovery from indium-based electrolytes. Accordingly, based on the most relevant findings, this doctoral investigation proposes the following conclusions:

- The kinetic study for indium reduction reaction was performed for Cu, Ti, Al, Ni and AISI 316L. CVs allowed to understand several features of indium reduction reaction on each cathode. Crossover points were observed on voltammograms: the first related to the equilibrium potential E_1 at -0.68 V, while another related to the nucleation process (E_2). The HER interference on Ni indicated this parasitic reaction started first than indium reduction reaction overlapping on CVs, while on the AISI 316L HER occurs contemporaneously or immediately after indium reduction, allowing depicting the first crossover points. This behavior confirmed the hydrogen electrocatalytic features for Ni and low hydrogen overpotential for AISI 316L. Regarding CVs, AISI 316L, copper and aluminum shows similar crossover points, although it was evident that steel is highly affected by the low hydrogen overpotential. Although the kinetic analysis is hardly performed, the indium reduction reaction is achieved on the metal supports.

- The nucleation process on Al was characterized by an indium higher overpotential discharge facilitating the formation of nuclei clusters much bigger in sizes and randomly distributed, while the formation of nuclei clusters very small and well-distributed, like a thin layer, was observed for Cu and Ti. Since Cu, Ti and Al are deprived of HER during the indium reduction, it was possible to calculate an average diffusion coefficient for indium ions of about $3.5 \cdot 10^{-8}$ cm^2/s. Kinetic analyses determined k_0 value equal to $7.1 \cdot 10^{-5}$ cm/s, $6.1 \cdot 10^{-5}$ cm/s and $5.4 \cdot 10^{-5}$ cm/s for Cu, Ti and Al, respectively. Moreover, it was also calculated other kinetic parameters such as exchange current density, α, R_{ct} values related to the electrocatalytic activity for indium reduction reaction on those metal supports. Therefore, it was necessary to determine the real surface of supports through the roughness factor calculation. That real surface was then utilized for the Tafel analysis performed after ohmic compensation. Based on the results and from the literature, the limiting step can be described by the In^{3+}/In^{2+} reaction (slowest step). Furthermore, concerning i_0 values, it was found that it was higher

for the Cu cathode with respect to Ti and Al cathodes. The findings of this work clarified the indium reduction mechanism kinetics on different metal supports from sulfate solutions.

- The best operative conditions for indium electrowinning from sulfate electrolytes using an AISI 316L cathode were determined. Varying CD, electrolyte composition, temperature, the best outcomes in CE and SEC were obtained at 25 A/m^2, 60 In^{3+}, 40 H_3BO_3, 20 $Al_2(SO_4)_3$, 30 Na_2SO_4, 40 °C and pH 2.3, respectively. A strong dependence on supporting additives were observed working with the AISI 316L cathode. The optimized operative conditions hindered the HER at 25 A/m^2 and obtained high CE and low SEC outputs (more than 90% CE and 1.71 kWh/kg, respectively). With those conditions, the morphology of grains changed in size and shape as CD increased. Moreover, XRD tests showed well-defined patterns with (110) as the preferential orientation at 25 A/m^2.

- By using the Ni cathode, two attractive conditions were found to be considered. Firstly, performing the indium electrowinning with an electrolyte containing 70 g/L In^{3+}, 5 g/L H_3BO_3, 20 g/L $Al_2(SO_4)_3$ and 30 g/L Na_2SO_4 and at 40 °C, pH 2.3, 80 A/m^2, it is possible to achieve CE and SEC close to 98% and 1.7 kWh/kg, respectively. Nonetheless, other conditions for the electrowinning process could be proposed to increase the productivity. Rising CD to 100 A/m^2 and varying the composition up to 70 g/L In^{3+}, 40 g/L H_3BO_3, 30 g/L Na_2SO_4, CE and SEC can reach 83.3% and 2.4 kWh/kg, respectively. Aluminum sulfate was not relevant to enhancing CE. Contrary, the sodium sulfate addition improved the CE on the Ni cathode, even altering the preferential orientation in the XRD pattern. Similar behavior also was observed at low CD and temperature.

- The best performance for the Cu cathode was achieved at 25 A/m^2 using 70 g/L In^{3+}, 20 g/L H_3BO_3. Both CE and SEC were achieved at 90% and 1.6 kWh/kg, respectively. When CD was increased using 70 g/L In^{3+} and 40 g/L H_3BO_3 at 50 A/m^2, 60 °C and pH 2.3, CE reached reasonable results lower than 90%, while SEC was about 2.5 kWh/kg. It seems that sodium sulfate and aluminum sulfate caused negative effects on CE and SEC values. From micrographs, some indium deposits showed very well-defined polygonal grains, while diffractograms showed crystalline deposit at low CDs.

- The best performance for the Ti cathode at 100 A/m^2 was achieved using a sulfate electrolyte containing 70 g/L In^{3+}, 40 g/L H_3BO_3. High CE and SEC outputs were

around 84% and 2.5 kWh/kg, respectively. Nevertheless, by modifying only the cathodic surface and eliminating supporting additives, relevant outputs also could be obtained. The etched titanium surface with 1M HF reached CE and SEC values around 80% and 4.3 kWh/kg at 150 A/m^2. The latter SEC output represented an increase of 40% concerning the initial result at 40 g/L H_3BO_3. Increasing CD at 200 A/m^2 even using the etched cathode did not show relevant outputs. The HF pretreatment was carried out to avoid the deposit detachment from the cathode due to the swelling phenomenon. Finally, working at different CDs and electrolyte compositions, XRDs were slightly changed. However, temperature increases remarkably altered the preferential crystallographic orientations, showing broad and small peaks.

- The aluminum cathode was tested in the indium electrowinning process starting from an aqueous solution containing 70 g/L In^{3+}. Both boric acid and sodium sulfate at any concentration had a detrimental effect on the CE and SEC, suggesting that the best composition to carry out the indium electrowinning was the electrolyte containing merely 70 g/L In^{3+}. Under that condition, it was possible to reach around 98% CE and 1.7 kWh/kg at 80 A/m^2 CD, 2.3 pH and 40 °C. Nonetheless, the optimizing process included the etching pretreatment with 1M HF to avoid the swelling phenomenon of deposit at CDs higher than 80 A/m^2. By using that pretreatment, the process reached around 92% CE and 2.2 kWh/kg at 100 A/m^2. Productivity improvements led to work at 150 A/m^2 giving outcomes near 87% and 2.7 kWh/kg. The addition of boric acid and sodium sulfate showed no clear improvements. Furthermore, the most representative results from XRD diffractograms suggested that high concentrations of boric acid gave peaks more intense and sharper, while the temperature increase caused progressively small and broadened peaks.

- The metal support and operative conditions played a relevant role in the indium electrowinning. When those parameters were changed, the electrowinning process suffered substantial changes, maintained in most cases at 40 °C as the optimal temperature (except Cu and Ti). The pH value at 2.3 was defined as the best acidic environment to perform the indium electrowinning for each metal support. The productivity for the indium electrowinning at optimized conditions was Ti > Al > Ni > Cu > AISI 316L cathode. To sum up, both Al and Ti cathode exposed the most attractive electrowinning outputs, achieving similar CE and SEC values after the surface is treated by using 1M HF. The fact that these cathodes can work at 150 A/m^2 without the assistance of additive reagents was a relevant feature to undertake the indium electrowinning at higher productive scales (i. e., semi-pilot scales). In this investigation, CE and SEC were the most remarkable outputs to analyze the electrowinning effectiveness. Therefore, Ti

and Al metal supports could obtain significant productivity and energy consumption profits.

Research outputs

Published papers from this doctoral study

- Process parameters affecting the efficiency of indium electrowinning results from sulfate baths, Alessandro Dell'Era, Erwin Ciro Zuleta, Mauro Pasquali, Carla Lupi. Hydrometallurgy, Volume 193, 2020, 105296, ISSN 0304-386X, https://doi.org/10.1016/j.hydromet.2020.105296.
- Indium electrowinning study from sulfate aqueous solution using different metal cathodes, E. Ciro, A. Dell'Era, M. Pasquali, C. Lupi. Journal of Environmental Chemical Engineering, Volume 8, Issue 2, 2020, 103688, ISSN 2213-3437, https://doi.org/10.1016/j.jece.2020.103688.
- Indium electrowinning kinetics on titanium, aluminum and copper supports from sulfate solution, E. Ciro, A. Dell'Era, M. Pasquali, C. Lupi. Journal of Electroanalytical Chemistry, Volume 885, 2021, 115099, ISSN 1572-6657, https://doi.org/10.1016/j.jelechem.2021.115099.
- E. Ciro, A. Dell'Era, M. Razzi, C. Lupi, Optimization of indium electrowinning from sulfate solutions on Ni cathode, J. Clean. Prod. (2022) 131309. https://doi.org/10.1016/j.jclepro.2022.131309.

Other products from this doctoral study

- Novel Lead Battery Recycling Process Combining Pyrometallurgical Anode Preparation and Electrorefining. Ciro, E., Lupi, C., Mondal, A., Pilone, D. J. Sustain. Metall. (2021). https://doi.org/10.1007/s40831-021-00447-y.
- Railway overhead contact wire monitoring system by means of FBG sensors, Lupi, C. Felli, F. Ciro, E. Paris, C. Vendittozzi, C. (2021). Frattura ed Integrità Strutturale, 15(57), pp. 246–258. https://doi.org/10.3221/IGF-ESIS.57.18.
- Neodymium recovery from scrap magnet using ammonium persulfate. Ciro, E. Alzate, A. Lopez E. Serna, C. Gonzalez, O. Hydrometallurgy. 186, pp 226–234. https://doi.org/10.1016/j.hydromet.2019.04.016
- Vendittozzi, C., Ciro, E., Felli, F., Lupi, C., Marra, F., Pulci, G., Astri, A. (2020). Static and dynamic weighing of rolling stocks by mean of a customized FBG-sensorized-patch. International Journal of Safety and Security Engineering, Vol. 10, No. 1, pp. 83-88. https://doi.org/10.18280/ijsse.100111
- Lupi, C.; Felli, F.; Dell'Era, A.; Ciro, E.; Caponero, M.A.; Kalinowski, H.J.; Vendittozzi, C. Critical Issues of Double-Metal Layer Coating on FBG for Applications at High Temperatures. Sensors 2019, 19, 3824. https://doi.org/10.3390/s19183824

Participation in congresses and academic activities

- Short-cycle course on Thermal Analysis. Doctoral school. SC-Thanma-Erasmus, 5-8 October 2021, Nicosia – Cyprus.
- The European Union Point of view on Sustainability & Circular Economy: Part 3. Presentation: “Potential in the management of Electrical and Electronic waste (E-waste) as a source of critical and strategic materials” 23 April 2021 Rome, Italy.
- Webinar on applied research, organized by the Directorate of Technology and Innovation of the Pascual Bravo University Institution, Medellin, Colombia. Entitled: "Indium coatings applied to industry", 26 May 2021.
- NanoInnovation 15-18 September 2020, assistant.
- International Congress SAFE 2019. Oral presentation. Presentation’s title: Static and dynamic weighing of rolling stocks by mean of a customized FBG-sensorized-patch. Ancona, Italy.

Copyright

References

[1] K. Schulz, R. Seal, D. Bradley, J. Deyoung, Critical mineral resources of the United States—Economic and environmental geology and prospects for future supply, 2017. https://doi.org/10.3133/pp1802.

[2] A. Amato, L. Rocchetti, V. Fonti, M.L. Ruello, F. Beolchini, Secondary indium production from end-of-life liquid crystal displays, Phys. Status Solidi Curr. Top. Solid State Phys. 13 (2016) 979–983. https://doi.org/10.1002/pssc.201600114.

[3] M. Hofmann, H. Hofmann, C. Hagelüken, A. Hool, Critical raw materials: A perspective from the materials science community, Sustain. Mater. Technol. 17 (2018) e00074. https://doi.org/10.1016/j.susmat.2018.e00074.

[4] A.L. Gulley, N.T. Nassar, S. Xun, China, the United States, and competition for resources that enable emerging technologies, Proc. Natl. Acad. Sci. U. S. A. 115 (2018) 4111–4115. https://doi.org/10.1073/pnas.1717152115.

[5] C. Lupi, D. Pilone, In(III) hydrometallurgical recovery from secondary materials by solvent extraction, J. Environ. Chem. Eng. 2 (2014) 100–104. https://doi.org/10.1016/j.jece.2013.12.004.

[6] A.M. Alfantazi, R.R. Moskalyk, Processing of indium : a review, Miner. Eng. 16 (2003) 687–694. https://doi.org/10.1016/S0892-6875(03)00168-7.

[7] S. Zhang, Y. Ding, B. Liu, C. Chang, Supply and demand of some critical metals and present status of their recycling in WEEE, Waste Manag. 65 (2017) 113–127. https://doi.org/10.1016/j.wasman.2017.04.003.

[8] C.S. Anderson, Indium Statistics and Information, Indium - MCS 2019 Data Sheet. (2019) 78–79. https://www.usgs.gov/media/files/indium-mcs-2019-data-sheet (accessed September 6, 2019).

[9] A.C. Tolcin, Minerals Yearbook: Indium, Reston, Virginia, 2015. https://www.usgs.gov/centers/nmic/indium-statistics-and-information.

[10] X. Zeng, R. Gong, W.Q. Chen, J. Li, Uncovering the Recycling Potential of "new" WEEE in China, Environ. Sci. Technol. 50 (2016) 1347–1358. https://doi.org/10.1021/acs.est.5b05446.

[11] W. Chou, Y. Huang, Electrochemical removal of indium ions from aqueous solution using iron electrodes, J. Hazard. Mater. 172 (2009) 46–53. https://doi.org/10.1016/j.jhazmat.2009.06.119.

[12] S. Lee, S.Y. Lee, B. Swain, S.S. Cho, C.G. Lee, A validation experiment on indium recovery by electrowinning of aqueous electrolytes: optimization of electrolyte composition, Mater. Test. 58 (2016) 1001–1004. https://doi.org/10.3139/120.110953.

[13] C.W. White, J.G. Martin, Chlorine gas inhalation: Human clinical evidence of toxicity and experience in animal models, Proc. Am. Thorac. Soc. 7 (2010) 257–263. https://doi.org/10.1513/pats.201001-008SM.

[14] F.C. Walsh, D.R. Gabe, The electrodeposition of indium, Surf. Technol. 8 (1979) 87–99.

[15] F.C. Walsh, D.R. Gabe, Electrode reactions during the electrodeposition of indium from

acid sulphate solutions, Surf. Technol. 6 (1978) 425–436.

[16] H. Kim, C.M. Gilmore, A. Piqué, J.S. Horwitz, H. Mattoussi, H. Murata, Z.H. Kafafi, D.B. Chrisey, Electrical, optical, and structural properties of indium-tin-oxide thin films for organic light-emitting devices, J. Appl. Phys. 86 (1999) 6451–6461. https://doi.org/10.1063/1.371708.

[17] A. Akcil, I. Agcasulu, B. Swain, Resources , Conservation & Recycling Valorization of waste LCD and recovery of critical raw material for circular economy : A review, Resour. Conserv. Recycl. 149 (2019) 622–637. https://doi.org/10.1016/j.resconrec.2019.06.031.

[18] N.N. Greenwood, A. Earnshaw, Chemistry of Elements, in: Alum. Gall. Indium Thallium, 2nd ed., Pergamon Press, Oxford, UK, 1984: pp. 217–224.

[19] E.F. Schubert, E.F. Schubert, Light-Emitting Diodes, second, E. Fred Schubert, Troy, New York, 2018.

[20] D.I. Bleiwas, Byproduct Mineral Commodities Used for the Production of Photovoltaic Cells, Circular 1, U.S. Geological Survey, Reston, Virginia, 2010. http://pubs.usgs.gov/circ/1365/Circ1365.pdf.

[21] U.S. Geological Survey, Mineral Commodity Summaries 2012, U.S. Geological Survey, Reston, Virginia, 2012. http://minerals.usgs.gov/minerals/pubs/mcs/2012/mcsapp2012.pdf.

[22] A. Kumar, C. Zhou, The race to replace tin-doped indium oxide: Which material will win?, ACS Nano. 4 (2010) 11–14. https://doi.org/10.1021/nn901903b.

[23] L. Ciacci, T.T. Werner, I. Vassura, F. Passarini, Backlighting the European Indium Recycling Potentials, J. Ind. Ecol. 23 (2019) 426–437. https://doi.org/10.1111/jiec.12744.

[24] L. Ciacci, T.T. Werner, I. Vassura, F. Passarini, Backlighting the European Indium Recycling Potentials, J. Ind. Ecol. 23 (2019) 426–437. https://doi.org/10.1111/jiec.12744.

[25] U.S. Geological Survey, Mineral Commodity Summaries 2011, Reston, Virginia, 2011. https://doi.org/http://dx.doi.org/10.3133/70140094.

[26] K. Zhang, Y. Wu, W. Wang, B. Li, Y. Zhang, T. Zuo, Recycling indium from waste LCDs: A review, Resour. Conserv. Recycl. 104 (2015) 276–290. https://doi.org/10.1016/j.resconrec.2015.07.015.

[27] U.S. Geological Survey, Mineral Commodity Summaries 2021, U.S. Geological Survey, Reston, Virginia, 2021.

[28] U.S. Geological Survey, Mineral commodity summaries 2019, U.S. Geological Survey, Reston, Virginia, 2019. https://doi.org/https://doi.org/10.3133/70202434.

[29] U.S. Geological Survey, Mineral Commodity Summaries 2020, U.S. Geological Survey, Reston, Virginia, 2020. https://doi.org/https://doi.org/10.3133/ mcs2020.

[30] Y. He, Z. Xu, Recycling indium from waste liquid crystal display panel by vacuum, J. Hazard. Mater. 268 (2014) 185–190. https://doi.org/10.1016/j.jhazmat.2014.01.011.

[31] L. Shi-qing, T. Mo-tang, H. Jing, Y. Sheng-hai, T. Chao-bo, C. Yong-ming, Extraction of indium fiom indium-zinc concentrates, Trans. Nonferrous Met. Soc. China. 16 (2006) 1448–1454. https://doi.org/10.1016/j.mineng.2009.09.007.

[32] H. Hui, Z. Fan, D. Zhigan, W. Chang, L. Xingbin, L. Minting, L. Cunxiong, Leaching of

Indium from Indium-and Iron-Bearing Sphalerite Concentrate in Sulfuric Acid – Ferric Sulfate Solution, Int. J. OfChemical React. Eng. (2019) 1–12. https://doi.org/10.1515/ijcre-2018-0301.

[33] F. Zhang, C. Wei, Z. Deng, X. Li, C. Li, M. Li, Reductive leaching of indium-bearing zinc residue in sulfuric acid using sphalerite concentrate as reductant, Hydrometallurgy. 161 (2016) 102–106. https://doi.org/10.1016/j.hydromet.2016.01.029.

[34] F. Zhang, C. Wei, Z. gan Deng, C. xiong Li, X. bin Li, M. ting Li, Reductive leaching of zinc and indium from industrial zinc ferrite particulates in sulphuric acid media, Trans. Nonferrous Met. Soc. China. 26 (2016) 2495–2501. https://doi.org/10.1016/S1003-6326(16)64342-X.

[35] Y. Zhang, X. Li, L. Pan, X. Liang, X. Li, Studies on the kinetics of zinc and indium extraction from indium-bearing zinc ferrite, Hydrometallurgy. 100 (2010) 172–176. https://doi.org/10.1016/j.hydromet.2009.10.015.

[36] Z. Deng, X. Li, C. Wei, G. Fan, Recovery of Indium from Hard Zinc Slag by Pressure Leaching and Solvent Extraction, JOM. 73 (2021) 721–728. https://doi.org/10.1007/s11837-020-04519-4.

[37] E. Ciro, A. Alzate, E. López, C. Serna, O. Gonzalez, Neodymium recovery from scrap magnet using ammonium persulfate, Hydrometallurgy. 186 (2019) 226–234. https://doi.org/10.1016/j.hydromet.2019.04.016.

[38] K. Binnemans, P.T. Jones, B. Blanpain, T. Van Gerven, Y. Yang, A. Walton, M. Buchert, Recycling of rare earths: a critical review, J. Clean. Prod. 51 (2013) 1–22. https://doi.org/10.1016/j.jclepro.2012.12.037.

[39] T. Vander Hoogerstraete, B. Blanpain, T. Van Gerven, K. Binnemans, From NdFeB magnets towards the rare-earth oxides: a recycling process consuming only oxalic acid, RSC Adv. 4 (2014) 64099–64111. https://doi.org/10.1039/C4RA13787F.

[40] A. Alzate, E. López, C. Serna, O. Gonzalez, Gold recovery from printed circuit boards by selective breaking of internal metallic bonds using activated persulfate solutions, J. Clean. Prod. 166 (2017) 1102–1112. https://doi.org/10.1016/j.jclepro.2017.08.124.

[41] A. Amato, F. Beolchini, End of life liquid crystal displays recycling : A patent review, J. Environ. Manage. 225 (2018) 1–9. https://doi.org/10.1016/j.jenvman.2018.07.035.

[42] I.H. Kuong, J. Li, J. Zhang, X. Zeng, Estimating the Evolution of Urban Mining Resources in Hong Kong, Up to the Year 2050, Environ. Sci. Technol. 53 (2019) 1394–1403. https://doi.org/10.1021/acs.est.8b04063.

[43] E. Ma, Z. Xu, Technological process and optimum design of organic materials vacuum pyrolysis and indium chlorinated separation from waste liquid crystal display panels, J. Hazard. Mater. 263 (2013) 610–617. https://doi.org/10.1016/j.jhazmat.2013.10.020.

[44] H. Yoshida, S. Izhar, E. Nishio, Y. Utsumi, N. Kakimori, S. Asghari Feridoun, Recovery of indium from TFT and CF glasses in LCD panel wastes using sub-critical water, Sol. Energy Mater. Sol. Cells. 125 (2014) 14–19. https://doi.org/10.1016/j.solmat.2014.02.009.

[45] M. Hübner, T. Dierkes, Emissive and Non-Emissive Displays, (2010) 1–29.

[46] J. Yang, T. Retegan, C. Ekberg, Indium recovery from discarded LCD panel glass by solvent extraction, Hydrometallurgy. 137 (2013) 68–77. https://doi.org/10.1016/j.hydromet.2013.05.008.

[47] M. Souada, C. Louage, J.Y. Doisy, L. Meunier, A. Benderrag, B. Ouddane, S. Bellayer, N. Nuns, M. Traisnel, U. Maschke, Extraction of indium-tin oxide from end-of-life LCD panels using ultrasound assisted acid leaching, Ultrason. Sonochem. 40 (2018) 929–936. https://doi.org/10.1016/j.ultsonch.2017.08.043.

[48] J. Li, S. Gao, H. Duan, L. Liu, Recovery of valuable materials from waste liquid crystal display panel, Waste Manag. 29 (2009) 2033–2039. https://doi.org/10.1016/j.wasman.2008.12.013.

[49] R.K. Chinnam, É. Ujaczki, L. O'Donoghue, Leaching indium from discarded LCD glass: A rapid and environmentally friendly process, J. Clean. Prod. 277 (2020). https://doi.org/10.1016/j.jclepro.2020.122868.

[50] A.V.M. Silveira, M.S. Fuchs, D.K. Pinheiro, E.H. Tanabe, D.A. Bertuol, Recovery of indium from LCD screens of discarded cell phones, Waste Manag. 45 (2015) 334–342. https://doi.org/10.1016/j.wasman.2015.04.007.

[51] K. Zhang, B. Li, Y. Wu, W. Wang, R. Li, Y.N. Zhang, T. Zuo, Recycling of indium from waste LCD: A promising non-crushing leaching with the aid of ultrasonic wave, Waste Manag. 64 (2017) 236–243. https://doi.org/10.1016/j.wasman.2017.03.031.

[52] C.H. Lee, M.K. Jeong, M. Fatih Kilicaslan, J.H. Lee, H.S. Hong, S.J. Hong, Recovery of indium from used LCD panel by a time efficient and environmentally sound method assisted HEBM, Waste Manag. 33 (2013) 730–734. https://doi.org/10.1016/j.wasman.2012.10.002.

[53] E.B. Pereira, A.L. Suliman, E.H. Tanabe, D.A. Bertuol, Recovery of indium from liquid crystal displays of discarded mobile phones using solvent extraction, Miner. Eng. 119 (2018) 67–72. https://doi.org/10.1016/j.mineng.2018.01.022.

[54] E.H. Moutiy, L.-H. Tran, K. Mueller, K. Coudert, J.-F. Lucie Blais, Optimized indium solubilization from LCD panels using H2SO4 leaching, Waste Manag. 114 (2020) 53–61. https://doi.org/10.1016/j.wasman.2020.07.002.

[55] M. Souada, C. Louage, J. Doisy, L. Meunier, A. Benderrag, B. Ouddane, S. Bellayer, N. Nuns, M. Traisnel, U. Maschke, Extraction of indium-tin oxide from end-of-life LCD panels using ultrasound assisted acid leaching, Ultrason. - Sonochemistry. 40 (2018) 929–936. https://doi.org/10.1016/j.ultsonch.2017.08.043.

[56] Q. Song, L. Zhang, Z. Xu, Indium recovery from In-Sn-Cu-Al mixed system of waste liquid crystal display panels via acid leaching and two-step electrodeposition, J. Hazard. Mater. 381 (2020) 120973. https://doi.org/10.1016/j.jhazmat.2019.120973.

[57] V. Savvilotidou, J.N. Hahladakis, E. Gidarakos, Leaching capacity of metals-metalloids and recovery of valuable materials from waste LCDs, Waste Manag. 45 (2015) 314–324. https://doi.org/10.1016/j.wasman.2015.05.025.

[58] L. Rocchetti, A. Amato, V. Fonti, S. Ubaldini, I. De Michelis, B. Kopacek, F. Vegliò, F. Beolchini, Cross-current leaching of indium from end-of-life LCD panels, Waste Manag. 42 (2015) 180–187. https://doi.org/10.1016/j.wasman.2015.04.035.

[59] V. Lahtela, S. Virolainen, A. Uwaoma, M. Kallioinen, K. Timo, T. Sainio, Novel mechanical pre-treatment methods for effective indium recovery from end-of-life liquid-crystal display panels, 230 (2019) 580–591. https://doi.org/10.1016/j.jclepro.2019.05.163.

[60] H. Hasegawa, I.M.M. Rahman, Y. Egawa, H. Sawai, Z.A. Begum, T. Maki, S. Mizutani, Chelant-induced reclamation of indium from the spent liquid crystal display panels with

the aid of microwave irradiation, J. Hazard. Mater. 254–255 (2013) 10–17. https://doi.org/10.1016/j.jhazmat.2013.03.028.

[61] T. Kato, S. Igarashi, Y. Ishiwatari, M. Furukawa, H. Yamaguchi, Hydrometallurgy Separation and concentration of indium from a liquid crystal display via homogeneous liquid – liquid extraction, Hydrometallurgy. 137 (2013) 148–155. https://doi.org/10.1016/j.hydromet.2013.06.004.

[62] G. Dodbiba, H. Nagai, L.P. Wang, K. Okaya, T. Fujita, Leaching of indium from obsolete liquid crystal displays : Comparing grinding with electrical disintegration in context of LCA, Waste Manag. 32 (2012) 1937–1944. https://doi.org/10.1016/j.wasman.2012.05.016.

[63] T. Boundy, M. Boyton, P. Taylor, Attrition scrubbing for recovery of indium from waste liquid crystal display glass via selective comminution, J. Clean. Prod. 154 (2017) 436–444. https://doi.org/10.1016/j.jclepro.2017.04.038.

[64] J. Qin, S. Ning, T. Fujita, Y. Wei, S. Zhang, S. Lu, Leaching of indium and tin from waste LCD by a time-efficient method assisted planetary high energy ball milling, Waste Manag. 120 (2021) 193–201. https://doi.org/10.1016/j.wasman.2020.11.028.

[65] S. Virolainen, T. Huhtanen, A. Laitinen, T. Sainio, Two alternative process routes for recovering pure indium from waste liquid crystal display panels, J. Clean. Prod. 243 (2020) 118599. https://doi.org/10.1016/j.jclepro.2019.118599.

[66] D. Fontana, F. Forte, R. De Carolis, M. Grosso, Materials recovery from waste liquid crystal displays : A focus on indium, Waste Manag. 45 (2015) 325–333. https://doi.org/10.1016/j.wasman.2015.07.043.

[67] F. Ferella, G. Belardi, A. Marsilii, I. De Michelis, F. Vegliò, Separation and recovery of glass, plastic and indium from spent LCD panels, Waste Manag. 60 (2017) 569–581. https://doi.org/10.1016/j.wasman.2016.12.030.

[68] H. Kang, K. Kim, J. Kim, Recovery and purification of indium from waste sputtering target by selective solvent extraction of Sn, Green Chem. (2013) 2200–2207. https://doi.org/10.1039/c3gc40589c.

[69] Y. Li, Z. Liu, Q. Li, Z. Liu, L. Zeng, Recovery of indium from used indium-tin oxide (ITO) targets, Hydrometallurgy. 105 (2011) 207–212. https://doi.org/10.1016/j.hydromet.2010.09.006.

[70] J.E. De-la-Cruz-Moreno, A.E. Ceniceros-Gómez, O. Morton-Bermea, E. Hernández-Álvarez, Recovery of indium from jarosite residues of zinc refinery by a hydrometallurgical process, Hydrometallurgy. (2021) 105697. https://doi.org/10.1016/j.hydromet.2021.105697.

[71] L. Wang, X.V. Wang, Cloud-based cyber-physical systems in manufacturing, Springer, Stockholm, Sweden, 2017. https://doi.org/10.1080/09537287.2019.1655069.

[72] B. Swain, C.G. Lee, Commercial indium recovery processes development from various e-(industry) waste through the insightful integration of valorization processes : A perspective, Waste Manag. 87 (2019) 597–611. https://doi.org/10.1016/j.wasman.2019.02.042.

[73] Mineralevivo.com, Sphalerite Gems in Crystalized Quartz Specimen Crystal, (2021). https://mineralevivo.com/en/sphalerite/2994-sphalerite-gems-in-crystalized-quartz-specimen-crystal-healing-minerals-chakra-7432044035039.html (accessed April 4, 2021).

[74] C.L. Chuang, M.W. Chang, N.P. Chen, C.C. Pan, C.P. Liu, Improving Performance of CIGS Solar Cells by Annealing ITO Thin Films Electrodes, Int. J. Photoenergy. 2015 (2015). https://doi.org/10.1155/2015/483147.

[75] R. Russell, How does the new POPs legislation affect producers, (2019). https://erp-recycling.org/uk/news-and-events/2019/08/how-does-the-new-pops-legislation-affect-producers/ (accessed April 4, 2021).

[76] G.Q. Jin, W.D. Li, K. Xia, Disassembly matrix for liquid crystal displays televisions, in: 2nd Int. Through-Life Eng. Serv. Conf., Elsevier, 2013: pp. 357–362. https://doi.org/10.1016/j.procir.2013.07.015.

[77] C. Lee, M. Jeong, M.F. Kilicaslan, J. Lee, H. Hong, S. Hong, Recovery of indium from used LCD panel by a time efficient and environmentally sound method assisted HEBM, Waste Manag. 33 (2013) 730–734. https://doi.org/10.1016/j.wasman.2012.10.002.

[78] A. Ryan, L.O. Donoghue, H. Lewis, Characterising components of liquid crystal displays to facilitate disassembly, J. Clean. Prod. 19 (2011) 1066–1071. https://doi.org/10.1016/j.jclepro.2011.01.009.

[79] H.Y. Wang, A study of the effects of LCD glass sand on the properties of concrete, Waste Manag. 29 (2009) 335–341. https://doi.org/10.1016/j.wasman.2008.03.005.

[80] K.L. Lin, W.K. Chang, T.C. Chang, C.H. Lee, C.H. Lin, Recycling thin film transistor liquid crystal display (TFT-LCD) waste glass produced as glass-ceramics, J. Clean. Prod. 17 (2009) 1499–1503. https://doi.org/10.1016/j.jclepro.2009.05.012.

[81] Y. Chen, L. Zhang, Z. Xu, Vacuum pyrolysis characteristics and kinetic analysis of liquid crystal from scrap liquid crystal display panels, J. Hazard. Mater. 327 (2017) 55–63. https://doi.org/10.1016/j.jhazmat.2016.12.026.

[82] R. Lu, E. Ma, Z. Xu, Application of pyrolysis process to remove and recover liquid crystal and films from waste liquid crystal display glass, J. Hazard. Mater. 243 (2012) 311–318. https://doi.org/10.1016/j.jhazmat.2012.10.035.

[83] R. Wang, Z. Xu, Pyrolysis characteristics and pyrolysis products separation for recycling organic materials from waste liquid crystal display panels, J. Hazard. Mater. 302 (2016) 45–56. https://doi.org/10.1016/j.jhazmat.2015.09.038.

[84] L. Zhang, Y. Chen, Z. Xu, Controllable Formation of Carbon Fiber in Pyrolysis Process of Liquid Crystals from Waste LCD Panels and Indium Recovery by Vacuum in Situ Reduction with Carbon Fiber, ACS Sustain. Chem. Eng. 6 (2018) 541–550. https://doi.org/10.1021/acssuschemeng.7b02828.

[85] L. Zhang, B. Wu, Y. Chen, Z. Xu, Energy and valuable resource recovery from waste liquid crystal display panels by an environment-friendly technological process: Pyrolysis of liquid crystals and preparation of indium product, J. Clean. Prod. 162 (2017) 141–152. https://doi.org/10.1016/j.jclepro.2017.06.031.

[86] J. Guan, S. Wang, H. Ren, Y. Guo, H. Yuan, X. Yan, J. Guo, W. Gu, R. Su, B. Liang, G. Gao, Y. Zhou, J. Xu, Z. Guo, Indium recovery from waste liquid crystal displays by polyvinyl chloride waste, RSC Adv. 5 (2015) 102836–102843. https://doi.org/10.1039/c5ra21871c.

[87] S. Itoh, K. Maruyama, Recoveries of Metallic Indium and Tin from ITO by Means of Pyrometallurgy, High Temp. Mater. Process. 30 (2011) 317–322. https://doi.org/10.1515/HTMP.2011.051.

[88] K. Takahashi, A. Sasaki, G. Dodbiba, J.U.N. Sadaki, Recovering Indium from the Liquid Crystal Display of Discarded Cellular Phones by Means of Chloride-Induced Vaporization at Relatively Low Temperature, Metall. Mater. Trans. A. 40 (2009) 891–900. https://doi.org/10.1007/s11661-009-9786-4.

[89] Y. Lu, Z. Xu, Recycling non-leaching gold from gold-plated memory cards : Parameters optimization , experimental verification , and mechanism analysis, J. Clean. Prod. 162 (2017) 1518–1526. https://doi.org/http://dx.doi.org/10.1016/j.jclepro.2017.06.094.

[90] E.Y. Yazici, H. Deveci, Extraction of metals from waste printed circuit boards (WPCBs) in H2SO4-CuSO4-NaCl solutions, Hydrometallurgy. 139 (2013) 30–38. https://doi.org/10.1016/j.hydromet.2013.06.018.

[91] S. Syed, A green technology for recovery of gold from non-metallic secondary sources, Hydrometallurgy. 82 (2006) 48–53. https://doi.org/10.1016/j.hydromet.2006.01.004.

[92] A. Akcil, C. Erust, C.S. Gahan, M. Ozgun, M. Sahin, A. Tuncuk, Precious metal recovery from waste printed circuit boards using cyanide and non-cyanide lixiviants - A review., Waste Manag. 45 (2015) 258–271. https://doi.org/10.1016/j.wasman.2015.01.017.

[93] C. Lupi, M. Pasquali, A. Dell'Era, Nickel and cobalt recycling from lithium-ion batteries by electrochemical processes, Waste Manag. 25 (2005) 215–220. https://doi.org/10.1016/j.wasman.2004.12.012.

[94] S.S. Behera, P.K. Parhi, Leaching kinetics study of neodymium from the scrap magnet using acetic acid, Sep. Purif. Technol. 160 (2016) 59–66. https://doi.org/10.1016/j.seppur.2016.01.014.

[95] S.S. Abhilash, P. Meshram, B.D. Pandey, Metallurgical processes for the recovery and recycling of lanthanum from various resources - A review, Hydrometallurgy. 160 (2016) 47–59. https://doi.org/10.1016/j.hydromet.2015.12.004.

[96] J.C. Park, The recovery of indium metal from ITO-scrap using hydrothermal reaction in alkaline solution, Bull. Korean Chem. Soc. 32 (2011) 3796–3798. https://doi.org/10.5012/bkcs.2011.32.10.3796.

[97] H. Kang, J. Lee, J. Kim, Hydrometallurgy Recovery of indium from etching waste by solvent extraction and electrolytic refining, Hydrometallurgy. 110 (2011) 120–127. https://doi.org/10.1016/j.hydromet.2011.09.009.

[98] S. Wang, Y. He, J. Yang, Y. Feng, Enrichment of indium tin oxide from colour filter glass in waste liquid crystal display panels through flotation, J. Clean. Prod. 189 (2018) 464–471. https://doi.org/10.1016/j.jclepro.2018.04.096.

[99] B. Swain, C.G. Lee, H.S. Hong, Value Recovery from Waste Liquid Crystal Display Glass Cullet through Leaching : Understanding the Correlation between Indium Leaching Behavior and Cullet Piece Size, Metals (Basel). 8 (2018) 1–10. https://doi.org/10.3390/met8040235.

[100] X. Li, Z. Deng, C. Li, C. Wei, M. Li, G. Fan, H. Rong, Direct solvent extraction of indium from a zinc residue reductive leach solution by D2EHPA, Hydrometallurgy. 156 (2015) 1–5. https://doi.org/10.1016/j.hydromet.2015.05.003.

[101] S. Virolainen, D. Ibana, E. Paatero, Recovery of indium from indium tin oxide by solvent extraction, Hydrometallurgy. 107 (2011) 56–61. https://doi.org/10.1016/j.hydromet.2011.01.005.

[102] H. Sawai, I.M.M. Rahman, Y. Tsukagoshi, T. Wakabayashi, T. Maki, S. Mizutani, H. Hasegawa, Selective recovery of indium from lead-smelting dust, Chem. Eng. J. 277 (2015) 219–228. https://doi.org/10.1016/j.cej.2015.04.112.

[103] S. Hsieh, C. Chen, W.C. Say, Process for recovery of indium from ITO scraps and metallurgic microstructures, Mater. Sci. Eng. B. 158 (2009) 82–87. https://doi.org/10.1016/j.mseb.2009.01.019.

[104] A. Shibayama, W. Tongamp, B. Altansukh, K. Haga, A. Hosoi, Electronic waste treatment: Part 1. Autoclave oxidation–leaching using pyrite waste from mine tailing, Hydrometallurgy. 137 (2013) 92–100. https://doi.org/http://dx.doi.org/10.1016/j.hydromet.2013.05.007.

[105] M.D. Turan, H. Arslanoglu, H.S. Altundogan, Optimization of the leaching conditions of chalcopyrite concentrate using ammonium persulfate in an autoclave system, J. Taiwan Inst. Chem. Eng. 50 (2014) 1–7. https://doi.org/10.1016/j.jtice.2014.12.009.

[106] J. Jiang, D. Liang, Q. Zhong, Precipitation of indium using sodium tripolyphosphate, Hydrometallurgy. 106 (2011) 165–169. https://doi.org/10.1016/j.hydromet.2010.12.009.

[107] A. Alzate, M.E. López, C. Serna, Recovery of gold from waste electrical and electronic equipment (WEEE) using ammonium persulfate, Waste Manag. 57 (2016) 113–120. https://doi.org/10.1016/j.wasman.2016.01.043.

[108] L. Rocchetti, A. Amato, F. Beolchini, Recovery of indium from liquid crystal displays, J. Clean. Prod. 116 (2016) 299–305. https://doi.org/10.1016/j.jclepro.2015.12.080.

[109] M. Martin, E. Janneck, R. Kermer, A. Patzig, S. Reichel, Recovery of indium from sphalerite ore and flotation tailings by bioleaching and subsequent precipitation processes, Miner. Eng. (2014). https://doi.org/10.1016/j.mineng.2014.11.015.

[110] J. Cui, N. Zhu, F. Mao, P. Wu, Z. Dang, Science of the Total Environment Bioleaching of indium from waste LCD panels by Aspergillus niger : Method optimization and mechanism analysis, Sci. Total Environ. 790 (2021) 148151. https://doi.org/10.1016/j.scitotenv.2021.148151.

[111] M. Saidan, B. Brown, M. Valix, Leaching of Electronic Waste Using Biometabolised Acids*, Chinese J. Chem. Eng. 20 (2012) 530–534. https://doi.org/10.1016/S1004-9541(11)60215-2.

[112] M. Arshadi, F. Pourhossein, S. Mohammad, Green recovery of Cu-Ni-Fe from a mixture of spent PCBs using adapted A . ferrooxidans in a bubble column bioreactor, Sep. Purif. Technol. 272 (2021) 118701. https://doi.org/10.1016/j.seppur.2021.118701.

[113] T. Ogi, K. Tamaoki, N. Saitoh, A. Higashi, Y. Konishi, Recovery of indium from aqueous solutions by the Gram-negative bacterium Shewanella algae, Biochem. Eng. J. 63 (2012) 129–133. https://doi.org/10.1016/j.bej.2011.11.008.

[114] F. Pourhossein, O. Rezaei, S.M. Mousavi, F. Beolchini, Bioleaching of critical metals from waste OLED touch screens using adapted acidophilic bacteria, 3 (2021) 893–906.

[115] Z. Yu, H. Han, P. Feng, S. Zhao, T. Zhou, A. Kakade, Bioresource Technology Recent advances in the recovery of metals from waste through biological processes, Bioresour. Technol. 297 (2020) 122416. https://doi.org/10.1016/j.biortech.2019.122416.

[116] J. Wang, Q. Huang, T. Li, B. Xin, S. Chen, X. Guo, C. Liu, Y. Li, Bioleaching mechanism of Zn , Pb , In , Ag , Cd and As from Pb / Zn smelting slag by autotrophic bacteria, J.

Environ. Manage. 159 (2015) 11–17. https://doi.org/10.1016/j.jenvman.2015.05.013.

[117] J. Ran, X. Qiu, Z. Hu, Q. Liu, B. Song, Y. Yao, Effects of particle size on flotation performance in the separation of copper, gold and lead, Powder Technol. 344 (2019) 654–664. https://doi.org/10.1016/j.powtec.2018.12.045.

[118] M.J. Jowkar, N. Bahaloo-horeh, S.M. Mousavi, Bioleaching of indium from discarded liquid crystal displays, J. Clean. Prod. 180 (2018) 417–429. https://doi.org/10.1016/j.jclepro.2018.01.136.

[119] L. Ki-Woong, K. Hong-In, S. Hyun-Tae, A. Jae-Woo, K. Yong-Hwan, Separation and Recovery of Tin and Indium from Spent ITO Sludge, J. Korean Inst. Resour. Recycl. 23 (2014) 53–60. https://doi.org/10.7844/kirr.2014.23.2.53.

[120] Y. Fan, Y. Liu, L. Niu, W. Zhang, T. Zhang, Efficient extraction and separation of indium from waste indium tin oxide (ITO) targets by enhanced ammonium bisulfate leaching, Sep. Purif. Technol. 269 (2021) 118766. https://doi.org/10.1016/j.seppur.2021.118766.

[121] X. Li, C. Wei, Z. Deng, C. Li, G. Fan, H. Rong, F. Zhang, Extraction and separation of indium and copper from zinc residue leach liquor by solvent extraction, Sep. Purif. Technol. 156 (2015) 348–355. https://doi.org/10.1016/j.seppur.2015.10.021.

[122] W.S. Chen, Y.C. Wang, K.L. Chiu, The separation and recovery of indium, gallium, and zinc from spent GZO(IGZO) targets, J. Environ. Chem. Eng. 5 (2017) 381–390. https://doi.org/10.1016/j.jece.2016.12.005.

[123] J. Lahti, S. Vazquez, S. Virolainen, M. Mänttäri, M. Kallioinen, Membrane Filtration Enhanced Hydrometallurgical Recovery Process of Indium from Waste LCD Panels, J. Sustain. Metall. 6 (2020) 576–588. https://doi.org/10.1007/s40831-020-00293-4.

[124] Y. Cao, F. Li, G. Li, J. Huang, H. Zhu, W. He, Leaching and purification of indium from waste liquid crystal display panel after hydrothermal pretreatment: Optimum conditions determination and kinetic analysis, Waste Manag. 102 (2020) 635–644. https://doi.org/10.1016/j.wasman.2019.11.029.

[125] S. Fan, Q. Jia, N. Song, R. Su, W. Liao, Synergistic extraction study of indium from chloride medium by mixtures of sec -nonylphenoxy acetic acid and trialkyl amine, Sep. Purif. Technol. 75 (2010) 76–80. https://doi.org/10.1016/j.seppur.2010.07.015.

[126] Y. Sasaki, N. Matsuo, T. Oshima, Y. Baba, Selective extraction of In(III), Ga(III) and Zn(II) using a novel extractant with phenylphosphinic acid, Chinese J. Chem. Eng. 24 (2016) 232–236. https://doi.org/10.1016/j.cjche.2015.06.001.

[127] Y. Sasaki, M. Uto, T. Oshima, Y. Baba, Synthesis of a Carboxylic Acid Extractant Containing an Amino Group and its Selective Extraction of In(III) and Ga(III), Solvent Extr. Res. Dev. 23 (2016) 1–8. https://doi.org/https://doi.org/10.15261/serdj.23.1.

[128] Y. Zhang, B. Jin, B. Ma, X. Feng, Separation of indium from lead smelting hazardous dust via leaching and solvent extraction, J. Environ. Chem. Eng. 5 (2017) 2182–2188. https://doi.org/10.1016/j.jece.2017.04.034.

[129] Y.S. Zimmermann, C. Niewersch, M. Lenz, Z.Z. Kül, P.F.X. Corvini, A. Schäffer, T. Wintgens, Recycling of indium from CIGS photovoltaic cells: Potential of combining acid-resistant nanofiltration with liquid-liquid extraction, Environ. Sci. Technol. 48 (2014) 13412–13418. https://doi.org/10.1021/es502695k.

[130] M.C.B. Fortes, J.S. Benedetto, Technical note separation of indium and iron by solvent

extraction, Miner. Eng. II (1998) 447–451.

[131] B. Gupta, N. Mudhar, I. Singh, Separations and recovery of indium and gallium using bis (2,4,4-trimethylpentyl) phosphinic acid (Cyanex 272), Sep. Purif. Technol. 57 (2007) 294–303. https://doi.org/10.1016/j.seppur.2007.04.011.

[132] J. Yang, T. Retegan, B.M. Steenari, C. Ekberg, Recovery of indium and yttrium from Flat Panel Display waste using solvent extraction, Sep. Purif. Technol. 166 (2016) 117–124. https://doi.org/10.1016/j.seppur.2016.04.021.

[133] S. Dhiman, B. Gupta, Cyphos IL 104 assisted extraction of indium and recycling of indium, tin and zinc from discarded LCD screen, Sep. Purif. Technol. 237 (2020) 116407. https://doi.org/10.1016/j.seppur.2019.116407.

[134] S. Nusen, T. Chairuangsri, Z. Zhu, C.Y. Cheng, Recovery of indium and gallium from synthetic leach solution of zinc refinery residues using synergistic solvent extraction with LIX 63 and Versatic 10 acid, Hydrometallurgy. 160 (2016) 137–146. https://doi.org/10.1016/j.hydromet.2016.01.007.

[135] M. Matsumiya, M. Sumi, Y. Uchino, I. Yanagi, Recovery of indium based on the combined methods of ionic liquid extraction and electrodeposition, Sep. Purif. Technol. 201 (2018) 25–29. https://doi.org/10.1016/j.seppur.2018.02.027.

[136] F.J. Alguacil, Liquid-Liquid Extraction of Indium(III) from the HCl Medium by Ionic Liquid A327H+Cl− and Its Use in a Supported Liquid Membrane System, Molecules. 25 (2020) 5238. https://doi.org/10.3390/molecules25225238.

[137] H. Ma, Y. Lei, Q. Jia, W. Liao, L. Lin, An extraction study of gallium, indium, and zinc with mixtures of sec-octylphenoxyacetic acid and primary amine N1923, Sep. Purif. Technol. 80 (2011) 351–355. https://doi.org/10.1016/j.seppur.2011.05.018.

[138] S.M.J. Koleini, H. Mehrpouya, K. Saberyan, M. Abdolahi, Extraction of indium from zinc plant residues, Miner. Eng. 23 (2010) 51–53. https://doi.org/10.1016/j.mineng.2009.09.007.

[139] J. Chang, L.B. Zhang, Y. Du, J.H. Peng, G.Y. Hu, J. Chen, C. Srinivasakannan, Separation of indium from iron in a rotating packed bed contactor using Di-2-ethylhexylphosphoric acid, Sep. Purif. Technol. 164 (2016) 12–18. https://doi.org/10.1016/j.seppur.2016.03.017.

[140] B. Swain, C. Mishra, H.S. Hong, S.-S. Cho, Treatment of Indium-Tin-Oxide etching wastewater and recovery of In, Mo, Sn and Cu by liquid-liquid extraction and wet chemical reduction: A laboratory scale sustainable commercial green process, Green Chem. 17 (2015) 4418–4431. https://doi.org/10.1039/C5GC01244A.

[141] B. Swain, C. Mishra, H.S. Hong, S. Cho, S. Lee, Commercial process for the recovery of metals from ITO etching industry wastewater by liquid – liquid extraction : simulation , analysis of, Green Chem. 17 (2015) 3979–3991. https://doi.org/10.1039/c5gc00473j.

[142] M. Lee, Y. Oh, Analysis of ionic equilibria and electrowinning of indium from chloride solutions, Scand. J. Metall. 33 (2004) 279–285. https://doi.org/10.1111/j.1600-0692.2004.00693.x.

[143] S.S. ABD El Rehim, M.A. Mostafa, A.M. Ahmed, Structural studies on electrodeposited indium on steel surfaces, J. Mater. Sci. Lett. 7 (1988) 1350–1352. https://doi.org/10.1007/BF00719980.

[144] A.M.K. Gustafsson, F. Björefors, B. Steenari, C. Ekberg, Investigation of an electrochemical method for separation of copper, indium, and gallium from pretreated

CIGS solar cell waste materials, Sci. World J. 2015 (2015) 1–11. https://doi.org/10.1155/2015/494015.

[145] D. Choi, Y.S. Kim, Y. Son, Recovery of indium tin oxide (ITO) and glass plate from discarded TFT-LCD panels using an electrochemical method and acid treatment, RSC Adv. 4 (2014) 50975–50980. https://doi.org/10.1039/c4ra11085d.

[146] F.C. Walsh, D.R. Gabe, The electrodeposition of indium alloys, Surf. Technol. 53 (1981) 1–30. https://doi.org/0376-4883/81/0000-0000/S02.50.

[147] F.C. Walsh, D.R. Gabe, The electrodeposition of indium, Surf. Technol. 8 (1979) 87–99. https://doi.org/10.1016/0376-4583(79)90054-2.

[148] F.C. Walsh, D.R. Gabe, Electrode reactions during the electrodeposition of indium from acid sulphate solutions, Surf. Technol. 6 (1978) 425–436. https://doi.org/10.1016/0376-4583(78)90012-2.

[149] E. Ciro, A. Dell'Era, M. Pasquali, C. Lupi, Indium electrowinning study from sulfate aqueous solution using different metal cathodes, J. Environ. Chem. Eng. 8 (2020). https://doi.org/10.1016/j.jece.2020.103688.

[150] A. Dell'Era, E. Ciro Zuleta, M. Pasquali, C. Lupi, Process parameters affecting the efficiency of indium electrowinning results from sulfate baths, Hydrometallurgy. 193 (2020). https://doi.org/10.1016/j.hydromet.2020.105296.

[151] S. Xu, G. Wang, J. Fan, Z. Wang, J. Zhang, J. Chen, L. Zheng, J. Pan, R. Wang, Preparation of high purity indium by chemical purification: Focus on removal of Cd, Pb, Sn and removal mechanism, Hydrometallurgy. 200 (2021) 105551. https://doi.org/10.1016/j.hydromet.2020.105551.

[152] B. Burkitbayeva, A. Argimbayeva, G. Rakhymbay, K. Avchukir, K. Tassibekov, M. Nauryzbayev, Refining of rough indium by method of reactionary electrolysis, MATEC Web Conf. 96 (2017) 1–4. https://doi.org/10.1051/matecconf/20179600005.

[153] W. Monnens, C. Deferm, K. Binnemans, J. Fransaer, Indium electrodeposition from indium(iii) methanesulfonate in DMSO, Phys. Chem. Chem. Phys. 22 (2020) 24526–24534. https://doi.org/10.1039/d0cp03277h.

[154] M.H. Yang, I.W. Sun, Electrochemical study of indium in a water-stable 1-ethyl-3-methylimidazolium chloride/tetrafluoroborate room temperature ionic liquid, J. Chinese Chem. Soc. 51 (2004) 253–260. https://doi.org/10.1002/jccs.200400040.

[155] L. Xu, Y. Xiong, J. Meng, J. Wang, Z. Hua, Y. Tian, J. You, Z. Zhao, Redox behavior of indium in molten chlorides, Trans. Nonferrous Met. Soc. China. 31 (2021) 1496–1505. https://doi.org/10.1016/s1003-6326(21)65593-0.

[156] P. Hayes, Process selection in exactrive metallurgy, First Edit, Hayes Publishing Co, Brisbane, 1985.

[157] J.J. Moore, E.A.. Boyce, M.J. Brooks, B. Perry, P.J. Sheridan, Chemical Metallurgy, Second Edi, British Library, Colorado, USA, 1990.

[158] A.R. Kucernak, C. Zalitis, General Models for the Electrochemical Hydrogen Oxidation and Hydrogen Evolution Reactions: Theoretical Derivation and Experimental Results under Near Mass-Transport Free Conditions, J. Phys. Chem. C. 120 (2016) 10721–10745. https://doi.org/10.1021/acs.jpcc.6b00011.

[159] S.M. Grimes, N.G. Yasri, A.J. Chaudhary, Recovery of critical metals from dilute leach

solutions – Separation of indium from tin and lead, Inorganica Chim. Acta. 461 (2017) 161–166. https://doi.org/10.1016/j.ica.2017.02.002.

[160] Y.F. Wu, Y.S. Wang, Indium recovery in an electrochemical flow reactor. Simulation and experiment, Int. J. Electrochem. Sci. 12 (2017) 3516–3536. https://doi.org/10.20964/2017.04.24.

[161] B.N. Pradhan, P.G. Krishna, S.C. Das, Influence of Chloride Ion On Electrocrystallization of Copper, Plat. Surf. Finish. (1996) 56–63.

[162] S. Gurmen, A laboratory-scale investigation of alkaline zinc electrowinning, Miner. Eng. 16 (2003) 559–562. https://doi.org/10.1016/S0892-6875(03)00081-5.

[163] W. Cui, Effect and interactions of commercial additives and chloride ion in copper electrowinning, Missouri university of science and technology, 2014.

[164] Y.C. Liu, Y.C. Chen, Y.T. Hsieh, I.W. Sun, Anomalous voltammetric behavior observed for electrodeposition of Indium in the 1-Butyl-1-methylpyrrolidinium Dicyanamide ionic liquid; a result of the ionic liquid cation adsorption, J. Phys. Chem. C. 121 (2017) 8907–8913. https://doi.org/10.1021/acs.jpcc.7b01375.

[165] E. Barrado, S. García, J.A. Rodríguez, Y. Castrillejo, Electrodeposition of indium on W and Cu electrodes in the deep eutectic solvent choline chloride-ethylene glycol (1:2), J. Electroanal. Chem. 823 (2018) 106–120. https://doi.org/10.1016/j.jelechem.2018.06.004.

[166] M.F. Rahman, R. Bernasconi, L. Magagnin, Electrodeposition of indium from a deep eutectic solvent, J. Optoelectron. Adv. Mater. 17 (2015) 122–126.

[167] P.-K. Wang, W.-J. Lin, I.-W. Sun, A Glance of the Electrochemical Co-Deposition of Indium and Arsenic in a Choline Chloride/Ethylene Glycol Deep Eutectic Solvent, J. Electrochem. Soc. 166 (2019) D374–D380. https://doi.org/10.1149/2.0111910jes.

[168] J.C. Malaquias, M. Steichen, M. Thomassey, P.J. Dale, Electrodeposition of Cu-In alloys from a choline chloride based deep eutectic solvent for photovoltaic applications, Electrochim. Acta. 103 (2013) 15–22. https://doi.org/10.1016/j.electacta.2013.04.068.

[169] C. Van De Goor, Influence of Temperature and pH on the Hydrogen Evolution Reaction (HER) on Platinum, (2016) 35. http://essay.utwente.nl/68735/1/Bachelor verslag Chris van de Goor s1251066 - openbaar.pdf.

[170] T.J. Tuaweri, E.M. Adigio, P.P. Jombo, A Study of Process Parameters for Zinc Electrodeposition from a Sulphate Bath, Int. J. Eng. Sci. Invent. 2 (2013) 17–24.

[171] A.J. Bard, L.R. Faulkner., Electrochemical Methods: Fundamentals and Applications, 2nd ed., John Wiley & Sons, Inc., New York - United States, 2002.

[172] D. Pletcher, R. Greff, R. Peat, L.M. Peter, J. Robinson, Instrumental methods in electrochemistry, Woodhead Publishing, Cambridge, 2001. https://doi.org/https://doi.org/10.1016/B978-1-898563-80-8.50003-8.

[173] N. Aristov, A. Habekost, Cyclic Voltammetry - A Versatile Electrochemical Method Investigating Electron Transfer Processes, Cycl. Voltammetry - A Versatile Electrochem. Method Investig. Electron Transf. Process. 3 (2015) 115–119. https://doi.org/10.12691/wjce-3-5-2.

[174] S. Fletcher, C.S. Halliday, D. Gates, M. Westcott, T. Lwin, G. Nelson, The response of some nucleation/growth processes to triangular scans of potential, J. Electroanal. Chem. 159 (1983) 267–285. https://doi.org/10.1016/S0022-0728(83)80627-5.

[175] S.B. Emery, J.L. Hubbley, D. Roy, Voltammetric and amperometric analyses of electrochemical nucleation: Electrodeposition of copper on nickel and tantalum, J. Electroanal. Chem. 568 (2004) 121–133. https://doi.org/10.1016/j.jelechem.2004.01.012.

[176] R.J. Klingler, J.K. Kochi, Electron-transfer Kinetics from Cyclic Voltammetry. Quantitative Description of Electrochemical Reversibility, J. Phys. Chem. 85 (1981) 1731–1741. https://doi.org/10.1021/j150612a028.

[177] I. Lavagnini, R. Antiochia, F. Magno, An Extended Method for the Practical Evaluation of the Standard Rate Constant from Cyclic Voltammetric Data, Electroanalysis. 16 (2004) 505–506. https://doi.org/10.1002/elan.200302851.

[178] H. Djelad, A. Benyoucef, E. Morall, Reactive Insertion of PEDOT-PSS in SWCNT @ Silica Composites and its Electrochemical Performance, Materials (Basel). 13 (2020) 2–10. https://doi.org/10.3390/ma13051200.

[179] M. Velicky, D.F. Bradley, A.J. Cooper, E.W. Hill, I.A. Kinloch, A. Mishchenko, K.S. Novoselov, H. V Patten, P.S. Toth, A.T. Valota, S.D. Worrall, R.A.W. Dryfe, Electron Transfer Kinetics on Mono- and Multilayer Graphene, ACS Nano. 8 (2014) 10089–10100. https://doi.org/10.1021/nn504298r.

[180] K. Avchukir, B.D. Burkitbayeva, A.M. Argimbayeva, G.S. Rakhymbay, G.S. Beisenova, M.K. Nauryzbayev, The Kinetics of Indium Electroreduction from Chloride Solutions, Russ. J. Electrochem. 54 (2018) 1096–1103. https://doi.org/10.1134/s1023193518120042.

[181] Y. Chung, C.-W. Lee, Electrochemical behaviors of Indium, J. Electrochem. Sci. Technol. 3 (2012) 1–13. https://doi.org/10.5229/jecst.2012.3.1.1.

[182] V. Markovoc, B. Lovrecek, Studies of the Electrochemical Kinetics of Indium, J. Electrochem. Soc. 113 (1966) 838–841. https://doi.org/10.1149/1.2424131.

[183] E. Ciro, A.D. Era, M. Pasquali, C. Lupi, Indium electrowinning study from sulfate aqueous solution using different metal cathodes, J. Environ. Chem. Eng. 8 (2020) 103688. https://doi.org/10.1016/j.jece.2020.103688.

[184] M.T. Hsieh, C.T. Chen, T.J. Whang, Triethanolamine-facilitated one-step electrodeposition of CuAlSe2 thin films and the mechanistic studies utilizing cyclic voltammetry, J. Electroanal. Chem. 762 (2016) 73–79. https://doi.org/10.1016/j.jelechem.2015.12.041.

[185] Q. Huang, K. Reuter, S. Amhed, L. Deligianni, L.T. Romankiw, Electrodeposition of Indium on Copper for CIS and CIGS Solar Cell Applications, J. Electrochem. Soc. 158 (2011) D57–D61. https://doi.org/10.1149/1.3518440.

[186] Y.D. Gamburg, G. Zangari, Theory and Practice of Metal Electrodeposition, Springer New York, New York, NY, 2011. https://doi.org/10.1007/978-1-4419-9669-5.

[187] R.C. Valderrama, M. Miranda-Hernández, P.J. Sebastian, A.L. Ocampo, Electrodeposition of indium onto Mo/Cu for the deposition of Cu(In,Ga)Se2 thin films, Electrochim. Acta. 53 (2008) 3714–3721. https://doi.org/10.1016/j.electacta.2007.11.069.

[188] S. Banthia, S. Sengupta, M. Mallik, S. Das, Substrate effect on electrodeposited copper morphology and crystal shapes, Surf. Eng. 0 (2017) 1–8. https://doi.org/10.1080/02670844.2017.1321265.

[189] O. Degtyareva, V.F. Degtyareva, F. Porsch, W.B. Holzapfel, Face-centred cubic to tetragonal transitions in In alloys under high pressure, J. Phys. Condens. Matter. 13

(2001) 7295–7303. https://doi.org/https://doi.org/10.1088/0953-8984/13/33/310.

[190] A. Milchev, Nucleation phenomena in electrochemical systems : thermodynamic concepts, ChemTexts. 2 (2016) 1–9. https://doi.org/10.1007/s40828-015-0022-0.

[191] D.A.C. Brownson, C.E. Banks, The Handbook of Graphene Electrochemistry, 2014. https://doi.org/10.1007/978-1-4471-6428-9.

[192] V. Augustyn, P. Simon, B. Dunn, Pseudocapacitive oxide materials for high-rate electrochemical energy storage, Energy Environ. Sci. 7 (2014) 1597–1614. https://doi.org/10.1039/c3ee44164d.

[193] F. Ferrara, New materials for eco-sustainable electrochemical processes: oxygen evolution reaction at different electrode materials, Università degli studi di Cagliari, 2004.

[194] L.M. Da Silva, L.A. De Faria, J.F.C. Boodts, Determination of the morphology factor of oxide layers, Electrochim. Acta. 47 (2001) 395–403. https://doi.org/10.1016/S0013-4686(01)00738-1.

[195] I.G. Sharma, P. Alex, A.C. Bidaye, A.K. Suri, Electrowinning of cobalt from sulphate solutions, Hydrometallurgy. 80 (2005) 132–138. https://doi.org/10.1016/j.hydromet.2005.08.003.

[196] N. Ipek, N. Lior, M. Vynnycky, F.H. Bark, Numerical and experimental study of the effect of gas evolution in electrolytic pickling, J. Appl. Electrochem. 36 (2006) 1367–1379. https://doi.org/10.1007/s10800-006-9201-4.

[197] T. Fujimura, W. Hikima, Y. Fukunaka, T. Homma, Analysis of the effect of surface wettability on hydrogen evolution reaction in water electrolysis using micro-patterned electrodes, Electrochem. Commun. 101 (2019) 43–46. https://doi.org/10.1016/j.elecom.2019.02.018.

[198] F.W. Ntengwe, N. Mazana, F. Samadi, The dependence of current efficiency on factors affecting the recovery of copper from solutions, J. Appl. Sci. Res. 6 (2010) 1862–1870.

[199] S. Kumar, S. Pande, P. Verma, Factor Effecting Electro-Deposition Process, Int. J. Curr. Eng. Technol. 5 (2015) 700–703.

[200] R. Caminiti, G. Paschina, An x-ray diffraction study of the structure of the aqua indium (III) ion in indium sulphate solution, Chem. Phys. Lett. 82 (1981) 430–433.

[201] W.W. Rudolph, D. Fischer, M.R. Tomney, C.C. Pye, Indium(III) hydration in aqueous solutions of perchlorate, nitrate and sulfate. Raman and infrared spectroscopic studies and ab-initio molecular orbital calculations of indium(III)-water clusters, Phys. Chem. Chem. Phys. 6 (2004) 5145–5155. https://doi.org/10.1039/b407419j.

[202] C. Fink, R. Lester, The electrodeposition of indium from sulfate baths, in: Seventy-Eighth Gen. Meet., Ottawa, Ontario, 1940: pp. 349–372. https://doi.org/https://doi.org/10.1149/1.3071312.

[203] N. Zech, D. Landolt, The influence of boric acid and sulfate ions on the hydrogen formation in Ni-Fe plating electrolytes, Electrochim. Acta. 45 (2000) 3461–3471. https://doi.org/10.1016/S0013-4686(00)00415-1.

[204] K.M. Yin, B.T. Lin, Effects of boric acid on the electrodeposition of iron, nickel and iron-nickel, Surf. Coatings Technol. 78 (1996) 205–210. https://doi.org/10.1016/0257-8972(94)02410-3.

[205] J.P. Hoare, On the Role of Boric Acid in the Watts Bath, J. Electrochem. Soc. 133 (1986) 2491. https://doi.org/10.1149/1.2108456.

[206] M. Lukaszewski, M. Soszko, A. Czerwiński, Electrochemical methods of real surface area determination of noble metal electrodes - an overview, Int. J. Electrochem. Sci. 11 (2016) 4442–4469. https://doi.org/10.20964/2016.06.71.

[207] A. Kahyarian, M. Achour, S. Nesic, CO2 corrosion of mild steel, in: A.M. El-Sherik (Ed.), Trends Oil Gas Corros. Res. Technol., Elsevier, Cambridge, 2017: pp. 149–190. https://doi.org/10.1016/B978-0-08-101105-8.00007-3.

[208] R. Strauss, G.W. Brümmer, N.J. Barrow, Effects of crystallinity of geothite: I. Preparation and properties of goethites of differing crystallinity, Eur. J. Soil Sci. 48 (1997) 87–99. https://doi.org/10.1111/j.1365-2389.1997.tb00188.x.

[209] A.M.P. Sakita, E.C. Passamani, H. Kumar, D.R. Cornejo, C.S. Fugivara, R.D. Noce, A. V. Benedetti, Influence of current density on crystalline structure and magnetic properties of electrodeposited Co-rich CoNiW alloys, Mater. Chem. Phys. 141 (2013) 576–581. https://doi.org/10.1016/j.matchemphys.2013.05.066.

[210] R. Della Noce, A. V. Benedetti, M. Magnani, E.C. Passamani, H. Kumar, D.R. Cornejo, C.A. Ospina, Structural, morphological and magnetic characterization of electrodeposited Co-Fe-W alloys, J. Alloys Compd. 611 (2014) 243–248. https://doi.org/10.1016/j.jallcom.2014.05.157.

[211] E.B. Carneiro-Neto, M.C. Lopes, E.C. Pereira, Simulation of interfacial pH changes during hydrogen evolution reaction, J. Electroanal. Chem. 765 (2016) 92–99. https://doi.org/10.1016/j.jelechem.2015.09.029.

[212] J.P. Hoare, On the Role of Boric Acid in the Watts Bath, J. Electrochem. Soc. 133 (2019) 2491–2494. https://doi.org/10.1149/1.2108456.

[213] J. Horkans, On the Role of Buffers and Anions in NiFe Electrodeposition, J. Electrochem. Soc. 126 (1979) 1861. https://doi.org/10.1149/1.2128816.

[214] G.G. Stoney, The tension of metallic films deposited by electrolysis, Proc. R. Soc. Lond. 82 (1909) 172–175. https://doi.org/https://doi.org/10.1098/rspa.1909.0021.

[215] M. Mallik, A. Mitra, S. Sengupta, K. Das, R.N. Ghosh, S. Das, Effect of Current Density on the Nucleation and Growth of Crystal Facets during Pulse Electrodeposition of Sn − Cu Lead-Free Solder, Cryst. Growth Desing. (2014). https://doi.org/10.1021/cg501440a.

[216] Eurostat, Electricity price statistics - Statistics Explained, Eur. Comm. (2020) 1–12. https://ec.europa.eu/eurostat/statistics-explained/index.php/Electricity_price_statistics (accessed November 2, 2021).

[217] Tradingeconomics, Indium, (2022). https://tradingeconomics.com/commodity/indium (accessed January 28, 2022).